AUSTRALIAN NATIONAL UNIVERSITY

DOCTORAL THESIS

Energy dissipation in multinucleon transfer reactions

Dominic Charles RAFFERTY

A thesis submitted in fulfillment of the requirements
for the degree of Doctor of Philosophy

March 4, 2020

Preface

This thesis reports an experimental investigation of quasi-elastic scattering yields in reactions of various projectile isotopes with heavy target nuclei in the ^{208}Pb region. The data which is presented in this work was obtained from two experiments. One of the experiments was conducted at the Legnaro National Laboratory, of the Istituto Nazionale di Fisica Nucleare (INFN), in Padua, Italy, in June 2011. The other experiment was conducted at the Heavy Ion Accelerator Facility at the Australian National University, in Canberra, Australia, in June 2013. The experiments were in each case supported by local technical staff, as well as the research staff that were employed by the local and collaborating research groups at the time each was conducted.

As the first experiment (at INFN, Italy) preceded the candidacy of the author, the author was not present during the collection of data or set-up of the run. Rather, the author has lead the analysis of data from this experiment, the results of which are reported in this thesis. The analysis procedure involved the use of a dedicated software package (written in `C++`), which was produced and maintained by the local team, as well as some `ROOT` scripts which were developed by the author.

The author was involved in the construction of the ΔE-E telescope used in the ANU experiment in June 2013, and was present prior to and during the experiment during both set-up and data collection. The author was responsible for analysis of the data, the results of which are reported in this thesis. The author designed and implimented the analysis procedure for this experiment, which involved the development of a custom software procedure using the `ROOT` set of `C++` classes.

The results reported in this thesis have been published in part in the following publication:

- *Multinucleon transfer in 16,18 O, 19 F + 208 Pb reactions at energies near the fusion barrier*. In: Phys. Rev. C 94 (2016), p. 024607.

  D. C. Rafferty, M. Dasgupta, D. J. Hinde, C. Simenel, E. C. Simpson, E. Williams, I. P. Carter, K. J. Cook, D. H. Luong, S. D. McNeil, K. K. Ramachandran, Vo-Phuoc, K. and A. Wakhle.

The work conducted as part of this thesis has also been presented at several conferences and meetings. Details of these talks can be found in various conference proceedings, including:

- *Probing cluster structures through sub-barrier transfer reactions*. Heavy Ion Accelerator Symposium, HIAS 2015 123, 03004(2016) 1-5

  D. C. Rafferty, M. Dasgupta, D. J. Hinde, C. Simenel, E. Williams, I. P. Carter, K. J. Cook, D. H. Luong, S. D. McNeil, K. K. Ramachandran Vo-Phuoc, and A. Wakhle.

- *Investigating energy dissipation through nucleon transfer reactions* Heavy-Ion Accelerator Symposium, HIAS 2014 (2015) 7

  D. C. Rafferty, M. Dasgupta, D. J. Hinde, C. Simenel, E. Williams, I. P. Carter, K. J. Cook, D. H. Luong, S. D. McNeil, K. Ramachandran, and A. Wakhle.

During PhD candidacy, the author also contributed to the broader research aim of the nuclear reaction dynamics group at the Australian National University. Details of this work can be found in the following publications:

1. *Exploring Zeptosecond Quantum Equilibration Dynamics: From Deep-Inelastic to Fusion-Fission Outcomes in Ni 58+ Ni 60 Reactions*. Physical review letters, 120(2), p.022501. 2018

   E. Williams, K. Sekizawa, D.J. Hinde, C. Simenel, M. Dasgupta, I.P. Carter, K.J. Cook, D.Y. Jeung, S.D. McNeil, C.S. Palshetkar and D.C. Rafferty

2. *Capture cross sections for the synthesis of new heavy nuclei using radioactive beams*. Physical Review C, 97(2), p.021602. 2018

A. Wakhle, Hammerton, K., Kohley, Z., Morrissey, D.J., Stiefel, K., Yurkon, J., Walshe, J., K.J. Cook, M. Dasgupta, D.J. Hinde and Jeung, D.J.

3. *Fission cross sections as a probe of fusion dynamics at high angular momentum*. Physical Review C, 98(4), p.044603. 2018

   C.S. Palshetkar, D.J. Hinde, M. Dasgupta, E. Williams, K. Ramachandran, I.P. Carter, K.J. Cook, D.Y. Jeung, D.H. Luong, S.D. McNeil and D.C. Rafferty

4. *Nuclear structure dependence of fusion hindrance in heavy element synthesis*. Physical Review C, 97(6), p.064618. 2018

   J. Khuyagbaatar, David, H.M., D.J. Hinde, I.P. Carter, K.J. Cook, M. Dasgupta, C.E. Düllmann, D.Y. Jeung, B. Kindler, B. Lommel and D.H. Luong

5. *Interplay of spherical closed shells and N/Z asymmetry in quasifission dynamics*. Physical Review C, 97(5), p.054603. 2018

   Mohanto, G., D.J. Hinde, Banerjee, K., M. Dasgupta, D.Y. Jeung, C. Simenel, E.C. Simpson, A. Wakhle, E. Williams, I.P. Carter and K.J. Cook

6. *Evidence for the Role of Proton Shell Closure in Quasifission Reactions from X-Ray Fluorescence of Mass-Identified Fragments*. Physical review letters, 119(22), p.222502. 2017

   M. Morjean, D.J. Hinde, C. Simenel, D.Y. Jeung, M. Airiau, K.J. Cook, M. Dasgupta, A. Drouart, D. Jacquet, S. Kalkal and C.S. Palshetkar

7. *Fusion and quasifission studies for the Ca 40+ W 186, Os 192 reactions*. Physical Review C, 96(3), p.034608. 2017

   E. Prasad, D.J. Hinde, E. Williams, M. Dasgupta, I.P. Carter, K.J. Cook, D.Y. Jeung, D.H. Luong, C.S. Palshetkar, D.C. Rafferty and K. Ramachandran

8. *Asymptotic and near-target direct breakup of Li 6 and Li 7*. Physical Review C, 93(4), p.044605. 2016

   S. Kalkal, E.C. Simpson, D.H. Luong, K.J. Cook, M. Dasgupta, D.J. Hinde, I.P. Carter, D.Y. Jeung, Mohanto, G., C.S. Palshetkar and E. Prasad

9. *Reduced quasifission competition in fusion reactions forming neutron-rich heavy elements*. Physical Review C, 91(4), p.041602. 2015

   Hammerton, K., Kohley, Z., D.J. Hinde, M. Dasgupta, A. Wakhle, E. Williams, V.E. Oberacker, A.S. Umar, I.P. Carter, K.J. Cook and J. Greene

10. *Observation of mass-asymmetric fission of mercury nuclei in heavy ion fusion*. Physical Review C, 91(6), p.064605. 2015

    E. Prasad, D.J. Hinde, K. Ramachandran, E. Williams, M. Dasgupta, I.P. Carter, K.J. Cook, D.Y. Jeung, D.H. Luong, S.D. McNeil and C.S. Palshetkar, 2015.

11. *Evolution of signatures of quasifission in reactions forming curium*. Physical Review C, 88(3), p.034611. 2013.

    E. Williams, D.J. Hinde, M. Dasgupta, R. du Rietz, I.P. Carter, M. Evers, D.H. Luong, S.D. McNeil, D.C. Rafferty, K. Ramachandran and A. Wakhle

Declaration of Authorship

I, Dominic Charles RAFFERTY, declare that this thesis titled, "Energy dissipation in multinucleon transfer reactions" and the work presented in it are my own. I confirm that:

- This work was done wholly or mainly while in candidature for a research degree at this University.
- Where any part of this thesis has previously been submitted for a degree or any other qualification at this University or any other institution, this has been clearly stated.
- Where I have consulted the published work of others, this is always clearly attributed.
- Where I have quoted from the work of others, the source is always given. With the exception of such quotations, this thesis is entirely my own work.
- I have acknowledged all main sources of help.
- Where the thesis is based on work done by myself jointly with others, I have made clear exactly what was done by others and what I have contributed myself.

Signed:

_____

Date:

_____

Abstract

Nuclear reactions are incredibly complex, involving collisions between composite systems where many-body dynamics determine outcomes. Successful models have been developed to explain the particular behaviour of reactions in distinct energy and mass regimes, but a unifying picture remains elusive.

Particular problems have become evident in standard coupled channels approaches to calculating fusion cross sections, with hindrance effects having been identified both above and below the barrier. Recent work [1, 2] has demonstrated inadequacies in these approaches using static internuclear potentials, and have shown the need to address some hidden physics. The dissipation of energy from the relative motion of the collision partners to internal states is known to be important in these processes, but is yet to be successfully incorporated into reaction models.

Multinucleon transfer reactions are a useful tool to examine these aspects, as they span the transition from the quasielastic regime, where the colliding nuclei barely overlap, to the deep inelastic regime, where collisions are violent with significant redistribution of mass and charge between the fragments, as well as large dissipation of kinetic energy from the relative motion [3]. This PhD thesis examines the onset of dissipation as the bombarding energy approaches the Coulomb barrier over a range of light to medium mass projectiles incident on heavy targets.

This investigation has focussed on studying the quasielastic scattering yields that are detected at backward angles. These products are of interest to the question of mechanisms that hinder fusion, as they represent the flux that fails to penetrate the fusion barrier at low angular momentum and that is instead reflected. By identifying these products uniquely in mass and charge, together with an accurate measurement of total kinetic energy losses, I have been able to establish which reaction modes are the most important "doorways" for energy dissipation to proceed through.

I present in this work the systematic trends in dissipative effects as the mass asymmetry of the reaction system changes, with measurements at bombarding energies spanning the fusion barrier. This work illustrates the increasing importance of dissipative effects as the

charge product of the reactants increases, and identifies a stark distinction in the nature of the dominant transfer mechanism between light and medium mass projectiles when they are incident on heavy targets. While direct transfer involving clusters is very important in light nuclei, deep-inelastic transfer involving mutual nucleon exchange becomes much more important for reactions involving medium-mass projectiles.

There is a growing realisation in the nuclear reactions community that energy dissipation is an important effect in fusion dynamics both above and below the barrier, yet this remains an area that has not been studied in detail. This work makes a first attempt to identify the important parameters and steps towards a phenomenological footing for understanding dissipative processes in nuclear reactions.

Acknowledgements

The work presented in this thesis would not have been possible without the support of my friends and colleagues in the Department of Nuclear Physics at the Australian National University. I would like to extend my sincere gratitude to my supervisory panel, Prof. Mahananda Dasgupta, Prof. David J. Hinde, and Prof. Cédric Simenel for their patience and support throughout my project.

A special thanks to both Dr. Maurits Evers for his earlier work on the topic and being very helpful in getting me started on the project reported in this thesis, and for offering assistance and advice throughout my PhD candidacy, even long after moving on to new challenges. Dr. Daniele Montanari also deserves a special mention, having provided invaluable advice in conducting the analysis of the data obtained in the PRISMA experiment, again being willing to offer advice and assistance long after moving on from the PRISMA collaboratiion.

I would like to offer my gratitude to my labmates within the reaction dynamics group, who collectively made the group an interesting, challenging, and fun place to work. Many thanks to Dr. Elizabeth Williams for her electronics expertise in setting up experiments. Thanks to Dr. Edward Simpson and Ms. Lauren Bezzina for reading through my thesis chapters. And to all other group colleagues who have been a pleasure to work with and helped me along my way over the years: Kaitlin, Ian, Kirsten, Chandrima, Yun, Sunil, Prasad, Aditya, Huy, Chandni, Ramachandran, Steven, Gayatri, Alina, Ellen, Joe.

Many thanks also to the technical support staff at both Legnaro National Laboratory and the ANU Heavy Ion Accelerator Facility for providing excellent support in preparation of, and during the experiments.

Contents

Chapter 1

Introduction

Since ancient times, human societies and civilizations in every corner of the globe have gazed upon the night sky and contemplated their place in the cosmos. The vast expanse of the universe is evident in the thousands of tiny lights visible to the naked eye against the dark backdrop of empty space. The stars were thought by many early human cultures to be Gods or spirits, and rich mythologies were developed to describe the heavens.

In western cultures, the Orion constellation derives it name from the ancient Greek myth of Orion the hunter. Different versions of the legend exist, but the most complete account of the story was told in a lost work attributed to the poet Hesiod (650 - 750 BC)— the *Astronomia* [4]. Whilst the original text is unknown, the myth was retold in *Catasterismi*, thought to be written by the astronomer Eratosthenes (276 - 194 BC), on the constellations as they were interpreted in Hellenistic culture [5]. A supernaturally gifted but egocentric hunter, Orion boasted of his intention to slay every beast on earth. To stop him, the earth mother Gaia sent a giant scorpion to ambush him on his return from a hunt. On his death, his hunting companions, the goddess Artemis and her mother Leto, pleaded with Zeus to honour the great hunter by raising his physical form to the heavens. Zeus consented and granted their wish, but raised also the scorpion that killed him to serve as a warning to mortals to maintain humility amongst nature [6]. The constellations Orion and Scorpius are located on opposite sides of the sun, and never seen in the night sky together from any place on earth— Orion forever fleeing the beast that bested him. Perhaps the most recognisable feature of the constellation are the three star systems Alnitak, Alnilam, and Mintaka, known as Orion's belt.

In the southern hemisphere, Orion's belt is known by the indigenous Yolngu people of the Arnhem land in northern Australia as Djulpan. Aboriginal Australian cultures have a rich oral folklore tradition which has passed down through the generations over many thousands of years. The Yolngu tell the story of three brothers of the king-fish (or Nulkal) clan, who set off in a canoe on a fishing trip. After many hours at sea, they had no luck in catching anything other than king-fish. As members of the Nulkal clan, tradition forbade them from eating this type of fish, and they were obligated to return those caught unharmed to the water. Eventually, hunger got the better of them, and they broke with custom and ate one of their catch. This angered the ever-watchful Walu, the sun goddess. In her fury, she created a huge storm, and a powerful water spurt launched the brothers and their canoe into the sky, where they can still be seen today floating through the stars. The three star systems known to the Greeks as Orion's belt represent for the Yolngu the three brothers [7] in the canoe. Figures 1.1 and 1.2 show how these and other adjacent stars were represented in the constellation in the two interpretations.

Whilst stars have fascinated human cultures since prehistory, and have been studied extensively throughout the ages, it wasn't until the 20th century that the secrets of their energy source were finally revealed. The nuclear age arguably began with the experiments of Geiger and Marsden under the direction of Ernest Rutherford, who in 1911 published the results of their experiments scattering alpha particles from a gold foil, revealing the structure of atoms to the scientific community and identifying the dense core which became known as the atomic nucleus [8].

The next piece of the puzzle fell into place in 1920, when Francis William Aston reported his precise mass measurements of the lightest elements, noting importantly that helium atoms appeared to be lighter than the sum of the masses of four hydrogen atoms (the neutron would not be discovered until 1932 by James Chadwick [9]). By this time Albert Einstein has already established the mass-energy equivalence as a consequence of his special theory of relativity, neatly expressed in the famous equation $E = mc^2$. Sir Arthur Eddington immediately realised from these results that the sun and other stars could be fueled by the conversion of hydrogen into helium— the process we now call nuclear fusion [10, 11].

FIGURE 1.1: The Orion constellation. The hunter's sword is represented by the stars in the top of the image and those in the bottom right are the shield. Meissa is the head, while the three star systems Alnitak, Alnilam and Mintaka make up Orion's belt— the most recognisable feature of the constellation.

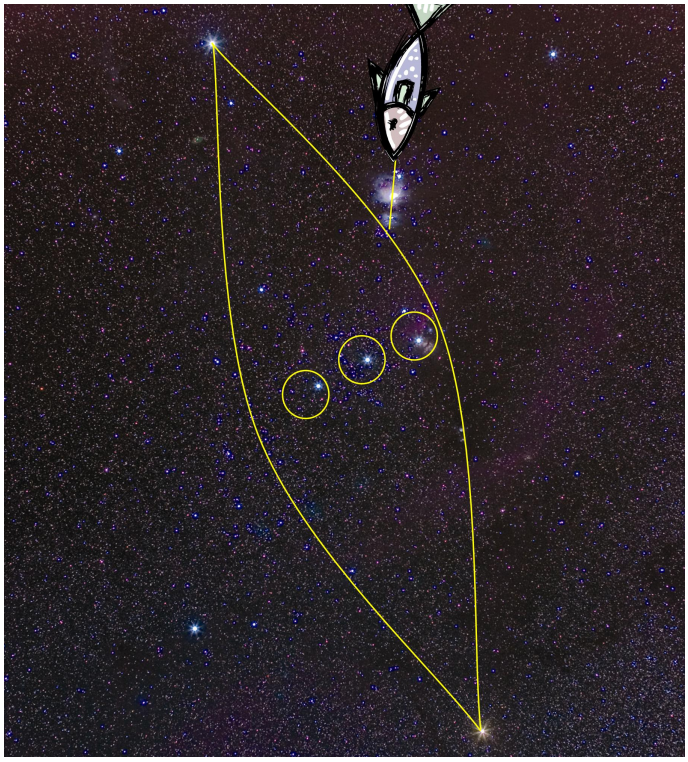

FIGURE 1.2: Djulpan— the canoe in Orion. The three brothers of the Yolngu tale are represented by the star systems Alnitak, Alnilam and Mintaka. The bow of the canoe is represented by the red giant star Betelgeuse, and the stern by Rigel. Permission for reproduction by Prof. Ray Norris [7]

The development of nuclear physics continued through the early 20th century with a series of rapid developments and discoveries [12, 13, 14, 15]. George Gamow made the first steps in developing a quantum mechanical understanding of nuclear processes in the 1920s [12]. In the 1930s, Carl von Weizsäcker [16] and, independently, Hans Bethe [13] worked out the CNO cycle, refining the models of energy generation in stellar furnaces. Meanwhile, research on radioactivity led to the discovery of nuclear fission at the end of the decade as a result of the work of Otto Hahn, Fritz Strassmann, and Lise Meitner [14, 15].

By the outbreak of the second world war, physicists around the world were well aware of the potential for the creation of a nuclear weapon by means of a nuclear chain reaction, the idea having been patented by Leó Szilárd in 1934 [17]. Fearful that Nazi Germany could be developing an atomic bomb, in 1939 Szilárd and Einstein drafted a letter of warning to U.S. president Franklin D. Roosevelt [18]. Nuclear fission research began in earnest by the U.S. government with the establishment of the Advisory Committee on Uranium, eventually evolving into what is today known as the Manhattan project, and culminating in the weapons dropped on Hiroshima and Nagasaki in August 1945, taking over 100,000 human lives and etching in the world's collective consciousness the awesome and terrifying power of nuclear reactions.

Today the prospect of nuclear annihilation continues to haunt the world, yet the nuclear revolution has brought many benefits to humankind. Our understanding of the evolution of the universe and astrophysical phenomena has been transformed. Medical uses of radiopharmaceuticals and radiation detection techniques offer physicians unprecedented insight into the workings of the human body. Controlled nuclear reactions hold promise of clean and practically limitless sources of energy to power the societies of the future. These and many other applications are the fruition of the amazing insights and work of the pioneers of the early 20th century.

Despite a century of advances in applications of nuclear phyiscs, many questions still remain as to the precise nature of the mechanisms and dynamics of nuclear reactions, as well as the limits of nuclear stability. Nuclei are many-body quantum systems, and

though the bulk properties of many nuclei and their interactions are now well understood, the microscopic dynamics are incredibly complex and remain an active area of research. The interactions between nucleons inside the nuclear medium are elusive to common probes so an advanced understanding relies on extremely computationally intensive calculations based on limited experimental information. These microscopic properties are known to have important effects on reactions but the precise role is still under scrutiny.

The understanding of nuclear reactions in the astrophysical regimes is extrapolated from measurements under laboratory conditions, where practical considerations constrain the possibility of measurement of reaction modes with small cross sections. As will be discussed in the following, some of these assumptions have in recent years been called into question. In this work the focus is on current unanswered questions surrounding fusion reactions involving heavy nuclei, with relevance to the synthesis of heavy elements in nature and current efforts to produce superheavy elements in the laboratory beyond the existing bounds of the periodic table.

1.1 The fusion process

In nuclear fusion two nuclei form a composite system that can become a compound nucleus that may remain, stabilise and exist as a new, larger nucleus containing most of the nucleons of the original two nuclei. A massive rearrangement of the nucleons and dissipation of kinetic energy of the collision into internal excitations of the constituents occurs as the two nuclei merge. The compound nucleus is fully equilibrated (in mass, energy and shape) and retains no memory of the reaction by which it is formed [19].

As nuclei are strongly interacting many-body quantum systems, it is difficult to model the multitude of processes that ultimately lead to the thermally equilibrated compound nucleus. Theoretical descriptions have therefore progressed in stages as experimental

measurements expanded from using light nuclei to those involving heavy nuclei. Increased sensitivity and precision of fusion measurements in the last two decades, together with the necessity to obtain a consistent description of reactions around the barrier has highlighted the need for a more realistic model of fusion. The studies in this thesis are aimed at understanding energy dissipation as the two nuclei start interacting en route to fusion as a possible reason why fusion does not occur.

1.2 A simple model of fusion

A natural starting point for any discussion of nuclear reactions begins with the internuclear potential. Whilst the mathematical details of the nuclear reactions of interest to this work will be discussed in detail in Chapter 2, a brief discussion of the important interactions is necessary for this introduction. When two nuclei are on a collision trajectory, the positively charged protons in each of the reactants produces a long range electrostatic repulsion between them. When the collision partners are close enough together, they begin to be influenced by the strongly attractive nuclear forces. The combined effect of these interactions, shown schematically in Figure 1.3, is to produce a potential barrier which must be traversed in order for the nuclei to amalgamate to form a single (fused) nucleus. The potential barrier is referred to as the fusion or capture barrier, and is characterized by its height (V_B) and radius (r_B). In the classical picture, any system of colliding nuclei with an energy of relative motion higher than the barrier V_B will lead to fusion (Figure 1.3), whilst all the flux with energy lower than the barrier energy will be reflected. In reality however, the wave nature of these quantum objects allows them to penetrate through the barrier, resulting in a non-zero probability for fusion even at energies far below the barrier energy, as illustrated schematically in Figure 1.3.

Determining the probability for fusion to occur is a matter of calculating the penetrability for each relevant value of the quantised angular momentum (partial wave l) through the (l-dependent) barrier, and summing the contributions from each partial wave to give the total fusion cross section. This value of course varies with the collision energy relative to the barrier energy, since the barrier penetrability is dependent on the barrier energy and

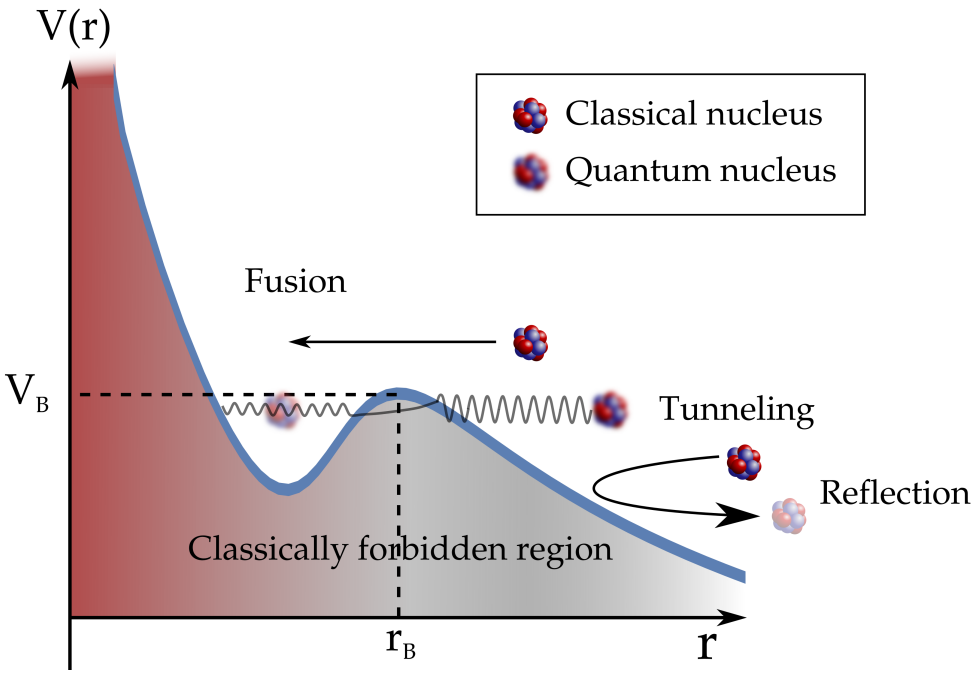

FIGURE 1.3: Schematic illustration of nuclear fusion in the classical and quantum picture. The superposition of the different forces acting between colliding nuclei gives rise to the internuclear potential (blue line), with the outer point of inflection called the fusion barrier, with height V_B at an internuclear separation of r_B. Classically, any nuclear binary system with an energy lower than the energy of the fusion barrier will result in reflection. In the quantum world, the classically forbidden region can be tunnelled through, allowing the nuclei to form a composite system even at incident energies below the barrier energy.

the width that must be tunnelled through. This is known as the single barrier penetration model (1DBPM) of fusion, so called as the relative motion of the collision partners is the only degree of freedom. Indeed, such approaches are reasonably accurate in calculating fusion probabilities in the energy region around the barrier in the simplest examples where the nuclei can be considered inert. For example, in fusion between light nuclei, where the internal structures and excitation spectra of the reactants are relatively simple such that they do not play a role in the fusion process. However, heavier nuclei have many low-lying excited states, and in particular the collective states can easily be excited as the colliding nuclei approach each other. It has been found that the quantum structure of the colliding nuclei affect the fusion of heavy nuclei and more complex models need to be considered.

1.3 Microscopic and macroscopic models of fusion

More complex nuclear reaction models generally fall into two main categories. In order to exactly describe the behaviour of nuclei, their nature of being composite systems of nucleons demands that the interactions between all of the constituent particles should be considered. Microscopic theories, such as the various dynamical mean-field models utilizing Hartree-Fock methods, treat all nucleons explicitly. The very large number of degrees-of-freedom mean that mean field approximations must be made, but the calculations are still extremely intensive— growing quadratically more so as the number of nucleons involved increases. At present there is also no effective theoretical framework for the treatment of the tunnelling of a quantum many-body system through a potential barrier.

Macroscopic theories, on the other hand such as the Coupled Reaction Channels (CRC) approaches, consider only the overall evolution of the two nuclei— the nuclei are pictured as a whole (with quantum states associated with the separated nuclei) as opposed

to composite systems of nucleons, an approximation that significantly simplifies the modelling of their behaviour [20]. Macroscopic models can generally be considered phenomenological, making use of empirical information on nuclear structure and the internuclear potential. On the other hand, microscopic models attempt to derive these properties from the fundamental interactions between nucleons. Some studies have additionally combined the two pictures— for instance using microscopically derived properties within the overall framework of the macroscopic models [21].

CRC models of sub-barrier nuclear fusion [22, 23, 24, 25, 26] were developed to describe the fusion process with a fully quantal representation of the physical reaction system, in which the colliding nuclei are considered to be in coherent superpositions of their intrinsic states. Due to practical reasons, a limited number of low energy states of the projectile and target are included. Couplings between internal degrees of freedom in the projectile and target and the relative motion of the system can be included in the Hamiltonian of the system of coupled equations and the Schrödinger equation is solved numerically. Such calculations can reproduce the observed enhancements in fusion cross sections (with respect to single barrier penetration models) at energies in the region of the fusion barrier across a wide range of reaction systems.

Though highly successful in the near-barrier region, and offering important insights into the physical mechanisms underlying fusion and other reaction modes, it has become increasingly apparent in the last $\sim$ 15 years that standard implementations of the coupled-channels formalism are not adequate for a complete description of fusion reactions [1, 27, 28, 29]. The shortcomings of CRC models of fusion are evident in the discrepancies observed both far below [2, 27, 30, 31, 32, 33] and above [2, 34] the fusion barrier, with overpredictions of cross sections compared to experimental data. The effects in these regimes, discussed briefly in the next two sections, have been referred to in the literature as the hindrance or suppression of fusion respectively.

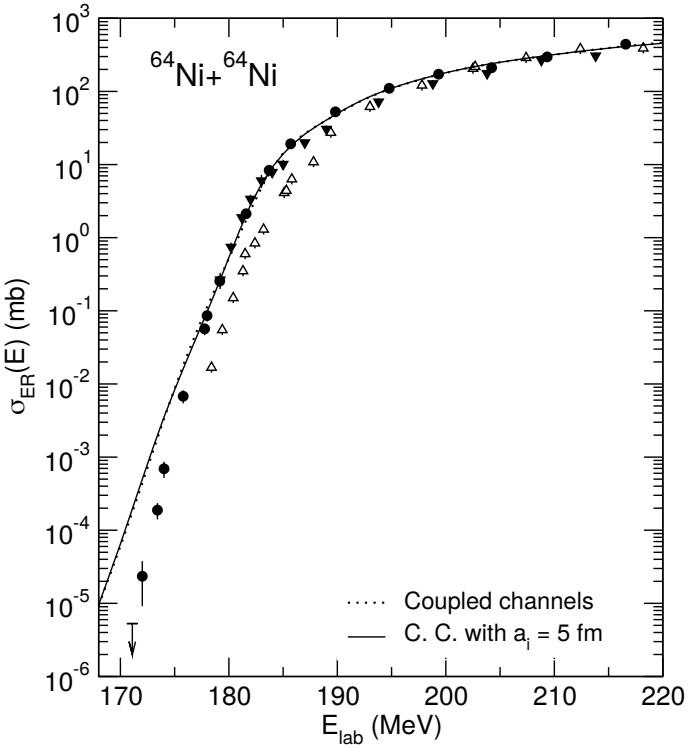

FIGURE 1.4: Fusion hindrance exhibited in ^{64}Ni + ^{64}Ni. Adapted from [35]. Data in the figure are taken from [35] (black circles), [36] (black triangles), and [37] (hollow triangles). The results of two calculations given in Ref. [35] are shown; the dotted line results from using 0.676 fm for the diffuseness parameter of the real part of the Woods-Saxon potential, and the solid line when the diffuseness parameter is changed to 0.5 fm, for radii inside the barrier. Further details can be found in Ref. [35].

1.4 Hindrance of fusion at energies far below the barrier

The standard CRC model increasingly over predicts the measured fusion cross-sections as the energies fall far below the barrier ($\sim 0.9V_B$), as can be seen in Figure 1.4. This has been referred to as *hindrance* in the literature. It was initially observed in the fusion of the heavy systems of ^{60}Ni + ^{89}Y [30] and ^{64}Ni + ^{64}Ni [35], and was later observed in the fusion of two closed shell nuclei ^{16}O + ^{208}Pb.

Since then, the deep sub-barrier fusion hindrance phenomenon has been seen to be present in many reaction systems, and appears like it could be a universal feature of fusion reactions in all systems at low enough energy [31, 32, 35, 38, 39, 40, 41, 42]. Hindrance effects have also been observed in some systems of astrophysical importance— such as ^{12}C + ^{12}C, ^{12}C + ^{16}O, and ^{16}O + ^{16}O [43]— reduced rates of such reactions in the relevant

energy regimes may have important consequences in determining the life cycle of the star. It has been suggested that such effects would include the delayed onset of carbon burning in stars [44]. The measurement of fusion cross sections of astrophysically important systems in the relevant energy regimes is plagued with experimental difficulties due to the very small cross sections and large background [45], meaning that it is difficult to observe some of the signatures of the onset of the hindrance effect. Alongside the complex resonant behaviour of the fusion cross sections observed in some reactions relevant to stellar nucleosynthesis [46, 47, 48], the presence or otherwise of a hindrance effect in the region of the Gamov window could be very important for the inputs to astrophysics models.

The physical origin of the observed hindrance has been a subject of contention, with a number of different theoretical models proposed to attempt to explain the phenomenon. Most phenomenological attempts have attempted to reconcile the hindrance effects with the otherwise successful CRC framework by modifying either the internuclear potential or the coupling effects. The form of the internuclear potential is a crucial component of CRC models and thus an important factor to scrutinize in the investigation of the hindrance phenomena. Generally the commonly used potential models (such as the double-folding or the Woods-Saxon forms— see Section 2.5.1) give a satisfactory description of the experimental data for elastic and inelastic scattering — these reaction modes being influenced only by the outer part of the potential. There is a consensus that the parameterisations of such models are suitable for the description of simpler scattering reactions at large separations (i.e. the flux reflected from the barrier, as illustrated in Figure 1.3). However, fusion reactions will also be sensitive to the inner part of the potential that is not so easily probed.

It has been shown [2] that varying the parameters of the Woods-Saxon nuclear potential (particularly the fall-off of the tail region) can improve agreement in certain energy regions (either in the deep sub-barrier or above barrier). However, optimizing the potential to improve agreement of the deep sub-barrier predictions causes a departure of the CRC predictions above barrier, and vice versa. It has become clear that CRC approaches using standard Woods-Saxon parameterizations are inadequate to treat this problem—

in particular it has been suggested that important dynamic effects en route to fusion are not being properly accounted for [2, 34, 49].

Mişicu and Esbensen [33, 50] proposed a model in which the hindrance arises as a result of the nuclear incompressibility due to large nuclear matter overlap. A phenomenological potential including an additional repulsive component (inside the barrier) is used within the CRC framework, leading to a shallower potential well and effectively cutting off the higher partial wave contributions to the fusion cross section. This approach has been seen to reproduce the fusion hindrance observations in several different systems [40, 41]. However, an additional imaginary term is needed in the potential model to reproduce the fusion suppression at above barrier energies (see next section).

Ichikawa, Hagino, and Iwamoto [51, 52, 53] alternatively proposed an extension to the standard CRC framework in which the fusion dynamics are treated differently once the nuclei come into contact and the matter densities overlap. At internuclear separations greater than the touching point (where the nuclear surfaces just come into contact—equal to the sum of the radii of the collision partners), a standard implementation of the CRC model is applied taking into account the coupling effects in the target and projectile through a two-body potential. Beyond the touching point, the dinuclear system is instead represented by a one-body potential to account for the evolution of the system following neck formation. This one-body potential results in a thicker potential barrier, with a consequent reduction in the fusion probability. Indeed, extracting the effective potential from deep sub-barrier fusion data using the potential inversion method results in a barrier shape that supports this idea [54]. They found that the energy threshold at which the hindrance begins to take effect correlates strongly with the potential energy of the system at the touching point.

Transitioning to a one-body potential cannot be directly implemented within the standard CRC framework, since this would result in a double counting of the channel coupling effects. Ichikawa and Matsuyanagi [55, 56] have instead incorporated the adiabtic dynamics by introducing an eigenchannel dependent damping factor in the coupling potential at separations smaller than the touching point, which results in a reduction in

the strength of excitations to the projectile/target vibrational states as the matter overlap between the collision partners increases. This damping of the quantum vibrations causes the couplings between the relative motion and collective excitations in the nuclei to vanish, and ensures a smooth transition between the two-body dynamics at large internuclear separations with the evolution of the dinuclear system beyond the touching point. This model has been applied to a number of systems with success.

The models described above represent two opposing pictures. The former, proposed by Mişicu and Esbensen, assumes that the fusion process happens very quickly, such that the densities of the collision partners do not evolve with time as the compound nucleus is formed. The effect of incompressibility has recently been tested more rigorously through fully microscopic density-constrained frozen Hartree-Fock calculations [57], where the Pauli exclusion effects are included exactly and the internuclear potential is derived from the fundamental interactions between nucleons. This analysis, whilst demonstrating a slight hindrance effect is indeed caused by the Pauli repulsion, has shown that this cannot be the full picture as only a fraction of the observed suppression is accounted for. In the approach suggested by Ichikawa, Hagino, and Iwamoto, the reverse is assumed— the system instead evolves smoothly between a diabatic two-body to an adiabatic one-body potential as the compound nucleus is formed.

These attempts to understand the deep sub-barrier fusion hindrance have shown that the effect can be reproduced by modifying the potential or couplings used in CRC calculations. However, these approaches do not address self-consistently the problems at above barrier energies [1, 2]. Moreover, whilst the approaches mentioned above have demonstrated success in reproducing the observed hindrance in the sub-barrier region, the inclusion of additional adjustable parameters whose magnitudes cannot be physically justified means that these models lack predictive power. As mentioned earlier, arguably the most important consequence of the deep sub-barrier hindrance phenomenon could be for the astrophysically relevent reactions. However, since the causes of the hindrance phenomena are not understood, it is difficult to know whether the reactions of astrophysical interest would be severely impacted or not. It is therefore important that the

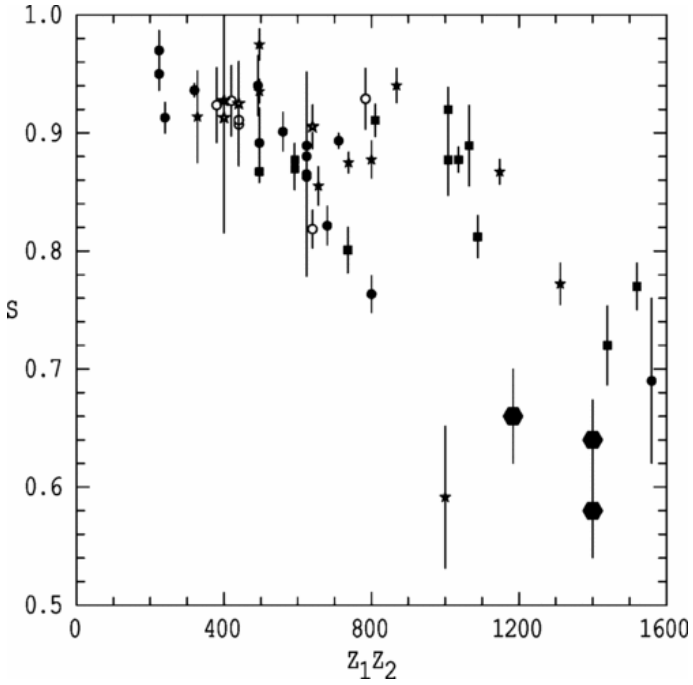

FIGURE 1.5: Fusion suppression factor (S) is found to decrease with increasing product of the projectile and target proton numbers ($Z_1 Z_2$). The line guides the eye. (Figure adapted from [28].

hindrance phenomenon is understood from a perspective that allows not only an explanation of existing data, but also enables predictions of reaction systems that cannot be measured.

1.5 Suppression of fusion at above barrier energies

Precision measurements of fusion cross-sections in the 1990s highlighted the fact that calculations (CRC or 1DBPM) using the standard Woods-Saxon form of the nuclear potential overestimate the measured cross-sections [58]. An increasing number of precision fusion measurements for a range of target-projectile combinations allowed a systematic study to be performed in 2004 [28]. This study found that the suppression of fusion increases with increasing projectile-target charge product ($Z_1 Z_2$), as can be seen in Figure 1.5.

The measured fusion cross sections had often been reproduced by increasing the diffuseness [58] of the Woods-Saxon nuclear potential from the expected value of $\sim$0.65 fm (obtained from elastic scattering data and consistent with nuclear matter distributions)

to values in the range of 0.75-1.5 fm. However, these values are inconsistent with that required to reproduce the measured quasi-elastic scattering [59], as well as fusion cross sections at deep sub-barrier energies [2].

It has been argued that elastic and quasi-elastic processes are sensitive to the nuclear potential at larger separations, whilst fusing nuclei probe the nuclear potential at smaller separations. Thus, modifying the potential at smaller separations, whilst keeping the exterior consistent with a standard Woods-Saxon form could be a possible solution. This idea was implemented in the prescription of Mişicu and Esbensen [33, 50], as discussed in Section 1.4. The small depth of ∼10 MeV of the attractive nuclear potential in this model results in the pocket rapidly disappearing with increasing angular momenta, and calculated fusion cross sections lie below those measured. An additional short-ranged imaginary potential [33] was introduced to describe the above-barrier data, but this does not reproduce the cross-sections at energies far below the barrier. A consistent description of fusion from far-below to above the barrier was thus not achieved, and the model cannot be used to make predictions either below or above the barrier. The Hartree-Fock calculations [57] that include Pauli exclusion effects show that the nuclear potential deviates from the Woods-Saxon form with increasing nuclear matter overlap. However, the modifications are not as large as proposed in [33]. Taken together these observations indicate that a crucial aspect of the underlying physics may be missing in the models.

1.6 Dissipation of kinetic energy en route to thermalisation

In the physical picture of fusion, the formation of a fully equilibrated compound nucleus is understood to occur as the kinetic energy in the centre-of-mass system is fully converted to a multitude of excitations of the constituent nucleons. However, dissipation of kinetic energy due to complex excitations (as opposed to excitations of distinct low energy states of the colliding nuclei) must also occur en route to fusion as evidenced by the observation of deep inelastic processes [60, 61]. Deep inelastic collisions, exhibiting strong dissipation of kinetic energy, have been observed in reactions of very heavy nuclei (typical $Z_1 Z_2 \sim 1600$ or more) at energies above the barrier.

In the CRC model as applied to peripheral and fusion reactions, the system is assumed to be in a coherent superposition of discrete low-energy states of the separated nuclei until they reach a separation well inside the barrier (typically at the position of the minimum of the potential pocket). Fusion, which occurs due to the physical process described above, cannot be treated explicitly in the CRC approach [2, 55]. It is instead (implicitly) assumed that damping of kinetic energy to complex excitations occur *only* after the barrier is passed, and thus an incoming wave boundary condition (or imaginary potential) is applied inside the barrier to mimic the formation of the fused nucleus. However, as discussed above, experimental evidence from reactions of heavy nuclei suggests dissipation of energy into complex excitations can occur even before the barrier is reached. Dissipation of kinetic energy in such a manner will result in a lower probability of the projectile penetrating the barrier, affecting both below- and above-barrier fusion.

Unfortunately, including dissipation in quantum mechanical models is difficult, and dissipation is therefore treated in classical models. However, it is clear that any realistic model of fusion must be quantum mechanical due to the critical role played by quantum superposition effects. There have been limited attempts to include dissipative effects within quantum models of nuclear reactions. One [62] has been based on the idea that since fusion involves a transition from two initially separated nuclei in a coherent superposition to an irreversible outcome (fusion), the process can be viewed as one of quantum decoherence [2]. The coupling of a quantum system to environmental degrees of freedom results in quantum entanglement and the loss of coherence. The question is what constitutes the environment, since nuclei are isolated quantum systems in the sense that they do not interact with an external environment (due to the high energy scales of nuclear interactions). It was argued that since the CRC model considers only a small subset of the internal states of the collision partners in the model space, only a reduced quantum system is considered, which can in principle interact with the environment of states neglected in the adopted representation of the reaction system. However, these states can't be considered to be connstituting an external environment. The work of Diaz-Torres [62] used a density matrix approach to model a gradual onset of decoherence as the projectile penetrates the barrier, allowing the dissipation of kinetic energy via the decay of giant

dipole vibrational states. A reduction of the tunnelling probability was observed, but significant model developments would be required to understand what constitutes an external environment to the colliding nuclear system before comparisons with experimental measurements can be made.

At present, theoretical models offering a fully quantal treatment of fusion alongside energy dissipation are in their infancy. For example, recent work [63] has studied quantum tunnelling in a one-dimensional potential in the presence of energy dissipation, and observed a reduction of tunnelling probability. Developing a quantum model incorporating dissipation is an attractive idea since it would have the potential to describe not only tunnelling in the sub-barrier regime, but also providing a fully quantal treatment of the deep-inelastic scattering phenomenon (which has traditionally been dealt with through classical or semi-classical models in the past [56]), and a self-consistent means of resolving both the above-barrier and sub-barrier hindrance effects.

1.7 This Work

It is clear that fusion will be suppressed if dissipation of kinetic energy to complex excitations (distinct from excitations of discrete states that can be treated explicitly in CRC) occurs at separations larger than the barrier radius. The main questions are:

- Do such dissipative effects occur in reactions of lighter nuclei ($Z_1 Z_2 << 1600$) and at energies around the barrier?
- What are the mechanisms that cause it?
- How do they evolve with increasing $Z_1 Z_2$?

This thesis aims to address these questions by measuring the backscattered nuclei (i.e. nuclei that did not fuse) and identifying individual isotopes to enable the determination of excitation energies of these (projectile-like) fragments. The measurements were carried out at energies spanning the barrier region to far-below barrier. Prior to this work, sub-barrier measurements of the back scattered flux in reactions of ^{16}O + ^{208}Pb showed that

transfer of 2-protons leads to excitation energies of up to 13 MeV, indicating that multi-nucleon transfer is perhaps the doorway to dissipation of kinetic energy into complex (irreversible) excitations.

1.8 Summary of thesis chapters

In this opening chapter the state of knowledge of nuclear fusion of heavy nuclei and the current open questions have been briefly presented. This thesis is structured as follows:

- Chapter 2 contains a discussion of the main background concepts underlying nuclear reactions in general in the vicinity of the fusion barrier, including (multi)-nucleon transfer.
- Details of an experiment conducted at the Australian National University Heavy Ion Accelerator Facility, in which multinucleon transfer probabilities and excitation energy spectra were measured in the systems ^{16,18}O, ^{19}F + ^{208,204}Pb, ^{209}Bi, are given in Chapter 3.
- Chapter 4 gives a description of a measurement of multinucleon transfer probabilities and excitation energy spectra in ^{32}S, ^{40}Ca + ^{208}Pb using the PRISMA magnetic spectrometer installed at the Legnaro National Laboratory of the Istituto Nazionale di Fisica Nucleare (INFN) (Italy), as well as the calibration and analysis procedures.
- The results of the two experiments are presented in Chapter 5, and the systematic trends across the different reactions are examined and discussed.
- The final chapter will discuss the overall conclusions of this investigation and suggest future research objectives.

Chapter 2

Background and concepts

In this chapter some of the main basic concepts concerning nuclear reactions relevant to this thesis are reviewed. As has been explained in the previous chapter, the problem of treating energy dissipation in nuclear fusion and reactions in general remains unsolved at this point in time. This thesis does not aim to develop an effective means of achieving this ambitious goal from a theoretical perspective, but rather to establish the empirical systematics through experiments that will provide a phenomenological foundation for doing so. As such, the concepts discussed in this chapter are provided to explain the current state of knowledge and identify the problems that exist in the present understanding. Reaction concepts that are relevent to the analysis presented in the later chapters are also presented.

2.1 Conservation laws and reaction energetics

Whilst the nature of nuclei as quantum many-body systems makes it very difficult to model their behaviour from first principles (i.e. using the fundamental interactions between nucleons), reactions obey a number of strict conservation laws which allow one to make some simple predictions about the range of possible outcomes for a given system.

With sufficient energy, it is possible for various exotic processes to take place that involve the conversion of nucleons into other types of particles (which are governed by the conservation of several quantum numbers e.g. strangeness). However, the energy

scales involved in near-barrier nuclear reactions are far below those in which nucleons can transmutate from one type to others. As such, for the nuclear reactions considered in this work, it is always assumed that the total proton and neutron numbers will be conserved between the entrance and exit channels.

The most important conserved quantities in reactions are energy, momentum (both linear and angular), and parity between the initial and final states.

Energy conservation must consider not only the kinetic energies of the fragments in the initial and final states together with their intrinsic excitation energies, but also their masses. As expressed in the Einstein relation $E = mc^2$, mass can be converted to energy and vice versa. An important quantity in nuclear reactions is the Q-value: a measure of the energy that is equivalent to the discrepancy in mass between the entrance and exit channels. In the general case, the ground state to ground state Q-value, $Q_{g.g}$ (both the input and output fragments start from and remain in their ground states), is given by:

$$Q_{g.g} = \left(\sum_i m_i - \sum_f m_f \right) c^2, \tag{2.1}$$

where the m_i and m_f are the masses of nuclei in the entrance and exit channels respectively. In the case of fusion, there are two nuclei in the entrance channel and one in the exit channel. In this work binary reactions of the form $1 + 2 \rightarrow 3 + 4$ will be almost exclusively discussed, in which the reaction Q-value can be expressed as:

$$Q_{g.g} = (m_1 + m_2 - m_3 - m_4)c^2. \tag{2.2}$$

$Q_{g.g}$ can take both positive and negative values, or, in the special case of elastic scattering, be equal to zero. Reaction processes with positive $Q_{g.g}$ are exothermic (release energy from mass), whilst those with negative $Q_{g.g}$ are endothermic (kinetic energy is converted to mass).

The Q-value for any given process can be determined by finding the differences in masses between the entrance and exit channels, or by examining the kinetic energies of all of the

exit fragments (together with the knowledge of a well defined energy in the entrance channel). The former gives a measure of $Q_{g.g}$— this value does not consider any dissipation of kinetic energy to excitations of the reaction products. In determining the extent of energy dissipation it is important to consider both the true Q-value (from kinematics) and $Q_{g.g}$ (from masses). The energy that is transferred from the relative motion to the intrinsic states of the reaction products can be calculated from the difference between these two quantities:

$$E^* = Q_{g.g} - Q. \tag{2.3}$$

In this thesis work, the focus is on identifying processes in which energy is dissipated from the relative motion to the intrinsic states, and as such the method explained above is one of the important tools in this analysis. The method for determination of the true Q-value from experimental quantities is explained in Appendix A.

2.2 Cross-sections

The probability for a nuclear interaction to take place is commonly expressed in terms of a cross-section. Consider a beam of particles with a flux of I_0 per unit area per unit time, incident on a target composed of n particles per unit area. The flux of scattered particles (reaction products) Y per unit time will be proportional to both I_0 and n. The cross-section, which should be considered an *effective* geometrical area presented to an incoming beam of particles for a particular outcome, has units of area (m^2) and is defined as the constant of proportionality between these quantities:

$$\sigma = \frac{Y}{I_0 n} \tag{2.4}$$

The absolute cross-section is defined as the *total* number of emitted particles, over all angles θ, ϕ. In general the products of a nuclear reaction are not emitted isotropically, and it is impossible to design a detector that provides a coverage of the full 4π sr solid angle,

so it is useful to define the differential cross-section $d\sigma(\theta,\phi)/d\Omega$ which can be extracted from a measurement of particles emitted into an element of the solid angle $d\Omega$. The total cross-section can be extracted by integration of the differential cross-section over all angles:

$$\sigma = \int_0^{4\pi} (d\sigma(\theta,\phi)/d\Omega) d\Omega. \tag{2.5}$$

2.3 Reaction outcomes

It is important to distinguish the terms *scattering* and *reaction* — the former encompasses both elastic and inelastic scattering, as the identities of the colliding nuclei do not change between the entrance and exit channels. *Reaction* is generally used to refer to processes that involve a change in the identity of the fragments compared to the entrance channel— e.g. transfer, fusion.

Besides the identity of the reaction partners and the energetics of the entrance and exit channels, the angular momentum of the system plays a decisive role in the possible outcome of a heavy-ion collision. The angular momentum in a nuclear collision is determined by the impact parameter b, which is a geometrical measure of the centrality of the collision. The impact parameter can be related to the (classical) angular momentum l of the colliding system [64]:

$$l = \frac{\mu v b}{\hbar}, \tag{2.6}$$

where μ is the reduced mass of the system $\mu = m_1 m_2/m_1 + m_2$, v is the relative motion in the entrance channel, and $\hbar$ is the reduced Planck constant $\hbar = h/2\pi$. The reaction cross-section can be expressed classically in terms of l:

$$\sigma_R(l) = 2\pi \lambda\!\!\!^{-2} \int_0^{l_{\text{grazing}}} l dl, \tag{2.7}$$

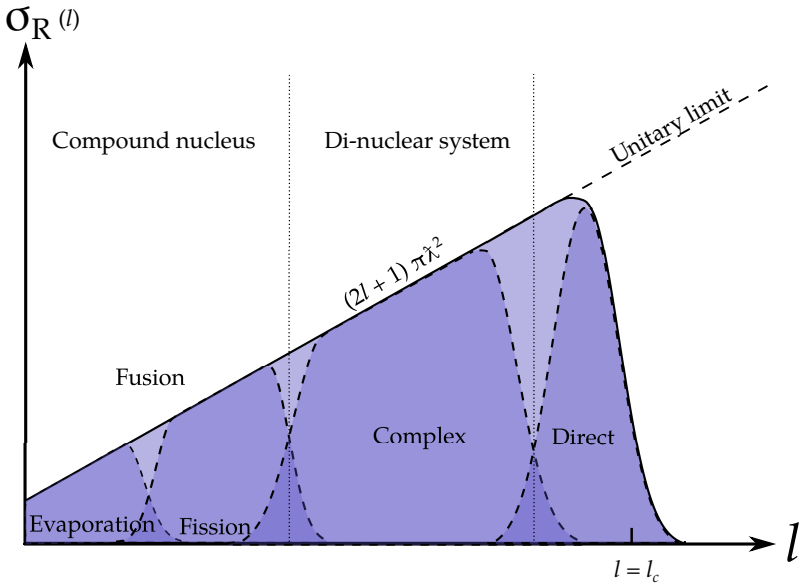

FIGURE 2.1: Contributions to the total reaction cross $\sigma_R(l)$ section from each partial wave l. Adapted from Ref. [65]. Note that the region labelled 'Direct' encompasses single and multi-nucleon transfer reactions as well as inelastic scattering. The region labelled 'Complex' encompasses both deep-inelastic scattering and quasi-fission. The complex regime is illustrated to exist somewhere between the extremes of direct and compound nucleus reactions. The ranges in l covered by the various reaction modes differ depending on the system, as well as the bombarding energy relative to the fusion barrier energy V_B — for instance, the complex regime is very broad for heavy systems (with high $Z_1 Z_2$), though may be negligible in the lightest ones. The total reaction cross-section corresponds to trajectories with $l < l_c$, the angular momentum that corresponds to a grazing collision.

where $\lambda\!\!\!^{-}$ is the reduced de Broglie wavelength $\lambda\!\!\!^{-} = \lambda/2\pi$, and l_{grazing} is the grazing angular momentum, corresponding to the grazing impact parameter $b_{\text{grazing}} = R_1 + R_2$ (where R_i are the nuclear radii) such that the nuclei just come into contact. At higher values of angular momentum nuclear reactions cannot take place. In the quantum mechanical formalism (discussed later in this chapter), l has to be replaced by $l + 1/2$ leading to the unitary limit $\sigma_R(l) \propto (2l + 1)\lambda\!\!\!^{-2}$, as shown in Figure 2.1.

The various components of $\sigma_R(l)$ and the dependence on the angular momentum are qualitatively illustrated in Figures 2.1 and 2.2. These different processes are described in the following, in order of decreasing angular momentum (i.e. increasingly more central collisions).

- *Elastic scattering:* When the collision energy is low relative to the fusion barrier, such

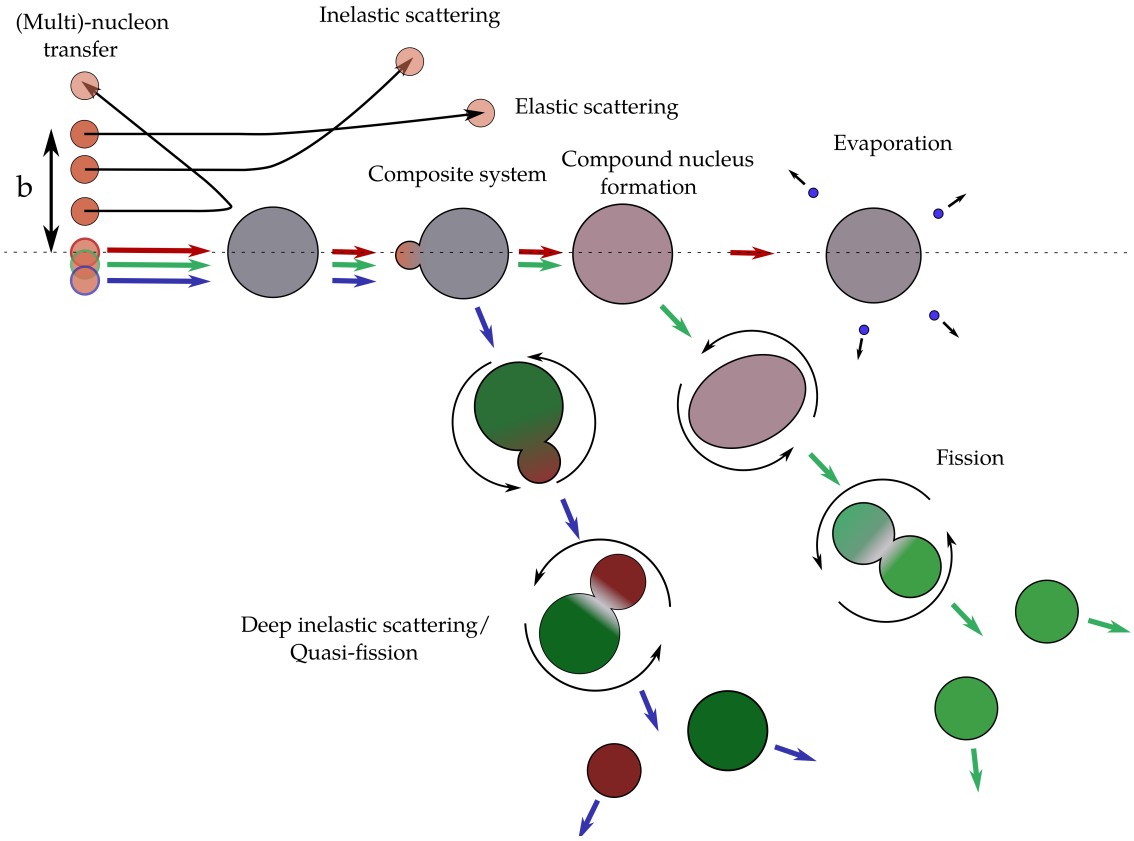

FIGURE 2.2: Schematic illustration of the effect of the impact parameter b on nuclear reaction outcomes involving heavy nuclei. The red arrows indicate the progression of a reaction following a central collision (i.e. $l = 0$). The green arrows indicate the progression of a reaction following a sufficiently non-central collision, where the higher angular momentum results in the fission decay of the compound nucleus. The blue arrows indicate a collision at yet higher angular momentum where the absence of a pocket in the internuclear potential prevents compound nucleus formation.

that the colliding nuclei encounter only the tail of the potential at large values of the internuclear separation r, and are scattered by the repulsive Coulomb interaction without exciting the internal nucleonic degrees of freedom of either nuclei. Kinetic energy is conserved completely. The reaction Q-value is equal to zero.

- **Direct or peripheral reactions**, in which the incident nucleus interacts only with the surface of the target, including:
  - *Inelastic scattering:* With bombarding energies bringing the collision partners closer together, the incoming nucleus reaches a region of sufficiently high Coulomb field such that the internal states of one or both of the partners may be excited. Kinetic energy is not conserved. The reaction Q-value is negative.
  - *Direct (Multi-)nucleon transfer:* The nuclei come close enough together that the strong nuclear force plays a significant role, resulting in the transfer of one or several nucleons between the partners. The Q-values may be positive or negative, such that the outgoing fragments may have more or less kinetic energy that the entrance channel.
- **Complex reactions**, in which the nuclei come into very close contact with a significant matter overlap leading to sufficiently large kinetic energy dissipation, such that the product fragments are highly excited. The partners may stick together for a short time, during which they exchange mass and charge, though retain a memory of the entrance channel through correlations between the masses and emission angles of the exit channel fragments. The relative kinetic energy may be in excess of the s-wave barrier, but the high angular momentum causes any potential pocket to disapppear. These modes include:
  - *Deep inelastic scattering:* Violent collisions in which the nuclei stick together, causing energy to be partially dissipated from the relative motion to intrinsic states. The dinuclear system may rotate before reseparating, during which time there is an exchange of mass and charge between the partners. Due to the short sticking time and hence a limited flux of mass and charge exchanged,

the outgoing fragments mostly preserve the mass asymmetry of the entrance channel.

  - *Fast fission or quasifission:* Where the partners stick together for a significantly longer time enabling full kinetic energy damping and drift towards mass symmetry, before separating again into two outgoing fragments.

- **Compound nucleus reactions**, where the incident nucleus has sufficient energy to overcome or penetrate the fusion barrier, with a low enough angular momentum that there is a trapping potential pocket preventing immediate reseparation. The full damping of kinetic energy leads to a single thermally equilibrated (compound nucleus) system that has no memory of the entrance channel. The Q-value for compound nucleus formation can be negative or positive. In the former case, the kinetic energy must be sufficient to exceed the mass defect to allow formation of the compound system. The compound nucleus formed in the fusion reaction can decay via two routes:

  - *Fusion-fission:* The high angular momentum in the center of mass frame (see Appendix A) causes the excited compound nucleus to break into two fragments of roughly equal mass.

  - *Fusion-evaporation:* The angular momentum of the compound nucleus is not sufficient for fission to occur. The compound nucleus evaporates nucleons (protons or neutrons), or clusters of nucleons, leading to a final state nuclei that have excitation energies below the particle emission thresholds. Such nuclei are referred to as evaporation residues.

It should be noted that the above list of reaction mechanisms is not exhaustive. For example, in the case of weakly bound and exotic nuclei, other reaction mechanisms such as fragmentation and breakup are also possible. These sorts of reaction mode are increasingly a popular research topic with the ongoing development and availability of radioactive beam facilities.

The various mechanisms described above exhibit characteristic features in the angular distributions of reaction products, and as such any experiment that aims to measure a

particular reaction mode must be designed such that the apparatus will be sensitive to those products. For example, fusion evaporation products will be exclusively found at very forward angles (relative to the direction of the incident velocity) owing to the high linear momentum of the projectile. On the other hand, direct reaction mechanisms have a broad angular distribution where the scattering angle is determined by the impact parameter in the entrance channel, and a detector placed at any particular angle therefore provides a window covering a finite range of angular momenta.

An important concept in nuclear experiments is scattering at large internuclear separations—where the influence of the attractive nuclear potential is effectively absent), therefore only the electrostatic interaction between the reactants comes into effect, and no *reaction* takes place. This is known as pure Coulomb or Rutherford scattering and is described briefly in the next section.

2.3.1 Rutherford scattering

The Rutherford scattering cross-section can be derived from the assumption of the scattering of two point charges, Z_1 and Z_2. The differential cross-section at the center of mass energy $E_{c.m}$ has the form:

$$\frac{d\sigma_{\text{Ruth}}}{d\Omega} = \left(\frac{Z_1 Z_2 e^2}{8\pi\epsilon_0 E_{c.m.}}\right)^2 \csc^4(\theta_{c.m.}/2) \tag{2.8}$$

Remarkably, Equation 2.8 is identical for both classical and quantum mechanical derivations of pure Coulomb scattering.

The scattering angle $\theta_{c.m}$ is dependent on both the distance of closest approach in the collision (i.e. the incident energy of the projectile) and the impact parameter b:

$$\cot\left(\frac{\theta_{c.m}}{2}\right) = \frac{2b}{r_{\text{min}}} \tag{2.9}$$

It can be seen from Equation 2.9 that $\theta_{c.m}$ increases for decreasing b, until $\theta_{c.m} = \pi$ when $b = 0$. As such, there is an equivalence between the scattering angle and the angular momentum of the collision.

Assuming that only the Coulomb field influences the trajectories of the nuclei, the distance of closest approach r_{min} can be calculated according to:

$$r_{\text{min}} = \frac{Z_1 Z_2 e^2}{4\pi\epsilon_0} \frac{1}{2E_{\text{c.m.}}} \left(1 + \csc\frac{\theta_{\text{c.m.}}}{2}\right). \tag{2.10}$$

Since the extent of the matter density differs for nuclei of different masses, a more useful quantity that can be considered to be proportional to the degree of matter overlap can be found in the surface separation parameter Δ, which can be used to compare different systems:

$$\Delta = r_{\text{min}} - r_0 \left(A_1^{1/3} + A_2^{1/3}\right), \tag{2.11}$$

where r_0 is the radius parameter (usually taken to be 1.2fm), and A_i are the mass numbers of the nuclei i. These concepts are illustrated in Figure 2.3, which shows the collision geometry. Strictly speaking, both r_{min} and Δ as defined above are valid only in the sub-barrier regime, as the form of r_{min} given in Equation 2.10 is derived based on an assumption of pure Coulomb scattering, where the influence of the nuclear potential is neglected.

When the incident energy of the projectile nucleus is sufficiently high (and impact parameter sufficiently small), the nuclear potential will influence the trajectories, and the angular distribution of elastically scattered particles will differ significantly from the Rutherford form (Equation 2.8). As such, the cross-sections for elastic scattering and for Rutherford scattering are not equivalent over the whole angular range. This difference is clearly manifested at backward scattering angles, where the projectile penetrates closer to the target nucleus and therefore will be affected to a larger extent by the nuclear field. This fact has been used to probe the fall-off of the nuclear potential [59, 66]. On the contrary, at forward angles (corresponding to large impact parameters), and at energies

near the barrier, the elastic yield is due to pure Rutherford scattering. As such, when extracting the probability for a given reaction mode, this quantity is normally deduced by comparing the yield of the product of interest to the Rutherford yield.

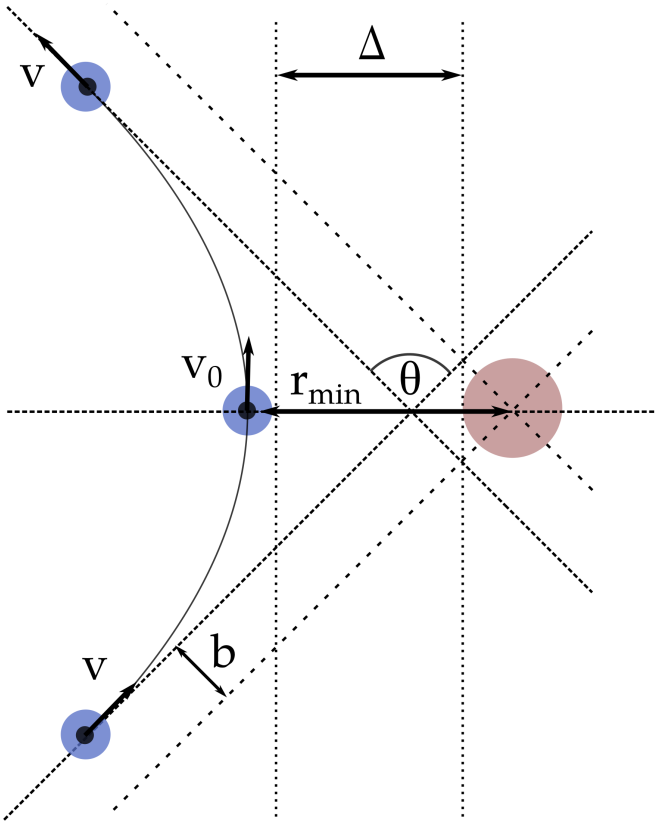

FIGURE 2.3: Illustration of the geometry of Rutherford scattering. The r_{min} dimension is the distance between the nuclear centers, whilst Δ is a measure of the distance between the nuclear surfaces. The scattering angle θ is related to the impact parameter b (see text). Adapted from Ref. [65].

2.4 Nuclear structure

Nuclei, as many-body quantum systems, display a rich variety of structure, which have an important influence on reaction dynamics. The study of the structure of nuclei is usually conducted through the detection of decay products such as the γ-rays that are emitted in transitions between states as an excited nucleus cools to its ground state. It is not the intention here to describe in detail the conceptual basis of nuclear structure

models. However, in anticipation of the discussions of the structure effects relevant to reactions that will come in the later sections of this chapter, a brief explanation of some of the concepts that are referred to in this thesis is given next.

2.4.1 Shell structure

As a composite system composed of fermions (nucleons), the Pauli exclusion principle results in the nucleons occupying discrete energy levels. The concept of nuclear shells is evident from a study of the nuclear binding energies. Nuclei with particular numbers of protons and neutrons exhibit particularly high binding energies— these are the nominal "magic" numbers, which correspond to the filling of a full shell of nucleons.

The nucleons couple together in pairs of opposite spins within the shells. The nucleons in the outermost shell completely determine the spin and parity of the bulk nucleus. If all nucleons are paired (i.e. the nucleus has an even number of both protons and neutrons), in its ground state the nucleus will have a net spin (J) of zero, and even parity according to the rule $P = (-1)^l$, where l is the orbital angular momentum of the unpaired nucleon.

Nuclei exhibit a rich spectrum of excited states that correspond to the promotion of nucleons from one shell to another — these are known as single-particle excitations. Heavier nuclei, with a much greater number of nucleons, have a very large number of ways of ordering the nucleons, and as such have a much more complicated spectrum of states, as well as a much greater density of states (i.e. a larger number of states within a given energy interval). Besides single-particle states, the many-body nature of the atomic nucleus gives rise also to collective excitations in which many of the nucleons participate in unison.

2.4.2 Collective structure in nuclei

The collective properties of nuclei, such as rotational and vibrational modes, are emergent phenomena of the interactions between nucleons and the many-body structure. Nuclei with magic numbers of protons and neutrons are typically spherical, whilst others

away from the shell closures can be deformed along one or more axes. Departures from spherical symmetry can be deduced from the measured electric quadrupole moment being non-zero.

For an axially symmetric nucleus the nuclear surface can be expressed as an expansion in spherical harmonics Y_{lm}:

$$R(\theta) = R_{\text{sp}} \left[1 + \beta_2 Y_{20} + \beta_4 Y_{40} + ...\right], \tag{2.12}$$

where $R_{\text{sp}} = r_0 A^{1/3}$ is the radius of the spherical nucleus, and β_2 and β_4 are the quadrupole and hexaducopole deformation parameters respectively. β_l takes the value zero for spherical nuclei, is negative for oblate shapes, and positive for prolate shapes.

The deformed nucleus can rotate around an axis that is perpedicular to the symmetry axis. This is known as a collective rotation. The energy of these rotational states can be calculated according to:

$$E = \frac{\hbar^2}{2\mathfrak{I}} I(I+1), \tag{2.13}$$

where $\mathfrak{I}$ is the moment of inertia of the rotating nucleus, and I is the total angular momentum quantum number.

In addition to rotational motion, both deformed and spherical nuclei can undergo dynamic deformations through quantum vibrations. In order of increasing multipolarity (illustrated in Figure 2.4, the first vibrational modes are the monopole ($\lambda = 0$), dipole ($\lambda = 1$), quadrupole ($\lambda = 2$), octupole ($\lambda = 3$), and soforth. The monopole vibration (also known as the breathing mode) typically requires a lot of energy to excite, and as such does not play a significant role in influencing reaction dynamics. The most easily excited vibrational modes tend to be the quadrupole and octupole modes, which appear at very low excitation energies in heavy nuclei and couple very strongly to the ground

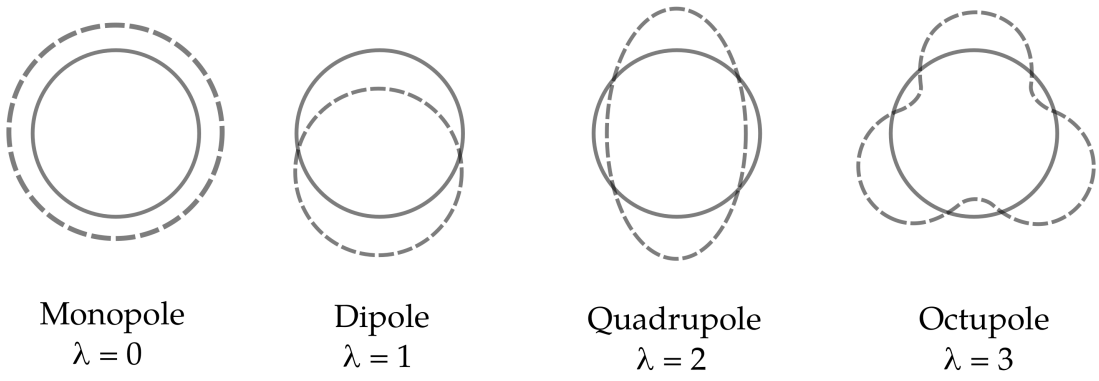

FIGURE 2.4: Illustration of the four lowest vibrational modes in spherical nuclei (not to scale). The multipolarity is given by the parameter λ. The average (and original) spherical shape is indicated by the solid line. The dashed line shows the instantaneous shape of the nucleus during the vibrational deformation. Adapted from Ref. [64]

states. The excitation of a vibrational mode involves the generation of a phonon in the nuclear medium— the vibrational bands in nuclear structure consist of a number of evenly spaced states that correspond to the generation of multiple phonons in the nucleus.

2.4.3 Clustering in nuclei

The extremely high binding energy of the ^{4}He nucleus (α-particle) is a longstanding curiosity in nuclear physics, and is yet to be fully understood. This stems from an enduring lack of understanding of the nucleon-nucleon interaction, being a residual consequence of the fundamental strong force which binds the quarks within the nucleon. The prevalence of α-decay leads to questions as to whether such a cluster of nucleons can exist within the nuclear medium or is formed at the moment of emission. Prior to the discovery of the neutron it was thought that the α-particle may be the basic building block of the atomic nucleus. This was suggested by the binding energies of the so-called α-conjugates (nuclei that are even-even with equal numbers of protons (Z) and neutrons N), which have a linear relationship with the number of bonds (i.e. contact points) required to arrange the nucleus as a collection of α-particles in a close-packing configuration [67] (e.g. ^{8}Be requires one bond, ^{12}C requires three, etc.). Whilst we now know that this is an inadequate picture, α-conjugation still appears to have an important effect on light nuclei,

those being particularly tightly bound compared to their non-conjugate neighbours.

It is now known that cluster structures can exist in nuclei typically at excitation energies that are close to the cluster decay thresholds. A classic example is that of the Hoyle state in ^{12}C [68], a 3-α state which is a bottleneck for nucleosynthesis: the production of ^{12}C can proceed from Helium fusion only via the 3-α process, through the intermediate and short-lived ^{8}Be, forming a resonance in ^{12}C that decays to the ground state of ^{12}C. Whilst the light and α-conjugate nuclei have well-formed cluster structures, and have been studied fairly extensively, it has now become clear that cluster structures are prevalent across the nuclear chart at energies close to the decay thresholds, and in exotic nuclei even in the ground states [69, 70]. Evidence for cluster structures has also been found in nuclei that are not α-conjugate: in these cases nuclei can form molecular structures, in which additional neutrons (beyond conjugation) play an analogous role to the electrons in covalent bonds, providing stability to an arrangement of localised clusters of nucleons [71, 72]. The presence of cluster structures in nuclei results in additional rotational bands and resonances in the spectrum of excited states.

In the case of weakly bound nuclei, clustering can promote particular outcomes of breakup reactions. Similarly, it might be expected that other reaction modes should be affected by intrinsic cluster structures in one or both of the reactants— for example, that transfer of clusters may be more prominent.

In the following section it will be shown how the structure of nuclei has a decisive influence on nuclear fusion.

2.5 Models of nuclear fusion

A brief description of the present theoretical understanding of nuclear fusion is presented next. The process of fusion is understood as the capability of a colliding pair of nuclei to overcome their mutual electrostatic repulsion such that the matter densities overlap and the strongly attractive nuclear forces come into effect, allowing the nuclei to be trapped by the attractive nuclear interaction to form a new nucleus (called the compound nucleus)

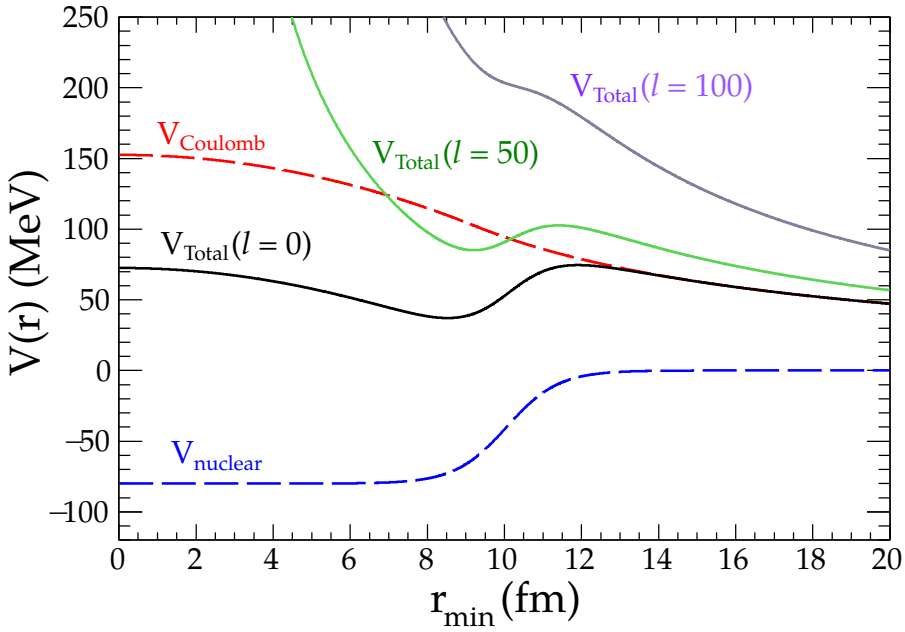

FIGURE 2.5: The internuclear potential and its constituent interactions. The Woods-Saxon has in this example been calculated using the appropriate parameters for the ^{16}O + ^{208}Pb reaction: The nuclear potential well depth V_0 is 80 MeV, the diffuseness a is 0.671 fm, and the radius parameter r_0 is 1.191.

that has no 'memory' of the reaction through which it formed [73]. The equilibrated compound system is understood to result from many collisions between the nucleons within the nuclei that cause the kinetic energy to be transformed into nuclear excitations (i.e. the compound nucleus is formed in an excited state). However, in most models of nuclear fusion the dynamics of the actual formation process beyond barrier passing is not considered, as explained in the next sections.

2.5.1 The internuclear potential

In a collision, the two nuclei, with a net positive charge as a consequence of the constituent protons, experience a long range repulsion as a result of the electrostatic force (commonly referred to as the Coulomb interaction). At short distances, the electrostatic repulsion is strongly cancelled by the attractive nuclear forces, resulting in a potential barrier which must be traversed in order for the nuclei to experience a net attractive potential. This situation is illustrated in Figure 2.5. The outer point of inflection of the

total potential is referred to as the fusion barrier. The Coulomb potential is well known from the theory of electrostatics, and for two nuclei with atomic number Z separated at a distance r is given by:

$$V_{\text{Coulomb}} = \begin{cases} \dfrac{Z_1 Z_2 e^2}{4\pi\epsilon_0 r}, & \text{if } r > R_c \\ \dfrac{Z_1 Z_2 e^2}{4\pi\epsilon_0 R_c}\left[\dfrac{3}{2} - \dfrac{1}{2}\left(\dfrac{r}{R_c}\right)^2\right], & \text{if } r < R_c \end{cases} \tag{2.14}$$

In the above the assumption is made that the nuclei can be represented as uniformly charged spheres. R_c is the Coulomb radius of the system $R_c = r_c(A_1^{1/3} + A_2^{1/3})$, where r_c is the Coulomb radius parameter. The subscripts 1 and 2 in the above and the following denote those properties relevant to the projectile and target respectively, though this distinction is arbitrary when modelling nuclear reactions. Throughout this thesis it can be assumed that "target" refers to the heavier reaction partner.

The short-range attractive nuclear potential is normally parameterized in Woods-Saxon form [74]:

$$V_{\text{Nuclear}} = -\frac{V_0}{1 + \exp\left[(r - R_0)/a\right]}, \tag{2.15}$$

where V_0 is the depth of the potential well, a is the nuclear surface diffuseness, and R_0 is the touching radius $R_0 = r_0(A_1^{1/3} + A_2^{1/3})$, the distance at which the nuclear densities of the collision partners just overlap. r_0 is typically treated as an adjustable parameter in Woods-Saxon potential models. The Woods-Saxon form is commonly used in reaction models, being able to closely reproduce the tail of the nuclear potential that is derived from the semi-microscopic double folding model using a simple parameterization. Validation of the Woods-Saxon parameterization can be achieved through a combination of optical model analyses of the angular distributions of scattered ions (which provides information about the surface diffuseness), and high energy fusion cross-sections (where the potential can be studied in the absence of the coupling effects that affect the fusion process in the barrier region— providing for instance information on the well depth of Woods-Saxon form potentials).

The centrifugal potential is then given by:

$$V_{\text{Centrifugal}} = \hbar^2 \frac{l(l+1)}{2\mu r^2}. \tag{2.16}$$

Here μ is the reduced mass of the system $\mu = \frac{m_1 m_2}{m_1+m_2}$, and l is the angular momentum. The resulting total internuclear potential is the combined effect of the interactions expressed in Equations 2.14 — 2.16:

$$V_{\text{Total}} = V_{\text{Coulomb}} + V_{\text{Nuclear}} + V_{\text{Centrifugal}}. \tag{2.17}$$

The total potential for a range of l values is plotted in Figure 2.5, using an example parameterization of the ^{16}O + ^{208}Pb system. With increasing l, the barrier moves up in energy, and the potential pocket gets progressively shallower, ultimately disappearing at some critically large value of l whereupon the attractive forces are not sufficient to counteract the repulsive potentials.

2.5.2 Classical model of fusion

In the classical picture, the necessary and sufficient condition for fusion to occur is that the nuclei come into close enough contact that the attractive forces dominate. Considering the angular momentum, the nuclei will come into contact only when the impact parameter b is equal to the sum of the radii of the collision partners. Calling this impact parameter b_{grazing} we have:

$$b_{\text{grazing}} = r_0(A_1^{1/3} + A_2^{1/3}) = R_1 + R_2. \tag{2.18}$$

In this simple view of the fusion reaction, the cross-section is directly related to the grazing impact parameter:

$$\sigma_{\text{fusion}} = \pi b_{\text{grazing}}^2 \tag{2.19}$$

The angular momentum of the system must be equal between the initial separated state and that when the nuclei come into contact at the fusion barrier. Denoting the linear momenta p of the initially separated system p_i and that at the barrier as p_B, and using the definition of the angular momentum $\mathbf{l} = \mathbf{r} \times \mathbf{b}$:

$$b_{\text{grazing}} p_i = r_B p_B. \tag{2.20}$$

Expressing the momenta in terms of the center of mass energy $E_{c.m}$ and the fusion barrier energy V_B, we get $p_i = \sqrt{2\mu E_{c.m}}$ and $p_B = \sqrt{2\mu(E_{c.m} - V_B)}$. Substituting these terms into Equation 2.20 and then inserting into Equation 2.19 leads to the following expression for the cross-section:

$$\sigma_{\text{fusion}} = \pi r_B^2 \left(1 - \frac{V_B}{E_{c.m}}\right) \tag{2.21}$$

Being a classical picture, fusion is only possible (i.e. $\sigma_{\text{fusion}} > 0$) when $E_{c.m} > V_B$; at $E_{c.m} < V_B$ the nuclei cannot pass the barrier. This picture is, of course, simplistic in light of the fact that stars are able to generate energy from fusion at temperatures far lower than those required to overcome the fusion barrier.

2.5.3 A quantum mechanical understanding— the single barrier picture

Nuclear fusion is a classic example of a barrier penetration problem within the context of quantum mechanics. The possibility of tunnelling of the incoming nucleus through the potential barrier allows fusion to occur even at energies far below the barrier energy.

The simplest quantum models of fusion treat the reacting nuclei as inert charged particles, with a short range attractive potential which cause the formation of a compound system if they pass the barrier. That is, there is no accommodation of the quantum structure of the colliding nuclei. In such a case, the relative motion of the system is the only degree of freedom, and the process is modelled by the transmission of the colliding nuclei through a single potential barrier. The total fusion cross-section for a system with energy

$E_{c.m}$ in the center-of-mass is then obtained by calculating the barrier penetrability T_l for each l-value (partial wave) and summing together all of the individual contributions:

$$\sigma_{\text{Fusion}} = \frac{\pi\hbar^2}{2\mu E_{c.m}} \sum_{l=0}^{\infty} (2l+1) T_l(E_{c.m}). \tag{2.22}$$

While the sum here is shown to be over all l, in practice $T_l \to 0$ for all l-values above the grazing angular momentum. Note that the fusion cross-section expressed above encompasses both the fusion-fission and fusion-evaporation reaction decay outcomes of compound nucleus formation (see Figures 2.1 and 2.2).

The transmission factor T_l is generally computed using numerical methods. A closed form expression can be found by using the WKB approximation, which assumes that the shape of the internuclear potential varies slowly compared with the de Broglie wavelength of the incoming particle. This allows one to calculate the penetrability of a potential barrier of arbitrary shape. The transmission factor can be expressed in the form:

$$T_l(E) = \frac{1}{1 + \exp[2S_l(E_{c.m})]}, \tag{2.23}$$

where $S_l(E_{c.m})$ is the WKB integral, given by:

$$S_l(E_{c.m}) = \sqrt{\frac{2\mu}{\hbar^2}} \int_{r_1(l)}^{r_2(l)} dr \left[V_l(r) - E_{c.m}\right]^{1/2}. \tag{2.24}$$

In the above expression, the $r_1(l)$ and $r_2(l)$ are the outer and inner classical turning points i.e where $E_{c.m} = V$. An analytical solution can be obtained if the shape of the potential is approximated by an inverted parabola:

$$V_l(r) = V_B - \frac{1}{2}\mu\Omega_l^2(r - R_B)^2 + \frac{\hbar^2(l(l+1)}{2\mu R_B^2}, \tag{2.25}$$

where V_B is the barrier energy for the $l = 0$ partial wave, and R_B is the barrier radius. $\hbar\Omega_l$ is referred to as the curvature of the barrier. Inserting the parabolic potential into the WKB integral gives the famous Hill-Wheeler expression for the barrier penetrability:

$$T_l = \frac{1}{1 + \exp\left[\frac{2\pi}{\hbar\Omega_l}(V_B - E_{c.m})\right]}. \tag{2.26}$$

Inserting this expression into Equation 2.22 and assuming that (i) the curvature of the barrier is independent of l (i.e. $\hbar_l\Omega = \hbar_0\Omega = \hbar\Omega$), and (ii) that the potential can therefore be approximated by:

$$V_l(r) = V_0(r) + \frac{l(l+1)\hbar^2}{2\mu R_B^2}, \tag{2.27}$$

leads to the well known Wong formula for the fusion cross-section:

$$\sigma_{\text{Fusion}} = \frac{\hbar\Omega R_B^2}{2E_{c.m}} \ln\left[1 + \exp\left[\frac{2\pi}{\hbar\Omega}(E_{c.m} - V_B)\right]\right]. \tag{2.28}$$

In obtaining Equation 2.28, the sum over l in 2.22 is replaced by an integral over l— this is justified as many partial waves contribute to the fusion of heavy nuclei. Considering high incident energies such that $E_{c.m} \gg V_B$, it can be seen that Equation 2.28 reduces to match the classical cross-section in Equation 2.21, yet at energies below the barrier allows for a non-zero cross-section for fusion.

The single barrier picture described in this section represents the penetration of the incoming projectile to the region where the attractive nuclear potential dominates. Whilst the one-dimensional barrier penetration model (1DBPM) works well in the case of fusion between very light nuclei, including those of astrophysical relevance such as ^{12}C + ^{14}N, it fails to describe the fusion of heavier nuclei. This is because the 1DBPM ignores the quantum structure of the colliding nuclei. In the case of heavy nuclei the quantum states are low-lying (in energy) compared with the reaction energies, and play a very significant role in determining fusion, as will be explained in the next section.

2.5.4 Including structure effects— the coupled channels treatment

The effects of the intrinsic structure of the colliding nuclei on fusion is brought to relief at energies below the fusion barrier V_B. A simple and famous example is in comparing the cross-section for fusion of ^{16}O with the spherical nucleus ^{144}Sm, with that of fusion with ^{154}Sm, which has a static prolate deformation.

Considering a one-dimensional barrier penetration calculation of the fusion cross-section, as described in the previous section, since the radius of the deformed nucleus is θ-dependent a distribution of potential barriers must exist depending on the orientation of the collision. In such a case, the transmission probability (and hence cross-section) will depend on the orientation as well as the relative energy of the colliding nuclei. The total fusion cross-section must then be over all possible orientations [26]:

$$\sigma_{\text{fusion}}(E_{c.m.}) = \int_0^1 \sigma_{\text{fusion}}(E_{c.m.}, \theta) dcos(\theta), \tag{2.29}$$

where θ is the angle between the axis of relative motion and the symmetry axis of the deformed nucleus. The fusion of ^{16}O with ^{154}Sm displays a marked enhancement of the sub-barrier cross-section compared with the spherical ^{144}Sm (as seen in Figure 2.6), due to the existence of fusion barriers lower in energy (than V_B) corresponding to collisions with the tip of the prolate deformation (despite the additional presence of barriers *higher* in energy corresponding to a collision with the side of the prolate shape).

The idea of many barriers, rather than a single one, can be generalised beyond the case of static deformations to include also the dynamic collective vibrations which are present in many heavy nuclei, and even single particle excitations in the shell structure of nuclei. All of these excitation modes can play a role in the reaction process, although in general it is found that the collective modes with low excitation energies and strong couplings to the ground state are most important. To fully capture the internal structure of the reacting nuclei they should be represented by coherent superpositions of their possible quantum states. To understand this, for simplicity it is useful to consider the case of a hypothetical two-level system consisting of the ground $|0\rangle$ and first excited states $|1\rangle$,

which is assumed to have a negligible excitation energy. This system can be described by the two coupled equations:

$$\left(-\frac{\hbar^2}{2\mu}\frac{d^2}{dr^2} + V(r) - E\right)\psi_1 = -F(r)\psi_2. \tag{2.30}$$

$$\left(-\frac{\hbar^2}{2\mu}\frac{d^2}{dr^2} + V(r) - E\right)\psi_2 = -F(r)\psi_1. \tag{2.31}$$

In the above, the factor $F(r)$ is known as the form factor, describing the coupling between the two states, and ψ_1 and ψ_2 are the wavefunctions of relative motion of the two nuclei. If the coupling between the two states 1 and 2, and vice versa, are assumed to be constant over the internuclear separation r (i.e. $F_{1\to2}(r) = F_{2\to1}(r) = F$), then the above equations can be decoupled by introducing a change of basis:

$$\chi_+ = \frac{1}{\sqrt{2}}(\psi_1 + \psi_2). \tag{2.32}$$

$$\chi_+ = \frac{1}{\sqrt{2}}(\psi_1 - \psi_2), \tag{2.33}$$

leading to:

$$\left(-\frac{\hbar^2}{2\mu}\frac{d^2}{dr^2} + (V(r) + F) - E\right)\chi_+ = 0, \tag{2.34}$$

$$\left(-\frac{\hbar^2}{2\mu}\frac{d^2}{dr^2} + (V(r) - F) - E\right)\chi_- = 0. \tag{2.35}$$

It now becomes clear how the coupling affects the fusion probability. The couplings between states lead to different effective potentials for each eigenchannel (i.e. $V+F$, $V-F$ in the above decoupled equations). The fusion cross-section is then given as weighted sum of the distribution of barriers, i.e:

$$\sigma_{\text{Fusion}} = \frac{1}{2}(\sigma_{\text{Fusion}}(V_B + F) + \sigma_{\text{Fusion}}(V_B - F)), \tag{2.36}$$

which is always greater than $\sigma_{\text{Fusion}}(V_B)$ at energies below V_B, since the fusion cross-section depend exponentially on the difference between the incident and barrier energies (Equation 2.28) i.e. $T_l((V_B - F) - E) >> T_l(V_B - E)$. This simple example illustrates the concept that there is effectively a distribution of barrier energies that replaces the single barrier. The transmission through a lower barrier, rather than tunnelling through the single barrier, leads to an enhancement of the fusion cross-section compared to the single barrier penetration model. This concept can be generalised to include very many channels with non-negligible excitation energies, allowing for realistic calculations. The full coupled equations can be expressed as:

$$\left[-\frac{\hbar^2}{2\mu}\frac{d^2}{dx^2} + V(r) - (E - \epsilon_n)\right]\psi_n(r) = -\sum_{m \neq n} V_{nm}(r)\psi_m(r). \tag{2.37}$$

In the expression above, ϵ_n is the excitation energy of state n, and the couplings are contained within the matrix V_{nm}.

Coupled Reaction Channels (CRC) models are phenomenological in the sense that there are required 'ingredients' that are (usually) informed by experimental data. The three main ingredients are: the internuclear potential $V(r)$, the excitation energies, and the coupling strengths between the included states. The internuclear potential has been described in Section 2.5.1. Excitation energies can be taken from known energies of excited states, whilst the coupling strengths (matrix elements) are derived from measured probabilities of transitions between states.

The effect of couplings is illustrated in Figure 2.6, where the fusion excitation functions for ^{16}O + ^{144,148,154}Sm are presented. This series of systems represents the transition from spherical (^{144}Sm) to statically deformed nuclei (^{154}Sm), emphasizing the important influence that highly collective and rotational structures at low excitation energy have on the fusion cross-section. A comparision of the calculated cross-sections in a single barrier picture for the three systems (dashed lines) does predict an enhanced cross-section for

the heavier isotopes, as the more extensive matter distribution results in a lower barrier and hence increased transmission probability. This effect is dwarfed by an additional enhancement that can be explained by including the couplings between structure and the relative motion, as shown by the CRC calculations (solid lines). All calculations were performed using the CCFULL code [75], with the single barrier examples conducted in the no-coupling limit. CCFULL numerically solves the coupled channels equations considering a nuclear potential of Woods-Saxon form, the parameters of which were taken from Ref. [34], where they were optimized to reproduce the high energy fusion data of each relevant reaction. Fusion in CCFULL results from the imposition of an incoming wave boundary condition (IWBC) at the position of the potential pocket. The IWBC demands that once the system reaches the potential pocket it does not return to the initial state— enforcing the irreversibility of the process and effectively fully damping the kinetic energy. The code also takes as inputs information on the intrinsic states, such as the excitation energies, deformation parameters β_λ (which are calculated from transition probabilities [26]), and multipolarities λ.

In the ^{144}Sm case, the model space includes only the single-phonon excitation of the octupole vibrational mode at 1.81 MeV, assuming the ^{16}O nucleus to be inert (including couplings to states in ^{16}O can be shown to have a minor influence on the calculations). In the ^{154}Sm case, the calculation takes account of the rotational state at 0.082 MeV, and the next 4 states in the rotational band (i.e. 2^+, 4^+, 6^+, 8^+, 10^+). It is shown in Figure 2.6 how including only these simple coupling schemes provides an excellent account of the experimental data. It is quite remarkable that only a simple coupling picture can almost completely describe the enhancement. The ^{16}O + ^{148}Sm case is slightly more complicated, ^{148}Sm being transitional between the near-spherical ^{144}Sm and the strongly deformed ^{154}Sm nuclei. There is a soft quadrupole vibration located 0.55 MeV above the ground state, though coupling only to this state does not fully explain the observed sub-barrier enhancement. Including couplings also to the 3^- state at 1.16 MeV, and allowing for all mutual excitations up to 3 phonons ($2^+ \otimes 3^- \otimes (3^-)^2$) provides an additional enhancement which can reproduce the data.

Whilst there are many combinations of coupling schemes and potential forms that may

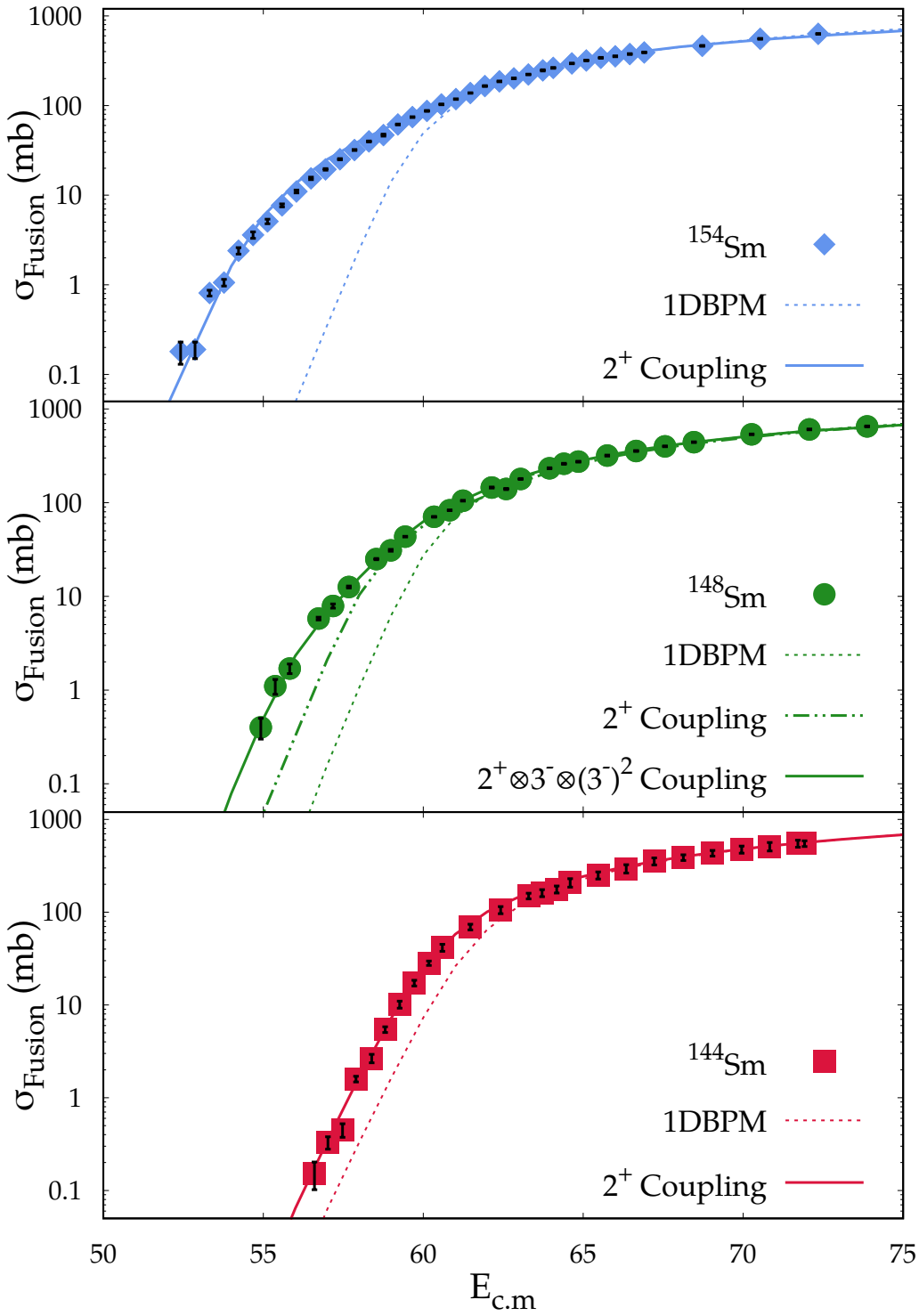

FIGURE 2.6: Fusion cross-sections for $^{16}O + ^{144,148,154}Sm$. The dashed lines in the figure show the results of single barrier calculations, whilst the solid lines show the calculations incorporating the coupling effects. The green dash-dotted line corresponds to a simple CRC calculation for ^{148}Sm coupling only to the first 2^+ state— a more realistic calculation including also the first 3^- state and 3-phonon excitations is shown by the solid line. See text for details of the calculations. The experimental data is taken from Ref. [58]

.

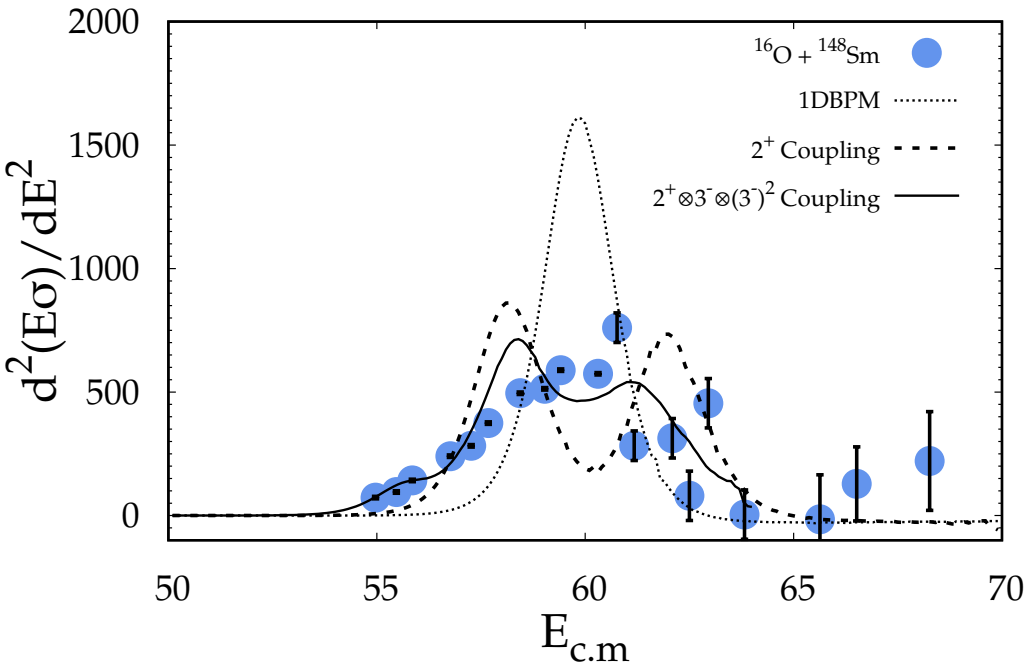

FIGURE 2.7: Fusion barrier distribution for ^{148}Sm + ^{208}Pb. The experimental data is taken from Ref. [58]. The data is compared with barrier distributions extracted from CRC calculations of the fusion cross-section.

similarly satisfactorily reproduce the experimental fusion excitation function, knowledge of the important effects can be gleaned by studying the experimental fusion barrier distribution. The experimental distribution can be extracted from precise data of the fusion cross-sections by taking the second derivative of the function $E\sigma$:

$$D_{\text{exp}} = \frac{d^2(E\sigma)}{dE^2}. \tag{2.38}$$

An example is shown in Figure 2.7, where the distribution is extracted from the experimental fusion cross-sections in the ^{16}O + ^{148}Sm reaction [58]. Also shown are barrier distributions extracted from CRC calculations— corresponding to those shown in Figure 2.6. In the no-coupling limit, the distribution shows a single barrier, which is contrary to the more complex structure observed in the data. Including only coupling to the first 2^+ state in ^{148}Sm is shown to result in a two barrier structure, whilst the calculations including couplings to higher order and mutual excitations results in further subtle changes to the shape of the barrier distribution, more closely resembling the experimental distribution. It is not the intention here to investigate the important couplings in this reaction

(nor is it claimed that the illustrated example makes use of the optimal coupling scheme), but to demonstrate the method through which understanding about the important reaction dynamics is achieved. The study of barrier distributions through CRC approaches has demonstrated definitively the importance of coupling effects in the fusion process.

2.5.5 Beyond coupled channels

Some of the problems that exist with the CRC approaches to heavy ion fusion have already been described in some detail in Chapter 1. Namely the need to restrict the model space for practical reasons, and the inability to properly account for irreversible dissipation of energy beyond the inclusion of imaginary potentials (which also account for the missing channels). The loss of flux from the entrance channel due to the imaginary potential (or application of an IWBC) is ascribed to the fusion cross-section, whilst in reality this may not be the case. For clarity about the intentions of this investigation, in the following section the problem that has come to be known as the nuclear potential surface diffuseness anomaly is discussed further [76, 34].

In brief, the problem is as follows. As described in Section 2.5.4, the form of the nuclear potential is normally determined by ensuring the agreement of CRC calculations with the fusion excitation function, or alternatively by reproducing elastic or quasi-elastic scattering angular distributions. In both cases, the resulting parameterisation should ensure that the energy of the fusion barrier matches that determined experimentally. In the case of the commonly used Woods-Saxon (WS) potential, the diffuseness parameters found by the two methods are quite different [1, 34]. Diffuseness parameters extracted from analyses of elastic and quasi-elastic scattering scattering are around $a = 0.6 - 0.7$fm. These values are believed to be reliable, since probing the potential through the reflected flux by definition only examines the nuclear surface. Reproduction of the fusion cross-sections at high energies typically requires a value for the diffuseness that can be up to twice as large as that which is found from optical model analyses of the scattering angular distributions [77, 58, 78, 79] (see Figure 2.8). In the past 20 years experimental methods have advanced to allow the measurement of fusion cross-sections with satisfactory precision

also at deep sub-barrier energies. The advent of these methods and facilities has shown the fusion cross-sections in this region to fall precipitously (below some energy threshold) below the expected exponential decrease. It has by now been made clear that it is impossible to reconcile the above and below barrier data simultaneously with CRC calculations using *any* set of WS parameters that satisfactorily reproduce the barrier energy [2]. This situation is illustrated in Figure 2.8.

The main proposals to deal with the hindrance problem in the deep sub-barrier region have already been described in Chapter 1. As was noted, most of the attempts to understand the origin of the discrepancy have investigated modifications to the internuclear potential [33, 50, 27] or the couplings [52, 51, 53, 55, 56] used in CRC calculations. There has also been discussion of the effect of the Pauli repulsion, which has been shown to produce a hindrance effect, though cannot explain in full the observed discrepancies [57]. Previous investigations of the surface diffuseness have pointed out that the diffuseness value required to fit the fusion cross-sections at above barrier energies generally increases with the charge product of the reactants $Z_1 Z_2$— in other words the magnitude of the hindrance effect above the barrier becomes greater as the charge product increases. With the greater Coulomb repulsion for heavier systems, the nuclear matter overlap at the barrier energy increases, and the increasing probability for the deep-inelastic reaction modes for these systems has therefore been linked to the fusion suppression [34, 28, 2].

The key question addressed by this thesis is the transition between the deep inelastic scattering phenomenon (see Section 2.8), expected at above-barrier energies, and the energy dissipative processes at near and below barrier energies that can affect fusion [3, 80]. It has been suggested that at low energies irreversible energy loss can proceed through doorway states such as giant resonances [62] and cluster transfer [81], which may occur even at large internuclear separation. Understanding the transition between the quasi-elastic and deep-inelastic scattering regimes in detail is an important step towards developing a complete picture of energy dissipation in both peripheral reactions and fusion.

Previous work at the ANU [1, 81] investigated transfer reactions in ^{16}O+ ^{208}Pb in the

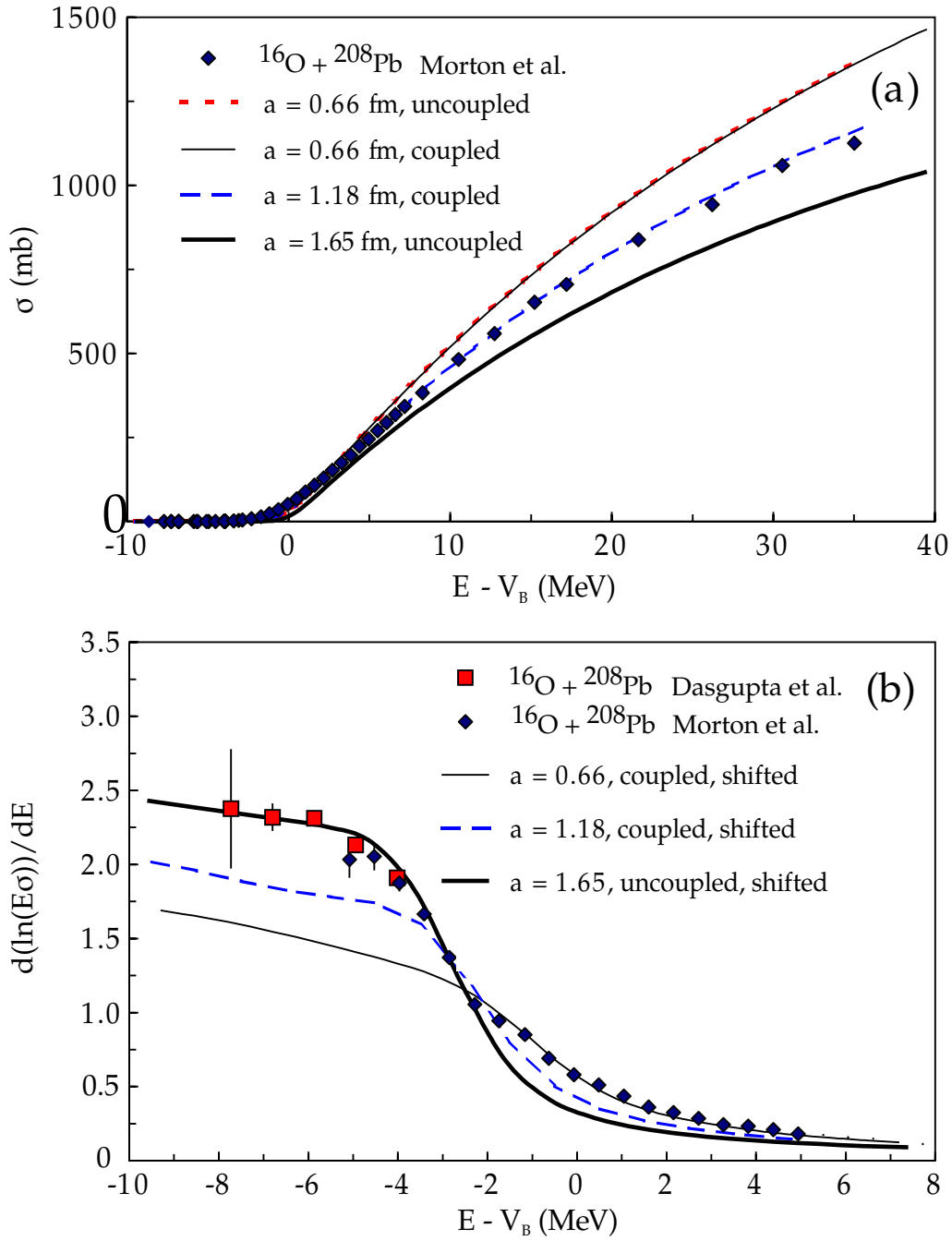

FIGURE 2.8: Fusion cross-sections in ^{16}O + ^{208}Pb compared with barrier penentration calculations within the coupled channels framework (a) on a linear scale, emphasizing the high energy data, and (b) the logarithmic slope, emphasizing the low energy measurements. Experimental data is taken from Refs. [2] (Dasgupta et al.) and [78] (Morton et al.). CRC calculations have been performed using a Woods-Saxon potential, with parameters constrained to reproduce the average experimental fusion barrier (V_B = 74.5 MeV). It is demonstrated that the potential parameters required to reproduce the data at high energy fail to reproduce that at the lowest energies, and vice versa. Note that the calculations in (b) are shifted downwards by 0.8 MeV. Figure is adapted from Ref. [2].

.

deep sub-barrier regime, and experiments showed strong evidence for correlated two-proton transfer, with this process being dominant over other transfer channels. Especially surprising was the dominance of this channel over alpha transfer, which was expected to be most important (as a result of the cluster structure of light $N = Z$ nuclei). Transfer mechanisms in this reaction were seen to result in highly excited states in the residual nuclei— it was suggested that this is indicative of dissipative processes being important even at very low energies. As such, if energy dissipation is indeed happening here, this may be a contributing factor towards the observed fusion hindrance in the sub-barrier region as well as above barrier.

In this work, the aim is to investigate (for a number of systems) the prominence of different transfer modes, how they evolve as the system energy varies in the region of the barrier, and the degree to which energy can be dissipated from the relative motion through such modes. Important also is the precise nature of the transfer mechanism: in the exchange of several nucleons, there are a number of paths that can result in the same final state— are the nucleons exchanged in a successive manner, or through a direct movement of a cluster? Since CRC calculations treat transfer in an approximate manner, semiclassical methods are normally used to model transfer during the fusion process. In the following section, the understanding of transfer in the semiclassical model is presented, which explains how some of these cases can be distinguished in an experiment.

2.6 Semiclassical model of (multi-) nucleon transfer

The semiclassical description of transfer developed by Broglia and Winther [82], treats the relative motion of the colliding system classically and the transfer process quantum mechanically. In the first order Born approximation, the transfer probability to state β with Q-value Q_β can be written in the form [83]:

$$P_{\mathrm{Tr}}(r_{\mathrm{min}}, Q_\beta) = \frac{\pi}{s^2} \left|F_\beta(r_{\mathrm{min}}, Q_\beta)\right|^2 g(Q_\beta), \tag{2.39}$$

where $\mathrm{F}_\beta(r_{min}, Q_\beta)$ is the transfer form factor, describing the transition from the entrance channel to state β, and r_{min} is the distance of closest approach. Of course, the transfer occurs over the whole trajectory, including either the incoming or outgoing trajectories, before and after the point of closest approach. The observed transfer probability is thus an integral over the whole trajectory.

The factor $g(Q_\beta)$ is the adiabatic cutoff function [82] which defines the Q-window (i.e. the range of kinematically favourable states produced in the reaction):

$$g(Q_\beta) = \exp\left(\frac{-(Q_\beta - Q_{opt})^2}{2s^2}\right). \tag{2.40}$$

Here, the width of the distribution is estimated by:

$$s = \sqrt{\frac{\alpha\hbar^2\ddot{r}}{2}}, \tag{2.41}$$

where α is related to the exponential slope of the transfer function as it varies with the internuclear separation, and $\ddot{r}$ is the acceleration of the projectile at the distance of closest approach [84]:

$$\ddot{r} = \frac{2E_{c.m.} - V_B}{\mu_i R_B}. \tag{2.42}$$

In the above, μ_i is the reduced mass of the system in the entrance channel, R_B is the fusion barrier radius.

The optimum Q-value, Q_{opt}, can be calculated based on the requirement that the classical trajectories join smoothly in the entrance and exit channels [85, 83]:

$$Q_{opt} = \left(\frac{Z_{\mathrm{Tr}}}{Z_2} - \frac{Z_{\mathrm{Tr}}}{Z_3}\right)E_b + \left(\frac{m_{\mathrm{Tr}}}{m_3} - \frac{m_{\mathrm{Tr}}}{m_2}\right)(E_{c.m.} - E_b) + \frac{m_{\mathrm{Tr}}\ddot{r}}{m_1 + m_2}(R_2 m_3 - R_1 m_4). \tag{2.43}$$

In the above equation, subscripts 1 and 2 denote the two incoming nuclei, 3 and 4 the outgoing nuclei. Z_{Tr} and m_{Tr} signify the charge and mass of the transferred particle and E_b is its binding energy. The R_i are the nuclear radii. It is worth mentioning that there have been several different formulations of the optimum Q-value [86, 87, 88, 89]. In the case that the relative energy is below the Coulomb barrier, and the target (2) mass is large relative to the projectile (1) (applicable to the systems that will be studied in this work), the effect of target recoil can be neglected and the above expression simplifies to [90]:

$$Q_{opt} \approx E_{\mathrm{c.m.}} \left[\left(\frac{Z_3 Z_4}{Z_1 Z_2} \right) - 1 \right]. \tag{2.44}$$

The Q-window (Equation 2.40) is one of the most important factors in determining the probability for a particular transfer mode, and whether a particular exit channel is possible in the reaction. The Q-windows computed for the ^{16}O + ^{208}Pb reaction (using Equation 2.40) at the barrier energy for a range of transfer processes are shown in Figure 2.9 by the red curves. The blue lines show the range of possible Q-values. The green shaded areas indicate the overlap between the Q-window and the Q-values leading to possible states. It can be seen that for most of the considered transfer processes, the overlap with the range of allowed states is minimal, and hence they are kinematically suppressed. It will be shown in Chapter 5 that those outcomes that show a strong overlap between the cutoff function and the range of available states are indeed those that are most prominent.

Assuming equal probability for all excited states, integrating equation 2.39 with respect to Q gives the total transfer probability for each mass partition [83]:

$$P(r_{\mathrm{min}}) = \frac{\pi}{s^2} |F(r_{\mathrm{min}})|^2 \int_{-\infty}^{Q_{\mathrm{g.g}}} \rho(Q) \exp\left(-\frac{(Q - Q_{\mathrm{opt}})^2}{2s^2} \right) dQ. \tag{2.45}$$

Where ρ (Q) is the density of possible transitions between states in Q. The density of possible transitions is known to be much higher for reactions involving heavier nuclei. This is due to the fact that heavy nuclei have a much greater density of excited states in any given range of excitation energies, and whilst excited states are discrete and well

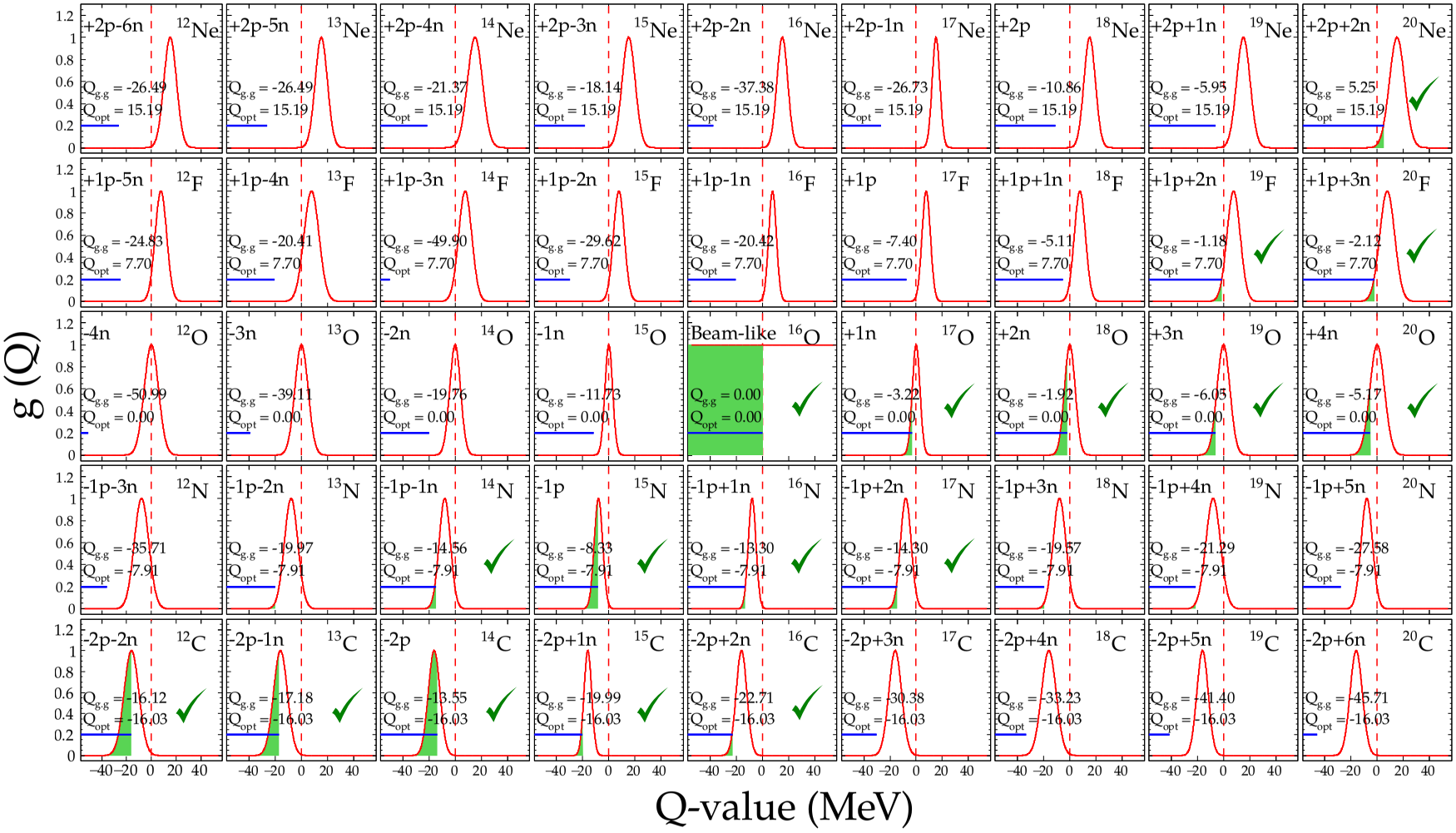

FIGURE 2.9: Adiabatic cutoff function for various transfer modes in ^{16}O + ^{208}Pb, where the system energy is $E_{c.m.}$ = 74.5 MeV (equal to the barrier energy). The vertical red dashed line indicated Q = 0 MeV. The solid red line shows the adiabatic cutoff function— given by Equation 2.40. The blue line shows the possible Q-values for the mode in question, extending up to $Q = Q_{g.g}$. The overlap with the adiabatic cutoff function is shaded in green. The number of nucleons transferred and the $Q_{g.g}$ and Q_{opt} values (see text) is indicated in each panel. Those transfer modes which are permitted according to consideration of the Q-window are indicated by green checkmarks.

spaced at low energies (particular in light nuclei), the density of states becomes exponentially larger as the excitation energy increases towards the decay thresholds. The Q-independent form factor F (r_{min}), is normally parameterized as:

$$F(r_{\text{min}}) = F_0 \exp(-2\alpha r_{\text{min}}). \tag{2.46}$$

The parameter $\alpha = \frac{\sqrt{2\mu E_{b,\text{eff}}}}{\hbar}$ is known as the slope parameter, in which μ_i is the reduced mass (in the entrance channel) and $E_{b,\text{eff}}$ is the effective binding energy of the nucleons being transferred. For neutrons, which are not influenced by the Coulomb field, $E_{b,\text{eff}}$ in this expression is taken as the binding energy. Where protons are transferred the effects of the Coulomb field of the approaching collision partner must be taken into account as well as the barrier that must be overcome by the transferred protons. The effective binding energy in those cases is given by [91]:

$$E_{b,\text{eff}} = E_b - \Delta V + V_C, \tag{2.47}$$

where ΔV is the change in the binding energy due to the Coulomb field of the approaching collision partner, and V_C is the Coulomb barrier that must be overcome by the transferred proton. When considering the possibility of clusters of nucleons being transferred, the effective binding energy for the cluster should be used in the calculation (e.g. for transfer of an α-particle, $E_{b,\text{eff}} = Q_\alpha$).

The slope parameter α is calculated as the average of the slopes in the donor (α_1) and acceptor nuclei (α_2) [84]:

$$\alpha = \frac{1}{2}\left(\alpha_1 + \alpha_2\right). \tag{2.48}$$

When considering multi-nucleon transfer, in the simplest picture the slope parameter should scale with the number of nucleons transferred (i.e. $\alpha_{2n} \simeq 2\alpha_{1n}$), with the absolute probability scaling accordingly. For example

$$P_{2n} \simeq (P_{1n})^2. \tag{2.49}$$

This scaling, together with the exponential dependence of the form factor given by Equation 2.46, suggests that at low energies, with larger internuclear separations, single nucleon transfer channels should be most important. As the energy increases and the barrier is approached, multi-nucleon transfer modes are likely to become more important.

Enhancements relative to this expectation have commonly been attributed to correlations beyond the simple model, and taken as evidence of a contribution to the yield from the transfer of clusters of nucleons in a single step, as opposed to a successive mechanism. Fully microscopic calculations based on the independent particle picture have shown that equation 2.49 serves only as an approximation to sequential nucleon transfer [92, 81]. In addition, the inclusion of pairing correlations [93], quantum fluctuations [94, 95], and particle evaporation [96] leads to a more complicated picture.

2.7 The quantum many-body problem: Independent particle models

The ultimate goal of theoretical approaches to modelling nuclear structure and reactions is to be able to deduce properties and dynamics from first principles. In order to avoid empirical assumptions, the starting point from which to build nuclear models is the nucleon-nucleon interaction (and at a more fundamental level, the quark-gluon coupling interactions which determine the structure of nucleons, and in turn give rise to the force between nucleons). The dynamics and properties of nuclei are of course emergent from these fundamental interactions [97]. It is beyond the scope of this thesis to examine these methods in detail, but it is necessary to mention that such methods, notably those utilizing Hartree-Fock methods, have matured to the extent that it is possible to model many properties of nuclear interactions and structure [98, 99], and there has been recent success in reproducing the observables in multinucleon transfer reactions that are predicted from

an empirical basis using direct reaction models, including the semi-classical methods described previously [100, 101]. However, at present there exists no effective microscopic theoretical framework that can describe the tunnelling phenomenon that is important to reactions in the sub-barrier region.

2.8 The transition between quasi-elastic and deep-inelastic scattering

As was illustrated in Figure 2.1, a given complex reaction outcome is not entirely distinct from the neighbouring modes (in terms of the angular momentum), as the modes evolve from one to another with increasing matter overlap. The contrast between direct or peripheral reactions, and compound nucleus reactions is clear: In the former, the binary nature of the entrance channel is generally preserved in the exit channel, whilst in the latter, an intermediate stage involves two nuclei fusing to form a single equilibrated compound system. Whilst these reaction modes at the opposite extremes of angular momentum can be easily distinguished, the boundaries between on one hand the direct processes and deep-inelastic ones, and on the other fission and quasifission, are poorly defined and somewhat arbitrarily distinguished.

It is useful to define the concept of quasi-elastic scattering [80]: these are the various scattering outcomes that involve a reflection of the incoming flux from the fusion barrier without being absorbed to form a single nucleus. What is included in the quasi-elastic yield has been defined differently in various studies depending on the theoretical model used to interpret the results. Generally it is taken to include those outcomes in which there are only small energy losses (i.e. the Q-value is close to $Q_{g.g.}$)— such as elastic and inelastic scattering— and/or those in which there is transfer of several nucleons (in other words those processes that can be described as direct reactions where interaction times are small and it can be assumed that the reactants only interact through their overlapping surfaces).

The distinction between deep-inelastic and quasi-elastic is thus often made according to an arbitrary cut in the total kinetic energy loss (TKEL— see Appendix A), a certain number of nucleons transferred, and through the expected differences in the angular distributions of the reaction products. In the case of a direct transfer mechanism, the angular distribution of the products is bell-shaped and peaked at the grazing angle — that is, the scattering angle θ_{grazing} that is to be expected from Coulomb scattering of the reactants at an impact parameter b_{grazing} where the nuclear surfaces just about touch (see Equation 2.20). In the deep-inelastic reaction regime where friction-like effects result in longer interaction times, the nuclei can no longer be assumed to travel on the classical (pure-Coulomb) trajectories, a large and irreversible energy damping takes place, and hence the semiclassical treatment that is appropriate for the direct transfer is no longer applicable. The formation of a di-nuclear system on initial contact, which then rotates with a partial statistical equilibration of the nucleon densities between the reactants before reseparation, results in angular distributions that can take a similar form to the direct transfer mechansim (the yield of the projectile-like fragment (PLF) peaking close to the grazing angle) but can be much broader. While only small energy losses may be present in the direct mechanism, the fragments which result from the deep-inelastic process will be highly excited and appear at much lower kinetic energy than the entrance channel [60]. The TKEL spectra will not be defined by the optimum Q-value, but rather be closer to the Coulomb barrier energy in the exit channel (described by the term full energy damping) and, again, much broader than those expected from direct transfer. So whilst the experimental signatures of each reaction mechanism are quite similar, they are the result of very different interaction histories and trajectories of the reacting nuclei.

The outstanding issue in properly understanding the transition between the quasi-elastic and deep-inelastic regime can be seen in the very different theoretical formalisms that are typically used to describe each of these reactions. In the case of quasi-elastic reactions, coupled-channels or Distorted Wave Born Approximation (DWBA) approaches can be used, whilst in the deep-inelastic case friction and diffusion models have historically been applied [102, 103].

Near to the Coulomb barrier energy, multinucleon transfer reactions make up the largest

fraction of the quasi-elastic reaction cross-section. Deep-inelastic scattering is understood to be the main process that competes with fusion in the above barrier regime, and likely responsible for the observed hindrance seen when measured fusion cross-sections are compared with coupled-channels calculations. Since the reaction mechanism is expected to evolve smoothly between the quasi-elastic (below the fusion barrier) and deep-inelastic (above the barrier) regimes, understanding the transition between them may be the key to explaining the cause(s) of the fusion hindrance phenomenon far below and far above the barrier. The obvious probe to use for this purpose is that of multinucleon transfer reactions, since these modes are present in both energy regimes [83].

2.9 Summary

Having discussed the background concepts related to this thesis work, at this point it is now possible to explain the methodology that will be used in this investigation.

The goal of this thesis is to examine in detail how energy dissipation may proceed through nucleon transfer reactions, covering a range of energies that spans from the vicinity of the Coulomb barrier to far below. This will contribute to a fuller understanding of the evolution of dissipative effects with the internuclear separation, which may lead to future efforts to move beyond the existing coupled-channels methods that implicitly assume energy dissipation (beyond the discrete states explicitly treated) occurs only inside the barrier radius.

In this investigation multinucleon transfer probabilities are measured at backward angles. These angles correspond to central collisions, where it can be expected that the incoming flux is partially transmitted through the fusion barrier, with the rest of the flux reflected from the barrier. Studying the properties of this reflected flux will yield information on the events that fail to fuse, potentially providing clues as to the mechanisms responsible for the observed hindrance effects.

Uniquely identifying the reaction products in terms of the mass and atomic number, together with their kinetic energies will reveal the modes that are important in facilitating

the dissipation of energy. By analysing the slopes of the measured transfer probabilities, it is possible to identify the contribution to particular product yields from cluster transfer mechanisms. Are there in fact particular transfer modes that can act as "doorway states" through which dissipation can occur, which in turn hinders fusion below the barrier?

In investigating the systematics of energy dissipation through multinucleon transfer, with a view to understanding how this might influence the fusion dynamics, it is prudent to begin with the well-studied ^{16}O + ^{208}Pb system. This system is seen as a benchmark in fusion studies, having been the subject of many investigations and exhibiting fusion hindrance effects in both the above and deep sub-barrier regimes. Involving the fusion of two spherical and doubly magic nuclei, the dynamics in this system should be relatively simple. In order to understand the importance of both the magic nucleon numbers and α-conjugate properties of this system, measurements are also made of the neighbouring reactions ^{18}O + ^{208}Pb, ^{19}F + ^{208}Pb, ^{16}O + ^{209}Bi and ^{18}O + ^{204}Pb. With a view to investigate how cluster transfer may facilitate the larger dissipation of energy expected with heavier nuclei, besides ^{16}O the reactions also of the medium mass α-conjugates ^{32}S and ^{40}Ca on ^{208}Pb have been examined.

These systems have been studied in two different experiments. In the next chapter the experiment involving ^{16,18}O and ^{19}F projectiles is described. The measurement of the ^{32}S + ^{208}Pb and ^{40}Ca + ^{208}Pb systems is then reported in Chapter 4.

Chapter 3

Experiment 1: ^{16,18}O & ^{19}F induced reactions on ^{204,208}Pb & ^{209}Bi (ANU)

This experiment was conducted at the Heavy Ion Accelerator Facility (HIAF) of the Australian National University (ANU) in June 2013. Experiments were carried out using accelerated beams of ^{16,18}O,^{12,13}C, and ^{19}F provided by the 14UD tandem accelerator. Projectile ions were accelerated to E/A = 3 - 5 MeV/u (corresponding to 0.9V$_B$ - 1.01V$_B$) for the different reactions. A summary of the HIAF accelerator and the beam production process are given in Section 3.1. Details of the experimental setup, detector configuration and measurement procedure are given in Section 3.2. The details of the calibration and analysis procedures are then given in Section 3.3.

The results of the experiment described in this chapter have been published in part in D.C. Rafferty et al. Physical Review C 94, 024607 (August 2016) [104].

3.1 ANU Heavy Ion Accelerator Facility

The experiment detailed in this chapter was conducted using beams produced by the 14UD Tandem van de Graaff accelerator operated by HIAF. The accelerator is a National Electrostatics Corporation (NEC) 14UD pelletron, and can hold voltages of up to 15 megavolts under optimal operating conditions.

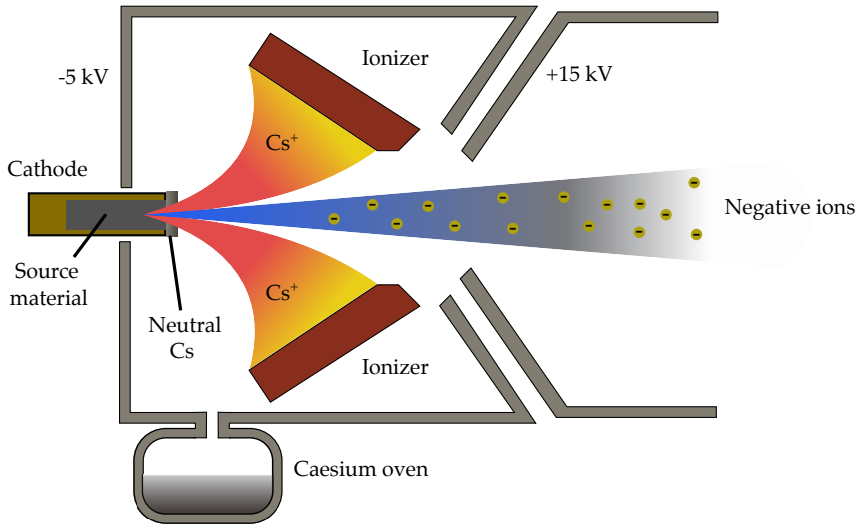

FIGURE 3.1: Schematic diagram showing the principle of operation of the SNICS (**S**ource of **N**egative **I**ons from **C**aesium). See text for details.

Negative ions are first produced using a NEC-style SNICS (**S**ource of **N**egative **I**ons from **C**aesium **S**puttering) ion source [105, 106, 107]. Figure 3.1 shows the basic operating principles of this device. The source material for the accelerated beam is packed into the cathode, a copper cylinder held at a negative bias of around 5 kV, and cooled with deionized water to around 20° C. Caesium is heated in an oven to temperatures of around 100° C, and the emanating vapour is carried into the active area of the ion source through a delivery tube. Some of the Caesium settles and forms a layer of neutral atoms on the cool cathode surface, whilst some diffuses towards the annular ionizer. The ionizer surface is a metal with high electron affinity— in this case Tungsten— and is heated to $\sim$ 1000° C. On contact with the ionizer surface, Caesium atoms lose an electron, becoming positively charged, and are then accelerated towards the cathode. On impact with the source material, atoms are sputtered out of the cathode and some pick up an electron when moving through the neutral Caesium layer. The now negatively charged ions are then ejected from the SNICS via an accelerating potential of 15 kV. The source is held at a potential of 150 kV, thus after passing through the acceleration tube isolating the source from ground, the ions, with a charge state of 1^- have a uniform initial kinetic energy E_{Initial} of 150 keV.

The injection magnet at the top of the accelerator selects ions for transmission according to mass. Between the poles of the magnet, the ions with charge state q (= 1^-) moving with a velocity $v_\perp$ perpendicular to the dipole field B are subject to the Lorentz force:

$$F = v_{\perp} qB = \frac{mv_{\perp}}{r} \tag{3.1}$$

The action of this force results in ions of mass m moving in a circular trajectory with a radius of curvature r. The mass can be selected by setting the field strength to a value that will result in a value of r appropriate to be injected into the accelerator vacuum tube. The field necessary to inject ions of mass m can be calculated according to:

$$B = \frac{\sqrt{2mE}}{qr} \tag{3.2}$$

Thus only ions of the desired mass are transmitted through to the accelerating elements of the 14UD, though this will contain possible isobaric contaminants.

Ions now enter the acceleration tube passing through the tank, and undergo a two stage acceleration process. The terminal in the center of the tank is charged to a positive potential of V_T via the pelletron charging system (see Figure 3.3). The whole tank is filled with SF_6 gas and pressurised at 700 kPa to provide resistance against electrical discharges resulting from the high electric field gradient. In the first stage of acceleration, ions are accelerated from the ground potential of the outside the tank towards the terminal. Upon reaching the terminal, the ions now have a total kinetic energy:

$$E = qV_T + E_{\text{Initial}} \tag{3.3}$$

Inside the terminal the ions are stripped of electrons by either a gas stripping cell or Carbon foil of $4\mu g/cm^2$ thickness, becoming positively charged. Upon stripping, the ions have a range of charge states, the most abundant of which can be predicted according to the semi-empirical formula for particles moving in solids (assuming a carbon foil stripper), which allows calculation of the average value $\bar{q}$ [108, 109]:

$$\bar{q} = Z\left[1 + \left(3.85Z^{-0.45}\sqrt{\frac{E}{A}}^{-1.67}\right)\right]^{-0.6}, \tag{3.4}$$

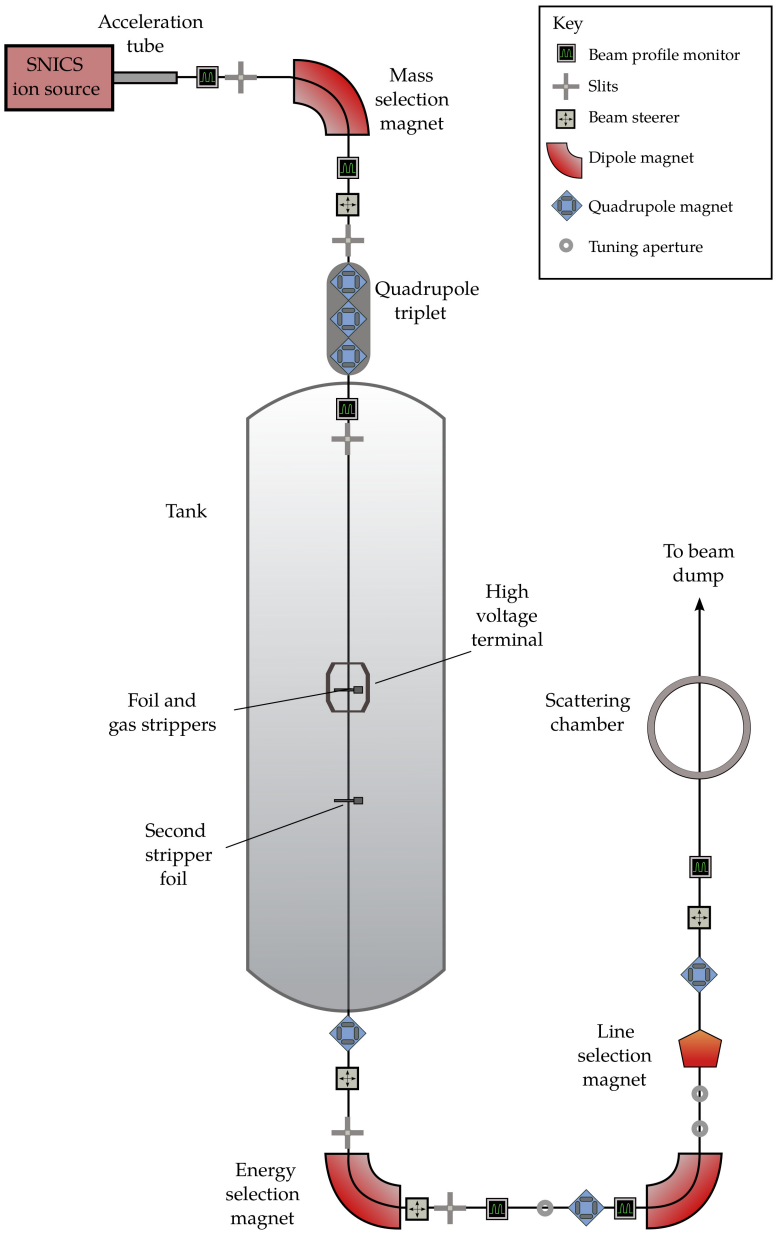

FIGURE 3.2: A schematic diagram of the 14UD electrostatic accelerator beamline. Negative ions are produced by the SNICS, and accelerated through a 150 kV potential towards the mass selection magnet. Ions of the selected mass are then injected into the acceleration tube passing through the SF_6 tank, where they are initially accelerated towards the positively charged high voltage terminal through a potential of up to 15 MV. In the terminal, the ions undergo electron stripping when passing through the gas and/or foil strippers. Now with a distribution of positive charge states, the ions undergo a second stage of acceleration towards the ground potential, where they arrive with a range of kinetic energies. A dipole magnet at the base of the accelerator selects the desired beam energy, with those ions being transmitted to the focussing elements of the beamline.

Now positively charged, the ions are accelerated away from the terminal towards the ground potential at the bottom of the tank. If particularly high beam energies are required, there is an optional second stage carbon foil stripper at $1/3$ of the distance between the terminal and the bottom of the tank. This can achieve a higher average charge state, though will reduce the yield of any particular charge state. The final energy of the ions at the tank exit is thus given by:

$$E = E_{\text{Initial}} + V_T + \frac{1}{3}q_1 V_T + \frac{2}{3}q_2 V_T \tag{3.5}$$

where q_1 and q_2 are the charge states after the first and (optional) second stage stripping. The accelerated ions next enter the energy selection magnet (also known as the analysing magnet), where they are again deflected according to the Lorentz force (see Equation 3.1). The field is set to select ions of the correct magnetic rigidity $\rho = \frac{mv}{q}$, such that they are deflected with a gyroradius $r = B\rho$ suitable for transmission to the ion-optical elements further downstream. The slits located just after the energy selection magnet read the beam current striking them, and are part of a feedback circuit which stabilizes the terminal voltage at the appropriate value for transmission of chargestates of the desired energy. From this point the selected beam ions pass through a series of focussing elements and are directed towards the scattering chamber. At various positions in the accelerator system and the beamline there are insertable Faraday cups which can provide a reading of the beam current. The focussing elements are adjusted to maximise the current at each point to ensure optimum transmission of the ion beam to the scattering chamber.

Prior to each beam tune, based on the desired beam ion and energy, the magnetic fields of the injecting and analysing magnets can be calculated, together with the necessary terminal potentials, for a range of different chargestates. Normally the combination is chosen to result in the highest beam current consistent with the energy required, though occasionally the decision is affected by the performance of the terminal charging system.

The 14UD also incorporates a bunching and chopping system to produce a pulsed beam. In the experiment reported in this chapter a direct current beam was utilized, so the details of this system are omitted. For further details the reader is referred to Ref. [110].

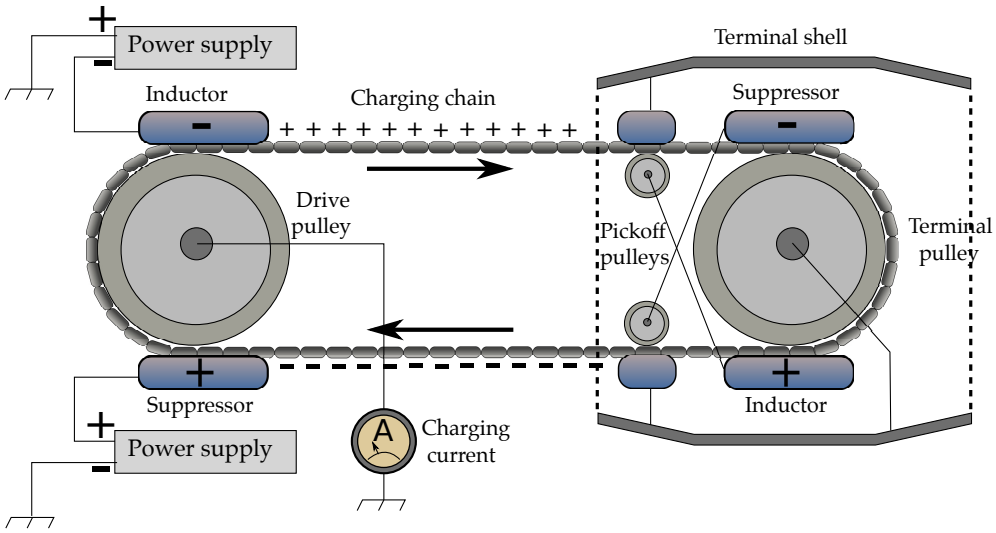

FIGURE 3.3: Schematic diagram showing the principle of operation of the 14UD pelletron charging system. Metal pellets on a chain, separated by nylon links, are induced with a positive charge at the base of the terminal tank. At the terminal, the chain picks up electrons and carries the negative charge away from the terminal, leaving the terminal with a net positive charge.

3.2 Experimental details

Quasi-elastic scattering products were detected using a gas ionization chamber and ion implanted Si detector, allowing separation of reaction products in mass and charge through the ΔE-E technique. This combination of detectors will henceforth be referred to as the ΔE-E telescope. The ΔE-E telescope for particle identification relies on the fact that ions of different masses and atomic numbers, travelling with the same kinetic energy, lose energy through interaction with a material layer at different rates. The details of the technique will be further explained in Section 3.3.3.

In combination with two monitor detectors positioned at forward angles on opposite sides of the beam axis, this detector configuration allowed normalization of back-scattered yields to the measured Rutherford cross section at the forward angles, giving absolute probabilities for the observed reaction modes.

The ΔE-E telescope was positioned at a lab scattering angle $\theta_{lab} = 160.6°$, and the two implanted Si monitor detectors were at angles $\theta_{M1} = \theta_{M2} = 22.5°$ relative to the beam axis. A schematic diagram of this experimental set-up is given in Figure 3.4. Figure 3.5

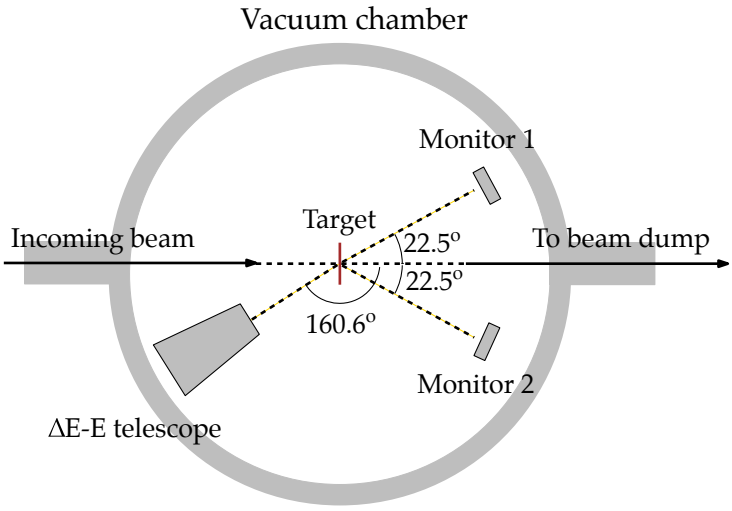

FIGURE 3.4: Schematic diagram of experimental arrangement

shows photos of the ΔE-E telescope as it was set up for the experiment, before and after the vacuum chamber lid was lowered over the setup.

3.2.1 Detector configuration

The detector configuration used in the present work was an improved design of one used in previous experiments [81, 111]. The previous setup was a similar Frisch grid design [112], recording the energy lost in a gas chamber together with residual energy of the ion in the Si detector beyond it. This detector configuration was used to examine transfer reactions in ^{16}O + ^{208}Pb, though the mass resolution was insufficient to separate adjacent isotopes in mass for the full range of reaction products observed in the experiment. The new electrode design (conceived by Dr. C. J. Lin) incorporated arrays of 36 conducting strips on circuit board panels on each side of the gas volume, which are connected in series and separated by 10MΩ resistors. This feature acts as a potential divider between the cathode and the Frisch grid, so that the electric potential varies linearly along the y axis inside the detector (where the beam path is along the z axis). The improved design consisted of a planar grid parallel to the anode plane with a highly uniform 1mm wire spacing, together with thinner wires (20μm thick gold plated tungsten). These changes were made in an attempt to make the electric field inside the detector more uniform in order to minimise the position-dependence of the ΔE signal. The electric field was oriented

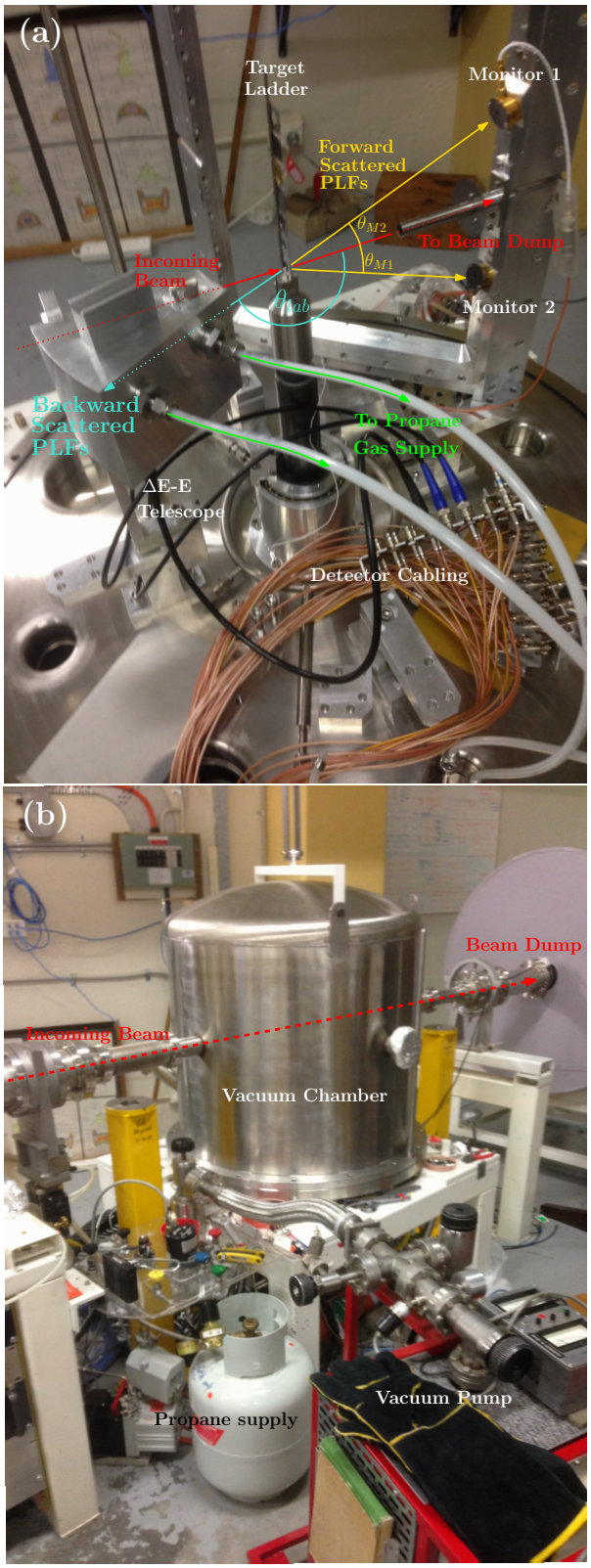

FIGURE 3.5: (a) Photo showing experimental setup, including the contents of the scattering chamber.
(b) Photo showing scattering chamber installed on the beamline.

along the vertical axis, in order to minimise recombination of ions and liberated electrons along the ionizing path of the incoming projectile. Recombination can contribute to a pulse-height defect, introducing non-linearities to the electrical signal response of the detector to incoming radiation, so it was important to attempt to minimize this effect. The particular design of the new configuration can be seen in Figures 3.6 and 3.7.

The Frisch grid is designed to remove position sensitivity in the ΔE-E telescope. Whilst passing through the gas portion of the detector, the incoming ions interact with molecules of the gas, ionising gas atoms along the path of the ion. After ionisation, the positive ions are drawn towards the cathode, and electrons toward the grid, which consists of equally spaced wires oriented along the length of the detector, held on a frame and held at a fixed potential, V_G, which is intermediate between that of the anode, V_A and cathode, V_C. The design of the Frisch grid means that no voltage drop will be measured on the anode while the electrons drift towards the grid. Only after passing through the grid, a signal begins to build up across the load resistor of the circuit. The electrons all travel across a fixed voltage difference (between the grid and the anode), thus the signal is independent of the vertical position of the ion trajectory. As the signal depends only on the electron drift time, and not the slower drift of the positive ions toward the cathode, the time constant of the amplifier can be set to a value much lower than otherwise necessary, allowing for higher counting rates.

The uniformity of the grid used in this experiment has been improved over that used previously. The grid wires for the new detector were mechanically wound on a rigid frame before being soldered onto the Frisch grid electrode. The process made it possible to achieve a uniformly spaced planar grid. Together with the addition of the potential dividing arrays between the cathode and anode this ensures a more uniform electric field. As such, these improvements aim to ensure that the position sensitivity of the detector is removed, and to reduce blocking of electron collection. The grid frame itself however presents a dead layer to the detector, since electrons formed along the path as they first enter the detector, as well as just prior to the silicon detector may be attracted to and likely blocked from entering the region between the grid and anode, and thus prevents them from contributing to the energy loss signal. The voltages on the Frisch grid and

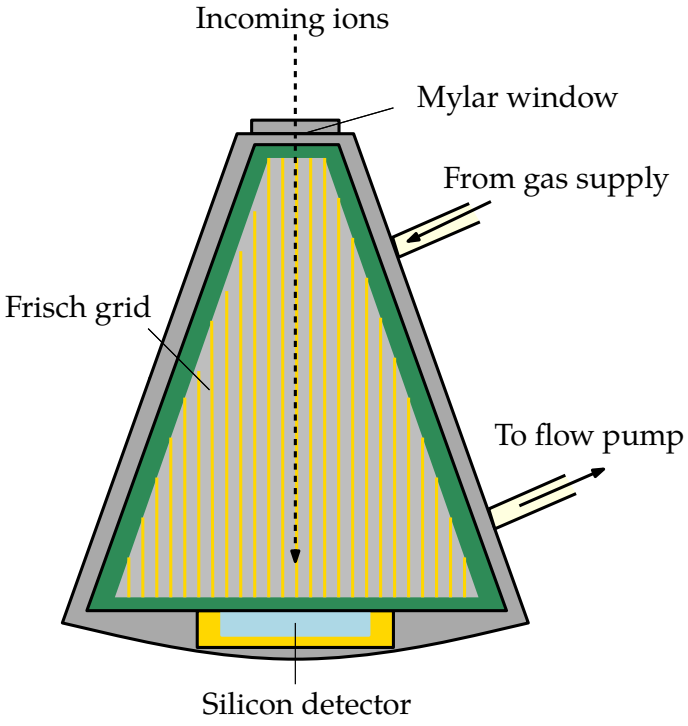

FIGURE 3.6: Schematic of ΔE-E telescope. Top view.

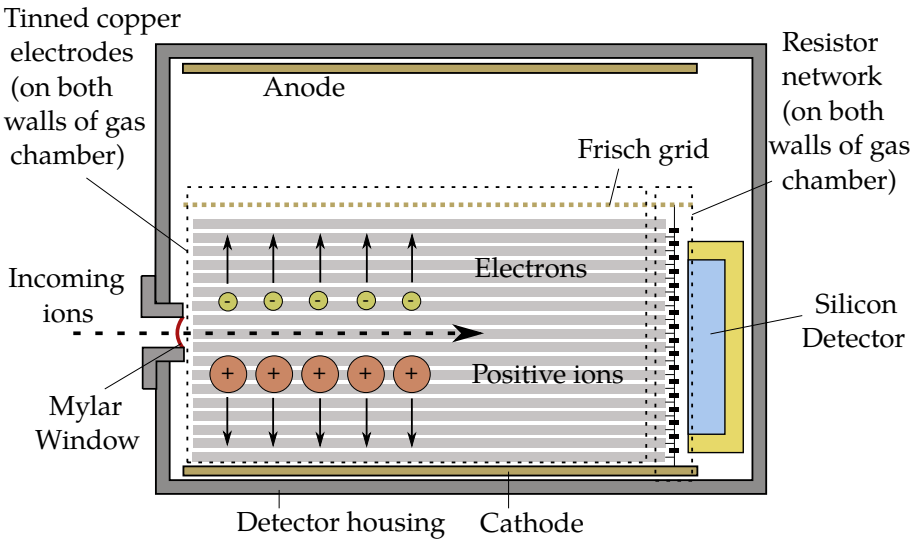

FIGURE 3.7: Schematic of ΔE-E telescope. Side view.

anode were adjusted to maximise the ΔE signal.

The telescope has a 5mm diameter entrance aperture sealed with a 0.9 μm mylar window. It was located $\sim$ 17 cm from the target, resulting in a very narrow acceptance of angles (equivalent to a solid angle of $\sim$ 0.2 msr). As such, differences in the path length of ions travelling through the gas is restricted to quite a small range. However, as there is a large pressure difference between the chamber housing the Propane (120 mbar) and the surrounding vacuum, the window will inevitably deform, resulting in an extension of the designed gas length. This was known to happen, as windows occasionally burst during initial experiments to determine the appropriate gas pressure. The deformation was estimated to result in a maximum possible extension of 1mm to the total gas length, which depends on the position of the ion with respect to the center of the window.

The detector housing and entrance window provide adequate shielding to eliminate most background sources (for example, beam ions back-scattered from the beam dump) which would otherwise distort the measured spectra.

3.2.2 Electronics set-up and data acquisition

Figure 3.8 is a schematic diagram showing the electronic setup for signal pulse processing. The detector signals are initially fed into charge-sensitive preamplifiers close to the scattering chamber to reduce noise. The energy outputs from each of the preamplifiers undergo secondary amplification and are sent to the analogue-to-digital converters (ADC).

The timing outputs of the silicon and monitor detector preamplifiers are first shaped by a multi-channel timing filter amplifier (TFA) and then sent to constant fraction timing discriminators. The much higher counting rates in the forward angle monitor detectors first required pre-scaling by a factor of 1/10, the signals then were fed into a logical 'OR' gate, generating a signal if either input was present. The output of this logic unit is then delayed before reaching a slow coincidence gate, which generates the DAQ trigger. The other input is the logic pulse from the constant fraction discriminator (CFD) connected to

#	Target Compound	Thickness ($\mu g/cm^{-2}$)	Carbon Backing Thickness ($\mu g/cm^{-2}$)
1	^{204}PbS	100	15
2	^{209}Bi	50	10
3	$^{206}PbCl_2$	80	10
4	Ta	$*$	-
5	^{197}Au	250	0
6	^{208}PbS	80	15
7	^{208}PbS	150	15
8	^{209}Bi	60	10

TABLE 3.1: Details of targets, numbered in the order mounted on the target ladder.
$*$ The thickness of the Ta frame was 0.25 mm, sufficiently thick to prevent transmission of any beam ions over the energy range considered in this work (see text).

the telescope silicon detector, to trigger the data acquisition system (DAQ) independent of the presence of a ΔE signal.

In order to account for the dead time in the data acquisition system, the prescaled monitors and telescope silicon detector triggers were recorded independently in the scalars.

3.2.3 Targets

Details of the targets used in this experiment are given in Table 3.1. Most targets were prepared through thin film deposition on Carbon backings, with the targets oriented with this Carbon layer facing downstream from the beam direction. Where the Carbon backing thickness is listed as zero in Table 3.1, this indicates that the target is self-supporting. These Carbon layers presented an additional layer through which energy losses had to be calculated in order to accurately calibrate the forward-angle monitor detectors, but did not affect the measurements in the ΔE-E telescope.

Targets were each mounted on a frame of Al or steel and attached to a ladder on a translation stage inside the target chamber. The translation stage allowed the ladder to be moved in the y-direction (where the beam direction is along the z-axis)— this meant it was possible to limit the radiation damage to any one point on the target by adjusting

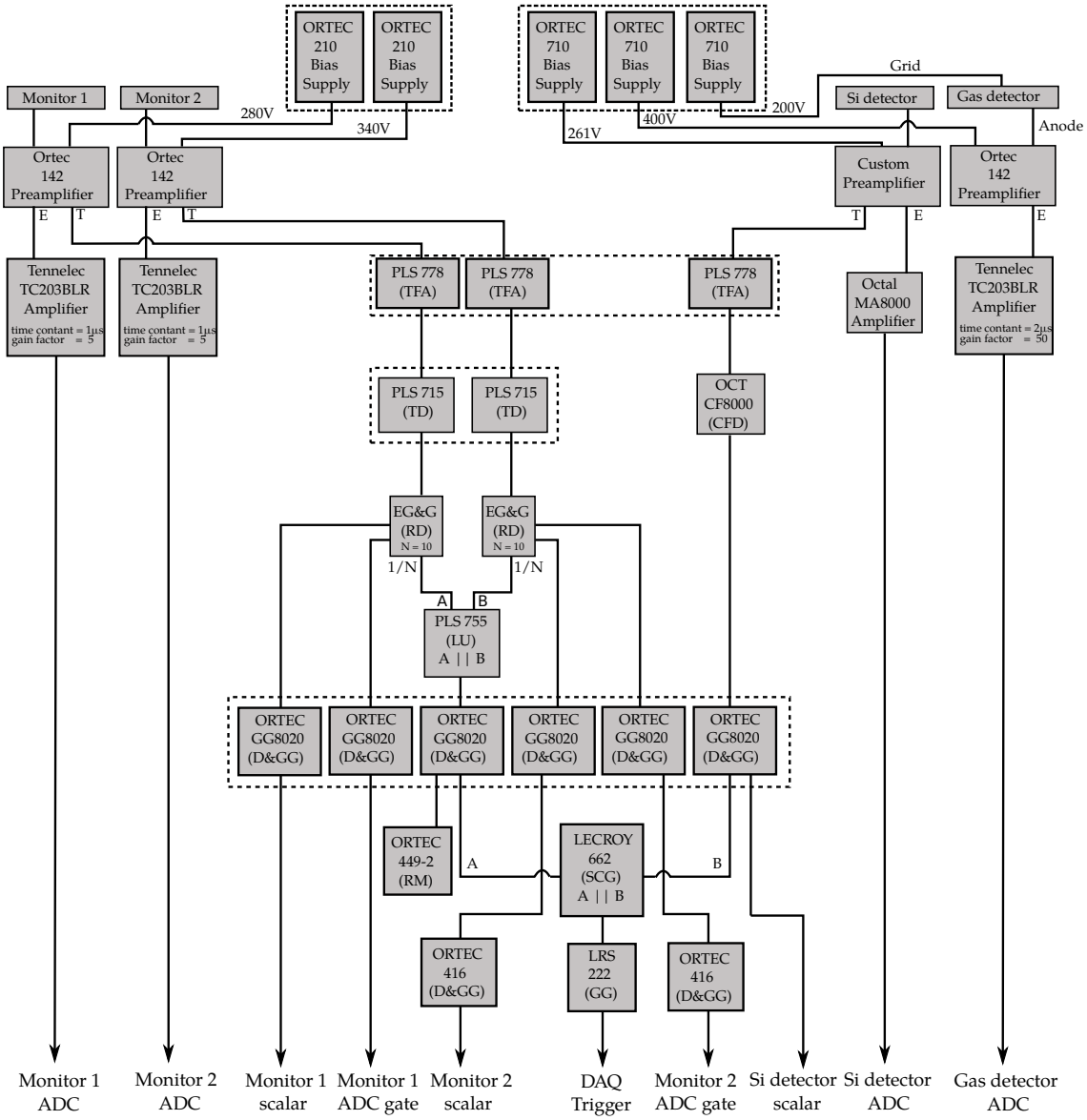

FIGURE 3.8: Electronic setup of detectors for pulse processing. The manufacturer and model numbers of the different components are indicated. The abbreviations in brackets indicate the type of component— in approximate order in which they process the detector signals: TFA (**T**iming **F**ilter **A**mplifier), CFD (**C**onstant **F**raction **D**iscriminator), TD (**T**iming **D**iscriminator), RD (**R**ate **D**ivider), LU (**L**ogic **U**nit), (D&)GG ((**D**elay and) **G**ate **G**enerator), SCG (**S**low **C**oincidence **G**ate), RM (**R**ate **M**eter). Where dashed contours are drawn around identical components this indicates a multi-channel device.

its position relative to the beam. Target 4 listed in Table 3.1 is actually an empty slot in the target ladder, consisting of a Tantalum frame with a 2 mm aperture. For beam tuning, such an aperture is normally included on the target ladder, and the beam focused through it whilst tuning to ensure the ion beam is precisely focused on the target with as little variation as possible in the beam spot position between runs. In this experiment the aperture served a dual purpose— for beam tuning in the manner described, and also, by displacing the aperture from the beam (using the controls of the translation stage described previously), presenting a thick Tantalum layer to the incoming beam. This caused projectile-like fragments to emerge from the target in the backward angles over a wide energy range aiding particle identification in the ΔE-E telescope, as will be described in Section 3.3.3.

The thickness of the gold target in position #5 was known prior to the experiment, whilst the thicknesses of the others were determined from a comparison of the number of elastic scattering counts in the monitor detectors following equivalent integrated charge measurements using a ^{16}O beam.

Some target impurities were expected to be present in the materials used due to the deposition of high melting point compounds to minimise target melting. Also, for example, the Bismuth targets develop a surface oxidation after prolonged exposure to air, which is evident in the iridescent hue of its outer surface. Prior to installation on the target ladder, target 2 was observed to have a dark blue colour, whereas the sample at position 8 appeared more metallic than iridescent. This indicated that the two target surfaces had oxidised to different extents and as such contained different proportions of oxide impurities.

3.2.4 Measurement procedure

A summary of the important experimental measurements conducted in this run is shown in Table 3.2. Runs were also recorded for the various projectiles on the ^{197}Au target (#5) and also scattering from the thick ^{181}Ta target frame (#4) in Table 3.1 for calibration and analysis purposes, as will be described in Section 3.3. Note that during the first attempted

run using the $^{206}PbCl_2$ target listed at position #3 in Table 3.1, the monitor spectra indicated a breakage. As such this measurement was not possible during this run, and is discussed no further in this work.

System	Barrier energy V_B (MeV)	Beam energies $E_{c.m}$ (MeV)
$^{16}O + ^{208}Pb$	74.5	73.0, 72.5, 70.9, 69.3
$^{16}O + ^{209}Bi$	75.3	73.1, 72.5, 70.9, 69.3, 67.9
$^{18}O + ^{208}Pb$	73.6	73.6, 71.6, 71.1, 70.3, 69.6, 68.0
$^{18}O + ^{204}Pb$	74.0	73.4, 71.5, 70.9, 70.2, 69.5
$^{19}F + ^{208}Pb$	82.4	83.3, 81.3, 80.6, 78.9, 77.2, 75.5, 74.1

TABLE 3.2: Fusion barrier and beam energies (both in the center-of-momentum frame) in systems studied in this work. The capture barrier for $^{16}O + ^{208}Pb$ is the average barrier energy extracted from the measured experimental barrier distribution [78]. The values for the other reactions are scaled according to the masses and charges of the projectile and target [113].

Due to the fragility and low melting points of some of the target materials (e.g. Bismuth $\sim 271°C$), in order to limit damage arising from radiative heating, during each run the target position was adjusted in a sinusoidal motion in the y- direction (where the z-axis is along the direction of the beam) with amplitude $\pm$ 2 mm to aid in heat dissipation.

It was necessary to correct the yields in the detectors due to electronic dead time, which was possible by using the integrated counts for each signal in the scalers indicated in Figure 3.8. As the scaler counts are not reliant on the DAQ processing speed limitations they were able to provide an indication of this effect and multiplicative factors by which to scale the recorded yields. Due to the low DAQ trigger rates, the necessary corrections were typically much less than 1 % throughout the experiment.

3.3 Calibration and analysis procedures

The underlying principle of particle identification using the ΔE-E technique is the different rates of energy losses between particles of differing atomic number Z_p and atomic mass A_p, travelling with the same kinetic energy E, when passing through a material layer. In the non-relativistic case, the rate of energy loss (also known as the stopping

power) for an ion travelling with kinetic energy E passing through a material characterised by atomic number Z and mass number A can be expressed through the Bethe-Bloch relation:

$$-\frac{dE}{dx} \propto \frac{Z_p^2 A_p}{E}\frac{Z}{A} \tag{3.6}$$

From this relation, it can be expected that the total energy loss through a material layer should vary quadratically with the projectile atomic number Z_p and linearly with its mass A_p. In practice, it is difficult to calculate precisely the stopping power in any particular case from the fundamental parameters. This is particularly true of complex compound materials where dE/dx cannot be simply expressed with a single combination of Z and A as in Equation 3.6. Rather, it is more common to rely on measurements of energy losses through common materials and to calculate the stopping power for an arbitrary combination of projectile and material based on the Bragg additivity rule [114], which determines the total stopping power through a weighted sum according to the stochiometric ratio of atoms in the molecules of the stopping material [115]. There are various software packages available which can calculate stopping powers in an arbitrary case based on these considerations— the most frequently used is `SRIM`[116], which is based on an extensive set of measurements of energy losses of protons and alpha particles through various media. The stopping powers for arbitrary projectiles are calculated based on the scaling laws defined by Equation 3.6. Unless otherwise specified, `SRIM` has been used throughout this thesis work to generate stopping powers for use in energy loss calculations.

3.3.1 Calibration of the ΔE-E telescope

Before an attempt can be made to calibrate the two electrical signals generated by the passage of ions through the ΔE-E telescope, considerations must first be made of processes which can reduce the energy of the ions without contributing to the signal pulses.

As mentioned in Section 3.2.1, the effect of recombination of electron-ion pairs following the ionization process prevents the energy required for ionization being registered in the

signal pulse. The dense plasma track along the ionization path of the incoming ion partially screens the electrons and positive ions from the external field, and the mutual electrostatic attraction between them can cause them to recombine before the electrons can escape to the region between the grid and anode. An analogous process can contribute to a pulse height defect in the silicon detector, where recombination of the electron-hole pairs can occur prior to collection. This effect is minimized in both components by maximizing the applied bias, though must be balanced against the need to prevent dielectric breakdown of the active material.

There are also non-electronic processes that can contribute to the total stopping power of a material. When travelling with low kinetic energies, incoming ions can lose energy through nuclear collisions. Whilst this should not be significant in the gas layer, this will contribute somewhat to a pulse height defect in the silicon detector at the end of the ion track, just prior to stopping. `SRIM` calculates both the electronic and nuclear contributions to the total stopping power, and an example is shown in Figure 3.9 for ^{18}O ions travelling in pure silicon under standard conditions. As can be seen, the nuclear contribution does not become similar in magnitude to the electronic contribution until the ^{18}O ions are reduced to energies below 50 keV. As such, any contribution to a discrepancy in the signal strength will be insignificant compared to the total energy resolution of the detector.

Both the Mylar window and the silicon detector aluminium surface layer present effective dead layers in the ΔE-E telescope. In both of these media, quite substantial energy losses can occur, which will not result in free charges in the active zones of the detectors. For example, in a typical measurement in this experiment of scattering of ^{18}O at a beam energy of 80 MeV from ^{208}Pb, after energy losses in the target are taken into account, the elastically scattered ions are expected to enter the ΔE-E telescope with a kinetic energy of 55.5 MeV. Such ions would be expected to lose $\sim$ 0.5 MeV in the entrance window ($DeltaE_{\text{Window}}$) and $\sim$ 2 MeV in the aluminium layer ($DeltaE_{\text{Al}}$)— around 5% of the total energy will not contribute to the electrical response of the detector system. As was previously mentioned in Section 3.2.1, beyond the entrance window of the ΔE-E telescope, there is an additional effective dead layer due to the presence of the non-transparent (to

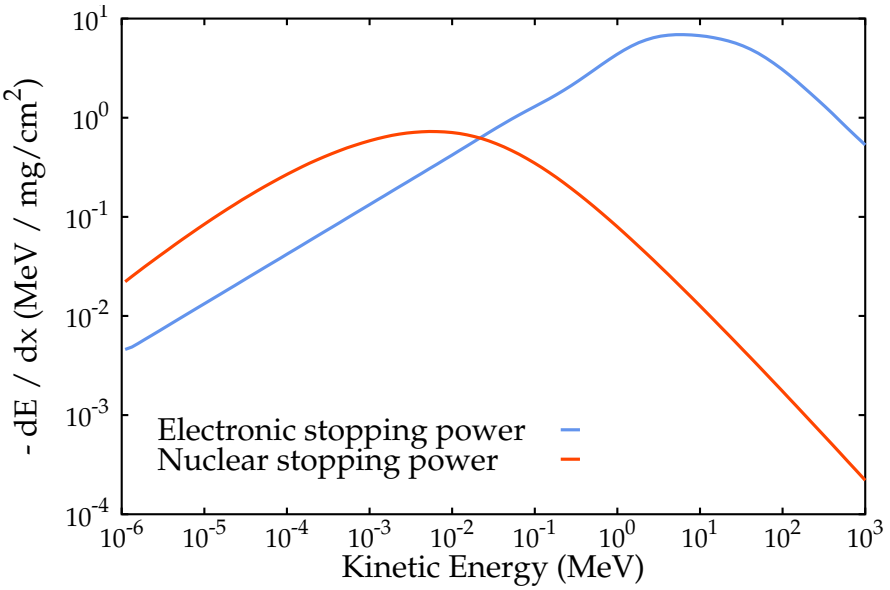

FIGURE 3.9: A comparison of the contributions to the total stopping power from electronic and nuclear collisions, for the example of ^{18}O ions travelling in pure Silicon.

electron motion) frame of the Frisch grid, which will attract the electrons liberated by the ionization process, but will not allow passage to the region between the grid and anode where the signal of the gas detector is measured. Since the ΔE-E telescope is required to identify reaction products covering a range of different Z_p and A_p, it was important to find a calibration of the two signals that has a good agreement with the expected energies of all of these different products.

The total energy deposited in the ΔE-E telescope can thus be expressed as:

$$E_{\text{Total}} = \Delta E_{\text{Window}} + \Delta E_{\text{gas}} + \Delta E_{\text{Al}} + \Delta E_{\text{Si}} \tag{3.7}$$

The silicon layer is sufficiently thick (300 μm) that all reaction products of interest in the experiments reported here will be stopped within it. The simplest way to account for the processes which do not contribute to the electrical responses of the active gas and silicon layers is to calibrate the two signals simultaneously, absorbing these effects into the calibration factors. The total energy of the elastically scattered beam ions can be calculated accurately, requiring only the calculation of the rather small energy losses in

the thin targets, together with a determination of the back-scattered energy through non-relativistic kinematics (see Appendix A). The total energy E_{Total} can then be expressed as:

$$\begin{aligned} E_{\text{Total}}(\text{MeV}) &= \alpha_0 + \alpha_1 \Delta E_{\text{gas}}(\text{channels}) + \beta_0 + \beta_1 \Delta E_{\text{Si}}(\text{channels}) \\ &= \delta + \alpha_1 \Delta E_{\text{gas}}(\text{channels}) + \beta_1 \Delta E_{\text{Si}}(\text{channels}) \end{aligned} \tag{3.8}$$

A linear gain factor is assumed for both the gas and silicon detector signals, and the offsets for each are combined into a single offset factor δ. Taking the centroid positions of Gaussian fits to the elastic scattering peaks for all runs, and fitting with a planar function (of the form $ax + by + cz + d = 0$), the linear gain factors α_1 and β_1, together with the overall offset factor $\delta = \alpha_0 + \beta_0$, are obtained. The resulting calibration of E_{Total} gives an excellent agreement with the expected total energy for elastic scattering of all of the beams generated in this experimental run (^{12,13}C, ^{16,18}O, ^{19}F). Having incorporated the losses in the dead layers into the calibration coefficients, henceforth I refer to all energy losses in layers other than the silicon layer as belonging to one quantity, ΔE.

In order to determine the distribution of the overall offset δ between the two signals, δ is first applied in full to either ΔE or E_{Si}. The calculated total energy E_{Total} can be represented in the ΔE-E spectrum as the function $\Delta E + E_{\text{Si}} = E_{\text{Total}}$. The intersection is found between this function and the `SRIM` calculated distribution of E_{Total} between ΔE (including the gas and dead layers) and E_{Si}, and the spectrum translated to relocate the elastic peak to the point of intersection, which will require some division of δ between α_0 and β_0. Since the translation does not change the sum of ΔE + E_{Si}, this action has no influence on the extracted total energy E_{Total}. This procedure is illustrated in Figure 3.10.

3.3.2 Calibration of the monitor detectors

The main purpose of the forward angle monitor detectors is for the measurement of the Rutherford cross section. A calibration in energy is not strictly necessary for this— all that is required is the number of counts in the elastic scattering peak. However, the monitors

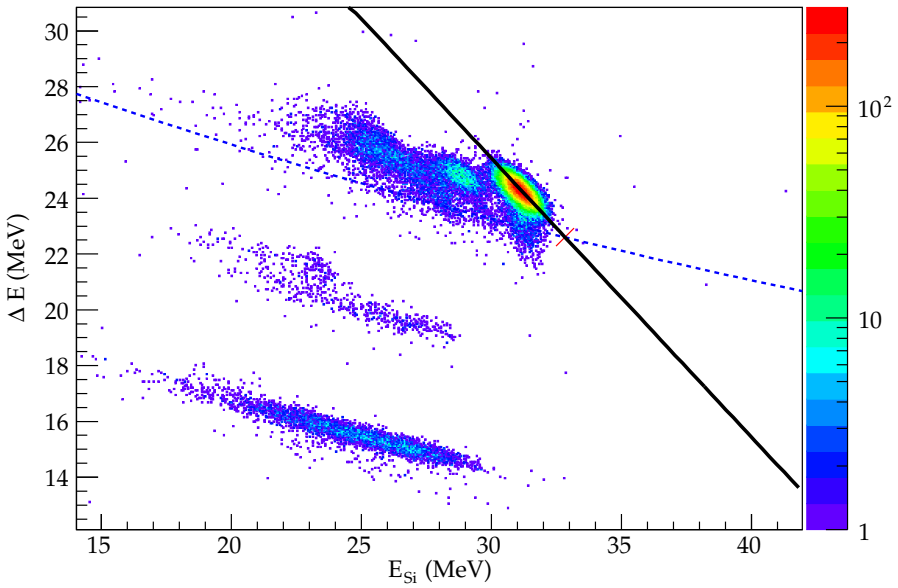

FIGURE 3.10: Procedure to determine the distribution of the overall offset δ from the plane fitting calibration method between the ΔE and E_{Si} axes. The dashed blue line is a SRIM calculation of the distribution of energy losses between the gas and silicon layers over a range of incident energies, giving the unique locus of ^{18}O ions in the ΔE-E spectrum. The thick black line represents the total expected energy in the ΔE-E telescope. The distribution of the fitted offset δ between the ΔE and E signals is found by fitting the elastic peak in both dimensions, and finding the necessary adjustments to reconcile the peak position with the intersection of the calculated locus of the beam species (dashed line) and the expected total incident energy (solid black line), indicated by the cross. The spectrum shown is that resulting from the measurement of ^{18}O + ^{208}Pb at E_{cm} = 71.7 MeV.

also provided a means of checking the intended beam energy was set correctly in each experimental run. Also, the monitor detectors can indicate the degree of impurity in the targets by identifying secondary elastic scattering peaks from suspected impurities in the recorded spectra. For this reason, a calibration in energy was obtained for each monitor. In general there was little evidence of any significant quantities of impurities in any of the targets, and any present (such as S, O, C) are not able to distort the results of the analysis in any way.

Similar to the discussion in the previous section, pulse height defects arising from the silicon surface dead layers can affect the recorded signal differently depending on the mass and charge of the incident ion. For this reason, a linear calibration was conducted separately for the different beam ions.

3.3.3 Identification of reaction products

Typical calibrated ΔE-E spectra of the reactions of interest are shown in Figure 3.11. In each case, the quality of the calibration is indicated by the agreement of the SRIM calculation of the locii of α-particles with the observed distribution. These events were observed in all runs and are thought to arise as a result of interactions between the beam ions and light target impurities, which could result in the production of α-particles over a wide energy range. A contribution may also be present as the result of the decay of activated target atoms. For example, transfer of 2 protons and 2 neutrons to the ^{208}Pb target would form ^{212}Po, which would be expected to decay via α-emission with a half-life of 0.3 μs. These are emitted at $\sim$ 9 MeV which is sufficiently energetic to penetrate the mylar and gas layers and to reach the silicon detector, subsequently triggering the DAQ. However, the absence of any obvious peak in the measured total energy of these events at the expected emission value suggests this is not a significant proportion of the total. Another contribution may arise from the fragmentation of reaction products— this possibility will be discussed in Chapter 5.

The main challenge in identifying reaction products is in determining their unique locii in the ΔE-E spectrum belonging to each isotope. Following the calibration procedure described in Section 3.3.1, the calculated locii from SRIM could be used for this purpose.

Alternatively, and more reliably, it was possible to derive the locii empirically for selected reaction products for which beams were available, where those beams were scattered from the thick tantalum target frame (listed in position #4 on the target ladder in Table 3.1). Such measurements were recorded for all of the beams used in the experiment. The projectiles can scatter at various depths in the target, and thus emerge over a wide energy range as shown in Figure 3.12, where the spectra obtained from elastic backscattering of ^{12}C, ^{18}O and ^{19}F from the thick target are superimposed. This allows us to map out the locii of the different isotopes in the ΔE-E spectrum, which remain constant throughout the experiment as long as the detector properties (biases and gas pressure) are unchanged. These measurements were made at energies well below the barrier to ensure that nearly all events seen in the detector correspond to the beam species, and not

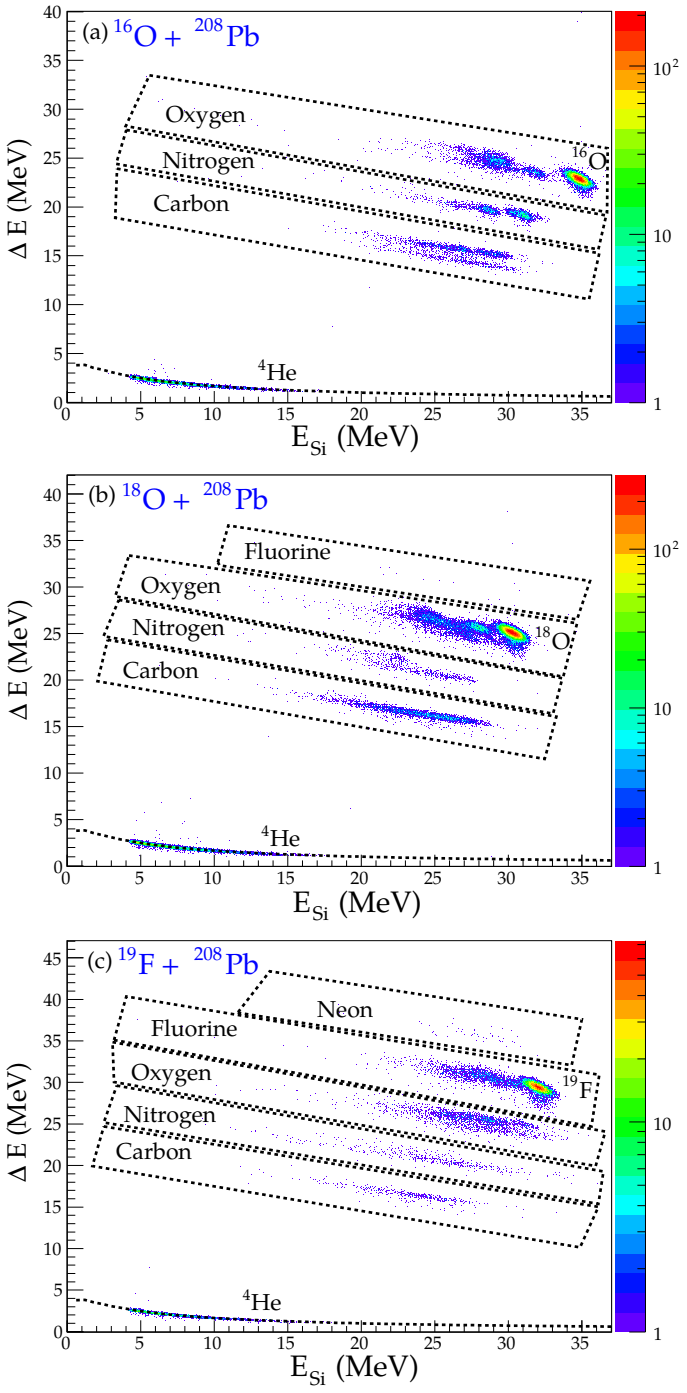

FIGURE 3.11: ΔE-E_{Si} spectra obtained for (a) ^{16}O + ^{208}Pb, (b) ^{18}O + ^{208}Pb, (c) ^{19}F + ^{208}Pb at $E_{c.m}/V_B \approx 0.98$. Main intense spots correspond to elastically scattered beam species. Products are shown to be well separated in charge, with the carbon band also showing separation of species by mass. Black dashed lines are SRIM [116] calculations showing the expected locus of alpha-particles in the ΔE-E telescope. In the ^{18}O + ^{208}Pb (b) and ^{19}F + ^{208}Pb (c) reactions, a small number of events corresponding to charge pickup by the projectile were observed. However, the vast majority of events correspond to charge stripping from the projectile, elastic/inelastic scattering and neutron transfer reactions.

reaction products. These empirically derived locii can be further extended to higher energies by stitching them together with the observed elastic scattering peaks of the same beam ions from the thin targets. The elastic peaks are interpolated with cubic splines, and the resulting graph is smoothly joined with the locus determined from the target frame scattering. Once these were determined, the locii of other reaction products (for which beams were not available) could be determined using the scaling laws in Z_p and A_p expressed in Equation 3.6. This was the preferred method of locus determination in this analysis, as it was found that those determined from SRIM calculations did not match the observed spectra as well as desired over the full energy range.

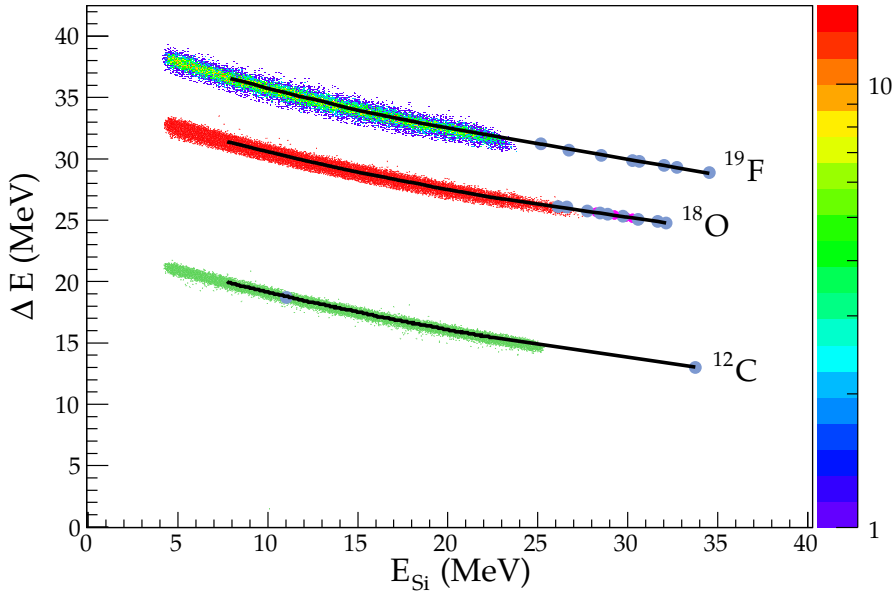

FIGURE 3.12: Mapping of ^{12}C, ^{18}O and ^{19}F locii in the ΔE-E$_{Si}$ spectrum. The intense bands of events are from scattering of each projectile from a thick tantalum target. The positions of the elastic peaks for scattering of each projectile from the thin Pb target are indicated by the blue circles, and are used to map the locii to higher energies. The locii determined through this method are shown in the figure by the solid black lines. The intensity scale on the right of the figure applies only to the ^{19}F band.

Once the locii have been identified, isotopes within each band can be separated by finding the relative energy loss ΔE_{Rel} in the ionisation chamber of all events relative to the nearest identified locus. An example is shown in Figure 3.13(a), where the identified locus of ^{12}C is overlaid on the measured ΔE-E$_{Si}$ spectra for ^{16}O + ^{208}Pb at 0.99V$_B$. Here I have defined ΔE_{Rel} as the deviation in ΔE with respect to the locus of ^{12}C. The resulting ΔE_{Rel} distribution is shown in Figure 3.13(b), and is analysed through a process of Gaussian

deconvolution— the distribution of the selected events (all corresponding to the same Z) is fitted with a function of the form:

$$F(\Delta E_{\text{Rel}}) = \sum_{i=1}^{n} \mathcal{G}_i(\Delta E_{\text{Rel}}), \tag{3.9}$$

where $\mathcal{G}_i$ are standard Gaussian functions of the form:

$$\mathcal{G}(x) = ae^{-\frac{(x-b)^2}{2c^2}}. \tag{3.10}$$

The peak widths c_i of all isotopes of the same element are taken to be equal, which reduces the number of parameters of the fit. The peak centroids are fixed by constraining to values determined through `SRIM` calculations of the expected separation in ΔE_{Rel} over the energy range of interest. The best fit was found by minimising the reduced χ^2 statistic with respect to the number of peaks, whilst constraining the common peak width to be consistent with the expected systematics (derived from the elastic scattering peaks for the various beam-species). Typically this process yielded χ^2 (per degree of freedom) values in the range $1.2 < \chi^2 < 4.0$, with the result dependent on the particular measurement and the reaction channels examined. The yields of each product are then found by taking the integrals of the individually separated Gaussian components.

3.3.4 Derivation of reaction Q-value and excitation spectra

To obtain Q-value and excitation energy spectra, gates were applied to the ΔE_{Rel} spectra to identify products on an event-by-event basis. These are guided by the mapped species locii, with adjacent isotopes separated by mapping the edges of the gates to the intersections between the adjacent fitted Gaussian components, as shown by the vertical dashed lines in Figure 3.13(b). This method was chosen to give optimal isotopic identification of each event, and to provide minimal mixing of adjacent isotopes.

After identification of the projectile-like fragments, the Q-value spectrum of the reaction can be reconstructed by tracing back to the centre-of-mass system on an event-by-event

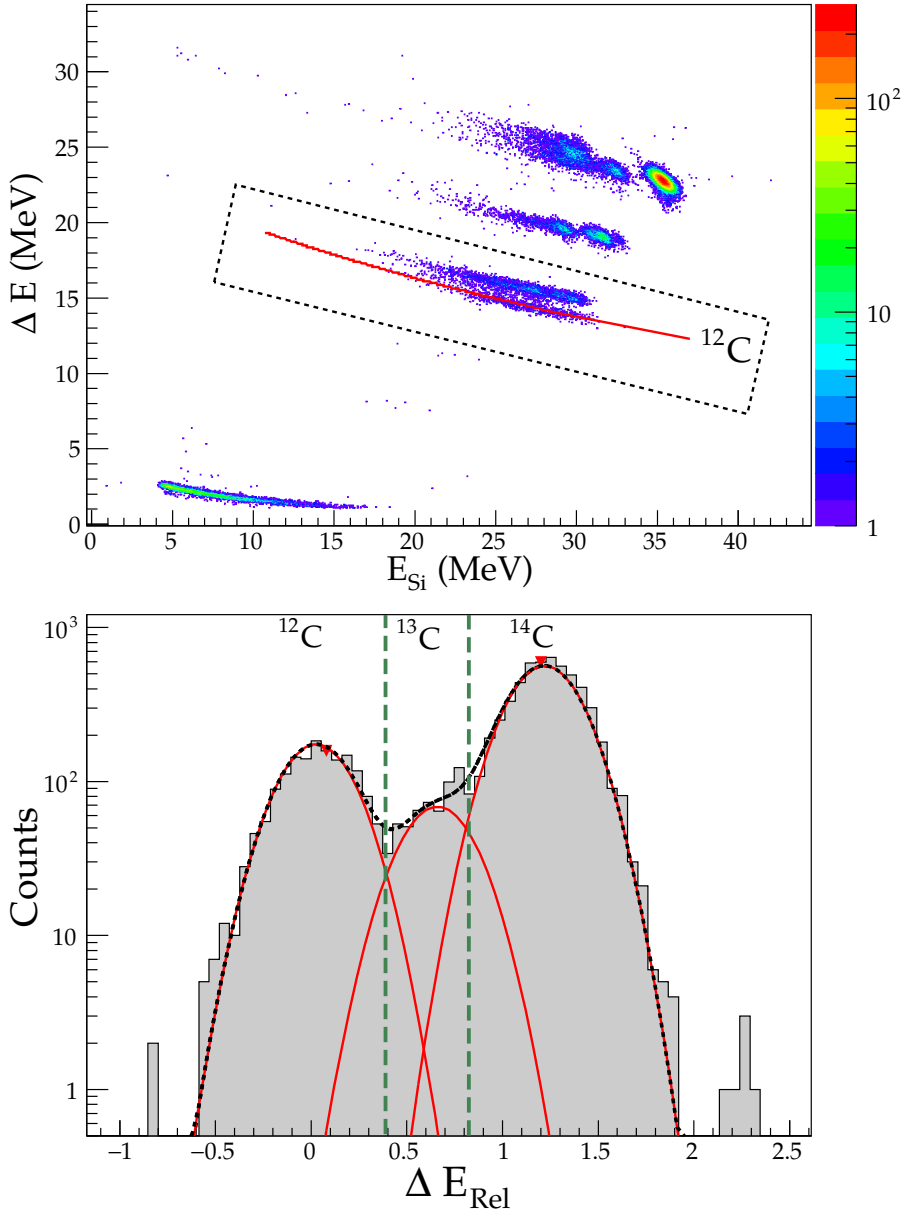

FIGURE 3.13: (a) ΔE-E_{Si} plot obtained in the reaction ^{16}O + ^{208}Pb at 0.98V$_B$. The red line shows the empirical ^{12}C locus (see text) from which the relative energy loss (ΔE_{Rel}) spectrum is calculated. The ΔE_{Rel} spectrum is determined from events within the dashed contour. (b) Resulting ΔE_{Rel} spectrum. Black dashed curve shows the multiple Gaussian function fitted to the distribution. Red curves indicate the corresponding fitted components, which are attributed to yields of the expected isotopes, in this case ^{12,13,14}C. Vertical green dashed lines show the gate limits for event-by-event analysis as determined by the intersections between adjacent fitted peaks.

basis from the known beam energy and measured final energies. The Q-value is calculated according to (see Equation A.11 in Appendix A):

$$Q = \frac{A_b + A_B}{A_B} E_b - \frac{A_B - A_a}{A_B} E_a - \frac{2\sqrt{A_a A_b E_a E_b}}{A_B} \cos\theta_{\text{lab}}. \tag{3.11}$$

In the above, subscripts are given in the standard reaction notation $A(a,b)B$, where a is the projectile, A the target, b the ejectile, and B the recoiling target-like nucleus, with A_i their masses and θ_{lab} the scattering angle in the laboratory frame. E_i are the energies, with E_a the projectile energy, and E_b the measured energy of the detected projectile-like product, after correction for energy losses in the target and detector dead layers. From the deduced Q-value and knowledge of the identity of each event, the excitation energy of the reaction products can be deduced according to:

$$E_{\text{x}} = Q_{\text{g.g}} - Q. \tag{3.12}$$

$Q_{\text{g.g}}$ is the ground-state to ground-state transfer Q-value, and Q is that given by equation 3.11. An example of the extracted Q-value spectrum and deduced excitation energy spectrum are shown in Figures 3.14 and 3.15 respectively, for the measurement of ^{18}O + ^{208}Pb at a center-of-mass energy of 71.6 MeV, corresponding to 97 % of the nominal barrier energy. It is important here to note that the excitation energy spectrum deduced in this manner is the sum of the energy of the states populated in both the target and projectile nuclei.

3.4 Summary

In order to establish the systematic trends of dissipation of energy via multinucleon transfer reaction modes, it is necessary to examine reaction systems covering a range of masses. The experimental setup described in this chapter has proven sufficient for the extraction of mass information in the region of elements with $Z < 10$. However, the mass resolution of the current ΔE-E detector system falls rapidly with an increase of the

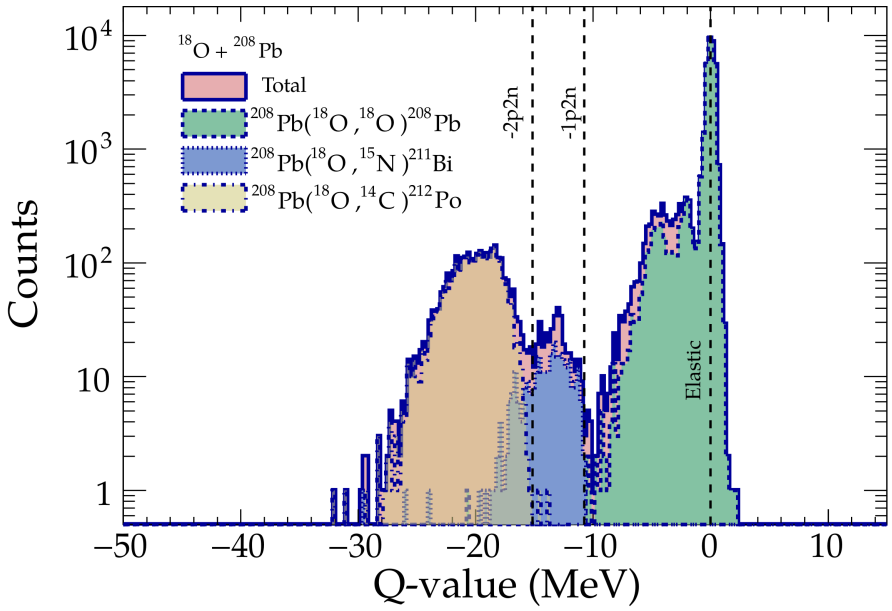

FIGURE 3.14: Example of a Q-value spectrum reconstructed from 2-body kinematics in the case of ^{18}O + ^{208}Pb at E_{cm} = 71.6 MeV. Only the most significant transfer modes are shown, which are seen to be the majority of the yield. The dashed vertical lines show the ground-state-to-ground-state Q-values $Q_{g.g}$ for the processes shown.

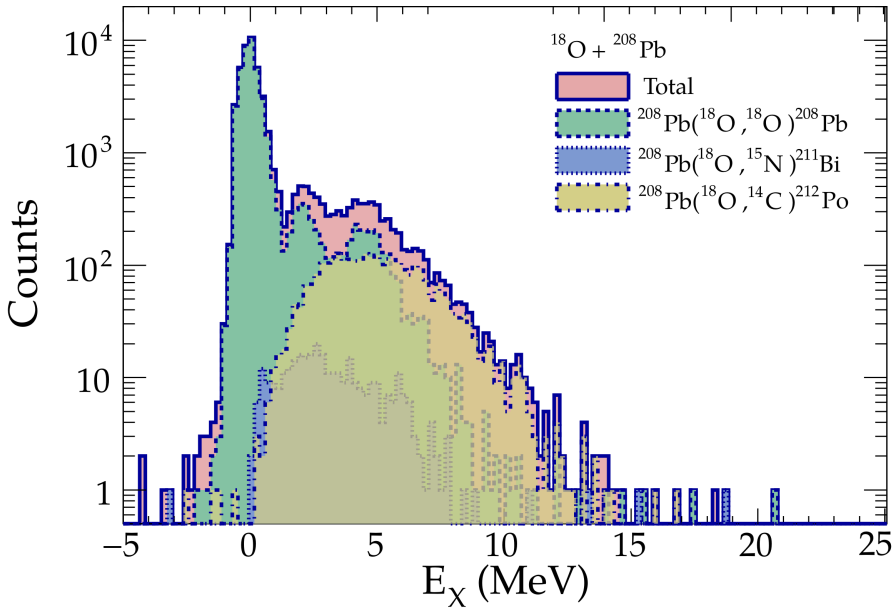

FIGURE 3.15: Example of an excitation energy spectrum resulting from Equation 3.12 considering the ground-state-to-ground-state Q-values $Q_{g.g}$, in the case of ^{18}O + ^{208}Pb at E_{cm} = 71.6 MeV. Only the most significant transfer modes are shown, which are seen to be the majority of the yield.

atomic number Z. Initial tests with a ^{32}S beam found that whilst the telescope was capable of identifying the Z of the scattered beam it was not possible to separate by isotopic mass. In the next chapter, the details of a second experiment using the large acceptance magnetic spectrometer PRISMA are discussed, in which measurements of the excitation energy spectra were made in the ^{32}S, ^{40}Ca + ^{208}Pb systems with excellent particle identification. With equivalent information being obtained from each of these experiments, the results are presented and discussed together in Chapter 5.

Chapter 4

Experiment 2: ^{32}S & ^{40}Ca induced reactions on ^{208}Pb (LNL)

In this chapter, details of a measurement of multinucleon transfer probabilities together with residual excitation energy spectra are reported for beams of ^{32}S and ^{40}Ca incident on a ^{208}Pb target. This experiment was conducted during June 2012 using the PRISMA magnetic spectrometer device at the Legnaro National Laboratory (LNL), one of four national facilites managed by the Italian National Institute of Nuclear Physics (INFN). The author did not attend the experiment in person, but the collected data was provided as part of this project. Dr. Duc Huy Luong and Dr. Maurits Evers attended the experiment representing the Nuclear Reaction Dynamics group of ANU. Since this experiment was conducted by the ANU team as external users, extensive details of the experimental systems and setup (such as electronics for detector pulse processing) are omitted. Rather, in this chapter a general overview of the components of the experimental system and the principles of operation relevant to the data analysis are presented. References are provided for a more detailed description of the facilities of LNL.

The analysis of PRISMA data is performed using software developed in-house at LNL. An initial conversion of the datafiles produced by the DAQ into `ROOT` format is performed by a preprocessing code written in `C++`, which reduces the datafiles to a format containing only the essential raw paramaters for analysis. The sorting of the data, including the application of calibration factors and sorting of events according to user-defined

gates, as well as the trajectory procedure, is then computed using a second sorting script. Both of these sorting scripts are ported to perform the same function as the `gSort` program of the `EGASPWARE` package that has traditionally been used at LNL for the analysis of PRISMA data [117]. The more recent software used in this analysis was originally developed for compatibility with the AGATA (Advanced GAmma Tracking Array) data format [118], a device which has been coupled with PRISMA in a recent experimental campaign. The dependent libraries and sorting scripts were written by E. Farnea of LNL.

This chapter is structured as follows: To begin, a brief description of the accelerator facilities of LNL are given in Section 4.1. Next, the important characteristics of the PRISMA device as they pertain to measurements of the focus of this thesis, as well as the principle of operation are discussed in Section 4.2. Section 4.3 describes the specific setup and details the beam energies and targets used for these measurements. Then, in Section 4.4, the methods used to ensure accurate calibration of the various components of the PRISMA system are explained. This is followed by a discussion of the analysis and trajectory reconstruction procedures necessary to separate reaction products by atomic number and mass, and finally the extraction of excitation energies, which are detailed in Section 4.5.

Appendix B gives details of the frames of reference relevant to the experiment that are referred to in this chapter, as well as the coordinate transformations which are necessary to the analysis.

4.1 Tandem-XTU + ALPI accelerator systems at LNL

Beams for the experiment were provided by the Tandem + ALPI complex at LNL. The tandem accelerator is very similar in design to that described in Section 3.1 in Chapter 3— a tandem-XTU manufactured by the High Voltage Engineering Company (HVEC), of Burlington, USA [119]. Negative ions of the source material are injected into the terminal tank, where they undergo a two-stage acceleration process in much the same manner as the 14UD of HIAF. The LNL tandem-XTU uses a similar charging system in a positive

configuration (HVEC laddertron), with the terminal able to hold a maximum high voltage of 16 megavolts under optimal operating conditions [120]. Precise energy selection of 1/300 is provided by the analysing magnet at the tank exit.

In this experiment it was also necessary to utilise the ALPI (**A**cceleratore **L**ineare **P**er **I**on) superconducting post-accelerating LINAC booster to perform the higher energy measurements. An important point of difference to note in the use of the accelerator system for the experiment described in Chapter 3 is that the LINAC requires a pulsed beam for post-acceleration. The Tandem-XTU-ALPI facility incorporates a bunching system which splits the DC beam into pulses of $\sim$ 100 ps width [121] for injection to ALPI.

ALPI consists of a series of superconducting cavities made of niobium (Nb) bulk (or Nb-coated copper) of quarter-wave resonator type, cooled with liquid Helium provided by the attached cryostats to temperatures of $\sim$ 4.2K for operation in the superconducting regime. The cavities drive a RF electric field (which is tuned to be in phase with the beam bunches) producing an accelerating field of up to 4.4 MV/m. There are eight cryostats housing 4 cavities each, driven at a frequency of 160 MHz. The maximum post-acceleration potential provided by the LINAC is 40 MV.

Further details of the LNL accelerator systems can be found in Refs. [122, 123, 124, 125]. The specific accelerator configurations used for the measurements reported in this chapter are reported in Table 4.4.

4.2 PRISMA

The PRISMA device operates on the principle of magnetic dispersion of reaction products according to their momentum and charge state. A schematic of the setup along with the important dimensions is shown in Figure 4.1. The essential characteristics and intended design specifications of the spectrometer are listed in Table 4.1. It consists of, in the order through which reaction products will pass along the flight path:

- Microchannel plate detector (MCP)
- Quadrupole Magnet

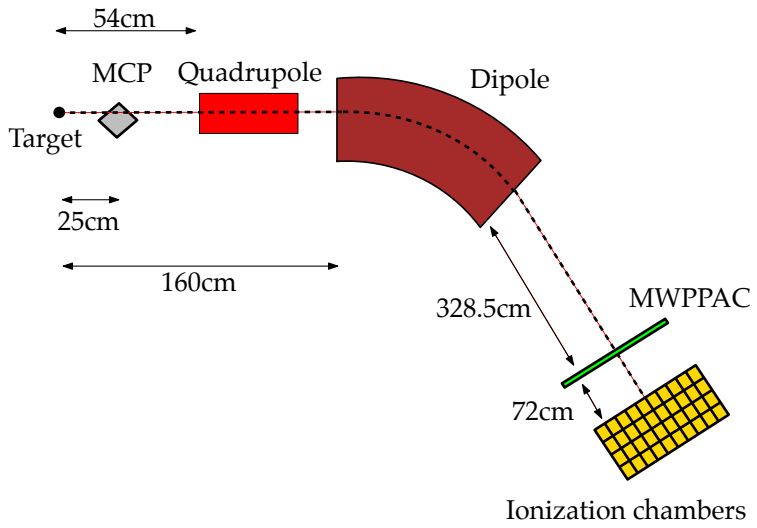

FIGURE 4.1: Schematic diagram of PRISMA magnetic spectrometer.

Solid angle	$\Delta\Omega$	~ 80	msr
Angular acceptance	$\Delta\theta_{lab}$	± 6	$^\circ$
Momentum acceptance	Δp	± 10	%
Z resolution	$\Delta Z/Z$	$\sim 1/60$	-
A resolution	$\Delta A/A$	$\sim 1/200$	-

TABLE 4.1: Essential characteristics of the PRISMA device.

- Dipole Magnet
- Multi-wire Parallel Plate Avalanche Counter (MWPPAC)
- Array of ionization chambers (IC)

The entrance and exit position coordinates of the ions, as well as start and stop signals for the time-of-flight measurement, are provided by the MCP and MWPPAC respectively. This information, together with the atomic number selection made possible with the IC through the E-ΔE technique, makes possible a precise reconstruction of the ion trajectory between the MCP and PPAC, enabling a separation of products in mass as well as measurement of total kinetic energy losses, and therefore excitation energy. The whole assembly can be rotated -30° to 130° relative to the beam axis.

Brief descriptions are given in the following subsections of the various components of the PRISMA system.

4.2.1 Microchannel Plate Entrance Plane Detector

The entrance coordinates of the ion to the magnetic elements are detected by a pair of large area rectangular (80×100 mm^2) Micro-Channel Plates [126], arranged in a chevron configuration as shown in Figure 4.2. The detector assembly is housed in a metal box of which two faces are open (allowing for passage of ions), whilst the others are solid walls. Reaction products emerging from the target first pass through a grid of gold-plated tungsten wires (20 μm diameter, 1mm spacing), and after passing through the detector assembly traverse another grid (inner grid) followed by a self-supporting Carbon foil of thickness $\simeq 20$ $\mu g/\text{cm}^2$, and then another wire grid (outer grid). The passing ions generate δ-electrons in the Carbon foil, which are then accelerated (to 300 eV) by the potential difference between the foil and inner grid towards the MCPs on the far side of the detector. The outer grid is included in order to balance the forces on the fragile C-foil, whilst the entrance grid (at high negative voltage) helps to suppress the background contribution from δ-electrons emitted from the nearby target. A magnetic field (parallel to the internal accelerating electric field) is applied by wire coils in order to guide the electrons toward the anode and preserving position sensitivity.

The Carbon foil of the detector is positioned 25 cm from the target. This together with the 1 mm position resolution gives an angular resolution of $\sim 0.5^\circ$. The assembly is positioned with the entrance grid at an angle of 45° to the PRISMA axis.

4.2.2 Magnetic Elements

Upon transmission through the MCP detector assembly, reaction products next enter the quadrupole magnet, and are thereafter dispersed in the dipole magnet. The quadrupole focusses the ions in the (vertical) y-direction and defocusses in the (horizontal) x-direction (where the z-axis, or optical axis, goes through the center of the quadrupole towards the dipole).

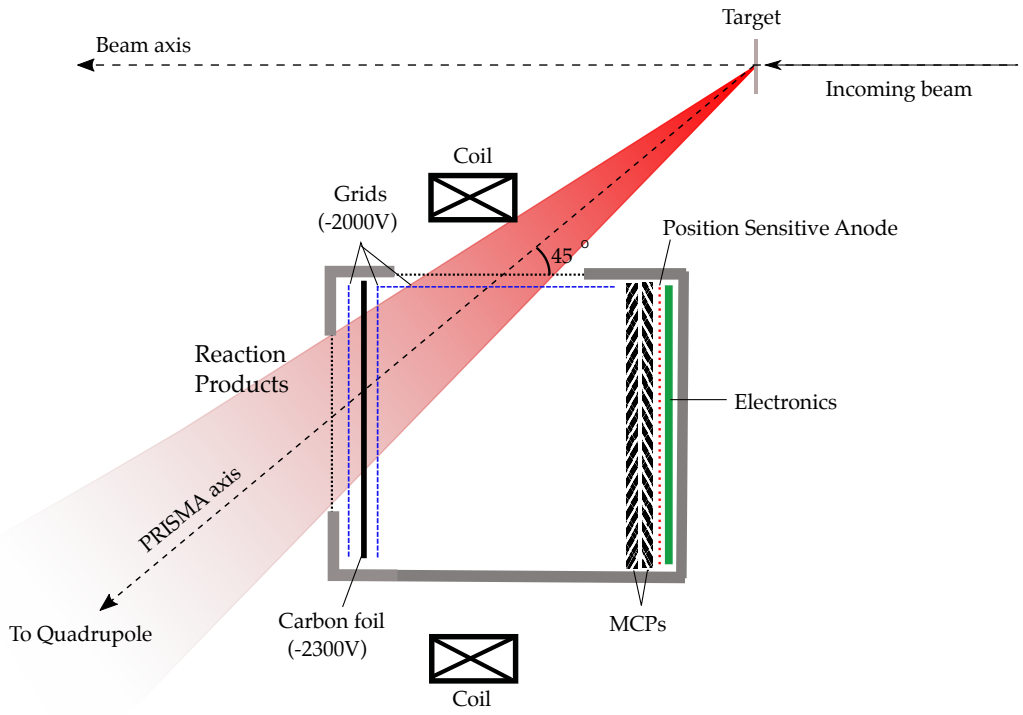

FIGURE 4.2: Schematic diagram of PRISMA MCP entrance detector.

Quadrupole magnet			
Max pole tip field	B_0	0.848	T
Max field gradient	G	5.3	T/m
Apperture diameter	d	320	mm
Length	l	420	mm

TABLE 4.2: Details of quadrupole magnet

Dipole magnet			
Max field	B_0	1	T
Bending radius	R	1200	mm
Bending angle	θ	60	°
Pole gap	d	200	mm

TABLE 4.3: Details of dipole magnet

The dipole has a large longitudinal dimension in comparison with the pole gap. This fact, in connection with the y-focussing of the quadrupole, mean that the ion trajectories can be well approximated as being planar in x-z in the PRISMA frame of reference. This simplifies the calculations required to reconstruct the trajectory length and radius of curvature in the analysis procedure.

Tables 4.2 and 4.3 list the important characteristics of the ion-optical elements described in this subsection.

4.2.3 Multiwire Parallel Plate Avalanche Counter (MWPPAC) Focal Plane Detector

The x and y coordinates of ions in the focal plane, as well as the stop signal for the time-of-flight, are recorded by the MWPPAC. The main elements of the MWPPAC are shown in Figure 4.3.

The detector consists of 3 electrodes. The X anode is made up of 10 segments, each with an active area of 10×13 cm^2. Each segment consists of 100 Au-plated Tungsten wires, of 20 μg thickness, with a 1 mm spacing between them. The Y anode extends across the whole width of the detector, with wires of the same spacing and thickness, with every other wire shorted to give a position resolution of 2 mm. The X and Y anodes are each placed symmetrically 2.4 mm from the Cathode on either side.

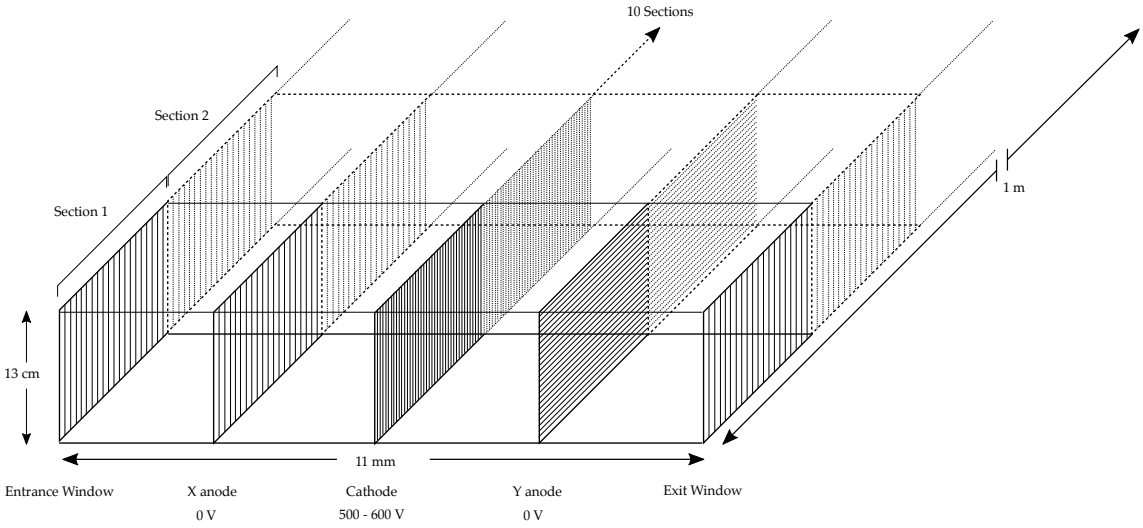

FIGURE 4.3: Schematic diagram of PRISMA MWPPAC focal plane detector.

The position in X and Y are measured through a delay line setup. The wires are connected by discrete LC elements with a fixed delay of 1.7 ns per wire. Figure 4.4 shows this configuration. The position information can be extracted by measuring the relative delay between the left-out and right-out signals, which is proportional to the position of the ion relative to the adjacent wires.

The Cathode is also segmented into 10 sections, each of 330 Au-plated Tungsten wires of 20 μg thickness and 0.3 mm spacing. Each section provides a fast timing signal for both the time-of-flight and the DAQ trigger. The electronic scheme for the cathode is shown in Figure 4.5.

The detector windows are 1.5 μm thick mylar foils supported by a stainless steel wire grid, with wires of 100 μm thickness and 3.5 mm spacing. The MWPPAC is filled with isobutane gas (C_4H_{10}) at a working pressure of 7-8 mbar.

4.2.4 Ionization Chambers (IC) array

The final component of the PRISMA assembly is an array of ionization chambers positioned 720 mm beyond the MWPPAC as shown in Figure 4.6. The active cells are arranged in a 10 (wide) $\times$ 4 (deep) configuration. Each cell (20 mm tall, 99 mm wide, 265 mm long) acts as an independent ΔE detector. In addition, there are extra sections on

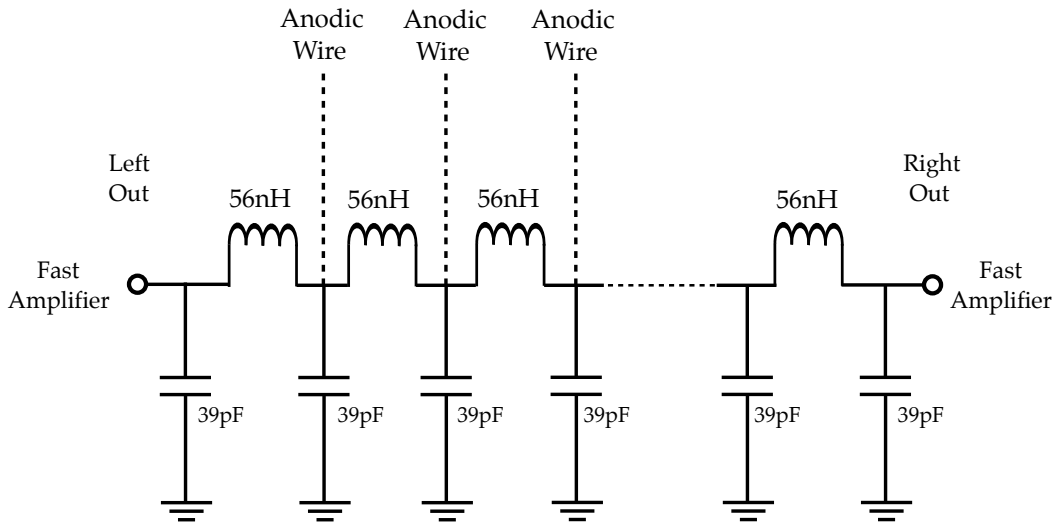

FIGURE 4.4: Schematic diagram of position readout from the MWPPAC anodes.

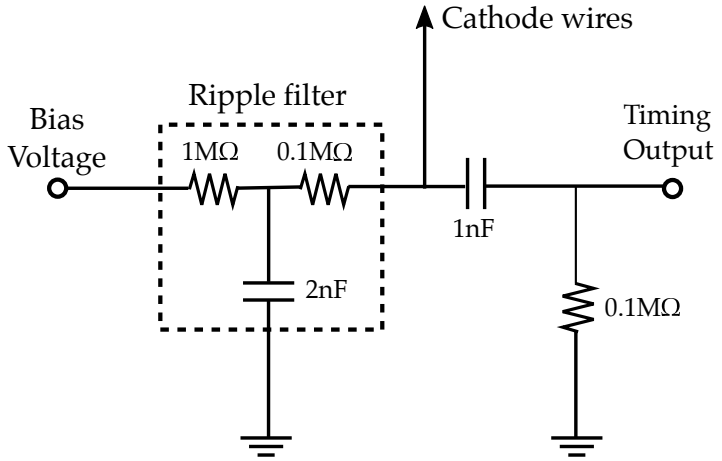

FIGURE 4.5: Electronics diagram of MWPPAC cathode.

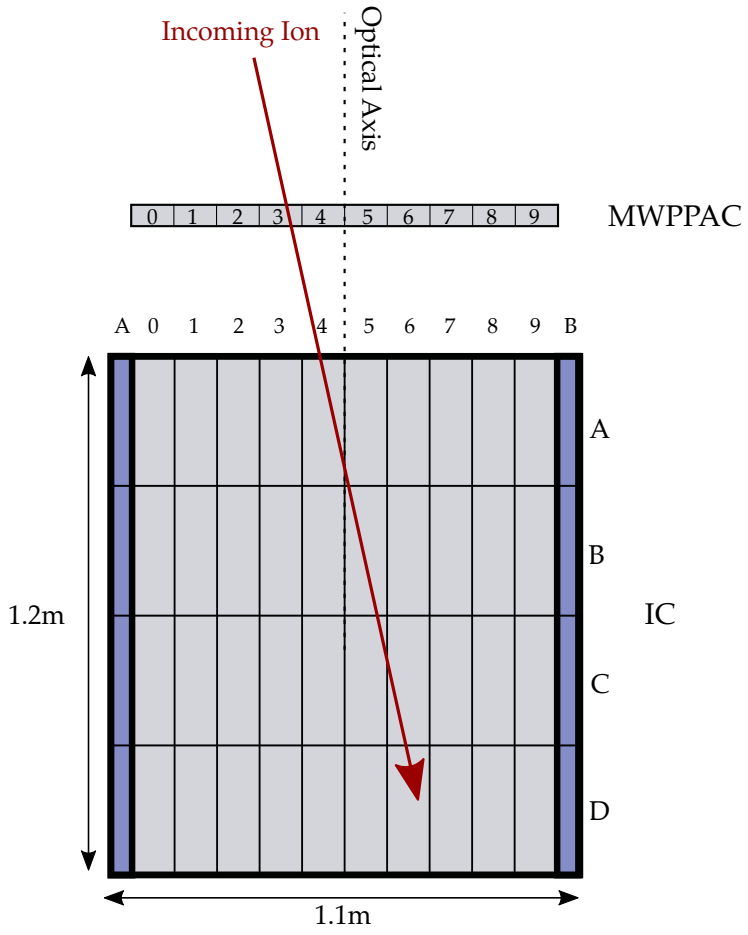

FIGURE 4.6: Focal plane detectors of PRISMA.

each side of the array (50 mm wide) which are operated in anti-coincidence in order to reject events with errant trajectories. These are labelled A and B in Figure 4.6. The IC array is positioned such that the cells are aligned horizontally with the MWPPAC sections, giving a rough measure of the ion direction in the focal plane.

The entrance window is a 1.5 μm mylar foil, supported by a grid of 100 μm thick stainless steel wires of 1 mm spacing (1000 in total). This assembly is able to handle filling gas pressures up to 100 mbar with a maximum 3 mm deformation. The filling gas is highly pure (99.99 %) methane (CH_4).

The large dimension of the IC array ensures that good Z resolution can be achieved over a wide range of incoming energies. By adjusting the gas pressure, it can be ensured that the most energetic ions are stopped in the final layer of the detector. The maximum pressure of 100 mbar can stop all ions heavier than ^{40}Ca at energies up to 6 MeV/amu.

The electronic setup of the IC sectors is shown in Figure 4.7. Each cell i has a unique pair of electrodes and gives an independent ΔE_i signal. The Frisch grid is common to the whole array, with the cathode-Frisch voltage being half that of the cathode-anode voltage.

4.3 Experimental details

In order to closely examine the behaviour of multinucleon transfer around the fusion barrier, it is necessary to make individual measurements at many different beam energies, with a small energy step between each run. For the higher energy measurements, post acceleration using the ALPI LINAC was neccessary to achieve the required beam energy. Due to the time restraints of the allocated beam time it was decided to make use of carbon degrader foils (mounted on the target ladder) in order to avoid the lengthy retuning process of the LINAC elements. By using two different thickness degraders (135 μg/cm^2 and 205 μg/cm^2), it was possible to measure 3 beam energies for every accelerator tune. Though this introduces additional straggling to the ion energies entering the PRISMA device therefore degrading the measured energy resolution, this sacrifice was necessary

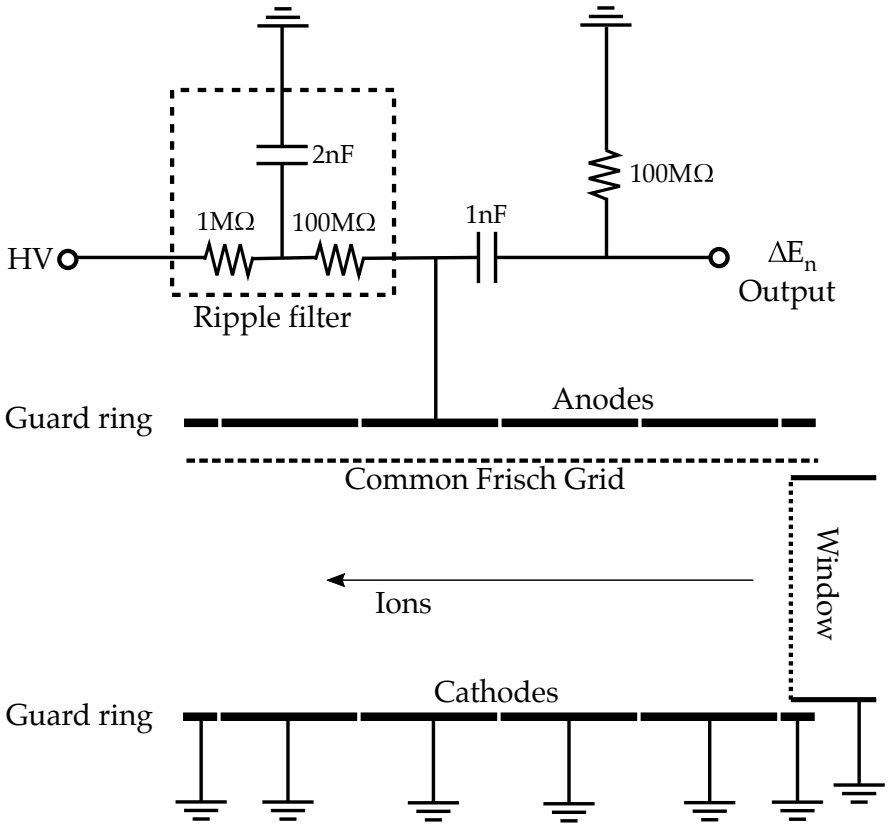

FIGURE 4.7: Electronics diagram of IC.

to complete the objectives of the experiment within the time constraints. In the case of the lower energy measurements (where post-acceleration was not required), the tandem was retuned for each run.

Targets were attached to a rotating switcher, which could be remotely operated to change the target presented to the beam. The switcher was mounted with six ^{208}PbS targets, ranging in thickness between 100 - 200 $\mu g/cm^2$ with an average of $\sim$ 150 $\mu g/cm^2$ PbS on a carbon backing of $\sim$ 20 $\mu g/cm^2$. The target switcher was oriented at an angle of 60° to the beam axis, with the carbon backing (and degrader) upstream of the target. This arrangement increases the thickness of the PbS layer through which the beam passes, maximising the counting rate, necessary for such measurements of reaction modes with very low cross sections. Figure 4.8 shows the configuration of the target and degrader relative to the beam axis.

The magnetic elements of PRISMA can only focus a subset of the reaction products onto the focal plane. A range of charge states of each possible product emerge from the target,

Beam species	Beam energy E_{Beam} (MeV)	PRISMA angle (°)	Tandem	ALPI	Degrader 1 ($135\mu g/cm^2$)	Degrader 2 ($205\mu g/cm^2$)	Quadrupole B field (T)	Dipole B field (T)	IC gas pressure (mbar)
^{40}Ca	235.0	115	✓	✓	×	×	0.477997	0.52626	48
^{40}Ca	230.5	115	✓	✓	✓	×	0.475385	0.523394	48
^{40}Ca	227.0	115	✓	✓	×	✓	0.472220	0.519918	48
^{40}Ca	223.5	115	✓	✓	×	×	0.470091	0.51758	48
^{40}Ca	220.0	115	✓	✓	✓	×	0.467522	0.514759	45
^{40}Ca	216.5	115	✓	✓	×	✓	0.464935	0.511916	45
^{40}Ca	213.0	115	✓	✓	×	×	0.462704	0.509462	45
^{40}Ca	210.0	115	✓	×	×	×	0.460082	0.506579	45
^{40}Ca	206.5	115	✓	×	×	×	0.457440	0.503676	45
^{40}Ca	203.0	115	✓	×	×	×	0.454779	0.500748	41
^{40}Ca	199.5	115	✓	×	×	×	0.452099	0.496685	41
^{40}Ca	195.0	115	✓	×	×	×	0.448157	0.493461	41
^{40}Ca	189.0	115	✓	×	×	×	0.443926	0.488804	41
^{40}Ca	235.0	102	✓	✓	×	×	0.493454	0.543230	53
^{40}Ca	223.5	102	✓	✓	×	×	0.484403	0.53329	53
^{40}Ca	210.0	102	✓	×	×	×	0.473924	0.521791	45.8
^{40}Ca	199.5	102	✓	×	×	×	0.465572	0.512614	42.8
^{32}S	192.0	102	✓	×	×	×	0.501081	0.551565	66
^{32}S	178.0	102	✓	×	×	×	0.486881	0.536007	60
^{32}S	164.0	102	✓	×	×	×	0.472199	0.519896	55
^{32}S	150.0	102	✓	×	×	×	0.456974	0.503161	50

TABLE 4.4: Details of the PRISMA measurements and the accelerator and degrader foil configurations required to achieve the desired beam energies, listed in the order in which they were conducted.

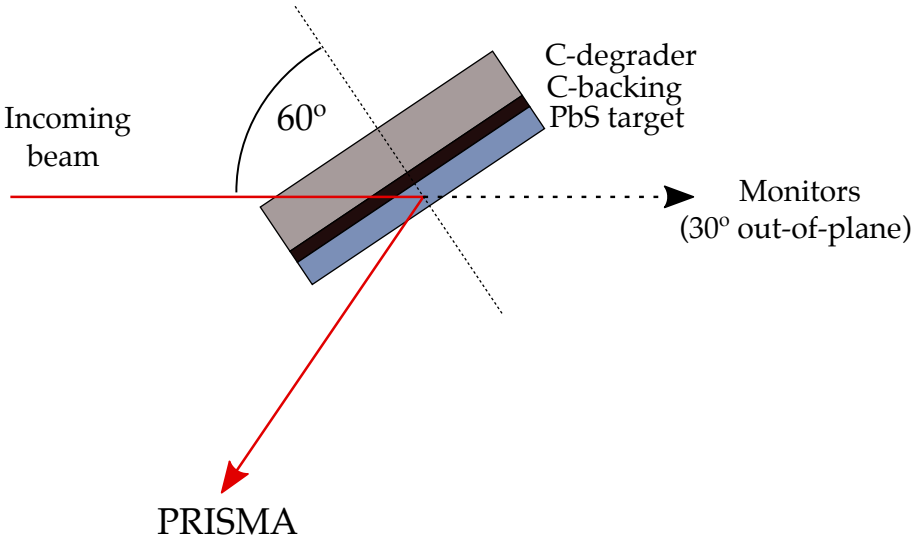

FIGURE 4.8: Target and carbon degrader configuration with respect to the beam direction.

and the position at which they will reach the focal plane will depend on their magnetic rigidity $\rho_M = mv/q$. The charge state distribution of each product ion can be calculated using semi-empirical models such as those developed in Refs. [127, 128]. An in-house code (`reaction`) authored by F. Scarlassara implements the model of Ref. [128], taking into account the target geometry, and (amongst other features), can calculate the likely charge state distribution of ions after emerging from the target, their kinematics, and the optimal field values for focusing each charge state on the center of the MWPPAC. During the experiment, these predicted values were used to initially set the magnets to maximise the transmission of the calculated most prolific charge state of the elastically scattered beam. The calculated charge state distribution does not consider the effect of the Carbon foil within the MCP assembly, though this is not expected to significantly affect those calculated through the comparatively thick target and degrader layers.

In order to maintain good Z separation at each measured energy, the gas pressure in the IC array needed to be adjusted depending on the beam energy. For best resolution, the elastically scattered beam needs to be stopped in the final (fourth) layer of the array. This means that there are potentially three ΔE layers to allow Z selection based on the $\Delta E - E$ method. The gas pressure was varied between 60 - 40 mbar during the experiment.

Table 4.4 lists the beam energies, accelerator and degrader foil configuration, and other important quantities for each measurement.

4.4 Calibration and pre-sorting procedures

This section details the necessary steps to eliminate noise and other erroneous signals prior to data processing and trajectory reconstruction. Steps taken to calibrate the raw detector signals to the corresponding physical dimensions are also described.

4.4.1 MCP noise rejection and calibration

The first step in processing the data recorded by the MCP is to identify the events of interest. Due to the close proximity of the detector to the target, there are several sources which trigger the MCP other than the reaction products (scattered beam, secondary electrons, decay products from the activated target, etc). A gate is drawn to accept the true events (indicated by the red contour in Figure 4.9a); the events outside this gate are excluded from the subsequent analysis. The calibration of the MCP detector is aided by a wire cross placed downstream of the outer grid on the back face of the MCP assembly, approximately 1cm from the Carbon foil. When a coincidence condition is enforced between the MCP and MWPPAC elements, the cross casts a shadow in the position spectrum, and the known coordinates of this cross and the screws fixing it to MCP assembly give reference points to facilitate calibration. Also identifiable in the entrance position spectrum are the shadows of two nails present in the dipole magnet, which were used in its construction and left as a reference point for calibration purposes.

As described in Section 4.2.1, the working principle of the MCP detector involves the acceleration of secondary (δ-) electrons away from the carbon foil on the back face, towards the plates with an external magnetic field applied in order to guide them. This process results in a deformation of the MCP image which must be corrected by software in order to generate an accurate map of the entrance coordinates of the reaction products. This can be achieved by performing a linear calibration between the position coordinates of

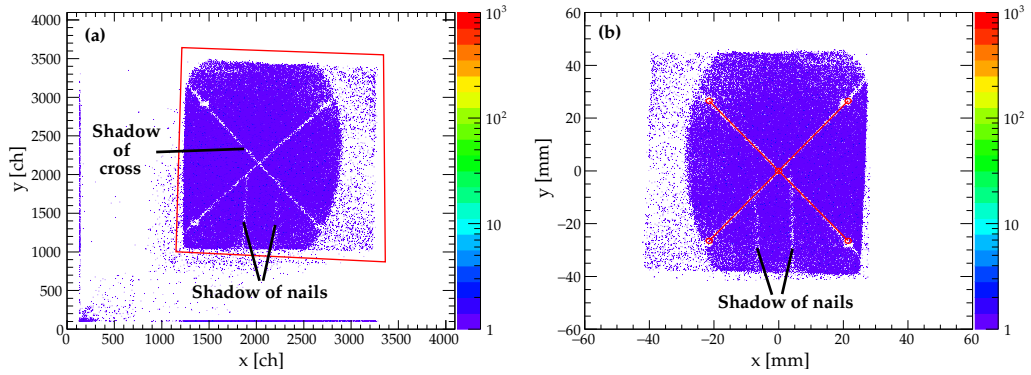

FIGURE 4.9: (a) Raw data collected by MCP detector. Red gate shows the events selected as being valid. All events outside this gate are rejected. (b) MCP data after position calibration. Red cross and circles indicate the physical position of the wires and screws in on the MCP.

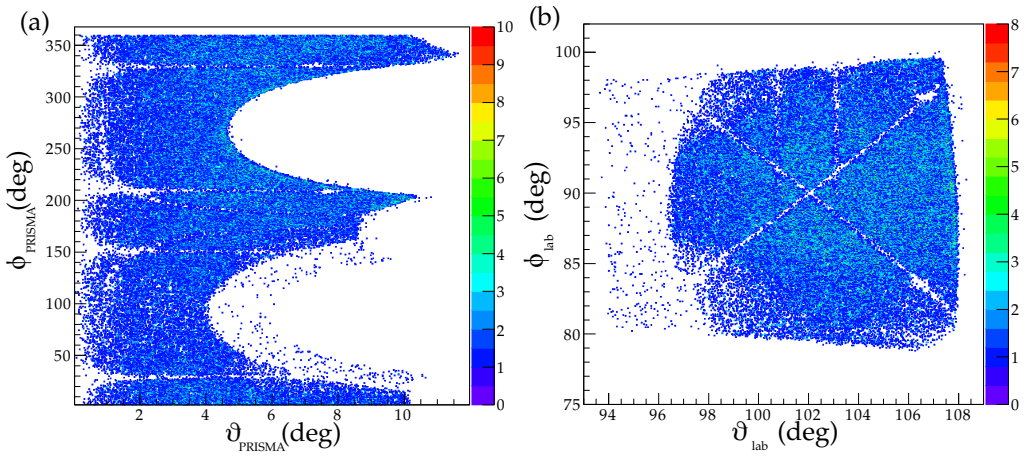

FIGURE 4.10: Entrance position spectra in spherical coordinates in the (a) PRISMA and (b) laboratory frames of reference.

the reference points in the raw spectrum with their known coordinates in mm. In addition, a rotation is applied to the raw data to ensure the shadows of the nails are aligned vertically. The result of this calibration procedure is shown in Figure 4.9b.

Once the entrance position spectrum is properly calibrated in mm, it is straightforward to transform the positional information into spherical polar coordinates (see Appendix B). Figure 4.10 shows the entrance position spectrum in the laboratory and PRISMA frames of reference.

4.4.2 MWPPAC preprocessing

The MWPPAC records six signals:

- Y-anode: Up (y_{up})
- Y-anode: Down (y_{down})
- X-anode: Left (x_{left})
- X-anode: Right (x_{right})
- Cathode
- Time

The y_{up} and y_{down} signals allow extraction of the Y position in the focal place. Since the Y-anode extends across the full width of the MWPPAC, one signal is recorded for each of up and down. Since only the horizontal position is important for the trajectory reconstruction it is not neccessary to perform a calibration of the y information, however these signals are useful online in the experiment for beam centering.

One set of each of the other signals are recorded for each of the 10 MWPPAC sections (see Section 4.2.3). The x_{left} and x_{right} signals allow extraction of the horizontal position in the focal plane. The cathode signal is used to recover events for which one of either x_{left} or x_{right} signals are missing (as will be described in the following), whilst the timing signal from the cathode gives the stop signal for the time-of-flight.

Firstly, noise is eliminated in the x_{left}, x_{right} and cathode signals by applying gates in the matrices x_{left} + x_{right} vs. cathode. Where both of the x_{left} and x_{right} signals are present, the sum is a constant for all events. Figure 4.11 shows an example these matrices for each of the MWPPAC segments in the measurement of ^{32}S + ^{208}Pb at E_{Beam} = 178 MeV. The bright central spot corresponds to those events for which both x_{left} and x_{right} signal are recorded. There are some events to be found at lower values of x_{left} + x_{right}. These are those for which only one of x_{left} or x_{right} are recorded, and can be recovered using the cathode signal. This effect can be observed in several of the MWPPAC sectors in Figure 4.11. Also evident in most of the sectors is a group of events at larger values in the x_{left} +

x_{right} axis (see the panel for section 3 of the MWPPAC in Figure 4.11)— these correspond to otherwise good events where the time-delay is shifted. It is not understood what the cause of this is and as such these events are excluded from the analysis. Considering the relatively small number of events in these groups, and assuming that this effect randomly applies to all ion species equally, excluding them should not affect the conclusions of the analysis. There are also some events appearing as a trail extending diagonally towards larger values of the cathode signal— this is indicated for section 5 of the MWPPAC in Figure 4.11 where the effect is seen most clearly. These seem to originate from a spurious source triggering the cathode and are not thought to be relevant to the analysis, so are likewise rejected.

Where one of the x_{left} or x_{right} signals are missing, the cathode signal can be used to reconstruct the missing signal as follows. In the case of a missing x_{right} signal, one can plot the events for which all three signals are present in a matrix of (cathode - x_{left}) vs. (x_{right} - x_{left}), for all MWPPAC sections; these plots are shown in Figures 4.12 (to reconstruct x_{right}) and 4.13 (to reconstruct x_{left}). Performing a linear regression on each section then provides an equivalence between the cathode signal and the missing $x_{\text{right/left}}$ signal. Figures 4.12 and 4.13 show these matrices and the results of the fitting procedure for missing x_{right} and x_{left} signals respectively.

The MWPPAC position is then calibrated with a set of coefficents for each section provided by the local PRISMA team, giving an absolute position in mm in the focal plane. An example of the calibrated focal plane position as measured by the MWPPAC is shown in Figure 4.14. The main peaks observed in the distribution of reaction products are shown to be due to the magnetic dispersion of the different charge states of the beam-like ions. All other reaction products show a similar lateral position separation according to the ionic charge state, each being deflected by differing magnitude by the fields in the magnetic elements.

The initial calibration of the time-of-flight is provided by the local PRISMA team. This is a set of calibration coefficients which match the gains of the timing signal in the different segments of the MWPPAC. An example is shown in Figure 4.15a, where the signals for

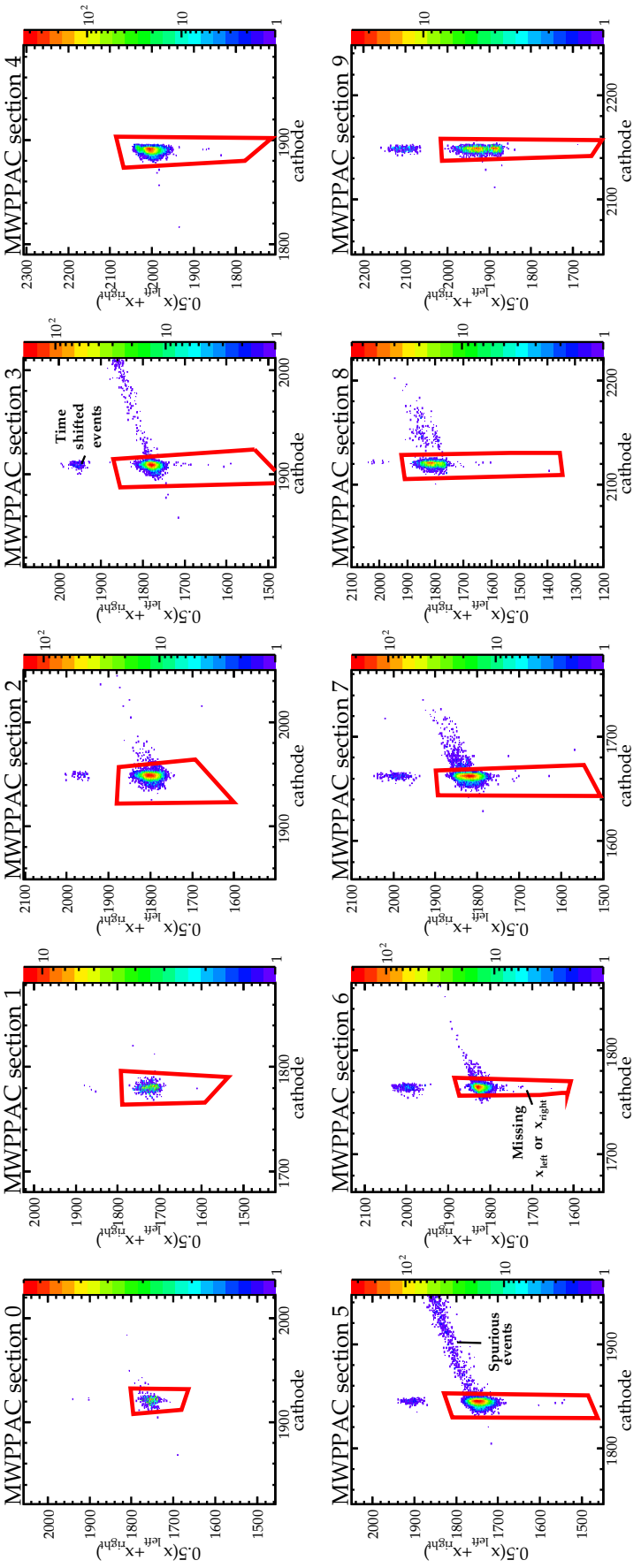

FIGURE 4.11: Gates applied to MWPPAC signals to select valid events. Red contours contain the events selected as being valid. All events outside are rejected.

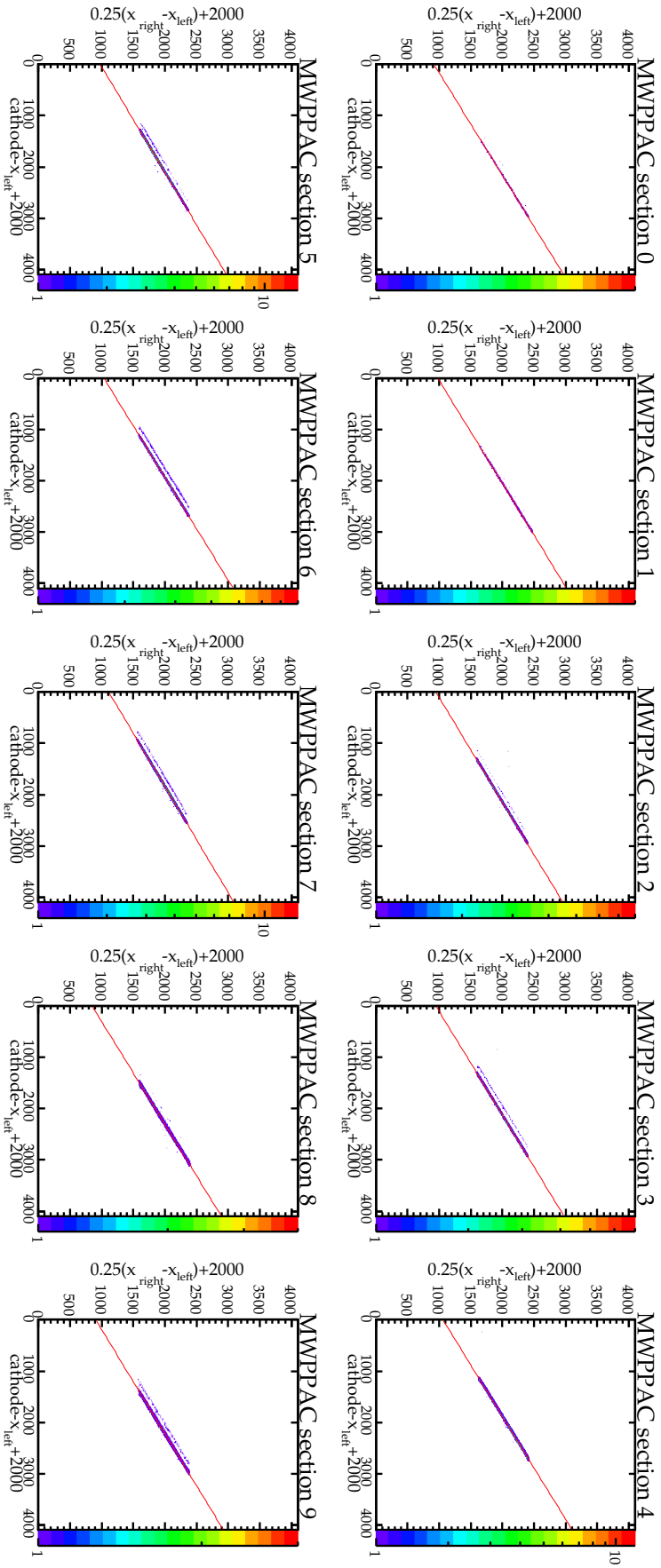

FIGURE 4.12: Reconstruction of MWPPAC x_{right} signal for each of the 10 sections. The red lines show fits which provide a transformation between the cathode signal and x_{right}.

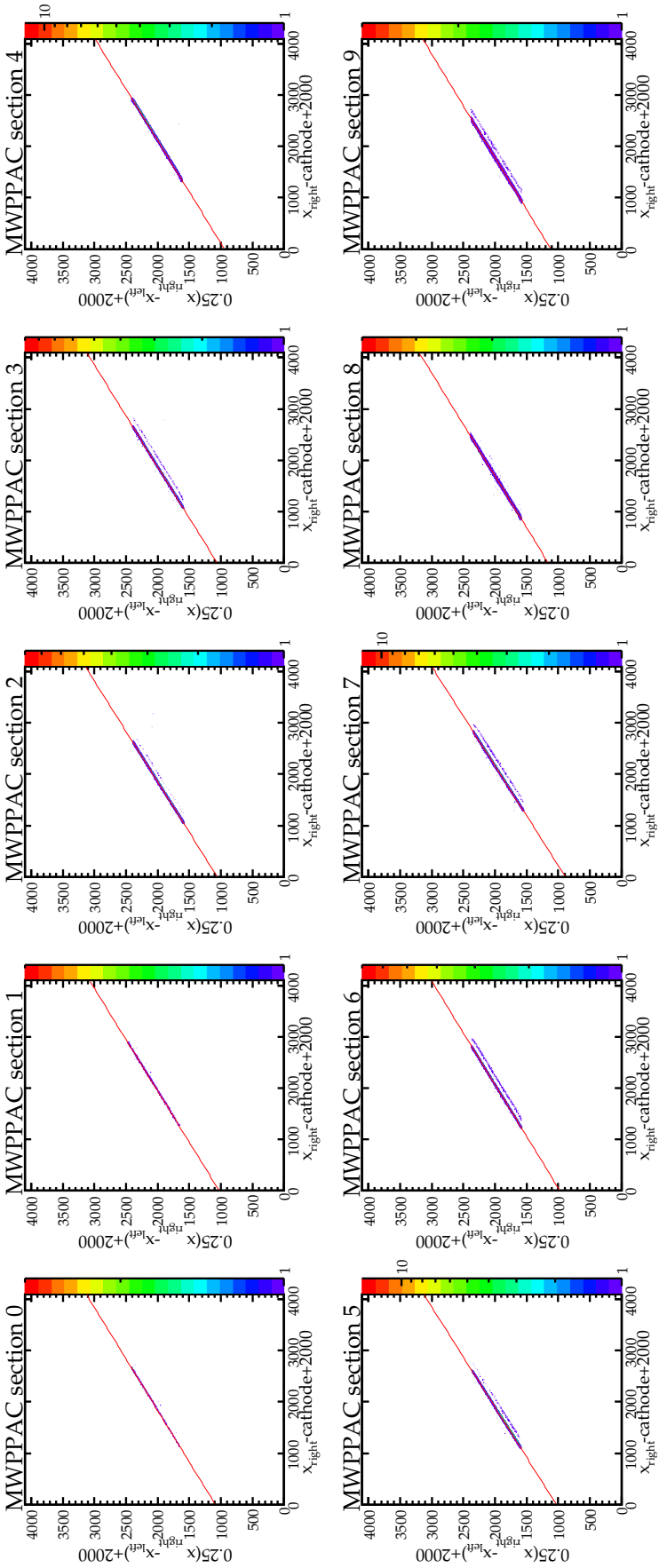

FIGURE 4.13: Reconstruction of MWPPAC x_{left} signal for each of the 10 sections. The red lines show fits which provide a transformation between the cathode signal and x_{left}.

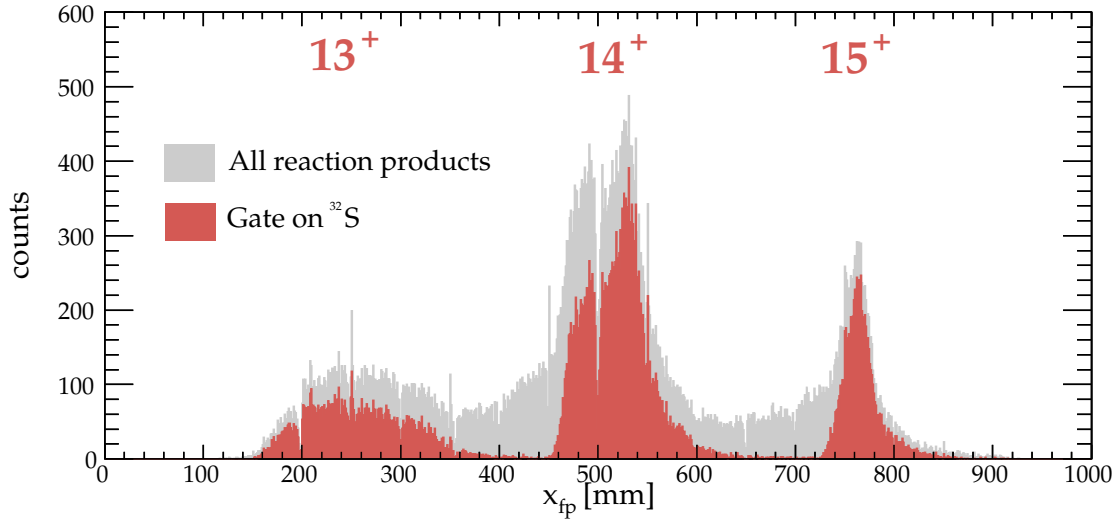

FIGURE 4.14: The calibrated focal plane position spectrum for the measurement of ^{32}S + ^{208}Pb at E_{Beam} = 178 MeV. The total distribution of reaction products is shown in grey. The distribution of the beam-like ions is shown in red.

each section are gain-matched but not yet aligned. A rough calibration of the time-of-flight can then be performed, whereby the offset applied to each section is modified in order to align the TOF signals across the different sections of the MWPPAC.

Considering as an example elastic scattering events emerging from the target and passing through the MCP foil, a range of chargestates is expected covering the full angular range entering the magnetic elements, with a range of kinetic energies given by Rutherford scattering kinematics. Each chargestate is focussed onto a different lateral position on the focal plane. A single charge state at a fixed energy is expected to have a spot size in the focal plane covering some range in the horizontal coordinate x_{fp} corresponding to the range of scattering angles— generally this will be spread over several sections of the MWPPAC. As such the alignment of the MWPPAC TOF signals can be achieved by ensuring a smooth joining of the distribution of the most prominent features of the x_{fp} vs. TOF matrix across the different sections. In addition, the main peak (presumably containing the elastic scattering events), can be aligned with a TOF value calculated via simple 2-body kinematics, assuming a central trajectory through the spectrometer along the optical axis and considering any possible energy losses in the target. The result of

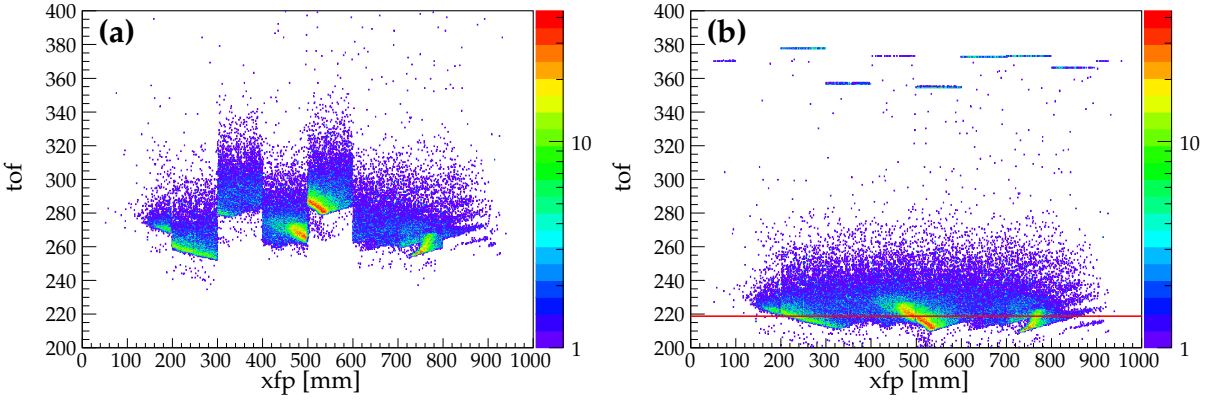

FIGURE 4.15: (a) Time-of-flight signals gain matched across different MWPPAC segments, prior to alignment of the sectors. (b)Time-of-flight signals aligned across the MWPPAC segments. Red line indicates the expected time-of-flight for elastic scattering events following a central trajectory through the spectrometer.

alignment of the MWPPAC TOF signals and matching to this simple kinematics calculation is shown in Figure 4.15b. The calibration of the TOF quantity is refined in the final stage of the analysis once a separation of the reaction products in mass and atomic number has been achieved, as will be described in Section 4.5.5.

The energy calibration factors for the IC array are provided by the local PRISMA team. This is not an absolute calibration in MeV, but rather to gain-match the signals from the different segments, similar to that provided for the MWPPAC time-of-flight signals. The energy measurement available from the IC is not necessary to the analysis as the time-of-flight offers an independent energy measurement with better resolution.

4.5 Data analysis

With an accurate position and time calibration of the detectors, it is then possible to reconstruct the ion trajectories through the spectrometer. This allows us to deduce the radius of curvature of the ions on an event-by-event basis, from which the masses A can be extracted. For this analysis, the author made use of a software package written by E. Farnea of LNL, as well as custom scripts written by the author using the ROOT data analysis framework.

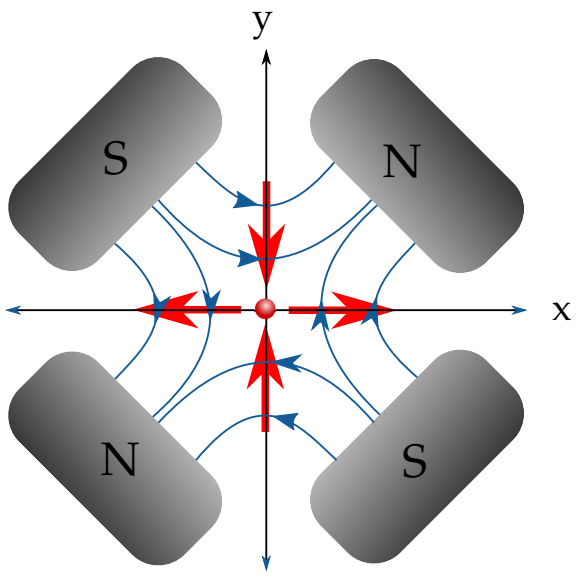

FIGURE 4.16: Quadrupole magnet geometry resulting in y-focussing and x-defocussing of a passing ion beam (with motion towards the page). The blue lines represent the magnetic field lines and the red arrows indicate the forces acting on charged ions in those regions of the field.

4.5.1 Trajectory reconstruction

The reconstruction of trajectories through the PRISMA device relies on a modelling of the ion motion within the magnetic elements. The entrance coordinates of the ions to the quadrupole magnet are determined by the recorded x and y position (by the MCP), assuming a straight line path from the target. Considering a quadrupole geometry such as that shown in Figure 4.16, where the z axis lies along the length of the element. The magnetic field **B** of an ideal quadrupole has two components:

$$B_y = -bx, \tag{4.1a}$$

$$B_x = -by, \tag{4.1b}$$

where b is the quadrupole field gradient. A traversing charged particle of charge q and velocity **v** is subject to the Lorentz force $\mathbf{F} = q(\mathbf{v} \times \mathbf{B})$, which in the x and y directions for a particle travelling with a velocity v_z in the z-direction results in the x- and y- force components [129, 130]:

$$\mathbf{F}_x = -qv_z B_y = qv_z bx, \tag{4.2a}$$

$$\mathbf{F}_y = qv_z B_x = -qv_z by. \tag{4.2b}$$

The ion motions within the quadrupole field along the x- and y- directions are decoupled, allowing the derivation of the following equations:

$$qv_z bx = m\frac{d^2x}{dt^2} = m\frac{d^2x}{dz^2}\left(\frac{dz}{dt}\right)^2 = m\frac{d^2x}{dz^2}v_z^2, \tag{4.3a}$$

$$-qv_z by = m\frac{d^2y}{dt^2} = m\frac{d^2y}{dz^2}\left(\frac{dz}{dt}\right)^2 = m\frac{d^2y}{dz^2}v_z^2. \tag{4.3b}$$

Rearranging and plugging in the magnetic rigidity $\rho_M = mv/q$:

$$\frac{d^2x}{dz^2} = \left(\frac{qb}{mv_z}\right)x = \left(\frac{b}{\rho_M}\right)x = k^2x, \tag{4.4a}$$

$$\frac{d^2y}{dz^2} = -\left(\frac{qb}{mv_z}\right)y = -\left(\frac{b}{\rho_M}\right)y = -k^2x. \tag{4.4b}$$

In the above expressions the quantity k has been introduced where:

$$k^2 = \frac{qb}{mv_z}. \tag{4.5}$$

Equations 4.4a and 4.4b are second order differential equations. The general solution for the motion in the x-direction is:

$$x(z) = A\sinh(kz) + B\cosh(kz), \tag{4.6a}$$

$$\dot{x}(z) = Ak\cosh(kz) + Bk\cosh(kz), \tag{4.6b}$$

and in the y-direction:

$$y(z) = C\sin(kz) + D\cos(kz), \tag{4.7a}$$

$$\dot{y}(z) = Ck\cos(kz) - Dk\cos(kz). \tag{4.7b}$$

Defining the z-position at the entrance of the quadrupole bore to be $z = 0$, and the corresponding x- and y-coordinates as $x(z = 0) = x_Q$ and $y(z = 0) = y_Q$, the coefficients A, B, C, D can be determined from the boundary conditions:

$$\left.\frac{dx}{dz}\right|_{z=0} = \frac{v_x}{v_z} = \tan(\alpha), \tag{4.8a}$$

$$\left.\frac{dy}{dz}\right|_{z=0} = \frac{v_y}{v_z} = \tan(\beta). \tag{4.8b}$$

The coefficients are then extracted as:

$$A = \tan(\alpha)/k \qquad B = x_Q \qquad C = \tan(\beta)/k \qquad D = y_Q \tag{4.9}$$

The effect of the quadrupole fields is thus a sinusoidal ion motion in the y-direction and a hyperbolic trajectory in the x-z plane. The quadrupole configuration in the PRISMA device focusses the ions in the y-direction and defocusses in the x-direction. The ions are focussed onto the x-z plane, which simplifies the trajectory reconstruction procedure, as well as shaping the cone of reaction products to maximise the acceptance of the spectrometer.

Upon exiting the quadrupole field, the ions travel a short distance before entering into the dipole field region. In the dipole field the action of the Lorentz force results in the ions moving in a circular trajectory or radius R. Since the component of the ion velocity along the optical axis is much greater than that in either of the perpendicular directions,

it can be assumed that $v_z \simeq v$ and $v_\perp = \sqrt{v_x^2 + v_z^2} \simeq v$. The force acting on an ion of mass m travelling with velocity v perpendicular to the dipole magnetic field B_D is given by:

$$F = \frac{mv^2}{R} = qvB_D. \tag{4.10}$$

The radius of curvature of the ion motion in the dipole magnet is then given by:

$$R_D = \frac{mv}{qB_D} = \frac{\rho_M}{B_D}. \tag{4.11}$$

The main steps of the trajectory reconstruction procedure are outlined in Figures 4.17 and 4.18. The reconstruction assumes that the particles travel in straight lines everywhere, except within the quadrupole, where they follow a hyperbolic trajectory, and within the dipole, where they travel in a circular arc (within the horizontal plane). In the sorting procedure the magnets are considered perfect elements, with no fringe field effects, although the influence of these are accounted for by using an effective quadrupole length, as will be described in Section 4.5.5. These approximations have been estimated elsewhere to give no more than a $\simeq 1\%$ error in the calculation of the total trajectory length between the MCP and MWPPAC [131].

The gyroradius of the ion motion within the dipole magnet is deduced by an iterative procedure which first assumes a guess value corresponding to a central path through the spectrometer (= 1.2m)— the associated rigidity ρ_M being assumed also within the quadrupole. With a knowledge of the field strengths in each of the magnetic elements, the ion motion is calculated and a prediction of the focal plane position can be made. If the measured position differs from this predicted value by more than 1mm, the process is repeated with a new guess value. The iteration is repeated until a satisfactory value of the curvature radius is found. Once the curvature radius is found, the trajectory length between the MCP and MWPPAC can be computed. This is given by:

$$L_{\text{Total}} = L_{\text{MCP - Quad}} + L_{\text{Quad}} + L_{\text{Quad - Dipole}} + L_{\text{Dipole}} + L_{\text{Dipole - MWPPAC}} \tag{4.12}$$

This procedure is outlined in Figure 4.17.

4.5.2 Z identification

The IC array is used to make a selection of the atomic number Z, utilizing a $\Delta E - E$ technique similar to that described in Chapter 3. In this case, however, the IC provides only Z selection, the masses being deduced instead from the reconstructed ion trajectories.

The modular design of the IC array gives some flexibility as to how events are disentangled using the $\Delta E - E$ technique— the ΔE layer can be chosen to consist of the first 1, 2, or 3 layers of the detector. The Z separation is better where the ΔE layer is thicker. However, choosing the first 3 layers for the ΔE signal then excludes any ions which are stopped before reaching the final layer. Referring to the schematic of the array in Figure 4.6, in Figure 4.19 the difference between using as the ΔE layer the combinations of layers A + B and A + B + C is demonstrated. In each of Figures 4.19a and 4.19b a diagonal group of events with ΔE = E_{IC} can be seen, and are excluded from the Z selection gates— these are those which are stopped within the chosen ΔE layer. As such, the choice of the thicker ΔE layer means a greater number of events are excluded. In order to maintain the best Z separation for all events that reach the focal plane, if those ions are stopped in layer X, the sum of the signals in all of the layers up to $X - 1$ is used as the ΔE signal. For a typical run, the IC gas pressure was such that the vast majority ($> 99\%$) of reaction products were stopped in the final 2 layers of the array, thus the ΔE signal was taken from the sum of the energy losses in the first two or three layers.

4.5.3 Identification of the ionic charge state q

The energy of the ions in the IC is given by:

$$E_{IC} = \frac{1}{2}mv^2. \tag{4.13}$$

Rearranging equation 4.10 and substituting into equation 4.13 results in:

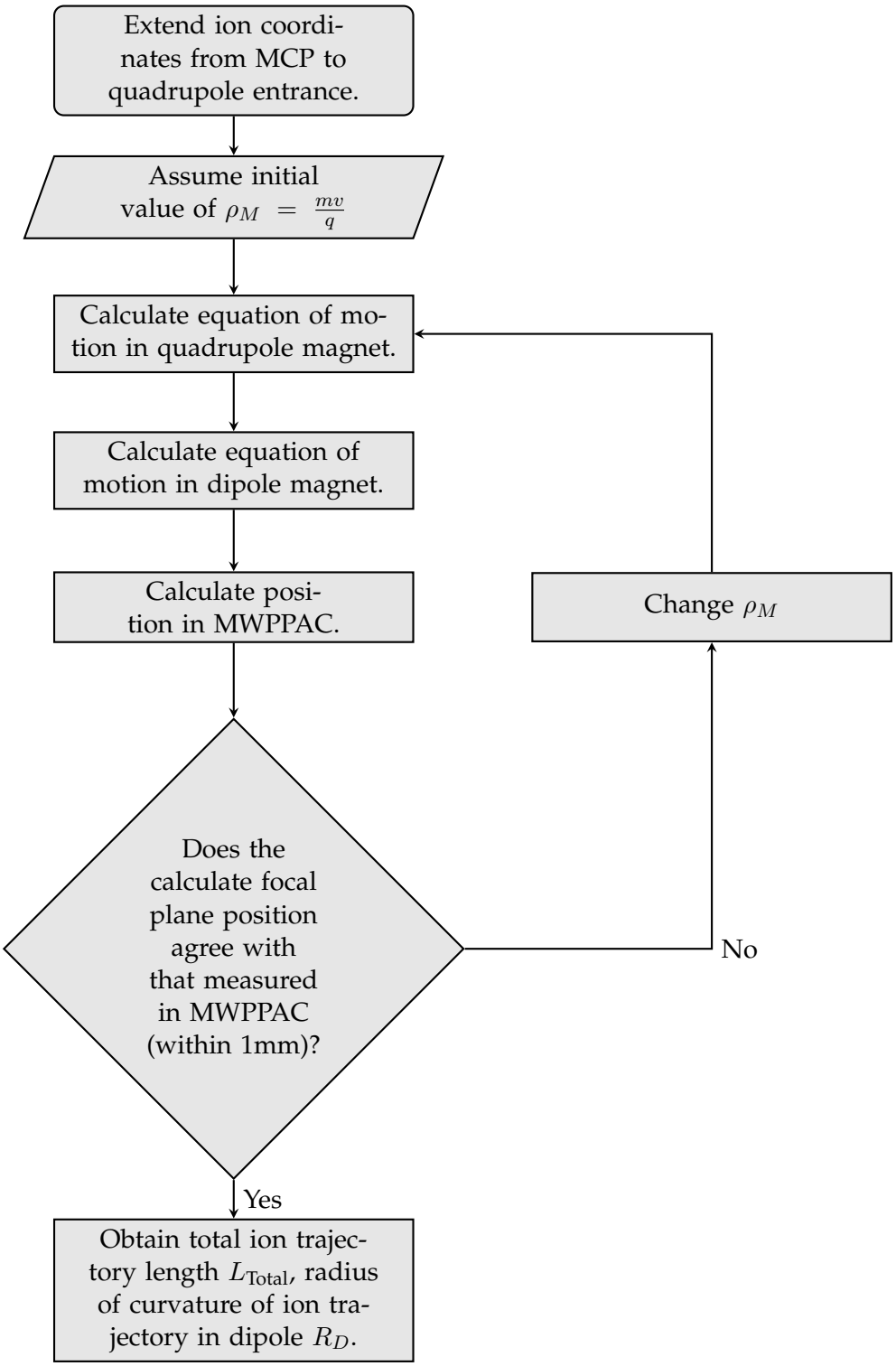

FIGURE 4.17: First step of trajectory reconstruction through PRISMA.

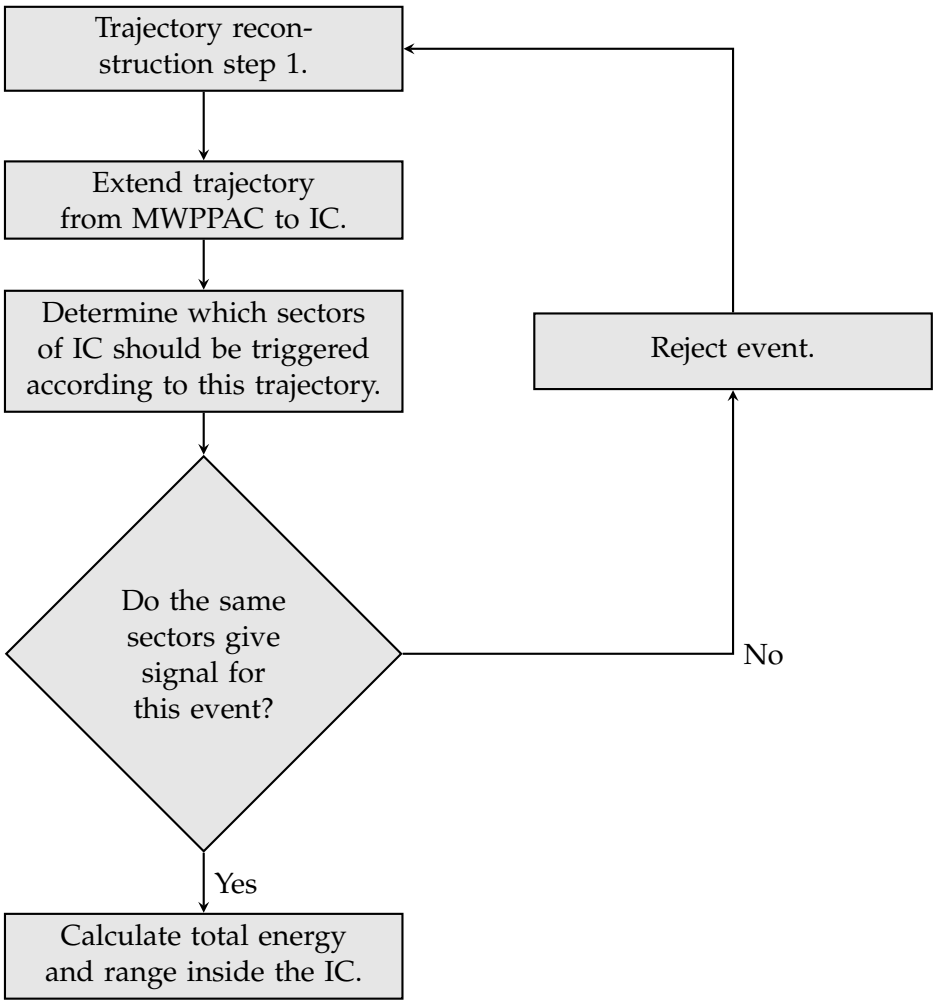

FIGURE 4.18: Second step of trajectory reconstruction through PRISMA.

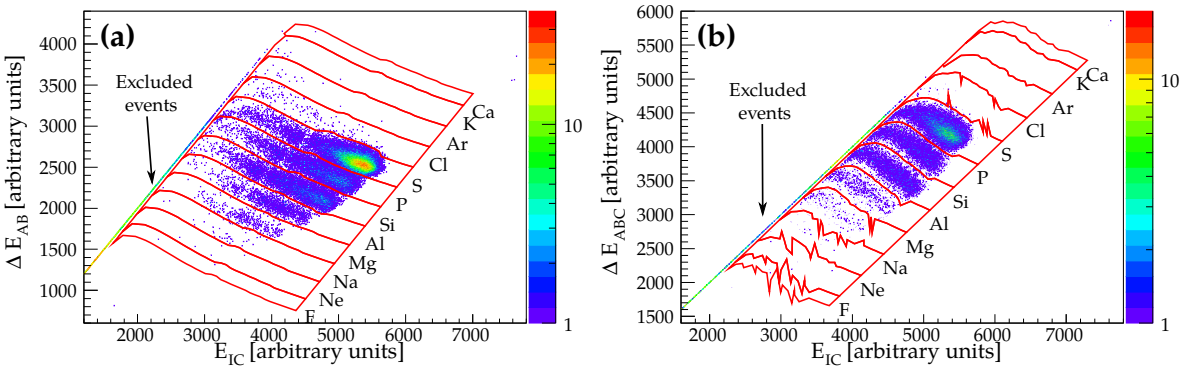

FIGURE 4.19: Z selection spectra. Red contours indicate the applied gates, which are labelled on the right side by the element the events within are assigned to. (a) Z selection spectrum where the ΔE signal is the sum of the energy lost in layers A and B of the IC array. (b) Z selection spectrum where the ΔE signal is the sum of the energy lost in layers A, B, and C of the IC array. Note that the gates are determined using an algorithmic process in which a fitting of slices of the events distribution is performed sequentially— this process is responsible for the scatter of points in the gates. These are smoothed out in the selection of events to gate for each Z value.

$$E_{IC} = \frac{1}{2} qvBR. \tag{4.14}$$

Or, expressed alternatively in terms of the relativistic velocity $\beta = v/c$,

$$E_{IC} = \frac{1}{2} q\beta BR. \tag{4.15}$$

Thus by plotting E_{IC} against $R\beta$, after first gating on Z, the events distribution exhibits a separation in terms of q, as shown in Figure 4.20. The charge states are identified by their relative yields, comparing to the calculation of charge state distributions given by the code `reaction`, which is based on Ref. [128]. Gates are defined on q separately for each value of Z. Figure 4.20 shows an example of the Z = 16 events presented in this way. At least 4 charge states can be clearly identified in this example. A comparison of the observed yields to the values calculated by `reaction` is shown in Figure 4.21.

Simulating the PRISMA response to elastic scattering under the same experimental conditions (e.g. magnetic field settings) can also inform the process of identifying charge

states, by predicting which charge states are expected to reach the focal plane and at what position in the horizontal plane. The quality of the matching between the simulated and experimental transport of the different charge states of the elastically scattered beam is shown in Figure 4.22, where the spectra display the correlation between the x-position in the MCP and MWPPAC detectors. The experimental distributions of the 16^+ and 15^+ (and to a small degree the 13^+) charge states are shown to be cut off at the edges of the focal plane detector— this is due to the veto provided by the side pads of the IC array, which rejects events that do not give a full profile of energy loss signals in the 4 longitudinal layers (thus being difficult to separate by Z). This is understood to be the main contributing factor to the discrepancies observed between the calculated and experimental charge state yields shown in Figure 4.21. In addition, as mentioned in Section 4.3, the calculation of the charge state distribution performed by `reaction` does not consider the effect of stripping processes in the MCP foil which would further alter the observed yields.

It is important for the subsequent stages of analysis that the charge state is identified unambiguously, as incorrect assignments result in an incorrect deduction of the product mass.

4.5.4 Mass number reconstruction

Starting again from 4.10, and substituting for v:

$$v = \frac{L_{\text{Total}}}{\text{tof}} \tag{4.16}$$

results in the following expression for the ratio A/q:

$$\frac{A}{q} = \frac{BR}{L_{\text{Total}}}\text{tof} \tag{4.17}$$

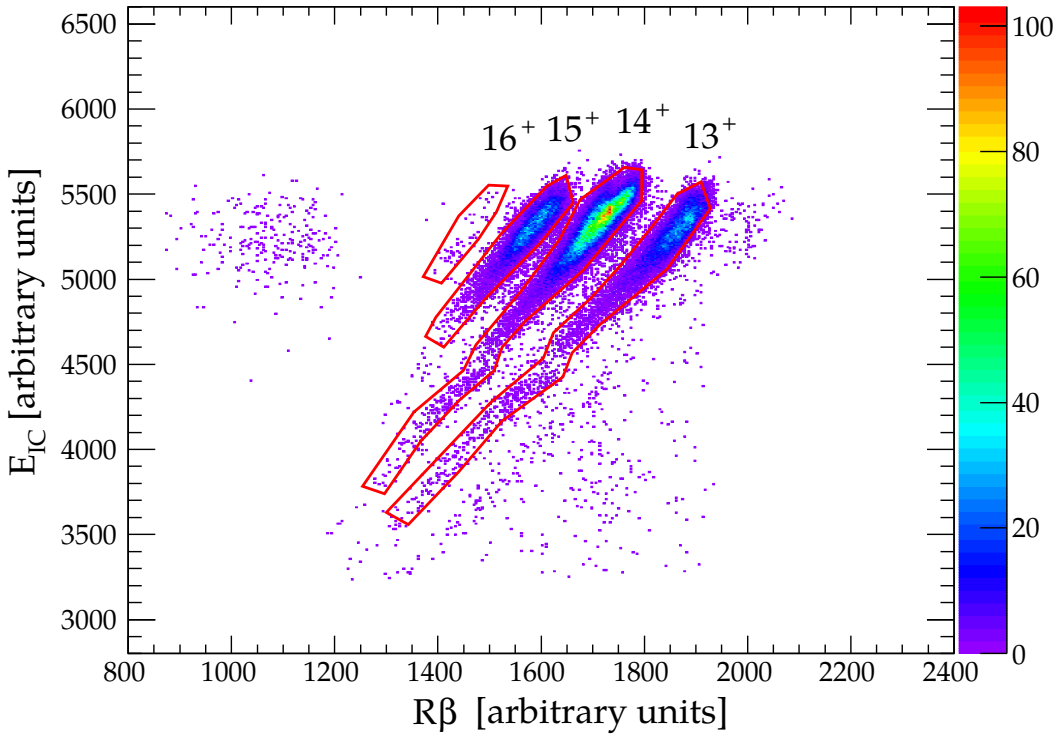

FIGURE 4.20: IC energy vs $R\beta$, in the measurement of ^{32}S + ^{208}Pb at E_{Beam} = 178 MeV, where a gate has been applied to events with Z = 16. Charge states are assigned to the different groups of events by comparing yields to model calculations of the charge state distribution.

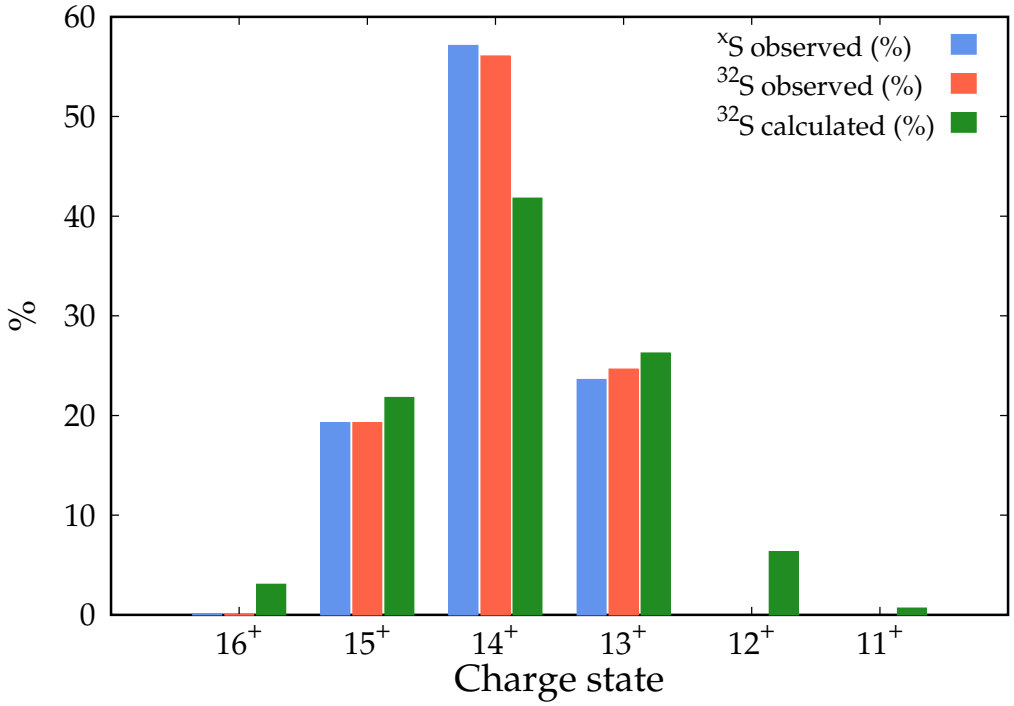

FIGURE 4.21: A comparison of the percentage charge state yields as calculated and observed in the measurement of ^{32}S + ^{208}Pb at E_{Beam} = 178 MeV. The observed percentage yields are shown for all Z = 16 events (blue column), as well as for ^{32}S following the mass reconstruction procedure described in Section 4.5.4 (to which the calculated distribution corresponds). In fact the charge state distribution is mainly sensitive to Z, not A, and the predicted most abundant charge state does not change across the different detected isotopes of sulfur.

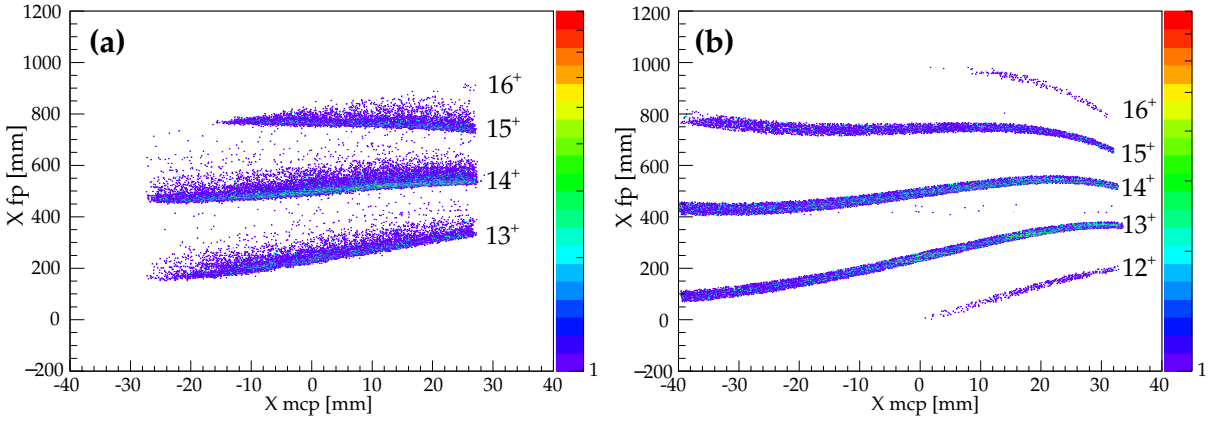

FIGURE 4.22: (a) Experimental and (b) simulated transport of different charge states of ^{32}S to the focal plane in the measurement of ^{32}S + ^{208}Pb at E_{Beam} = 178 MeV.

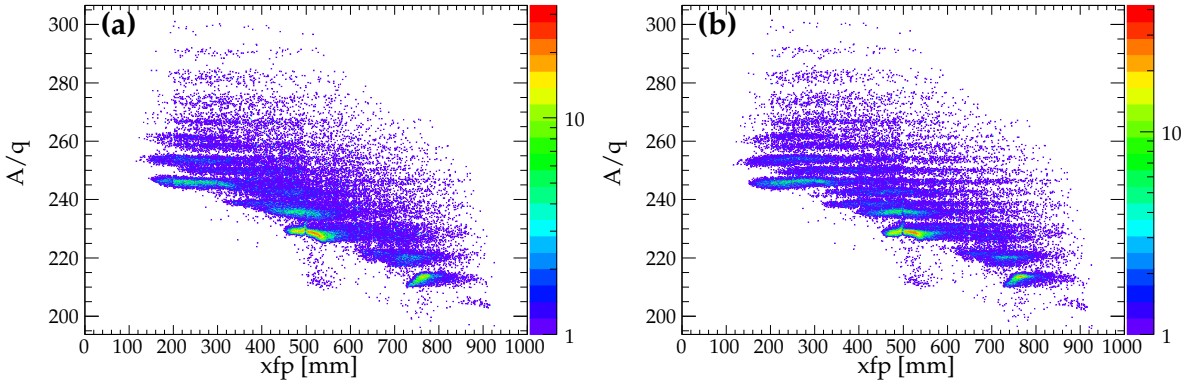

FIGURE 4.23: A/q vs x_{fp} matrix where the (a) physical (450mm) and (b) effective (510mm) length of the quadrupole is used in the reconstruction of ion trajectories. Example shown is the measurement of ^{32}S + ^{208}Pb at E_{Beam} = 178 MeV.

As the mass number and charge state are both integers, plotting the spectrum $\frac{A}{q}$ vs. x_{fp} should result in a series of horizontal lines. Where this is not the case, the effective quadrupole length used in the calculation of the ion trajectories is adjusted until the distribution of events becomes horizontal in this matrix. Using an effective quadrupole length in this manner absorbs the effect of the fringe fields outside the physical dimensions of the dipole and quadrupole magnets into the sorting method treating the magnets as perfect elements. An optimization of these quantities is necessary for best agreement between the calculated and reconstructed total kinetic energy distributions, as will be described in Section 4.5.6. At this stage it is sufficient to adjust these values to make the distributions for each charge state in $\frac{A}{q}$ vs. x_{fp} horizontal.

To ensure a correct reconstruction of the ion masses, care must be taken that the different charge states are aligned at the correct values in the A/q spectrum. Looking back at Equation 4.17, the experimental value of A/q is derived from the properties of the reconstructed trajectory as well as the experimental value of the dipole magnetic field strength. The agreement between the experimental spectrum and the expected values can thus be achieved by varying the global offset of the time-of-flight or applying a scaling to the A/q coordinate. The latter may be necessary if, for example, the dipole field strength calibration to the currents supplying the magnet (provided by the PRISMA team) is not optimal [132, 133]. For simplicity, at this stage the global time-of-flight offset was adjusted to

match the expected A/q ratios in order to guarantee correct mass reconstruction (departing from the value that may have been set from the first stage time-of-flight calibration described in Section 4.4.2). Note that since the recorded time-of-flight affects the properties of the reconstructed trajectory (such as the curvature radius), this step necessitates a redrawing of the gates in the E_{IC} vs. $R\beta$ spectrum to select the charge state q. Since the peak in $R\beta$ scales linearly with the magnitude of the applied time-of-flight offset, it was possible to set up an optimization routine to find the best value. Figure 4.24a shows the reconstructed A/q with the expected values for the different charge transfer products.

Once the experimentally determined A/q events distribution matches well with the expected ratios (across various Z and q values), the masses are simply obtained by multiplying the A/q spectra by the assigned masses. This is shown in the right panels of Figure 4.24, where the top panel corresponds to the sum of the spectra in the 3 left panels, once the A/q value is multiplied by the assigned charge state q_{gate}. With the reaction products now identified in terms of both Z and A, a spectrum of particle identity can be constructed as shown in Figure 4.25.

4.5.5 Absolute time-of-flight calibration

With a sorting of the reaction products by Z and A at this stage of the analysis, the optimal global offset for the time-of-flight signal can be found by seeking agreement between a calculation of the elastic scattering and the identified beam ions in total kinetic energy (TKE), following a central trajectory through the spectrometer. Similar to that described in the previous section, with the TKE scaling linearly with the applied time-of-flight offset, an optimization routine was used to find the final required value for best agreement with the calculated TKE. Once this value was found, the required scaling factors to apply to the reconstructed A/q spectra could be determined by performing a linear regression fit between the expected A/q ratios and the peaks in the reconstructed spectrum.

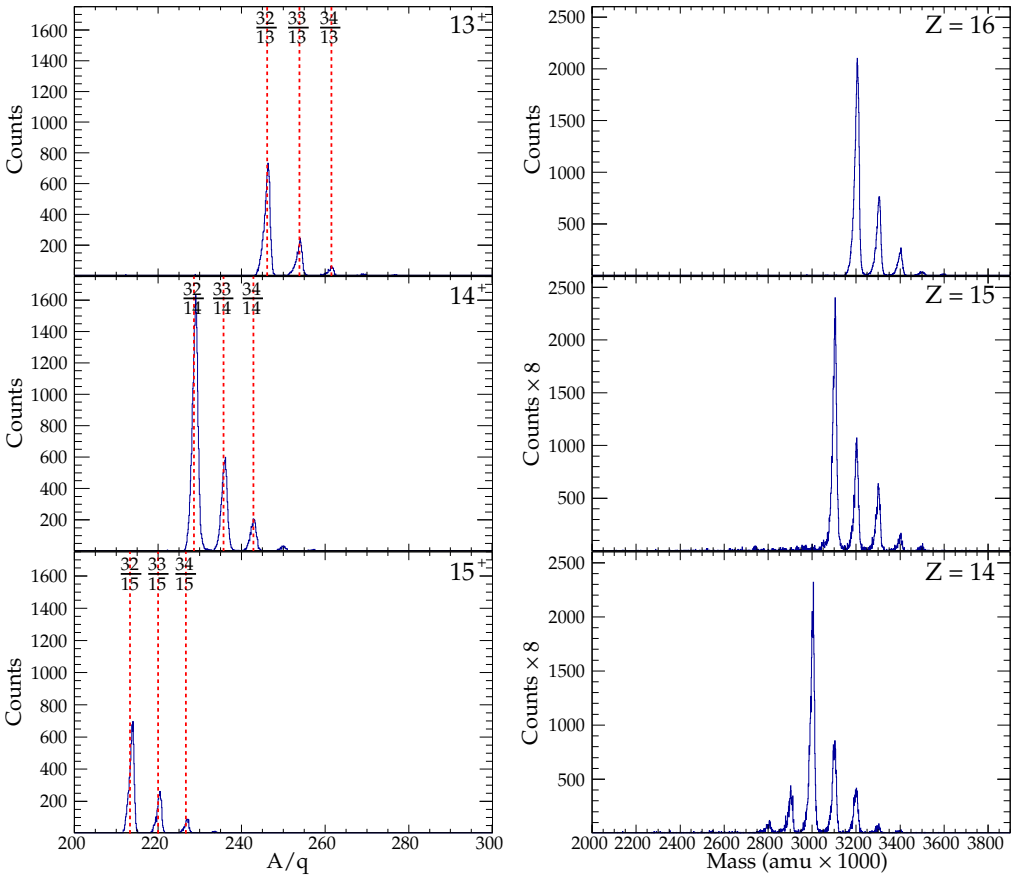

FIGURE 4.24: Reconstructed A/q (Left panels) and mass (Right panels) spectra for the measurement of ^{32}S + ^{208}Pb at E_{Beam} = 178 MeV. In the left panels the A/q spectrum is shown where a gate has been applied to Z = 16 (Sulphur products).

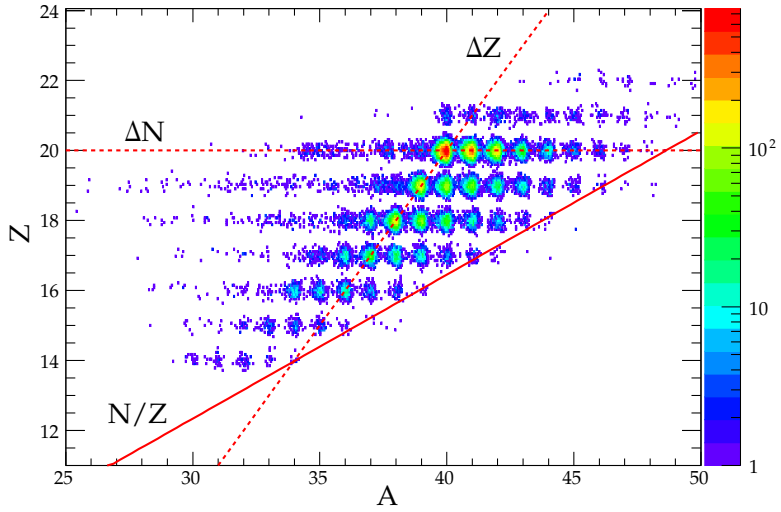

FIGURE 4.25: A vs. Z spectra for ^{40}Ca + ^{208}Pb at E_{Beam} = 223.5 MeV. The dashed lines indicate pure proton and neutron transfer. The solid line shows the charge equilibration (N/Z ratio) of the compound nucleus. Note that the Z distribution is folded with a Gaussian function to mimic the width of the mass distribution, as this quantity is attributed to the ions on an assigned rather than reconstructed basis.

4.5.6 Optimization of the effective quadrupole dimensions for treatment of magnet fringing fields

The chosen effective length of the quadrupole used in the trajectory reconstruction procedure (as well as its geometric relation to the entrance of the dipole) have a subtle effect on the reconstructed total path length of the ions between the MCP and MWPPAC detectors, and hence the deduced total kinetic energy. In particular, the variation of the deduced TKE with the scattering angle is modified according to the chosen values. Thus, there are two criteria for selecting the optimum values of the effective quadrupole length and the effective distance between the target and quadrupole:

1. Events distribution in the A/q vs. x_{fp} matrix should be a series of horizontal lines, since it represents a reconstruction of the ratio between two integer values.

2. The reconstructed variation in TKE with the scattering angle should match as closely as possible the expectation from a 2-body kinematics calculation. This is essential for reconstructing the reaction Q-value without introducing any artificial broadening to the shape of the distribution.

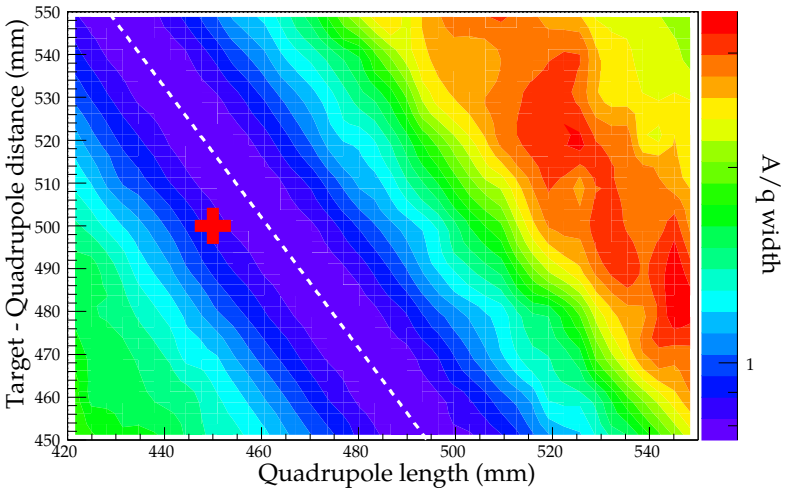

FIGURE 4.26: Optimization of effective quadrupole length and target-quadrupole distance used in trajectory reconstruction procedure to account for fringing fields of the magnets. The white dashed line is a fit to the minima of the A/q width. The red cross indicates the physical dimensions of the experimental apparatus. The measurement shown here is that of ^{40}Ca + ^{208}Pb with a beam energy of 223.5 MeV at PRISMA angle 102°.

To find the optimal values, a subset of the experimental data (corresponding only to elastic scattering) was processed repeatedly whilst varying the effective quadrupole length and target-quad distance in small steps. After each step, spectra of the reconstructed A/q were plotted (gating on the most prevalent charge state), and the root mean square (RMS) of the distribution extracted. This value acts not only as an indicator of the 'sharpness' of the events distribution in A/q but also as a useful proxy for the gradient in the A/q vs. x_{fp} matrix. From the extracted RMS values it is possible to construct a contour plot such as shown in Figure 4.26. Clearly shown are a set of quadrupole paramaters which best satisfy criteria # 1 in the list above— this is indicated by the white dashed line which is a fit to the minima of the 3D surface. The physical dimensions of the system are indicated by the red cross.

In order to satisfy both of the criteria listed above simultaneously, a procedure is implemented whereby the experimental data subset was repeatedly sorted using values for the effective quadrupole dimensions that lie along the white dashed line in Figure 4.26. After each sorting step, matrices of the laboratory frame scattering angle θ_{lab} vs TKE were

plotted (as shown in Figure 4.27), and the agreement with the kinematics calculation extracted in the form of the sum of the residuals between the calculated TKE and the fitted peak position across the angular range in constant steps (which varied in range over θ_{lab} depending on the level of statistics for the run in question). The effective quadrupole dimensions were chosen so as to minimize this quantity.

The optimization procedure described in this section generally gave optimum values for the effective quadrupole length between 500-520 mm (as opposed to the 450 mm physical length), which is in good agreement with the values that have been reported in other works concerning the PRISMA system [133, 130, 132].

4.5.7 Determination of Q-value

In the same way as described in Section 3.3.4 of Chapter 3, the Q-value is reconstructed from the measured energy of the reaction products following particle identification, assuming 2-body kinematics, as per Equation 3.11. The energy measurement derived from the trajectory reconstruction procedure and the time-of-flight between the MCP and MW-PPAC is used in this calculation, providing superior resolution to the independent energy measurement in the IC array. The excitation energy is then deduced from the ground-state-to-ground state Q-value as expressed in Equation 3.12. Examples of the deduced Q-value and excitation energy spectra are shown in Figures 4.28 and Figure 4.29 respectively, for the measurement of ^{32}S + ^{208}Pb at E_{Beam} = 178 MeV.

4.6 Summary

This chapter has described in detail the principle of determining product identities and their energetics using the PRISMA spectrometer, as well as the analysis procedure involved in extracting the quantities of interest. In summary:

- Atomic number is identified in the segmented ionization chamber using the ΔE-E technique.

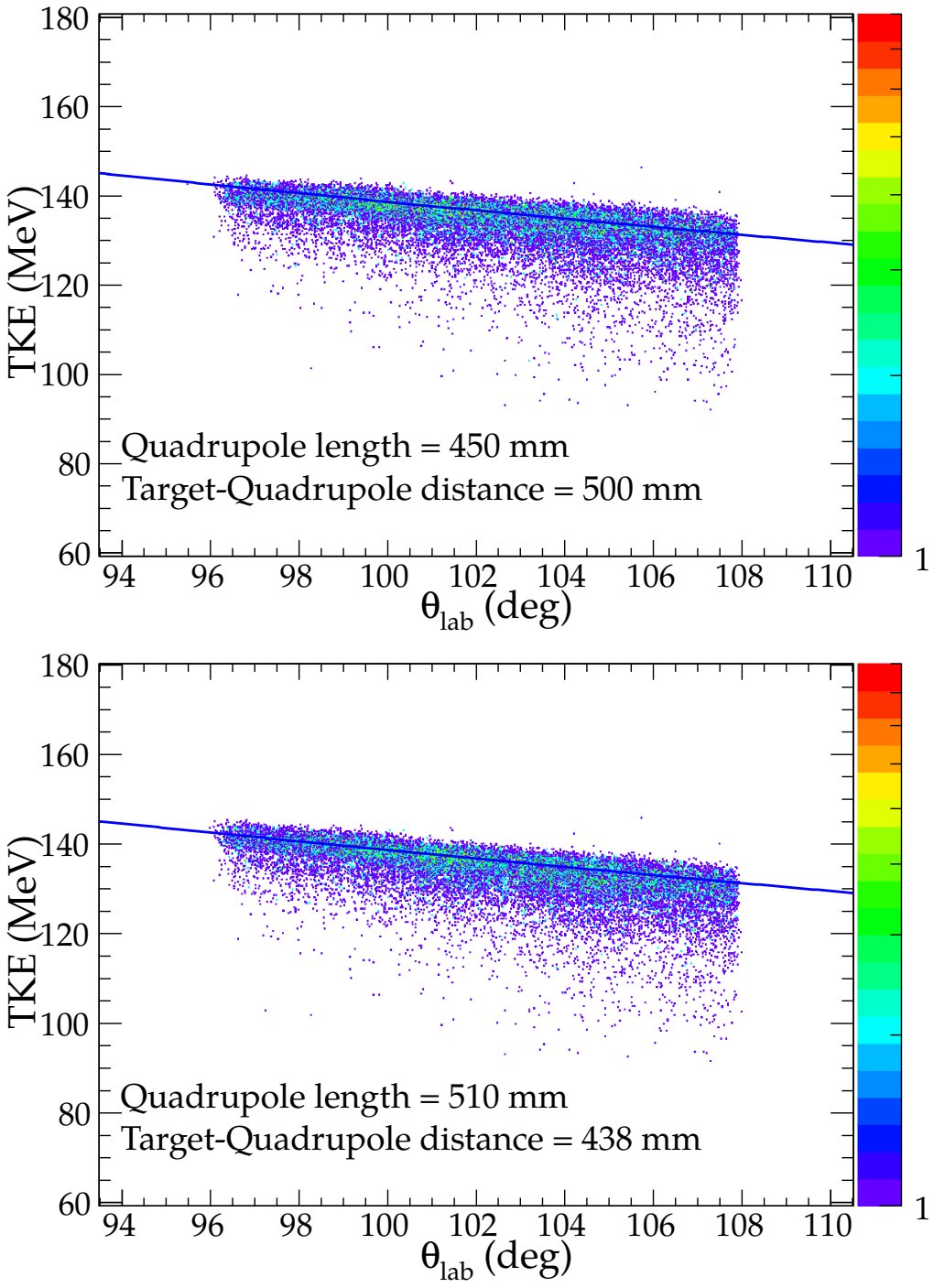

FIGURE 4.27: Reconstructed θ_{lab} vs. TKE spectrum in the measurement of ^{40}Ca + ^{208}Pb at E_{Beam} = 223.5 MeV with PRISMA positioned at θ_{lab} = 102°
Top panel: where the quadrupole dimensions considered in the trajectory reconstruction procedure correspond to the physical values.
Bottom panel: where the quadrupole dimensions give optimal agreement with the kinematic calculation.

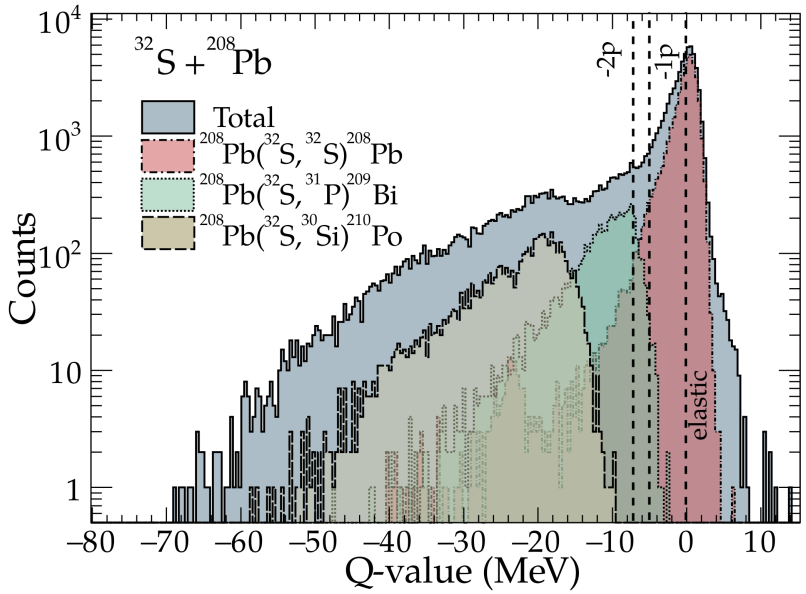

FIGURE 4.28: Example of a Q-value spectrum reconstructed from 2-body kinematics in the case of ^{32}S + ^{208}Pb at E_{Beam} = 178 MeV. The total Q-value spectrum includes all events which fall within the gates applied during the sorting procedure. Also shown are the spectra for -1p and -2p transfer, which are the most prominent charge transfer modes from this measurement.

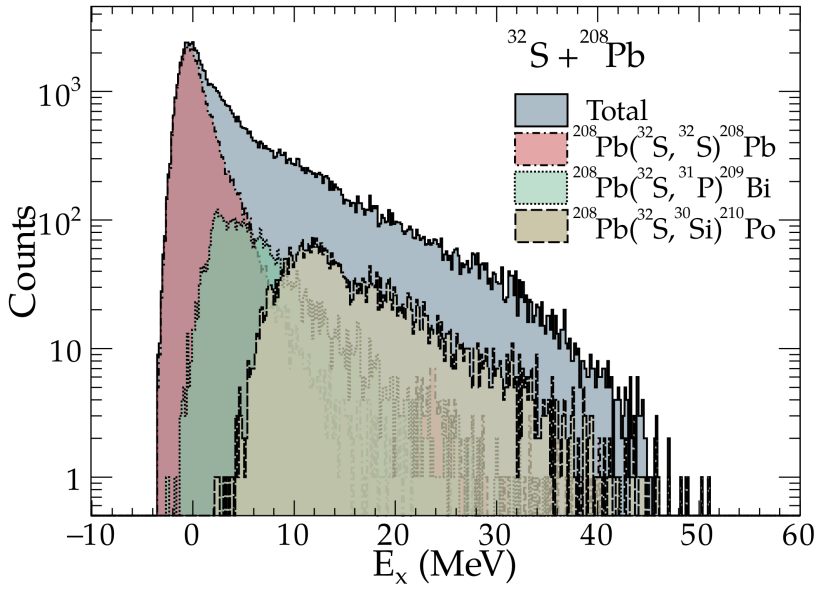

FIGURE 4.29: Example of an excitation energy spectrum resulting from Equation 3.12 considering the ground-state-to-ground-state Q-values $Q_{g.g}$, in the case of ^{18}O + ^{208}Pb at E_{Beam} = 178 MeV. The total Q-value spectrum includes all events which fall within the gates applied during the sorting procedure. Also shown are the spectra for -1p and -2p transfer, which are the most prominent charge transfer modes from this measurement.

- Charge state is deterined by comparing the observed dispersion in the MWPPAC for each Z to expected charge state distributions calculated using the `reaction` code.
- Reconstruction of ion trajectories through the spectrometer, allowing determination of mass numbers.
- Optimization of set-up parameters (including the effective quadrupole length) to ensure accurate reconstruction of Q-value and excitation energies.

This is a complicated procedure that involves a multitude of steps, all of which have been described in detail in this chapter. An overview of the analysis of PRISMA data is shown in Figure 4.30.

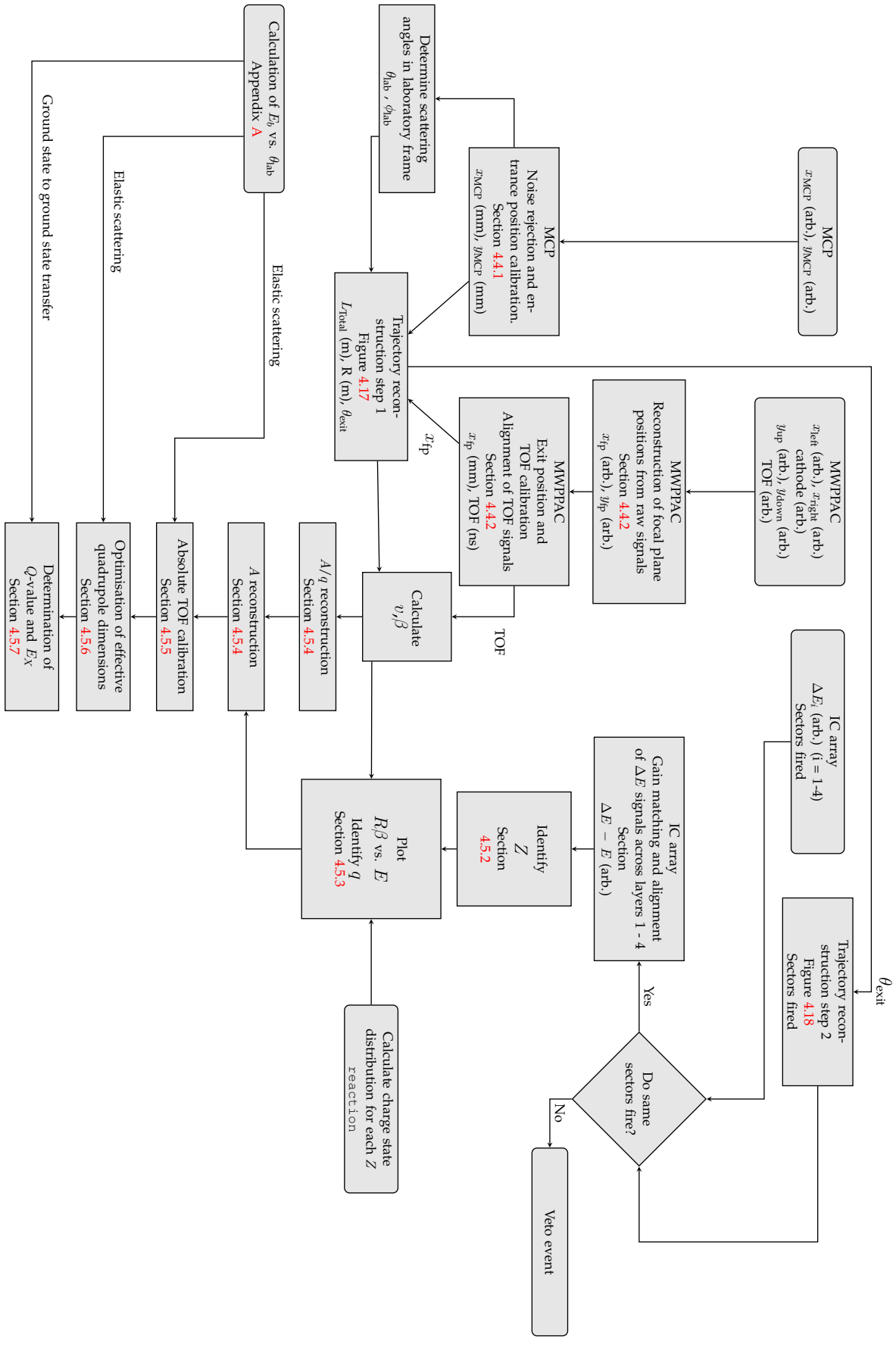

FIGURE 4.30: Overview of the analysis procedure for PRISMA data.

Chapter 5

Multinucleon transfer and doorways to energy dissipation

In this chapter the results of the experiments described in Chapters 3 and 4 are presented. Firstly, the method of extracting the transfer probability from the measured yields of various reaction products is discussed. This is followed by an interpretation of the results in terms of the reaction Q-value. The energy dependence (or equivalently the internuclear separation dependence) is then examined for each reaction with an analysis of the slopes of the transfer excitation function for each observed mode. Next is an examination of the excitation energy distributions of the exit channels as they vary both with the transfer mode and the bombarding energy relative to the barrier height. The chapter will close with a consideration of how the observed results are relevant to the problems of interpreting fusion reactions within the CRC framework as was explained in the opening chapters.

5.1 Extraction of absolute transfer probabilities

It is customary in the analysis of measurements of multinucleon transfer reactions to examine the transfer probability as a function of the distance of closest approach (see Equation 2.10 and Figure 2.3). An analysis of the transfer function, and particular the exponential slope α that can be extracted from fitting the data, yields information about

the reaction mechanism — namely that comparing the slopes of the single and multi-nucleon functions can identify whether there are contributions from cluster transfer or if a purely successive transfer mechanism is responsible for the observed yields. This has made multinucleon transfer reactions an important method through which to study particle correlations in nuclei [83, 134].

The transfer probability at a given angle is a useful quantity also in that it is easily extracted in an experiment. At backward angles, where the yields of transfer products are measured in this work, the elastic yields deviate significantly from the Rutherford prediction due to the occurence of non-elastic processes. To extract the transfer probability at those angles, it is necessary to deduce the number of events that would be expected in pure Rutherford scattering in order that one may quantify the degree to which the elastic channel is depopulated.

The yield of elastic scattering events in the monitor detectors, positioned at a forward angle θ_{Mon} is proportional to the Rutherford scattering cross section at that same angle:

$$Y_{\mathrm{Ruth}}^{\mathrm{Mons}} = In\epsilon_{\mathrm{Mons}}\frac{d\sigma_{\mathrm{Ruth}}(\theta_{\mathrm{Mons}})}{d\Omega}\Delta\Omega_{\mathrm{Mons}}. \tag{5.1}$$

In the above, the ϵ_{Mons} is the efficiency of the monitor detectors, which in this case are Silicon detectors operating in singles mode, and can be assumed to be close to 100 % efficient (though this may degrade if the detector rate becomes too high leading to event pile up). The $\Delta\Omega_{\mathrm{Mons}}$ is the solid angle subtended by the detectors. I and n are the beam flux and area density of the target atoms respectively.

Since the monitor yield $Y_{\mathrm{Ruth}}^{\mathrm{Mons}}$ is an essential component of the normalisation of the processes observed at backward angles, it is important to be aware and to account for external factors that may affect it from run to run in an experiment. The most important of these is variations in the beam spot position on the target after retuning, which can slightly change the relative angular position of the monitor, and thus consequently subtly affects the Rutherford scattering cross section. In order to avoid errors arising from this source, it is customary to use either an annular monitor detector or several positioned

symmetrically around the beam axis. In both of the experiments reported in this thesis, two monitor detectors were used, and the geometric mean of the elastic counts between them used for normalisation.

The expected Rutherford yield in the backward angle detector is then given by:

$$Y_{\text{Ruth}}^{\text{Back}} = Y_{\text{Ruth}}^{\text{Mons}} \frac{d\sigma_{\text{Ruth}}(\theta_{\text{Back}})}{d\sigma_{\text{Ruth}}(\theta_{\text{Mons}})} \frac{\Delta\Omega_{\text{Mons}}}{\Delta\Omega_{\text{Back}}}. \tag{5.2}$$

The probability for a given reaction mode i at a scattering angle θ_{Back} is given by:

$$P_i(\theta_{\text{Back}}) = \frac{d\sigma_i(\theta_{\text{Back}})}{d\sigma_{\text{Ruth}}(\theta_{\text{Back}})} = \mathcal{N} \frac{Y_i^{\text{Back}}}{Y_{\text{Ruth}}^{\text{Mons}}}, \tag{5.3}$$

where $\mathcal{N}$ is a normalisation factor that is determined by setting the probability for quasi-elastic scattering, $P_{\text{QEL}}(\theta)$, to unity for the lowest energy measurement, where it can be assumed that the fusion probability drops to zero. The normalisation factor is dependent on the efficiencies of the detectors and the target properties and orientation. As such, $\mathcal{N}$ needs to be determined independently for measurements on different targets.

In the later sections of this chapter in which the excitation spectra are presented, in order to directly compare different reactions the product yields are displayed as a function of the differential probability per bin in E_x. This quantity is obtained by dividing the counts per bin by $\mathcal{N}/Y_{\text{Ruth}}^{\text{Mons}}$, ensuring that:

$$P_i = \int_{E_x} \frac{dP_i}{dE_x}. \tag{5.4}$$

5.2 Q-value dependence of transfer probabilities

The change in mass between the entrance and exit channels in a nuclear reaction, which is commonly expressed as the Q-value, is usually a first consideration in estimating the likelihood of a given reaction mode. Multinucleon transfer cross sections have been shown to have an approximately exponential dependence on the reaction Q-value [135, 60], with

the cross sections for production of each element lying on parallel lines, shifted relative to each other according to the difference in the Coulomb potential between the entrance and exit channels. Correcting the ground-state Q-values $Q_{\mathrm{g.g}}$ by the change in the Coulomb potential, evaluated at the distance of closest approach, gives an effective Q-value:

$$Q_{\mathrm{eff}} = Q_{\mathrm{g.g}} - \Delta V_C, \tag{5.5}$$

with $\Delta \mathrm{V}_C$ the Coulomb energy shift. This provides a rough basis for estimating the relative strength of different channels. The Q-values $\mathrm{Q_{g.g}}$ for the ground-state-to-ground-state transfer processes and the $\mathrm{Q_{eff}}$ (incorporating the relevant $\Delta \mathrm{V}_C$) are listed in Table C.1 (see Appendix C) for all of the transfer modes which exhibited significant yields in the systems studied.

Figure 5.1 shows the absolute transfer probabilities of reaction modes involving the stripping of up to three protons for all of the systems studied, at an energy approximately equivalent in bombarding energy; equivalent to around 95% of the barrier height. In considering the energy equivalence, it is important to consider the angular momentum shift in the fusion barrier, which differs between the two experiments that are reported in this thesis due to the fact that the detection apparatus was positioned at different scattering angles. In estimating E/V_B throughout this chapter, the center-of-mass energy of the reaction is adjusted according to the (average) center-of-mass scattering angle $\theta_{c.m}$ [136, 137] :

$$E_{\mathrm{eff}} = 2E\frac{\sin(\theta_{c.m}/2)}{1+\sin(\theta_{c.m}/2)} \tag{5.6}$$

The data are plotted in separate panels according to the ΔZ value in order to illuminate the relationship between the considered quantities. In this thesis, a distinction will be drawn between transfer modes that can be considered *direct* (where the nucleon flux is in one direction only or can *conceivably* be considered as a one-step process- e.g. two proton

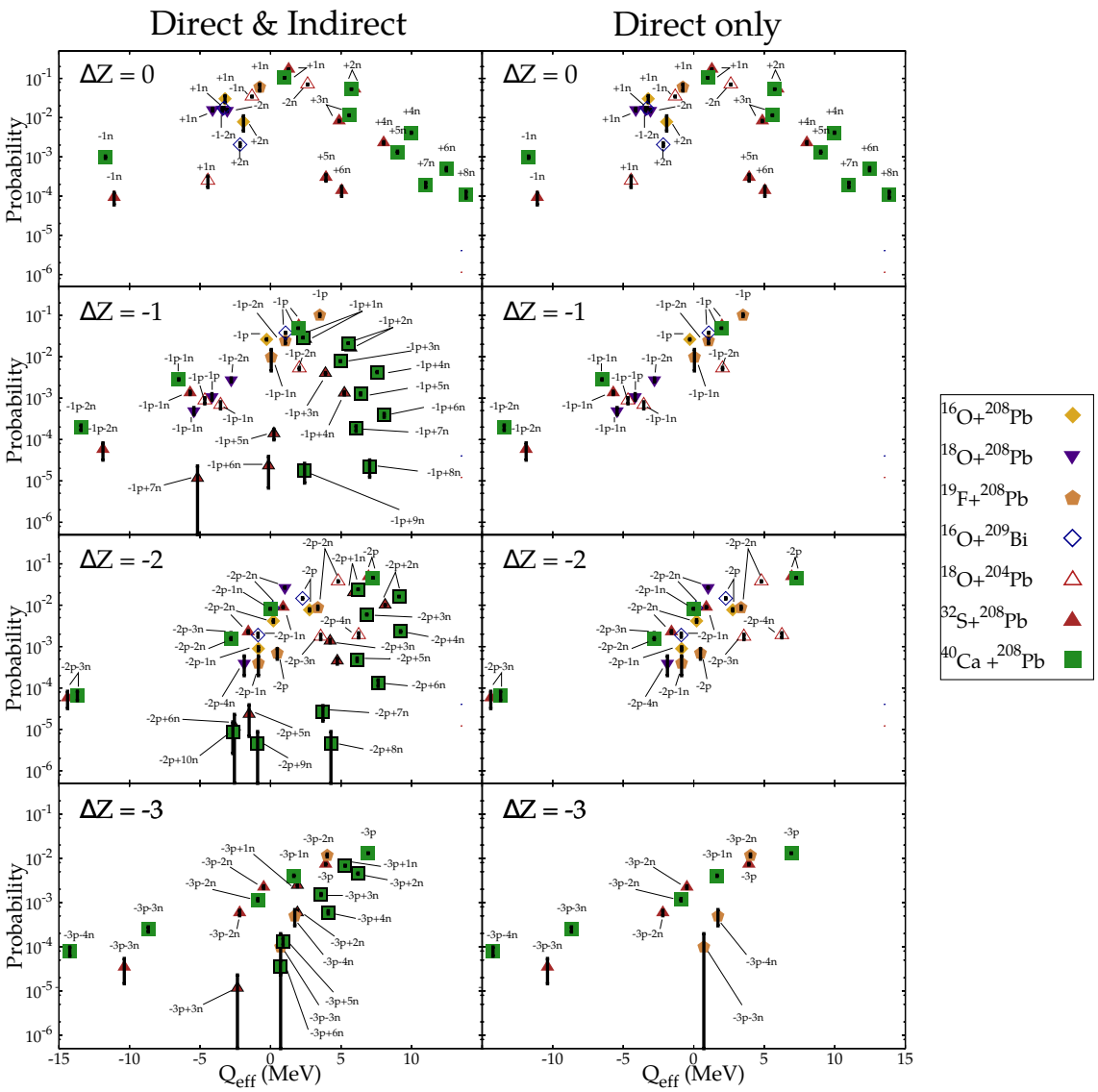

FIGURE 5.1: (Left panels) Comparison of the probabilities for different transfer modes as a function of the effective Q-value for all of the reaction systems studied at $\sim$ 95% of the respective barrier energy (see text). Transfer modes are displayed in different panels vertically according to the number of charge units exchanged. Indirect modes are highlighted by black borders around the points. (Right panels) Same as left panels but indirect modes are excluded to emphasize the correlation between transfer probabilty and Q_{eff} which can be observed when direct transfer modes are considered in isolation.

stripping -2p) separately from those that are *indirect* (where the nucleon flux is in both directions, and therefore cannot be conceived of as a one-step process- e.g. stripping of one proton and pickup of two neutrons -1p+2n). In the left panels, all of the observed transfer modes are included (both direct and indirect), whilst in the right panels only direct modes are displayed. Examining first the left panels, there does not appear to be a

correlation between Q_{eff} and the absolute probabilities of each transfer mode. However, when direct modes are considered in isolation, it can be seen that there is a clear positive correlation. This correlation appears to become weaker as the number of protons transferred increases, and importantly only appears to be present in the modes that involve at least one unit of charge transfer. Those modes in which there is a transfer of nucleons in both directions (in the terminology that will be used in the rest of this thesis, indirect), the transfer probabilities do not fit into these systematics, and appear to be affected mainly by the number of nucleons transferred.

5.3 Analysis of Q-integrated transfer probability

To obtain a full picture of the effects of transfer on fusion and its relation to the dissipation of kinetic energy from the relative motion, it is important to understand the energy dependence of these processes. This allows us to build an idea of what processes occur in the barrier region as well as at large separations that might have a bearing on the fusion mechanism. Furthermore the energy dependence is required for extrapolation of the transfer probabilities to the barrier radius for use in phenomenological models [138, 139] which include transfer channels.

Here I consider the global behaviour of the reflected flux for the reactions under study, and how it varies with internuclear separation. In order to compare different reactions, the surface separation parameter Δ is used (Equation 2.11), as it eliminates the dependence on the reactant masses [134, 140, 141].

The total quasielastic scattering cross sections (elastic + inelastic + transfer) as a fraction of those for Rutherford scattering are shown in Figure 5.2(a). The total probability for transfer as a function of the surface separation is shown in Figure 5.2(b). As the internuclear separation is reduced there is a corresponding reduction in the quasielastic flux due to increased fusion. At large distances, the total transfer probability depends exponentially on the internuclear separation. The total transfer probability increases as Δ is reduced before saturating near the barrier energy, where it is $\sim 50\%$ of the total, and then

falling for smaller Δ due to the increasing probability for fusion. The transfer channels become an increasingly large fraction of the backscattered flux as Δ is reduced.

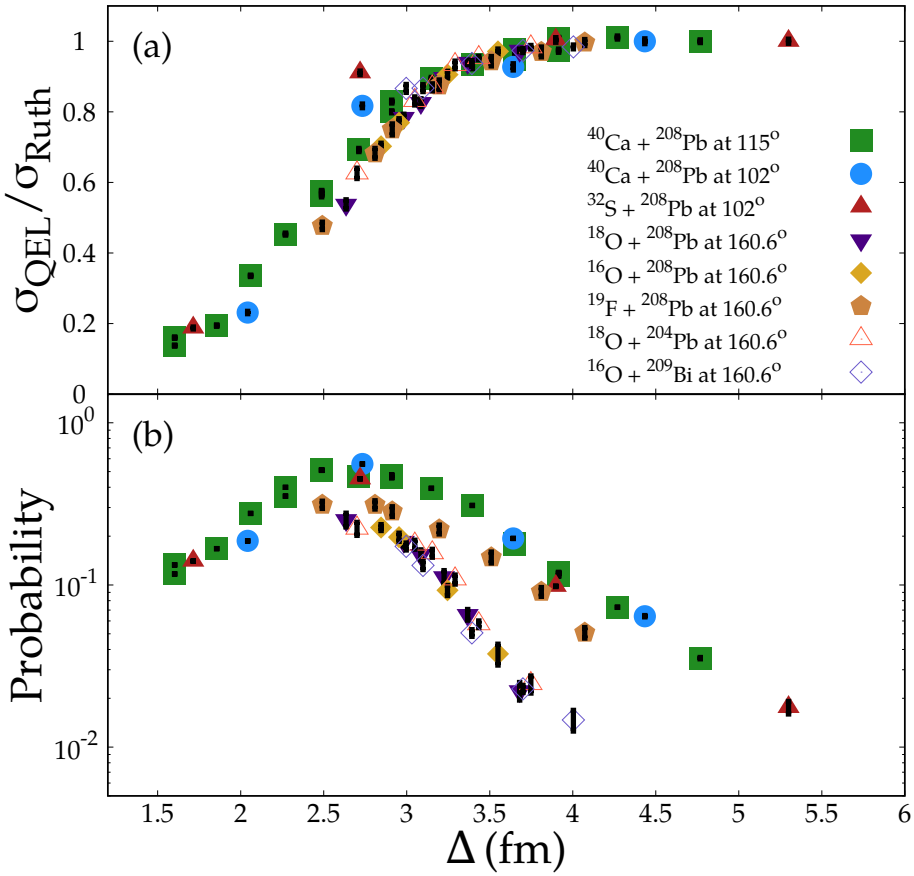

FIGURE 5.2: **(a)** Ratio of quasielastic scattering to Rutherford scattering, $\sigma_{QE}/\sigma_{Ruth}$ as a function of the surface separation parameter Δ (see text) for all of the systems studied in the two experiments. **(b)** The probability for transfer processes, summed over all modes. Symbols correspond to the key shown in (a).

The systematic trends are broadly the same for all of the reactions studied. The ^{19}F-induced reaction (orange pentagons) has a markedly higher probability for transfer than those of ^{16,18}O. At large Δ the ^{19}F + ^{208}Pb system behaves similarly to the sulfur and calcium projectiles, whilst at smaller separations looks more like the lighter projectiles. As will be shown later in Figure 5.7, single proton stripping from the fluorine projectile is the dominant transfer mode in ^{19}F + ^{208}Pb. This difference in the transfer behaviour of Fluorine is likely associated with the single proton outside the Z = 8 shell. Despite this difference, the total quasielastic flux is very similar to the other reactions. Not only are a large number of multinucleon transfer channels observed, but they also represent a large

fraction of the backscattered flux close to the barrier energy.

In the following subsections, the measurements of each reaction are discussed on a case-by-case basis.

5.3.1 Results for ^{16}O + ^{208}Pb

Multinucleon transfer at sub-barrier energies in the ^{16}O + ^{208}Pb system has been the focus of several previous studies [81, 142, 143, 144]. With the enhanced mass resolution of the new ΔE-E detector used in the experiment described in Chapter 3, this system was measured again in order to clarify the trends of (in particular) the $\Delta Z = -2$ modes, and to extend these measurements to lower energies (larger r_{min}).

Figure 5.3 shows the most significant transfer channels identified in the ^{16}O + ^{208}Pb system, along with the results of the previous ANU experiment [81]. Figure 5.3(a) shows neutron transfer, with transfer of one and two neutrons from the target to the projectile being seen in the experiment. The blue line is a fit to the 1n data, and the red dashed line is the square of this, which is expected to correspond to a sequential transfer of two neutrons according to equation 2.49. The measured 2 neutron transfer is shown to exceed the square of the fitted 1n data by around an order of magnitude, though is in agreement with the calculated slope.

Figure 5.3(b) shows ΔZ = -1 products, in which the only ejectile significantly populated is ^{15}N, associated with single proton transfer. Other ΔZ = -1 products are too weak to separate in this reaction. Figure 5.3(c) shows ΔZ = -2 products. The -2p transfer exceeds the prediction of equation 2.49 (green dashed line). The -1p trend is indicated by the purple line for comparison. At the highest energies (smallest r_{min}) the -2p transfer is comparable in strength to -1p transfer. The -2p-2n transfer (unsurprisingly) also far exceeds the expectation of equation 2.49, and is stronger than -2p-1n transfer. Of particular note is the behaviour of the -2p and -2p-2n channels as the internuclear separation increases, where their probabilities become almost equal. Extrapolating to larger distances, it appears likely that the -2p-2n channel producing ^{12}C will become dominant over that producing ^{14}C. In the previous experiment with a similar experimental set-up [81], the

dominance of -2p over -2p-2n transfer was reported, but with improved mass resolution the low energy behaviour the low energy behaviour can be elucidated. At the fusion barrier the strongest channels are one nucleon stripping, followed by two-nucleon and -2p-2n stripping.

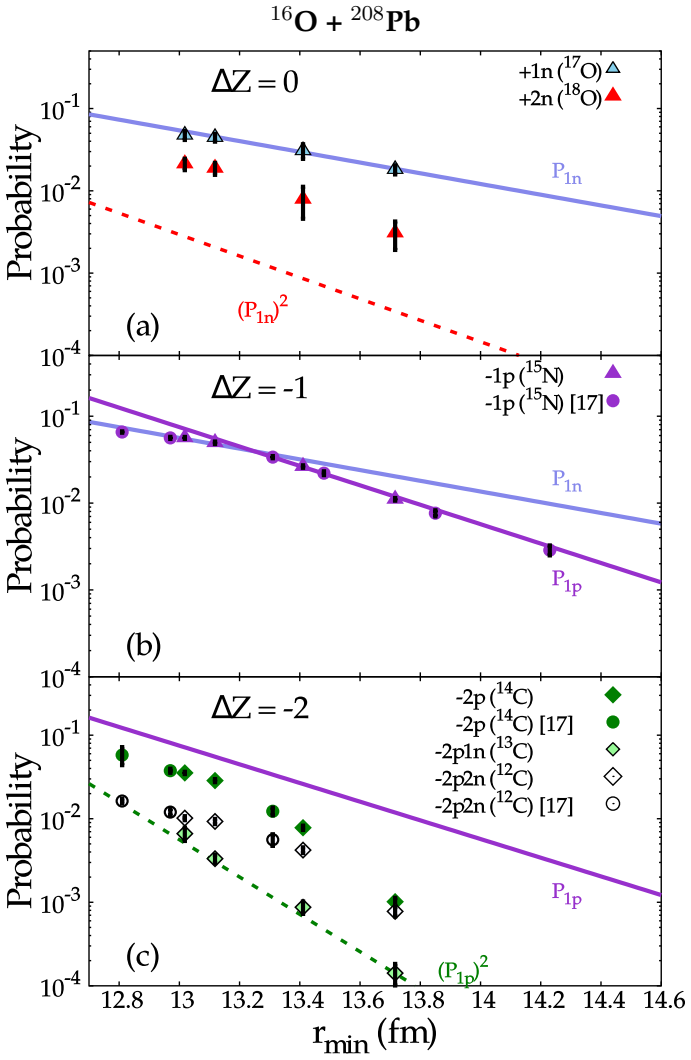

FIGURE 5.3: **(a)** Measured one and two neutron pickup probabilities. Blue line is a fit to the 1n transfer data (ΔN = +1), and the red dashed line is the expected pickup of 2 independent neutrons (ΔN = +2) according to equation 2.49. **(b)** One proton stripping probability as a function of the separation (triangles), along with those reported in Ref. [81] (circles). The purple line is a fit to the data in the range 13.1 fm $\leq r_{min} \leq$ 14.5 fm. **(c)** Measured ΔZ = -2 channels in this experiment (diamonds), along with those reported in Ref. [81] (circles). Shown again is the fit to the 1p stripping data shown in panel (b), along with its square (green dashed line), which is the expected probability of stripping of 2 independent protons according to equation 2.49.

5.3.2 Results for ^{16}O + ^{209}Bi

Figure 5.4 displays the results of the ^{16}O + ^{209}Bi measurement. It can be seen that the observed trends are very similar to those shown in Figure 5.3 with the ^{208}Pb target. There are a couple of points of difference that should be noted.

Some variation is observed in the extracted slope parameters α compared to the ^{208}Pb measurement- generally they are steeper with internuclear separation in this case, though the larger experimental uncertainties for the ΔZ = -2 modes make a conclusive comparison difficult.

This measurement extends further into the sub-barrier regime than the ^{16}O + ^{208}Pb case, with energies ranging from around 97 % to 90 % below barrier. As such, the effect of absorption levelling off the transfer probability at the smaller separations is not so obvious here. The observed trends fit very well with the expectation of an exponential falloff in the transfer probability with separation, in agreement with the expected transfer form factor from the semiclassical model (Equation 2.46 in Chapter 2).

An interesting feature to notice in this measurement is that the tendency of the -2p and -2p-2n modes to approach equivalence at larger separations (as noted in the ^{16}O + ^{208}Pb case) is repeated here. As this measurement extends further below barrier, there is indeed evidence of a crossing over, though the data points remain within error of one another.

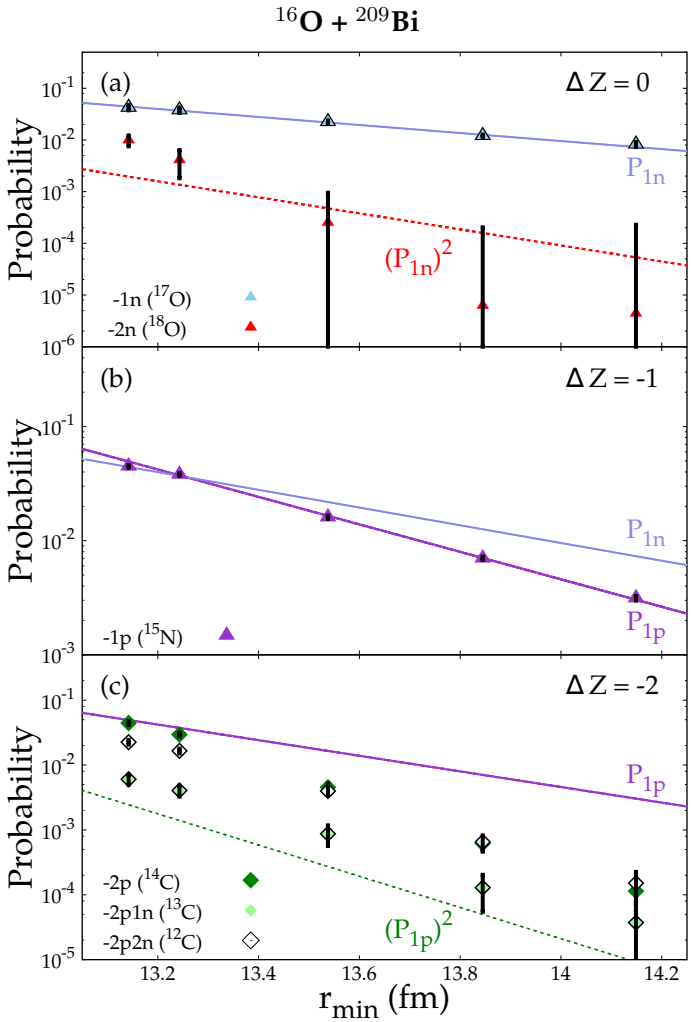

FIGURE 5.4: **(a)** Measured one and two neutron pickup probabilities. Blue line is a fit to the 1n transfer data ($\Delta N = +1$), and the red dashed line is the expected pickup of 2 independent neutrons ($\Delta N = +2$) according to equation 2.49. **(b)** One proton stripping probability as a function of the separation. The purple line is a fit to the data in the range 13.2 fm $\leq r_{min} \leq$ 14.3 fm. The fit to the -1n data (panel (a)) is also shown for comparison. **(c)** Measured $\Delta Z = -2$ channels. Shown again is the fit to the 1p stripping data shown in panel (b), along with its square (green dashed line), which is the expected probability of stripping of 2 independent protons according to equation 2.49.

5.3.3 Results for ^{18}O + ^{208}Pb

Figure 5.5 shows the measured transfer probabilities in the ^{18}O + ^{208}Pb system. In Figure 5.5(a), the experimental data for the observed -1n and -2n transfer is shown. The probability for -2n transfer is comparable to that of -1n neutron transfer. This behaviour has been observed previously in several reactions involving ^{18}O [145, 146], and is thought to

be due to the valence dineutron configuration in this nucleus, where the two neutrons outside the closed shell are weakly bound and easily removed. It is likely that the -2n transfer is underestimated here, as it is difficult to separate the ^{16}O yield arising from ground-state transfer from elastic scattering events, as there is some overlap in the ΔE-E_{Si} spectrum. The probabilities for transfer of a single neutron in either direction (pickup or stripping) appear to be very similar, as might be expected due to their similar Q-values (-3.412 and -4.108 for pickup and stripping respectively). For comparison, the measured trends for -2p-2n (the strongest transfer mode) and -1p are shown by the dashed green and solid purple lines respectively.

Figure 5.5(b) shows the mass partitions associated with single proton stripping. 1p stripping is comparatively weak in this reaction, with the -1p-2n transfer mass partition the most intense of the ΔZ = -1 modes at all separations. Similar behaviour in ^{18}O has been reported elsewhere [146], and was interpreted as being due to a correlated transfer of the three nucleons. As the internuclear separation is increased, this effect appears to be diminished, with the -1p-2n channel nearing equivalence to proton transfer at the lowest energy measured here. The -2p-2n trend is plotted here to emphasise the extent to which this transfer mode exceeds all of the ΔZ = -1 channels.

Figure 5.5(c) shows the data for ΔZ = -2. The -2p-2n channel is dominant over all others involving charge transfer in this system, over the entire energy range studied. The transfer products of -2p-3n and -2p-4n are weak, though comparable to -1p transfer, which is indicated by the full (purple) line.

5.3.4 Results for ^{18}O + ^{204}Pb

The extracted transfer probabilities for the ^{18}O + ^{204}Pb measurements are shown in Figure 5.6. Similar to the parallels between the ^{16}O reactions on ^{208}Pb and ^{209}Bi described in Section 5.3.2, the ^{18}O projectile exhibits almost identical behaviour between the ^{204}Pb and ^{208}Pb targets. The differing structure of the heavy reaction partner seems to play a relatively insignificant role in determining the important transfer modes, though has an effect on the absolute strength which can be related to the Q-value.

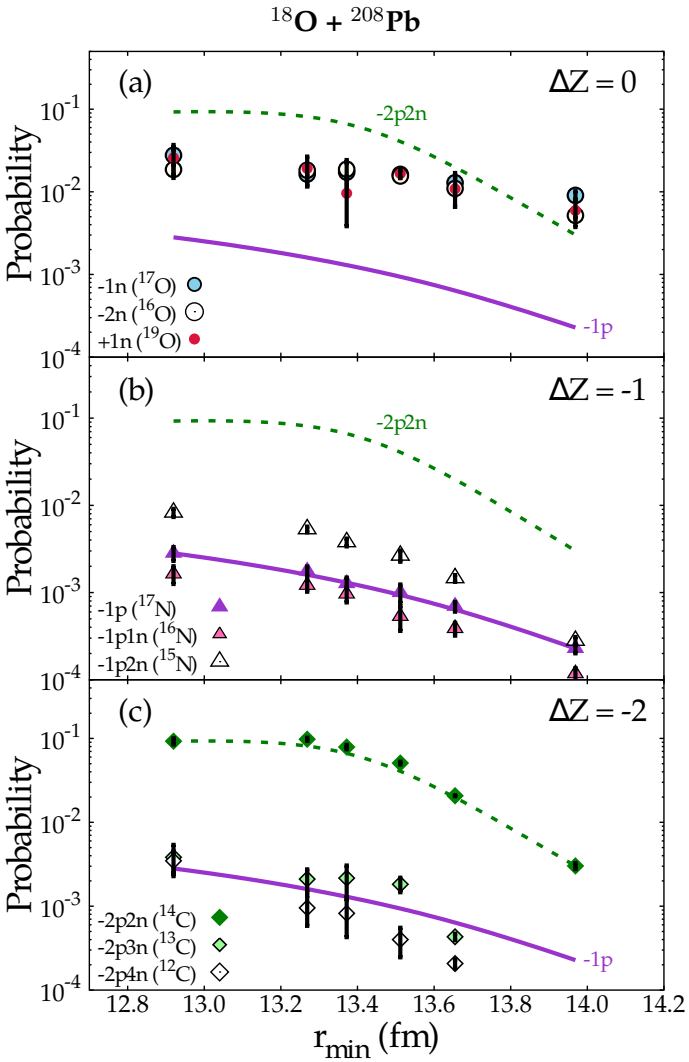

FIGURE 5.5: **(a)** Measured neutron transfer probabilities. The trends in the -1p and -2p-2n (α) modes are also shown for the sake of comparison by the solid purple and dashed green lines respectively. **(b)** Measured probabilities for channels involving the transfer of one proton, again with the -2p-2n and -1p trends for comparison. **(c)** ΔZ = - 2 channels, along with the measured -1p and -2p-2n trends.

The main point of difference to be observed in this reaction is that the -2n mode is slightly enhanced with respect to the ^{18}O + ^{208}Pb reaction, likely due to its positive Q-value (+2.631 MeV), resulting from the more neutron defficient ^{204}Pb target. As was described in Section 5.3.3, the obscuring effect of the elastic peak prevents an accurate extraction of the yields of the pure neutron stripping channels. The particle identification procedure (described in Section 3.3.3 of Chapter 3) was performed after making a cut around the elastic peak in the ΔE-E spectrum, with the selected events excluded from the subsequent fitting and gate determination processes. As some ^{16}O and ^{17}O products would

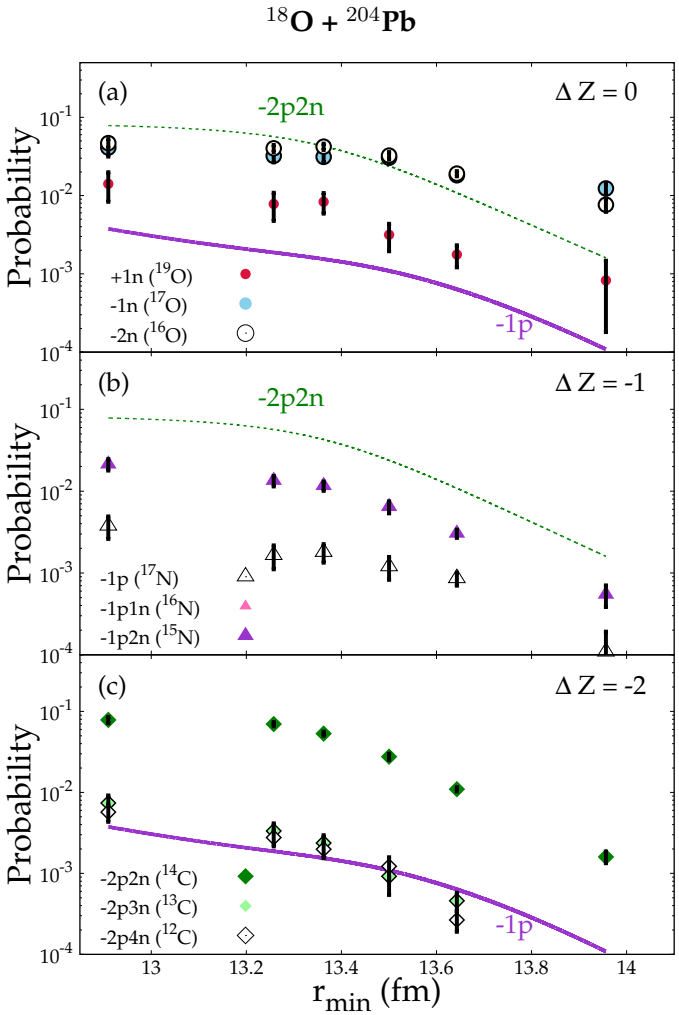

FIGURE 5.6: **(a)** Measured neutron transfer probabilities. The trends in the -1p and -2p-2n (α) modes are also shown for the sake of comparison by the solid purple and dashed green lines respectively. **(b)** Measured probabilities for channels involving the transfer of one proton, again with the -2p-2n and -1p trends for comparison. Note that the probabilities for -1p-1n fall outside the selected range. **(c)** ΔZ = - 2 channels, along with the measured -1p and -2p-2n trends.

also be expected to be in the vicinity of the excluded events, it is likely their yields (and consequently the extracted probabilities) are underestimated. Nonetheless, an increase in the relative yields of these two modes are both seen compared to the measurement on the ^{208}Pb target.

5.3.5 Results for ^{19}F + ^{208}Pb

Transfer probabilities for ^{19}F + ^{208}Pb are shown in Figure 5.7. In Figure 5.7(a), the data for 1n and 1p pickup is displayed. Neutron pickup, forming ^{20}F, is reasonably strong in this reaction, being comparable to 1p stripping, which is the strongest transfer mode, indicated in this panel by the full (blue) line. Charge pickup is present in this reaction, with a small yield of Z = 10 events observed at all bombarding energies. Several ΔZ = +1 channels have positive Q-values in this system, as shown in Table C.1 (see Appendix C). There are not sufficient statistics to conclusively separate these events by mass, though the +1p+2n pickup mode has the most favourable Q-value conditions.

In this system, one proton stripping is by far the strongest mode involving charge transfer. Figure 5.7(b) shows ΔZ = -1 transfer modes. The production of ^{16,17,18}O are observed, with single proton transfer being strongest. Significantly, -1p-2n transfer is stronger than -1p-1n over the entire range of distances except at the lowest energy.

Figure 5.7(c) shows -2p-2n transfer to be the most significant ΔZ = -2 mode, which also exceeds all ΔZ = - 1 channels other than single proton stripping. The -1p transfer trend is indicated by the solid blue line for comparison. Very few events corresponding to -2p or -2p-1n transfer are seen: in fact ^{15}N has a significantly more favourable Q-value and is produced with by far the highest abundance of all nitrogen isotopes. This may also be in part due to the low neutron separation thresholds in ^{17}N (5.88 MeV) and ^{16}N (2.49 MeV), meaning a contribution from evaporation to the high ^{15}N yield. However, any such contribution is likely to be very small on the basis of Q-value considerations.

Figure 5.7(d) displays the ΔZ = - 3 modes, of which -3p-2n is very prominent. For comparison, the -1p and -2p-2n trends are indicated by the blue solid and purple dash dotted lines, respectively. Transfer producing ^{14}C is almost as likely as -2p-2n at intermediate energies, before the -3p-2n probability falls off quickly at larger separations. The enhancement of the -3p-2n channel was found at higher energies in Ref. [147], which was interpreted as some kind of correlated p-α transfer. However, these results show that the ^{14}C yield is much diminished at the largest separations, and it seems that the behaviour of

this channel might also have a contribution from a more complex transfer + evaporation mechanism, as will be described in Section 5.4.2.

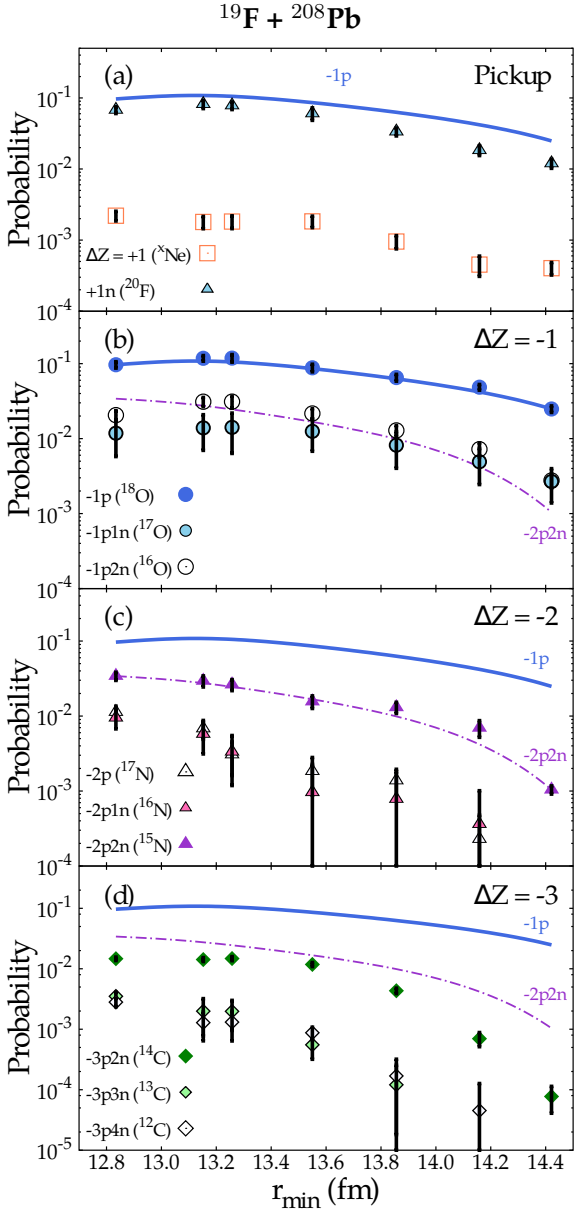

FIGURE 5.7: **(a)** One proton and one neutron pickup probabilities. Note that the Neon products cannot unambiguously be separated in mass, so the square symbols represent the total ΔZ = +1 probabilities. **(b)** Measured ΔZ = -1 probabilities. Solid blue line and dashed blue line indicate -1p and -1p-2n trends to guide the eye. **(c)** ΔZ = -2 probabilites. Shown also are the trendlines of the most significant ΔZ = -1 modes for comparison, with the trend in -2p-2n indicated by the purple dash dotted line. **(d)** ΔZ = -3 probabilities, along with the most significant ΔZ = -1 and ΔZ = -2 trends for comparison.

5.3.6 Results for ^{32}S + ^{208}Pb

The limited time available for the measurement of the ^{32}S + ^{208}Pb system using PRISMA meant that it was only possible to make measurements at four bombarding energies. These measurements were taken at energies corresponding to $0.8V_B$, $0.88V_B$, $0.96V_B$ and $1.03V_B$. At the lowest energy, no significant yield involving the transfer of protons was observed, though there was a reasonable yield of one and two-neutron pickup from the target.

Whilst the small number of measurements spanning the barrier energy is sufficient to examine the variation of the dissipation with bombarding energy, the few measurements below the barrier means it is not possible to perform a slopes analysis of the transfer probabilities in the manner conducted for the other systems. As such it is not possible to conclusively determine the presence or otherwise of correlations between transferred particles or cluster transfer processes. For this reason the transfer probabilities are not presented as a function of r_{min}, but are displayed as a function of the surface separation Δ alongside the other systems in Figure 5.10.

Comparing Figure 5.14 with, for instance, Figure 5.12, the distribution of the transfer products in atomic mass A and charge Z is much smoother, with none of the transfer modes exhibiting an obvious enhancement such as the ^{14}C yield in the ^{18}O + ^{204,208}Pb reactions. In fact the Z vs. A distribution of the ^{32}S + ^{208}Pb transfer products appears much more similar to that of the ^{40}Ca + ^{208}Pb system than to any of those involving the lighter projectiles. Indeed one of the notable features of the product distributions as the mass of the projectile increases is for the distribution to become more extensive, vary smoothly with both A and Z, and for sharp peaks (indicative of cluster dynamics) to be washed out.

5.3.7 Results for ^{40}Ca + ^{208}Pb

Measurements were made for ^{40}Ca + ^{208}Pb with the PRISMA device positioned at two mean scattering angles θ_{PRISMA} (i.e. the angle corresponding to beam trajectories entering the quadrupole magnet along the optical axis of the spectrometer) of 115° and 102°. In the former case the transfer excitation functions were measured with small energy increments over a reasonably wide range of values, spanning from $\sim$ 103% to $\sim$ 83% of the barrier energy (once the centrifugal shift is accounted for). This large dataset permits an analysis of the slopes of the exponential falloff of the transfer probability with the distance of closest approach, in the manner done for the lighter systems studied in the ANU experiment.

Unfortunately, a drawback of the experimental design results in diminishing quality of the atomic number Z separation of the reaction products with decreasing bombarding energy. The reason for this is that for a given measurement, the maximal separation of ions in Z is achieved by adjusting the gas pressure in the IC array such that the most energetic particles (likely to be elastics) are stopped in the final layer of the array. This provides the largest possible effective thickness of the gas to provide the ΔE signal, and maximal distinction between different elements. Despite this procedure for optimizing the Z-resolution in each measurement, it nethertheless is reduced due to the overall reduction in the effective gas length. This means that a limit is reached at which it becomes impossible to separate ions using a fitting method such as that described in Section 3.3.3.

The poor Z-separation which persisted for many of the measurements in the deep subbarrier region meant that there were inevitably contaminations from adjacent elements that would be carried through from the Z-selection stage of the analysis procedure (described in Section 4.5.2) to the charge state selection stage (described in Section 4.5.3). Some of the contaminations can be rejected at this point where they do not obviously corresponds to the groups of events that are otherwise observed in the spectra of E_{IC} vs. $R\beta$. In the case of the lowest energy measurements however, it was impossible to prevent contaminations showing up in the final product yields.

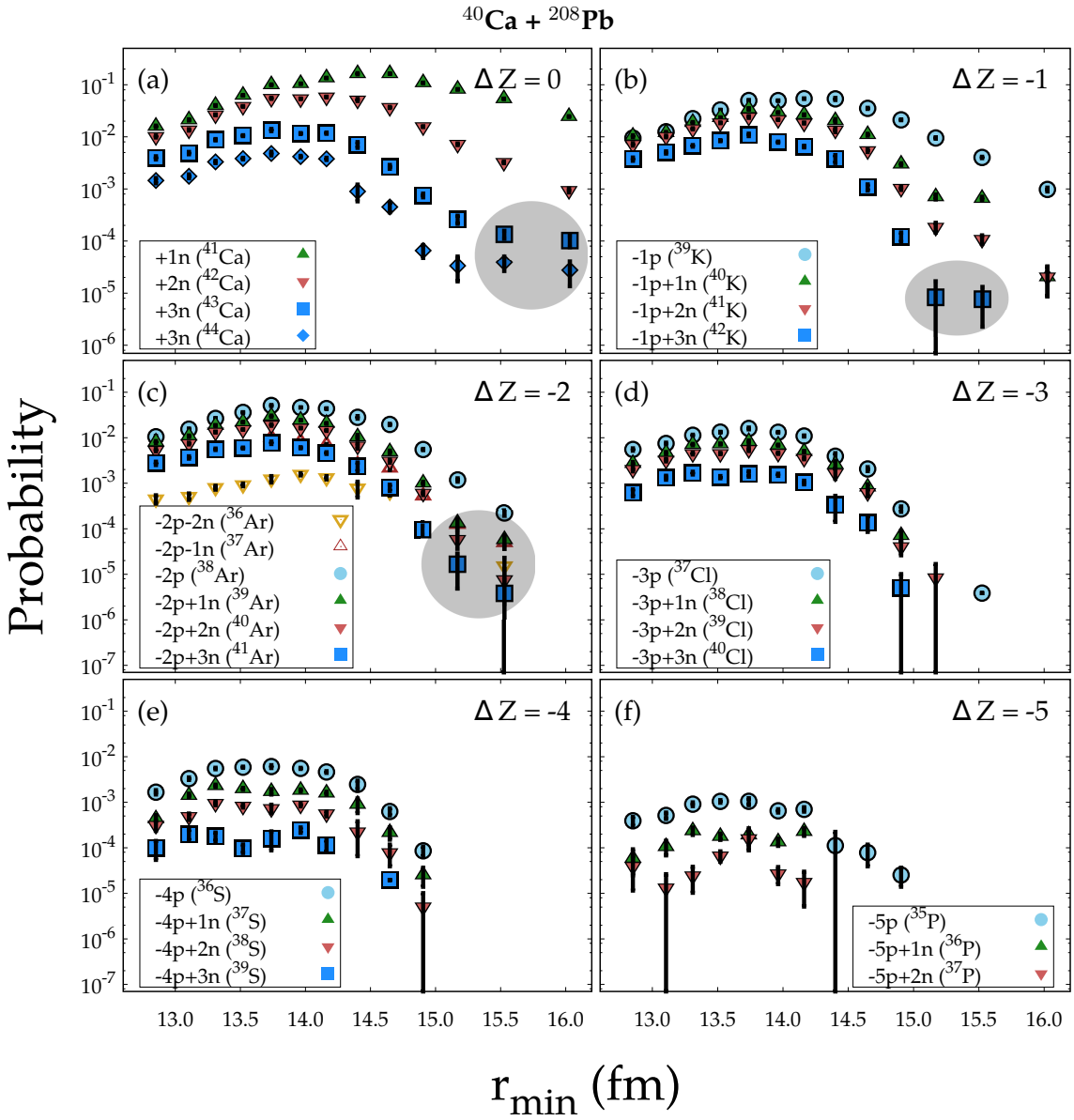

FIGURE 5.8: Measured Q-integrated probabilities of transfer modes in ^{40}Ca + ^{208}Pb. Transfer modes involving the exchange of different numbers of protons are shown in separate panels. The number of protons transferred is indicated in the upper right of each panel by the ΔZ value. Highlighted by the grey areas are points for which the extracted transfer probabilities are not held in confidence, due to the suspected presence of contaminants from adjacent ΔZ transfer modes (see text).

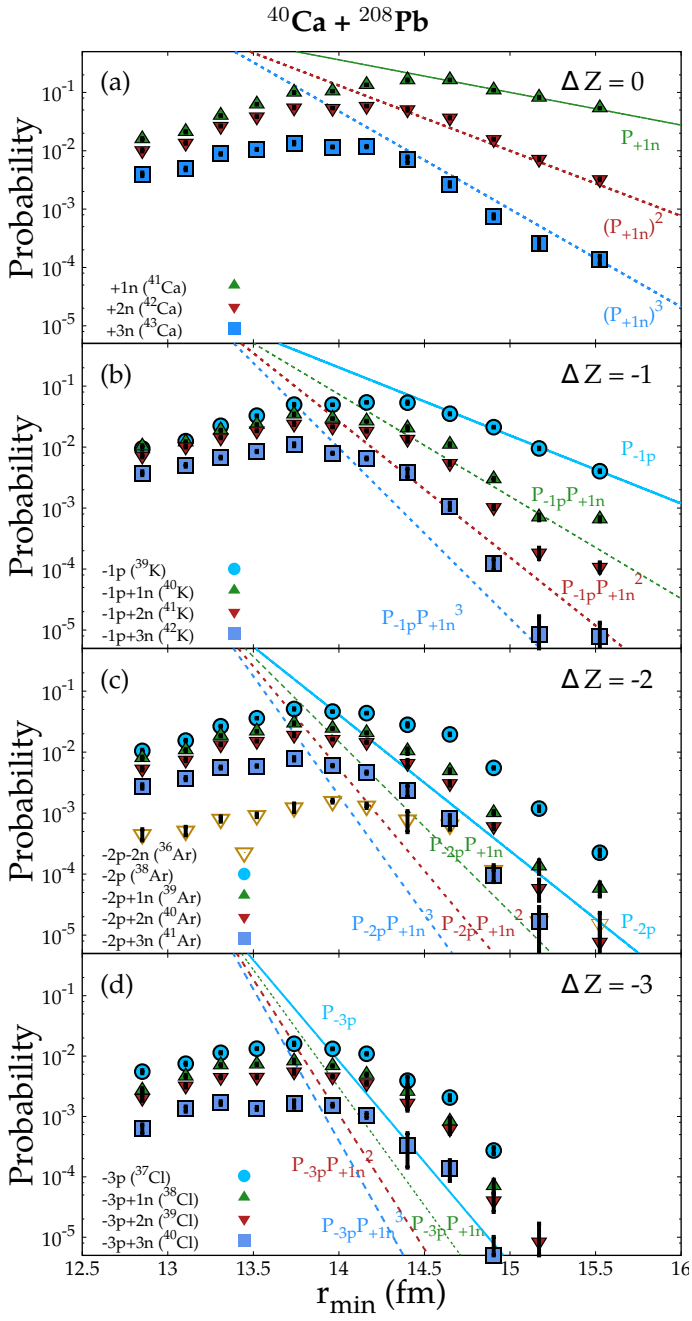

FIGURE 5.9: Measured Q-integrated probabilities of selected transfer modes in ^{40}Ca + ^{208}Pb. A reproduction of the data shown in Figure 5.8, where transfer modes up to $\Delta Z = -3$ are compared with the expectations of Equation 2.49, assuming a purely successive mechanism for multinucleon transfer.

Contaminants can be further minimized by examining the E_x spectra for each of the energy measurements. Where events have been assigned an incorrect value of Z, the subsequent calculation of the Q-value from the measured energy is also incorrect. In

some cases, this can result in the calculation of the E_x yielding values that are negative far beyond the width of the elastic peak. These events are all rejected, reducing the contaminants in the product yields and thus restoring the deduced transfer probabilities to a value closer to the true value.

Despite these efforts to reduce contaminants, it is impossible to reduce them completely, and as a result many of the transfer probabilities that are extracted at the lowest energies cannot be held in great confidence. This can be seen very clearly in Figure 5.8, where the measurements at the largest separations (lowest energies) appear to depart from the expected exponential decrease with increasing r_{min}— these measurements are highlighted in Figure 5.8 by the grey circles. For this reason, in the extraction of slopes, only the values of P_{Tr} at distances r_{min} between 14.5 and 15.5 fm are considered in the fitting procedure. This range was chosen to ensure that all considered values were well below (< 90%) the barrier, where the falloff in the excitation functions could be expected to be truly exponential, whilst also avoiding the problems with Z selection that troubled the lowest energy measurements (and would otherwise affect the experimental slopes, which were extracted by fitting the data). In practice this meant that it was only possible to extract experimental slopes for transfer modes up to ΔZ = -3 for the θ_{PRISMA} = 115° setting, as all modes involving larger charge transfer were not observed at separations beyond around 15 fm. Only those modes for which there were at least three measurable values of P_{Tr} between the stated range of internuclear separations r_{min} are listed in Table C.1 (see Appendix C).

It is clear from Figure 5.8 that, compared to the lighter projectiles, ^{40}Ca + ^{208}Pb exhibits very many open channels even in the sub-barrier regime (i.e. permitted according to Q-window considerations), and a vast array of ejectile nuclides are observed. Figure 5.9 displays separately the most prominent observed transfer modes for this system for each charge transfer mode, where the data are compared with the expectations of successive nucleon transfer based on a simple product of the probabilities for single proton and neutron transfer in the sub-barrier region. These are based on fitting the single nucleon transfer probabilities in the manner described in the previous paragraph, similar to the analyses performed on the lighter systems. Notably, the transfer of up to three neutrons

follows almost exactly the expected systematics in this picture. On the other hand, the probabilities for transfer modes involving charge transfer depart immediately from those systematics where more than one charge unit is transferred.

Two proton stripping exhibits a marked enhancement over the successive transfer prediction, similar to what was observed in the reactions with the ^{16}O projectiles, indicating a possible contribution to the yield from a direct transfer of two correlated protons. There is no apparent enhancement of the -2p-2n mode, which in fact presents very weakly, and as such no evidence for α-cluster transfer in this system. The cause of the enhancement relative to the successive limit, in the case of those transfer modes in which the neutrons and protons move in opposite directions (e.g. stripping of two protons and pickup of one neutron), cannot be attributed to correlated nucleon or cluster transfer as such dynamics cannot be conceived. The enhancement must therefore be attributed to a transfer mechanism that is neither direct, nor due to nucleon correlations. As will be shown in later sections, these modes are typically associated with large kinetic energy losses (and hence excitation energies in the outgoing fragments), which is remarkable for the fact that such modes are identified with a large fraction of the product yield even at bombarding energies quite far below the barrier, a characteristic typically attributed to deep-inelastic processes in which frictional forces cause a longer reaction time, the transfer of a larger number of nucleons, and damping of the initial kinetic energy into internal degrees of freedom.

5.3.8 Comparison of the distribution of transfer products between systems, and the evolution with bombarding energy

Having discussed the unique features exhibited by the different reaction systems, the global evolution of the transfer dynamics between reactions involving light and medium mass nuclei can be examined.

This evolution can be visualised though plotting transfer probabilities (colour scale) as a function of ejectile mass and charge as shown in Figs. 5.11-5.13 for the ^{16}O + ^{208}Pb, ^{209}Bi, ^{18}O + ^{204}Pb, ^{208}Pb and ^{40}Ca + ^{208}Pb systems. This subset has been chosen to show the

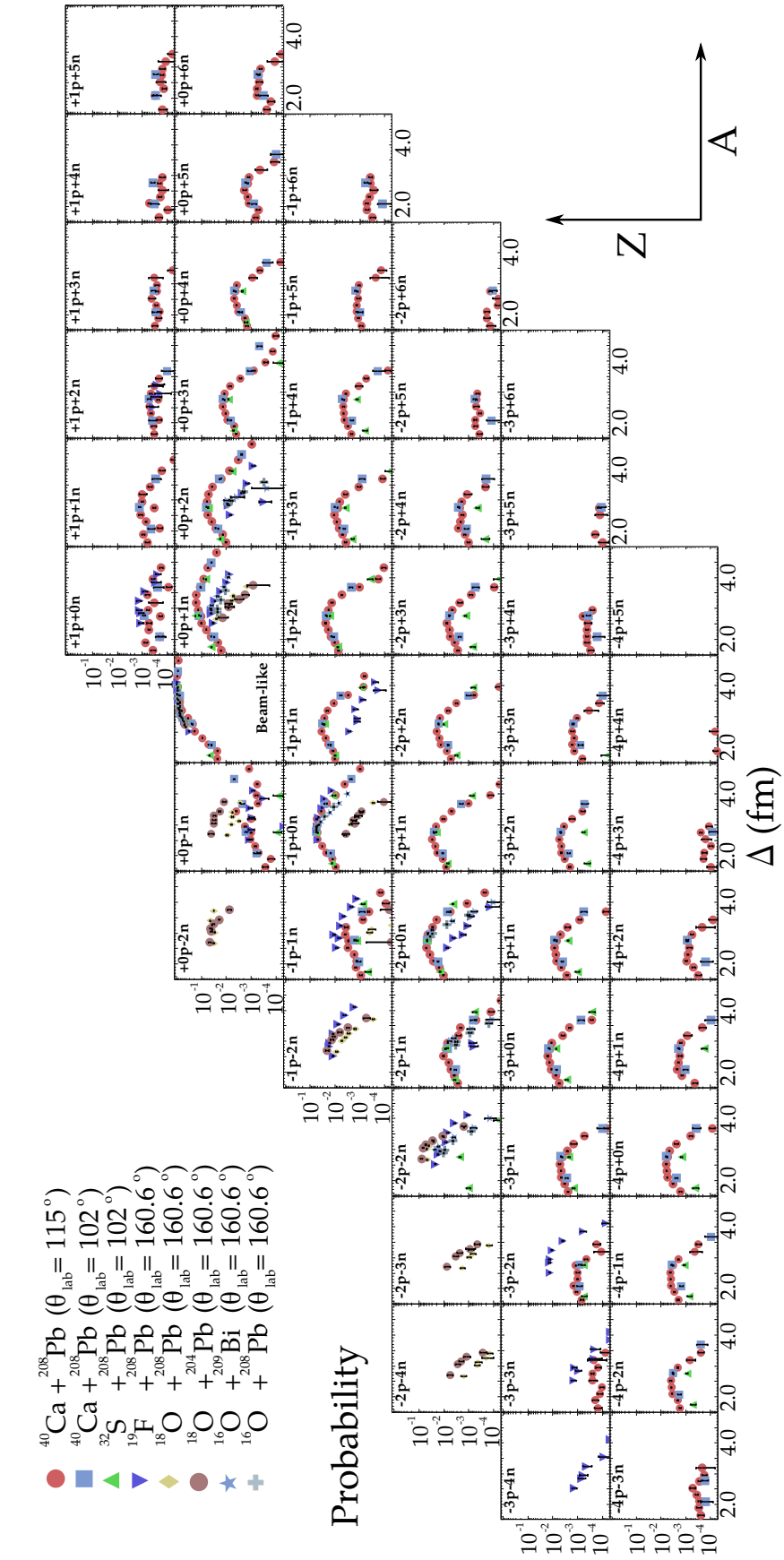

FIGURE 5.10: Comparison of the probabilities for a subset of the observed transfer modes between the systems studied, as a function of the surface separation parameter Δ. The subset is chosen such that at least two of the measured systems exhibit that particular transfer mode, allowing a comparison to be made by the reader. As such, measurements of more than four proton stripping are not shown (though are observed in the ^{40}Ca + ^{208}Pb cases).

changes in going from the lightest to the heaviest projectile studied in this work, and to highlight unique features in particular systems. Plots for the ^{19}F + ^{208}Pb and ^{32}S + ^{208}Pb show similar general features, and are presented in Appendix C.

In Figs. 5.11-5.13, the dashed white lines show the changes in A and Z of the projectile-like nucleus following pure neutron (marked ΔN) and pure proton transfer (marked ΔZ). The solid white lines are the N/Z ratios of the compound nucleus that would be formed for each system, if fusion were to occur. As will be discussed below, mass and charge drift towards the solid line shows exchanges as the system evolves towards (mass and charge) equilibration. For a given column of panels, beam energy increases from the bottom to the top. The most intense feature (red) at sub-barrier energies in all the panels is naturally elastic scattering. Other common features are: (i) an increase in the range of transfer products with increasing beam energy (compare bottom to top panels), (ii) an increase in the range of transfer products with increasing charge product (compare Fig. 5.10 with Fig. 5.13), and (iii) the transfer probabilities gets smoother (i.e. less variation in the colour scale) with increasing number of transferred nucleons. There are clear exceptions to point (iii), as the -2p-2n mode in ^{18}O-induced reactions (Fig. 5.11) is dominant amongst neighbouring nucleon transfer modes. As has been discussed previously, this is indicative of cluster or correlated-nucleon transfer mechanisms. It appears that this is only an important factor in the reactions of the lightest nuclei, despite the α-conjugation of the ^{32}S and ^{40}Ca nuclei.

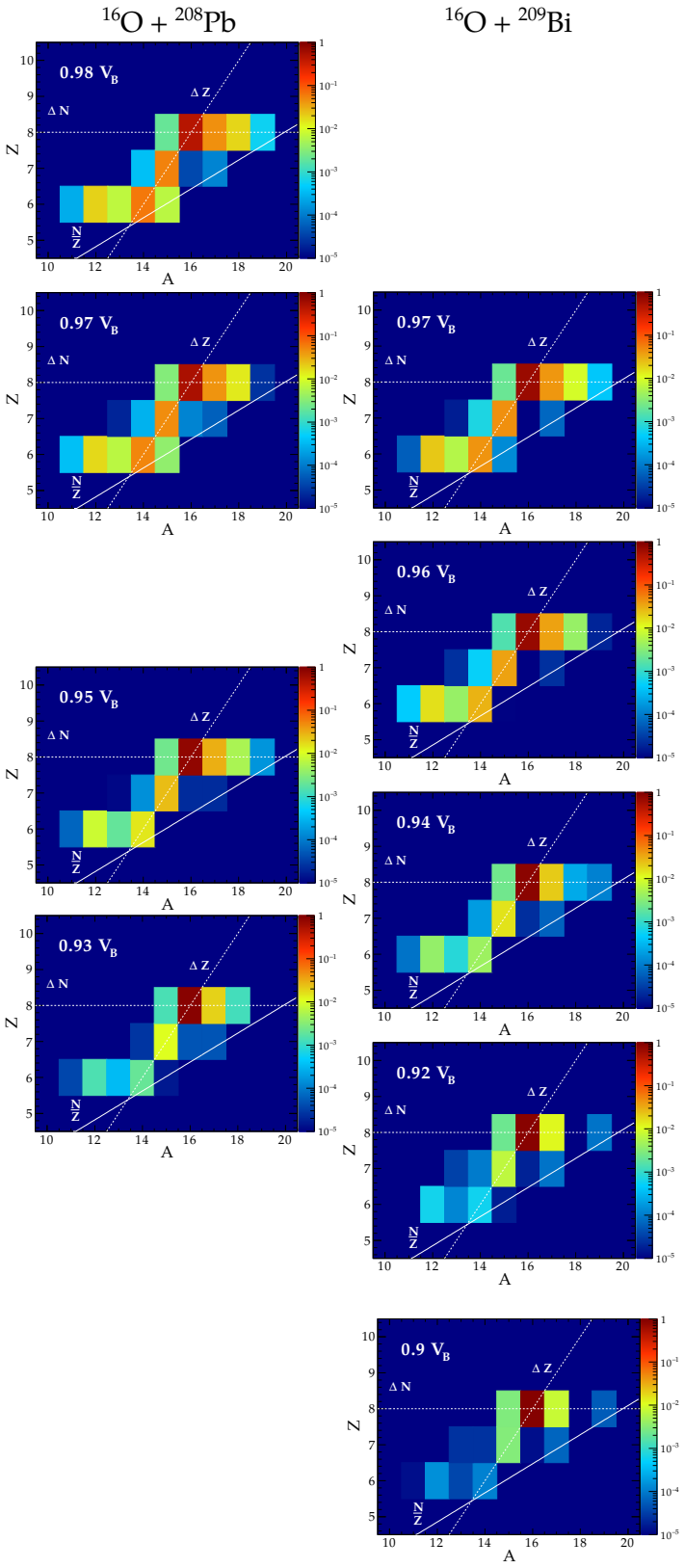

FIGURE 5.11: Transfer probability as a function of the ejectile mass A and atomic number Z for each energy measurement for the ^{16}O + ^{208}Pb (left column) and ^{16}O + ^{209}Bi (right column) systems. In each panel, the solid white line shows the N/Z ratio of the compound nucleus that would be formed in the reaction were fusion to occur. The dashed white lines show the directions in A and Z in which the projectile properties change following pure neutron and proton transfer. The bombarding energy relative to the barrier E/V_B is indicated in each panel.

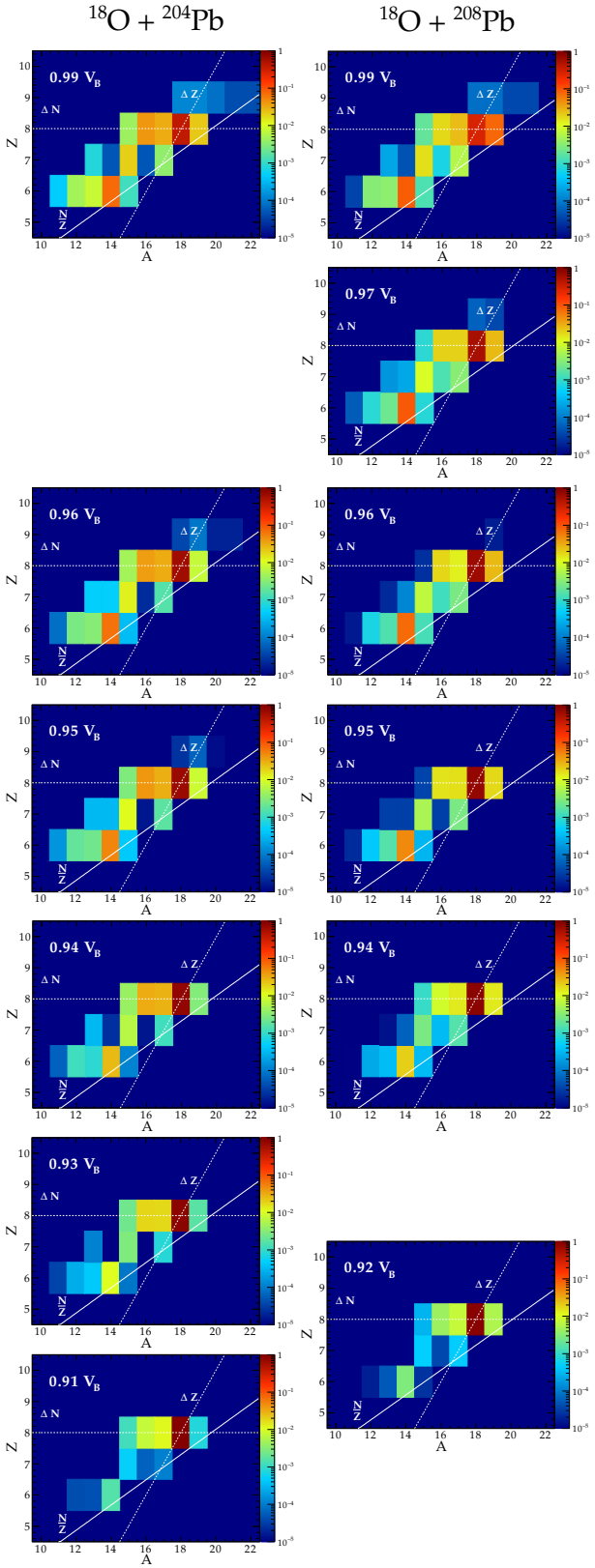

FIGURE 5.12: Transfer probability as a function of the ejectile mass A and atomic number Z for each energy measurement for the ^{18}O + ^{204}Pb (left column) and ^{18}O + ^{208}Pb (right column) systems. In each panel, the solid white line shows the N/Z ratio of the compound nucleus that would be formed in the reaction were fusion to occur. The dashed white lines show the directions in A and Z in which the projectile properties change following pure neutron and proton transfer. The bombarding energy relative to the barrier E/V_B is indicated in each panel.

As has been discussed in Section 5.2, in this thesis the interpretation distinguishes between *direct* modes where the nucleon flux is in one direction only (and can conceivably occur as a one-step direct transfer of a single or multiple nucleons), and *indirect* modes in which nucleons are donated and received by both reactants. Whilst a (near-)simultaneous mutual exchange of nucleons in the peripheral scattering region (where the ion densities barely overlap) is certainly conceivable, it has been shown already, and will be emphasized in later sections, that direct and indirect events exhibit very different characteristics. It can be seen that in moving from the lighter to the heavier systems, an increasing proportion of the yield is populated by fragments that are closer to the charge equilibration of the compound nucleus (solid white lines) than the projectile nucleus. It will be shown in later sections that these products are typically associated with large energy losses. These are characteristics typical of a deep-inelastic reaction mechanism [83]. It is remarkable that in the ^{32}S + ^{208}Pb and ^{40}Ca +^{208}Pb systems such events make a dominant contribution to the product yield even reasonably far below the barrier energy.

The transfer modes of the different reaction systems can be compared directly by comparing their probabilities as a function of the surface separation Δ, as shown in Figure 5.10, for transfer modes that are present in more than one system. A notable feature is that many modes in the ^{32}S + ^{208}Pb and ^{40}Ca + ^{208}Pb systems display remarkably similar behaviour (at least for modes closer to the beam-like ions), whilst the lighter systems behave very differently to each other and to the heavier systems, though transfer probabilities for the same projectile nucleus on different targets are almost identical.

Figure 5.2 demonstrated that the total transfer probability (and hence cross section) generally increases for heavier systems, and indeed this appears to be the case in general for each mode as is seen in Figure 5.10. However there are notable exceptions to this trend, as nuclear structure plays an important role in determining the dominant transfer mechanism. The ^{19}F + ^{208}Pb system has a very strong 1p stripping mode, which is likely due to the shell structure of the ^{19}F nucleus, where a single proton occupies the 1d shell outside a semi-magic ^{18}O core. Similarly the very strong -2p-2n stripping mode in the ^{18}O-induced reactions may be attributed to a cluster structure in the ^{18}O nucleus. In addition, the -2n stripping mode is equivalent in strength to single neutron stripping,

in support of a picture of the ^{18}O nucleus having paired valence neutrons which can be transferred in a correlated manner (an exhibition of nuclear superfluidity). This is a very good example of the quantum superposition of different structures that exist in nuclei.

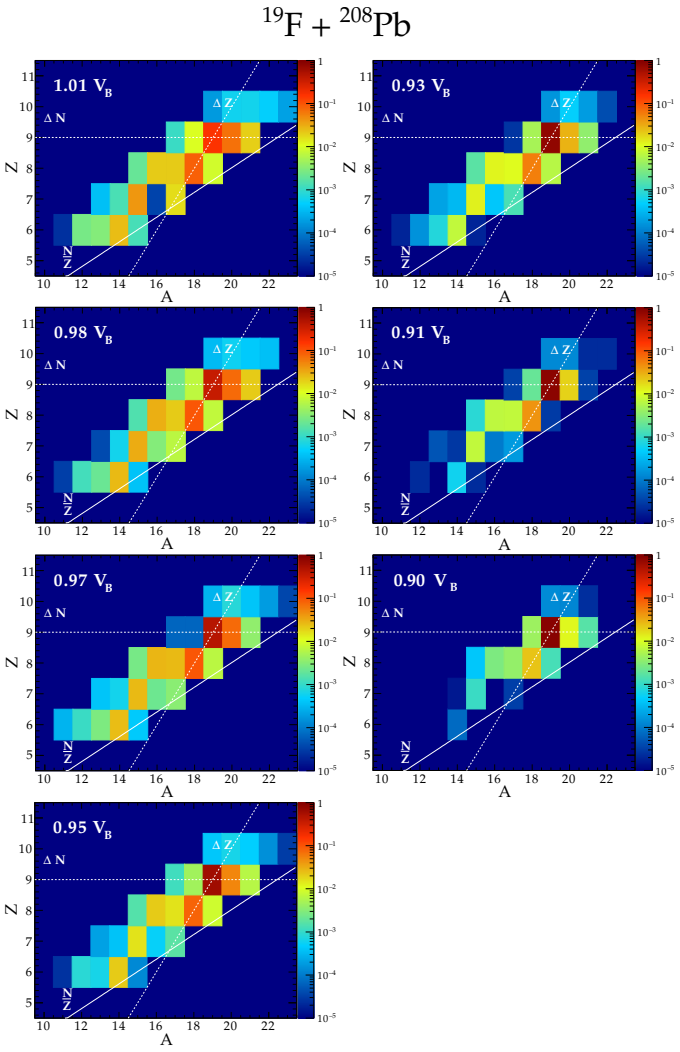

FIGURE 5.13: Transfer probability as a function of the ejectile mass A and atomic number Z for each energy measurement for the ^{19}F + ^{208}Pb system. In each panel, the solid white line shows the N/Z ratio of the compound nucleus that would be formed in the reaction were fusion to occur. The dashed white lines show the directions in A and Z in which the projectile properties change following pure neutron and proton transfer. The bombarding energy relative to the barrier E/V_B is indicated in each panel.

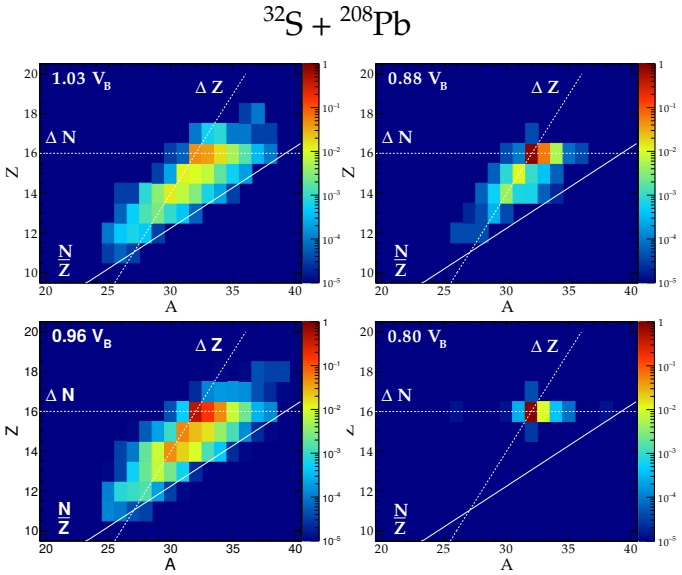

FIGURE 5.14: Transfer probability as a function of the ejectile mass A and atomic number Z for each energy measurement for the ^{32}S + ^{208}Pb system. In each panel, the solid white line shows the N/Z ratio of the compound nucleus that would be formed in the reaction were fusion to occur. The dashed white lines show the directions in A and Z in which the projectile properties change following pure neutron and proton transfer. The bombarding energy relative to the barrier E/V_B is indicated in each panel.

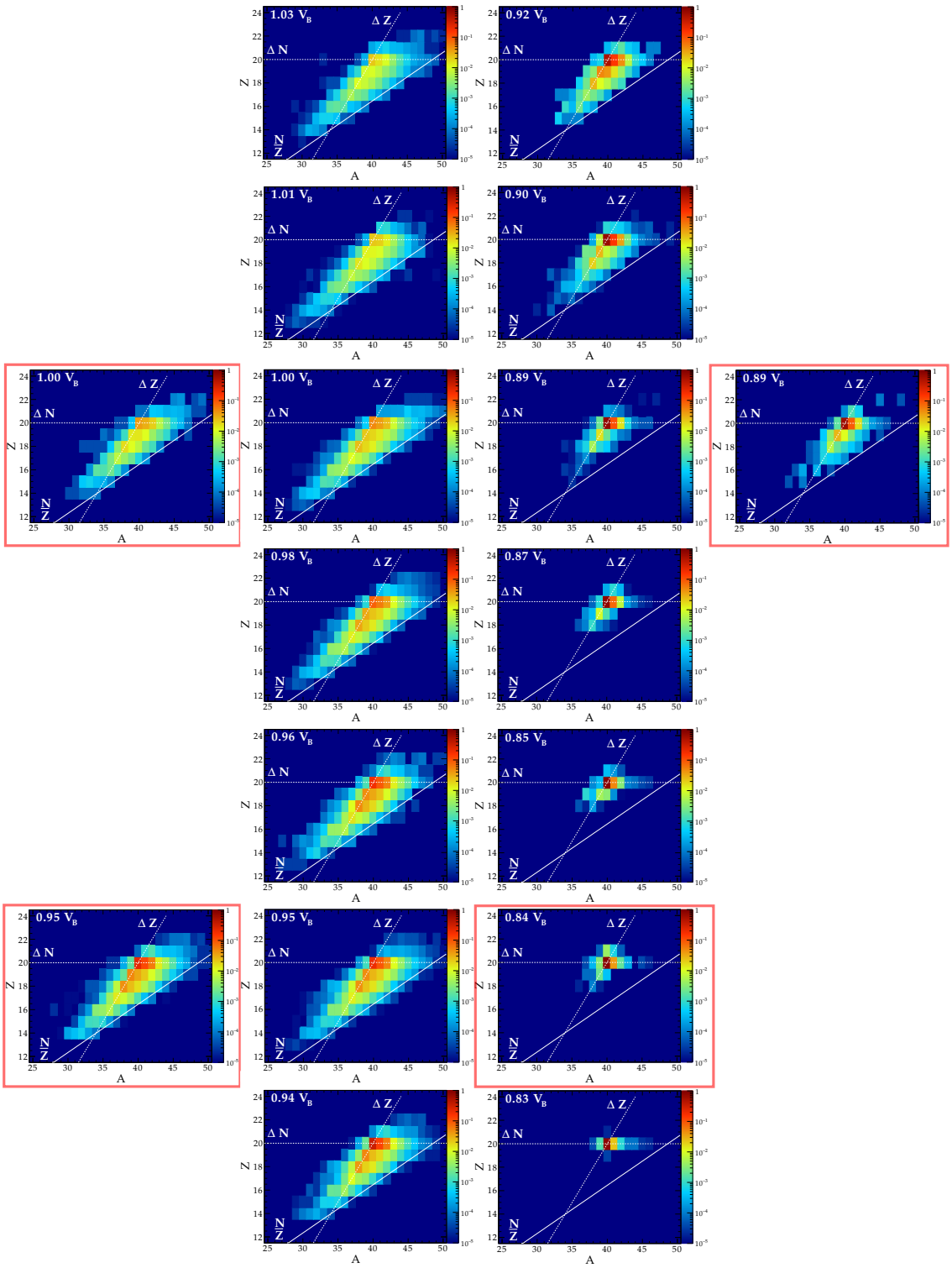

FIGURE 5.15: Distribution of detected PLFs in mass and atomic number in the ^{40}Ca + ^{208}Pb measurement as a function of the center-of-mass energy E_{cm} relative to the barrier. The panels highlighted with red boxes indicate the measurements with PRISMA positioned at θ_{lab} = 102°, with all the others those at θ_{lab} = 115°. In each panel, the solid white line shows the N/Z ratio of the compound nucleus that would be formed in the reaction were fusion to occur. The dashed white lines show the directions in A and Z in which the projectile properties change following pure neutron and proton transfer. The bombarding energy relative to the barrier E/V_B is indicated in each panel.

5.4 Dissipation of energy to internal excitations

The main questions of this thesis can now be addressed. How significant is the energy dissipation at sub-barrier energies? How does this vary across different systems, how do the different transfer modes facilitate this, and are there particular modes that act as strong doorways to energy dissipation? These questions are examined by determining the total excitation energies of the systems (the sum of those in the target-like and projectile-like nuclei in the exit channel), and from that inferring the extent of kinetic energy damping and thus dissipation.

5.4.1 Distribution of excitation energy between different transfer modes, and comparison with GRAZING model calculations

Figures 5.16 to 5.23 display the reconstructed excitation energy E_x distributions for all observed transfer modes in each system, where the measurements represent bombarding energies of approximately 95% of the barrier energy. For each mode the optimal E_x value, determined from the optimal Q-value (see Equations 2.43 and 3.12), is shown by the red arrow. The vertical dotted lines represent $E_x = 0$.

The general trend in each system is for the E_x distribution to become broader, and for the mean value to depart further from the calculated optimum value (shown by the red arrow), as a greater number of nucleons are transferred. It is remarkable that even at sub-barrier energies excitation energies up to 15 MeV results for reactions involving lighter projectiles, and E_x of up to 60 MeV are present for ^{40}Ca-induced reactions. The difference in excitation energies between the lighter and heavier systems is discussed further in Section 5.4.2.

The grey shaded areas in each panel are calculations of the E_x distribution performed using the semiclassical GRAZING code [85], which have been renormalised to match the measured integral transfer probability, since the semiclassical calculations in general underpredict the overall probability for each mode. These calculations have been performed including couplings to low lying states in each of the entrance channel nuclei. Calculated

distributions are not displayed where the GRAZING code predicts no cross section for that mode. The agreement between the calculated and the experimentally determined E_x, while reasonable for lighter systems, gets progressively worse for heavier projectiles where large excitation energies are measured.

Due to the different experimental setups used to measure the different systems, there is some difficulty in directly comparing the data from the two experiments. The superior energy resolution of the $E - \Delta E$ detector used in experiment 1 (ANU) means that some subtle features in the E_x distributions can be identified, while they may be obscured in the PRISMA data— for instance, one can observe in the measured E_x spectra of the ^{16}O-induced reactions a distribution that exhibits multiple peaks for the -1p mode, which likely correspond to the excitation of single particle states in the recipient target-like fragment. The ANU data, displayed in Figures 5.16 to 5.20, shows that although all channels qualitatively follow the systematics expected from optimum Q-value considerations, there are distinct differences in the E_x distributions between multinucleon transfer channels and those in which only a single nucleon is transferred. Whilst single proton transfer leads to a distribution exhibiting regions of low and high population, suggesting the population of well defined discrete states, the distributions of multinucleon transfer processes have higher mean E_x, and are essentially featureless. This suggests that there are a large number of states populated in these processes. Even at the lowest bombarding energies, there remains a spread in E_x over 10 MeV for these channels. This flags the possible beginning of dissipative processes even at large internuclear separation.

As the charge product increases and the mass asymmetry of the system decreases, the greater number of open channels in the reactions of the heavier projectiles provides a greater number of doorways for the kinetic energy to be dissipated from the relative motion.

5.4.2 The evolution of energy dissipation with bombarding energy

Some of the most important aspects of the evolution of dissipation with bombarding energy through transfer are demonstrated in Figure 5.24 through contour plots of the

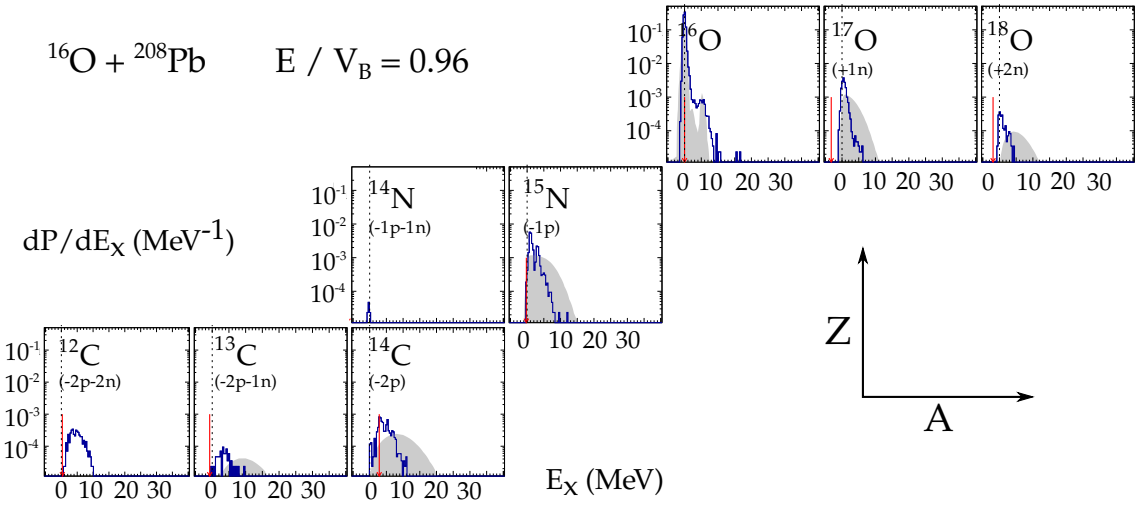

FIGURE 5.16: Excitation energies for the various observed transfer modes in the measurement of ^{16}O + ^{208}Pb at $0.96V_B$ (adjusted from the s-wave barrier according to the mean scattering angle). $E_x = 0$ is indicated by the vertical dashed line in each panel. The red arrows indicate the optimum E_x values. The shaded areas represent GRAZING calculations of the E_x distribution for the mode in question.

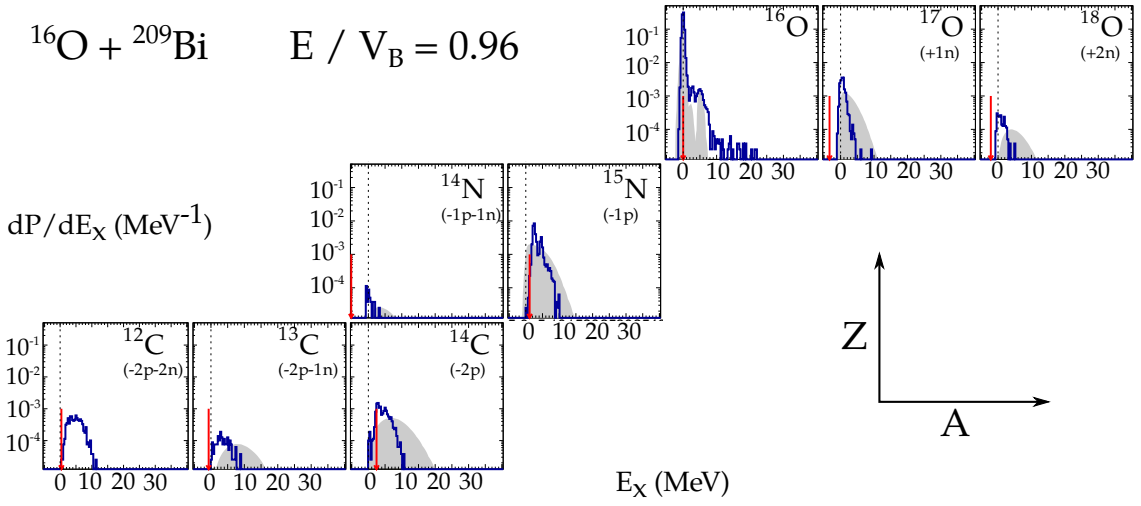

FIGURE 5.17: Excitation energies for the various observed transfer modes in the measurement of ^{16}O + ^{209}Bi at $0.96V_B$ (adjusted from the s-wave barrier according to the mean scattering angle). $E_x = 0$ is indicated by the vertical dashed line in each panel. The red arrows indicate the optimum E_x values. The shaded areas represent GRAZING calculations of the E_x distribution for the mode in question.

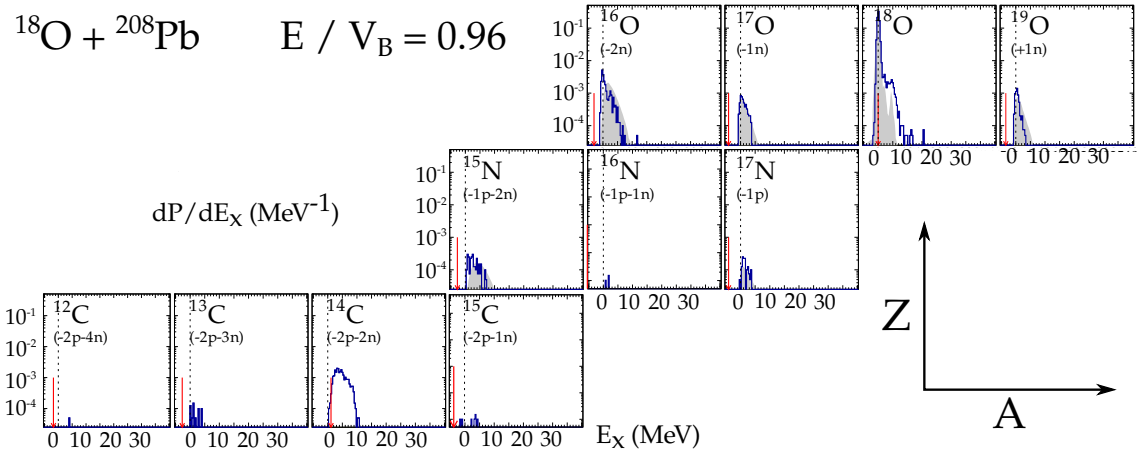

FIGURE 5.18: Excitation energies for the various observed transfer modes in the measurement of ^{18}O + ^{208}Pb at $0.96V_B$ (adjusted from the s-wave barrier according to the mean scattering angle). $E_x = 0$ is indicated by the vertical dashed line in each panel. The red arrows indicate the optimum E_x values. The shaded areas represent GRAZING calculations of the E_x distribution for the mode in question.

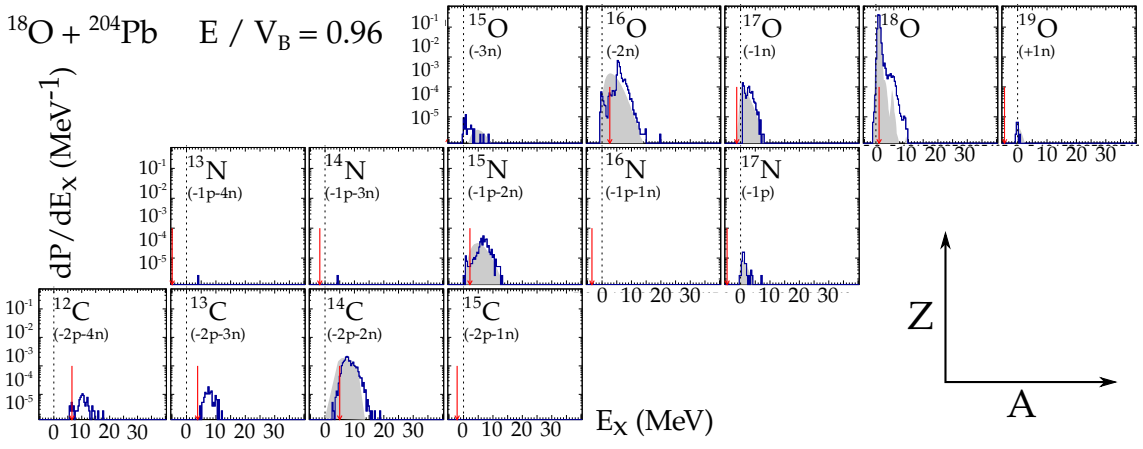

FIGURE 5.19: Excitation energies for the various observed transfer modes in the measurement of ^{18}O + ^{204}Pb at $0.96V_B$ (adjusted from the s-wave barrier according to the mean scattering angle). $E_x = 0$ is indicated by the vertical dashed line in each panel. The red arrows indicate the optimum E_x values. The shaded areas represent GRAZING calculations of the E_x distribution for the mode in question.

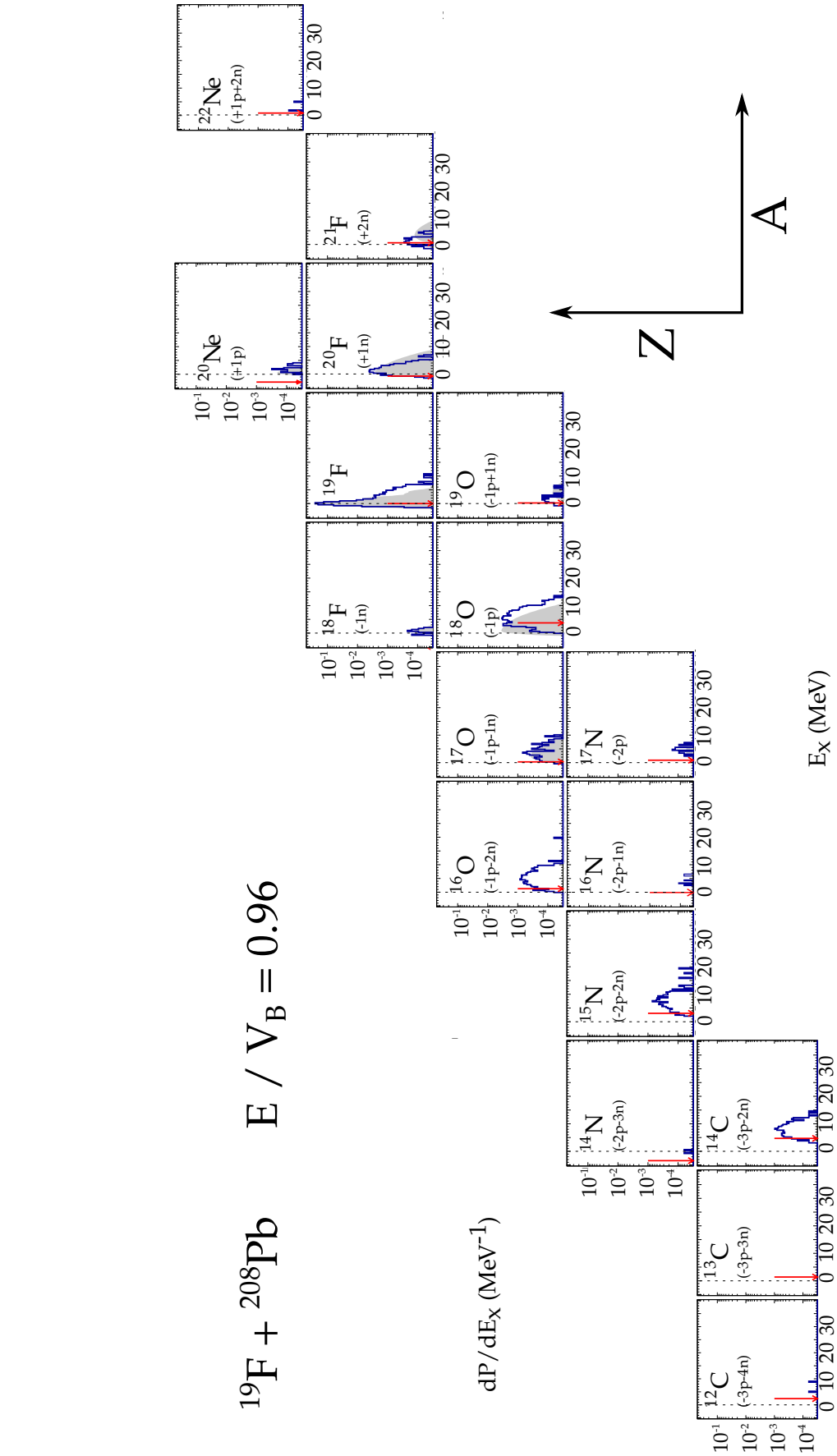

FIGURE 5.20: Excitation energies for the various observed transfer modes in the measurement of ^{19}F + ^{208}Pb at $0.96V_B$ (adjusted from the s-wave barrier according to the mean scattering angle). $E_x = 0$ is indicated by the vertical dashed line in each panel. The red arrows indicate the optimum E_x values. The shaded areas represent GRAZING calculations of the E_x distribution for the mode in question.

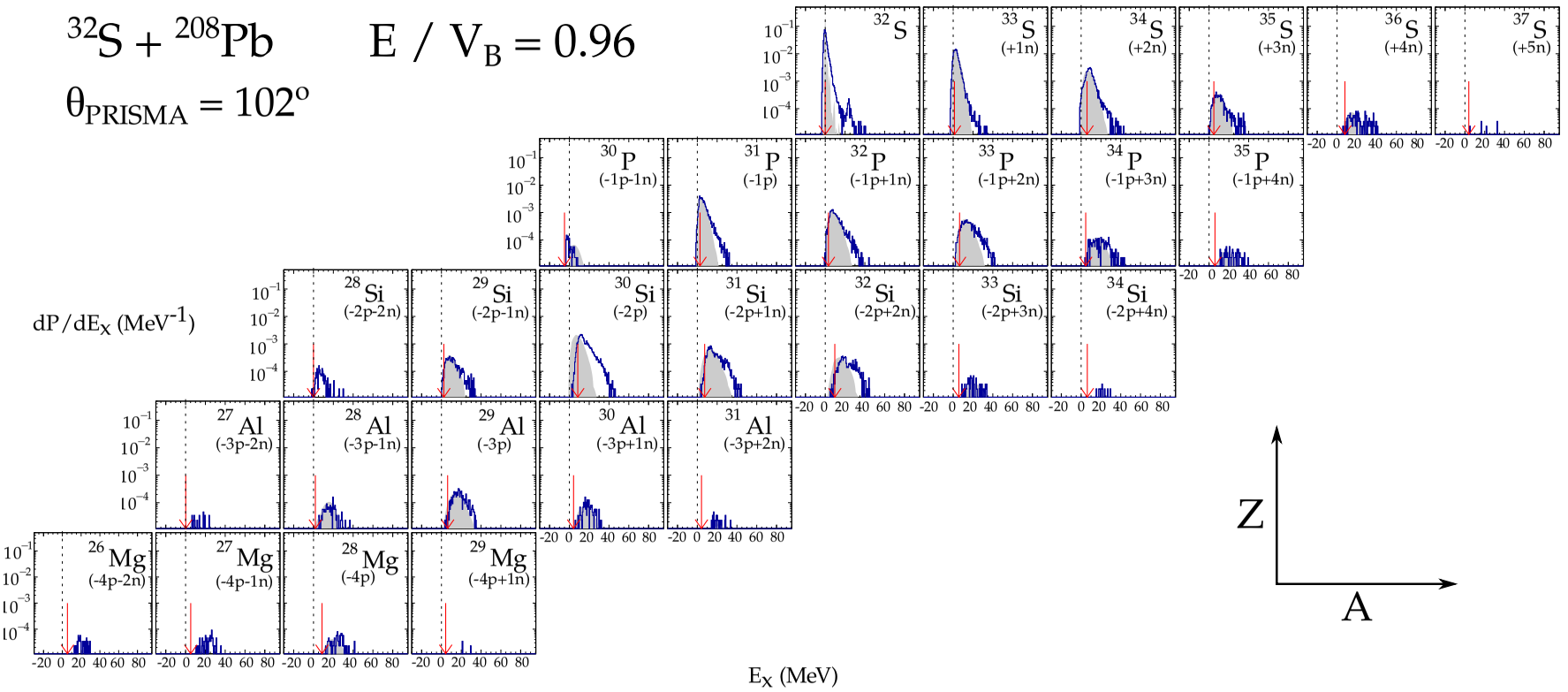

FIGURE 5.21: Excitation energies for the various observed transfer modes in the measurement of ^{32}S + ^{208}Pb at $0.96V_B$ (adjusted from the s-wave barrier according to the mean scattering angle), for the $\theta_{\text{PRISMA}} = 102°$ setting. $E_x = 0$ is indicated by the vertical dashed line in each panel. The red arrows indicate the optimum E_x values. Modes with a very low number of counts have been excluded from this figure. The grey shaded region indicates the distribution of excitation energy calculated with GRAZING (see text for details).

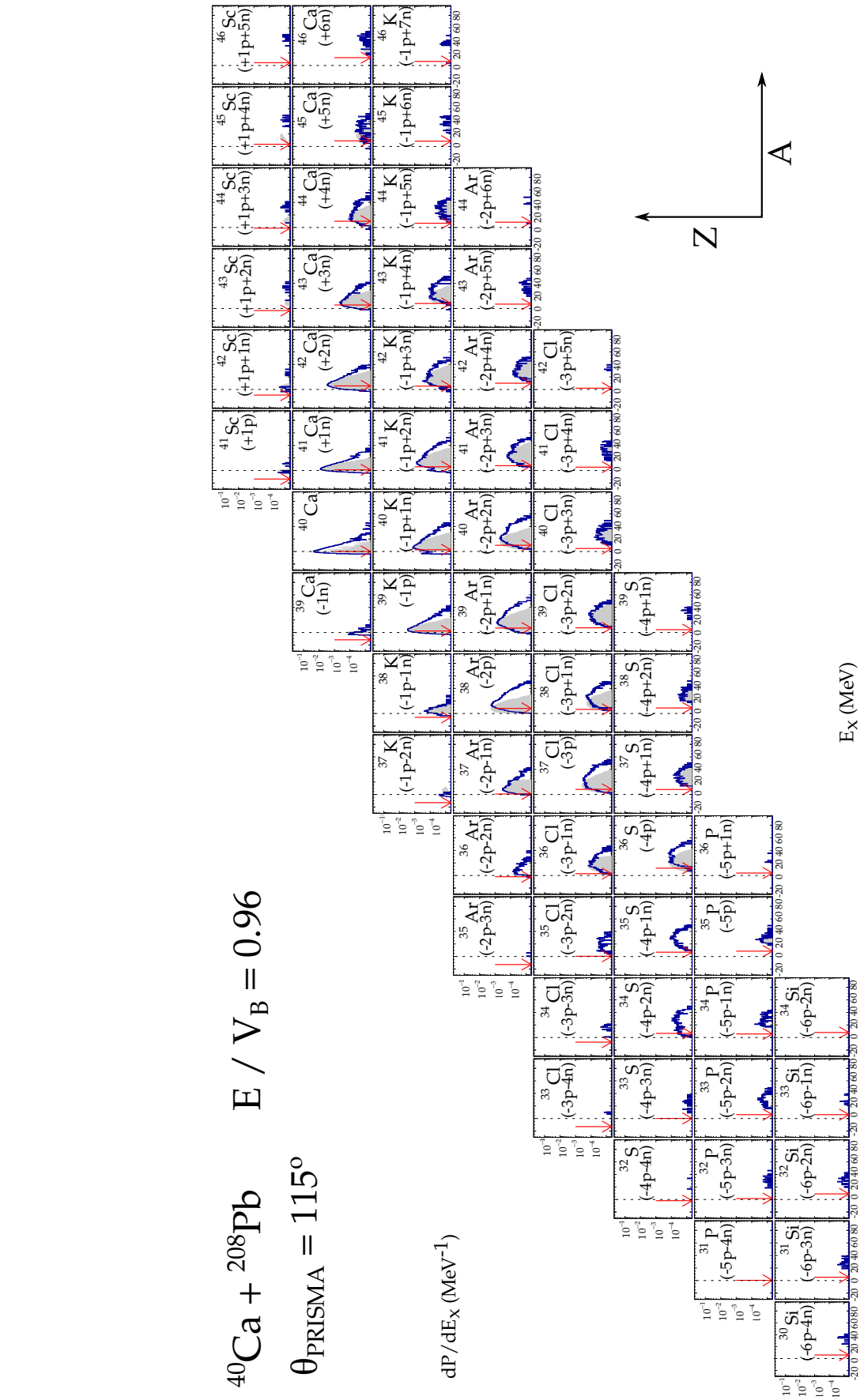

FIGURE 5.22: Excitation energies for the various observed transfer modes in the measurement of ^{40}Ca + ^{208}Pb at $0.95V_B$ (adjusted from the s-wave barrier according to the mean scattering angle), for the $\theta_{\text{PRISMA}} = 115°$ setting. $E_x = 0$ is indicated by the vertical dashed line in each panel. The red arrows indicate the optimum E_x values. Modes with a very low number of counts have been excluded from this figure. The grey shaded region indicates the distribution of excitation energy calculated with GRAZING (see text for details).

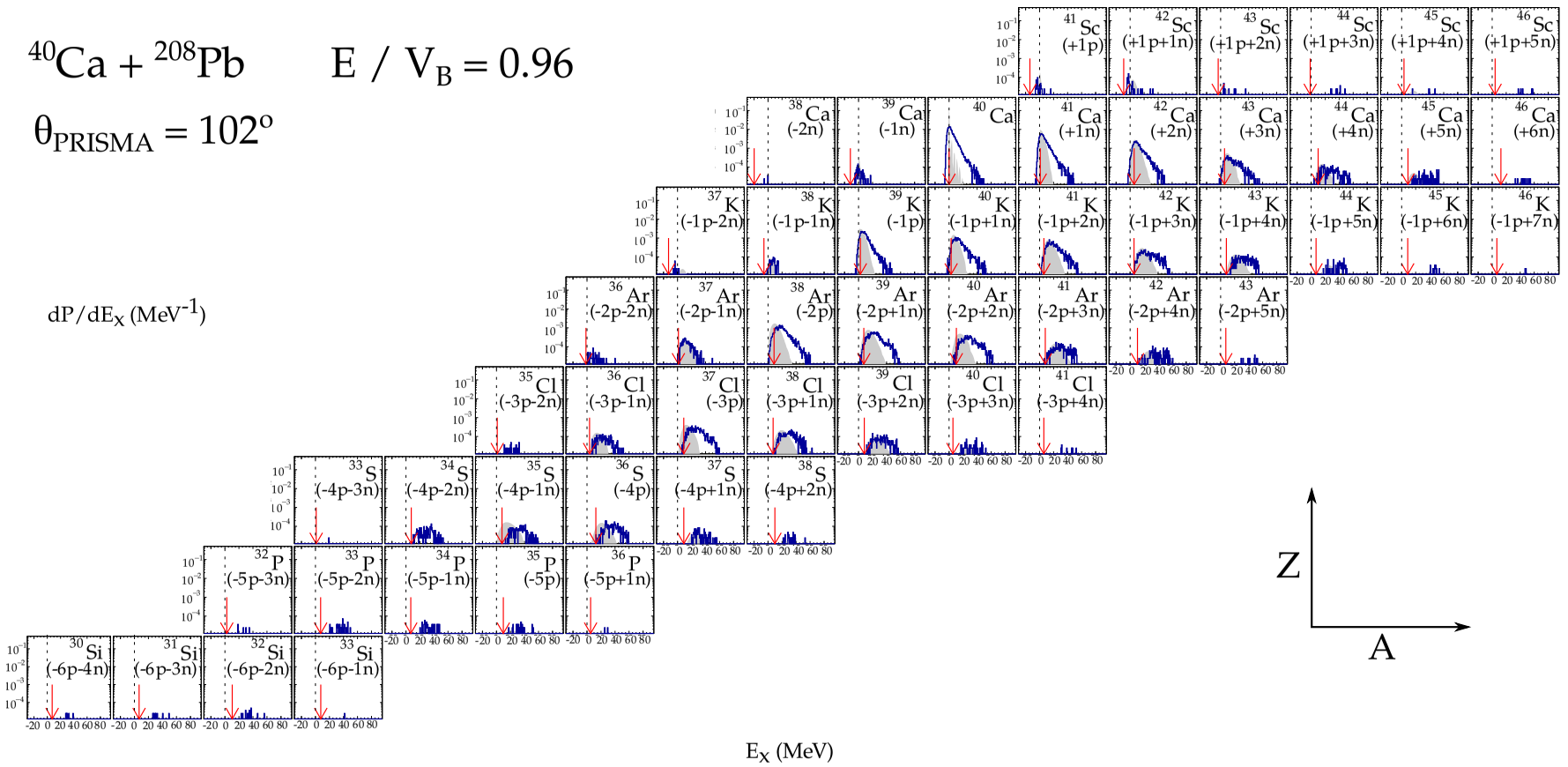

FIGURE 5.23: Excitation energies for the various observed transfer modes in the measurement of ^{40}Ca + ^{208}Pb at $0.95V_B$ (adjusted from the s-wave barrier according to the mean scattering angle), for the $\theta_{\text{PRISMA}} = 102°$ setting. $E_x = 0$ is indicated by the vertical dashed line in each panel. The red arrows indicate the optimum E_x values. Modes with a very low number of counts have been excluded from this figure. The grey shaded region indicates the distribution of excitation energy calculated with GRAZING (see text for details).

differential probability per bin in both excitation energy and bombarding energy relative to the fusion barrier for all of the studied systems, with separate panels showing (from left to right) all quasielastic reaction products, all transfer products, all neutron transfer products, and all transfer products where at least one unit of charge is exchanged. As measurements were taken only at discrete values of E/V_B, in order to produce the contours it was necessary to perform an interpolation between the measurements at each bombarding energy for each reaction. In Figure 5.25, the data is presented in the same sets of product types, with the mean excitation energy plotted against E/V_B, essentially making the information in Figure 5.24 easier to understand.

A general feature that is seen in all of the systems is that the majority of the yield which emerges from the reaction exhibiting kinetic energy damping (and consequently higher excitation energies) both above and below the barrier is associated with transfer, and charge transfer in particular. In the lighter systems, transfer of only neutrons leads only to small excitation energies in the outgoing fragments, as would be expected from consideration of the optimum Q-value, which is always zero for these modes as there is no change in the Coulomb field between the entrance and exit channels. The exception to this is where the neutron transfer modes have positive Q-values (see Table C.1 in Appendix C), such as the ^{18}O + ^{204}Pb, ^{32}S + ^{208}Pb, and ^{40}Ca + ^{208}Pb systems, where the neutron transfer modes are still able to reach high excitation energies due to the favourable energetics.

The most striking feature of these plots is the difference in the extent of the dissipation between the light systems and the heavier ones. Between the systems measured in the first experiment, there is little discernible difference in the extent of the excitation energy distributions. Generally in each of these systems, the distribution extends to larger excitation energies as the bombarding energy moves towards and across the barrier threshold. Due to the growing importance of absorption towards the barrier energy, and the consequent reduction of flux to backward angles, in the heavier systems the probability distribution peaks for the highest excitation energies in the region of 96% of the barrier energy. With the measurements of the lighter systems (those measured in experiment 1) focused mainly in the sub-barrier region, this effect is not observed.

An overall difference between the lightest and heaviest systems studied is that the mean excitation energy increases as the charge product increases. This is to be expected, since the additional Coulomb repulsion requires an increasing matter overlap in order for the reactants to reach the same separation relative to the barrier radius. However, in the light systems this rule is not obeyed strictly. For example, the ^{18}O-induced reactions do not appear into the systematics as would be expected according to the degree of matter overlap. Both the ^{18}O + ^{204}Pb and ^{18}O + ^{208}Pb systems ($Z_1Z_2 = 656$), when considering the mean excitation energy of all of the transfer yield against the bombarding energy, lie higher than the ^{16}O + ^{209}Bi ($Z_1Z_2 = 664$) and ^{19}F + ^{208}Pb ($Z_1Z_2 = 656$) systems, but lower than both the ^{32}S + ^{208}Pb ($Z_1Z_2 = 1312$) and ^{40}Ca + ^{208}Pb ($Z_1Z_2 = 1640$) systems.

This effect seems to arise as a result of the specific transfer modes that dominate the yield in each of these systems. This is highlighted in Figures 5.26 to 5.33 by plotting the differential probability per bin in excitation energy for each individual transfer mode against the bombarding energy relative to the fusion barrier.

In both the ^{18}O + ^{204}Pb and ^{18}O + ^{208}Pb systems the very strong -2p-2n stripping channel is identified with a high mean E_x, as can be seen by comparing the ^{14}C ejectiles with neighbouring panels in Figures 5.28 and 5.29. This therefore pulls the overall mean E_x to large values when transfer with charge exchange is considered. In addition, the strong -2n stripping channel in ^{18}O + ^{204}Pb forming ^{16}O (Figure 5.29), with favourable energetics, means that this reaction exhibits otherwise unusually high mean E_x values compared to the other reactions in all considered cases of transfer. In the heavier systems (measured in experiment 2), the large number of open channels, and the comparatively smooth distributions of the product yields, mean that there are no particular modes that dominate the mean E_x value, and the plots against the bombarding energy more closely resemble the expectations based on consideration of the matter overlap.

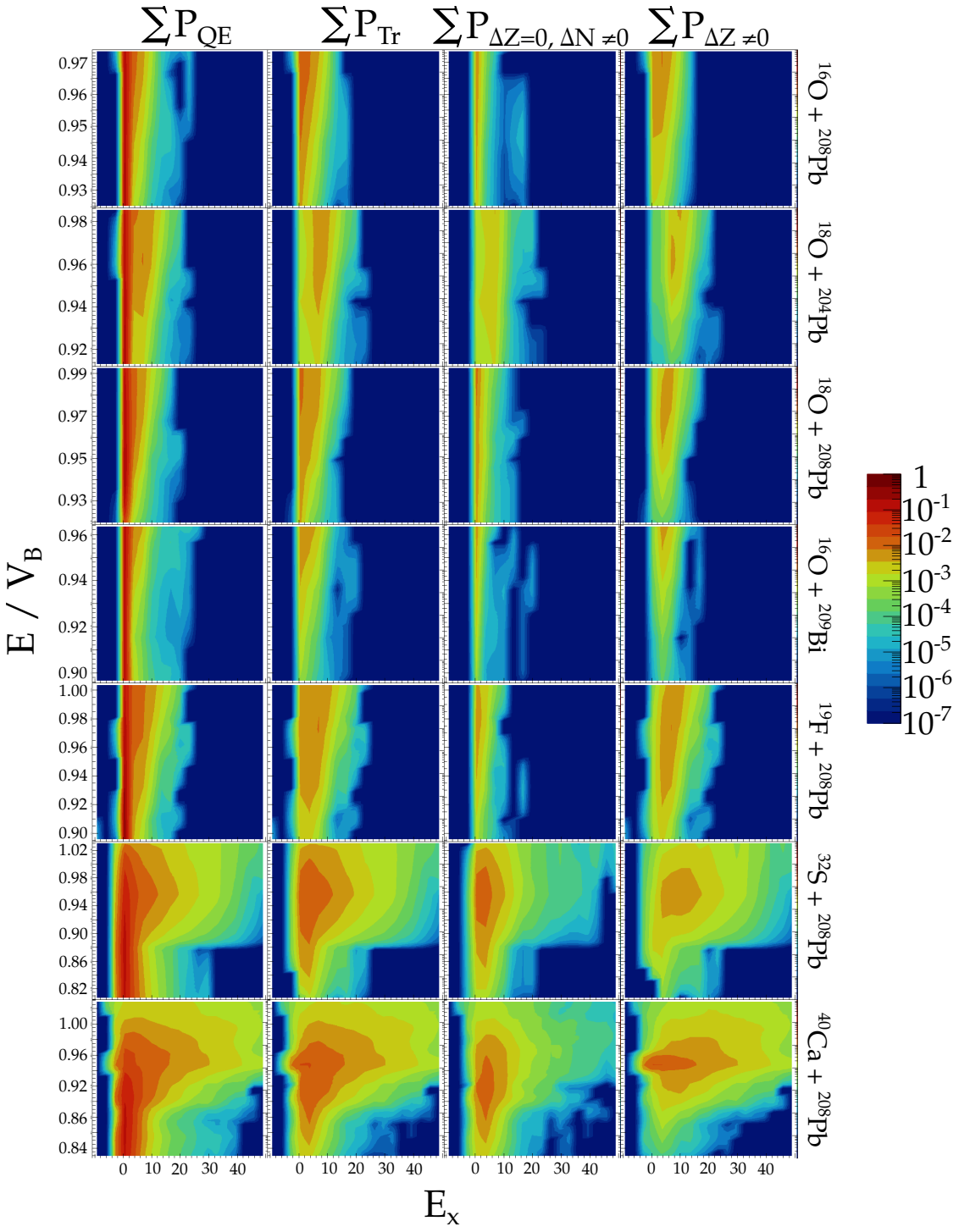

FIGURE 5.24: Contour plots showing the distribution of excitation energy between different types of transfer modes, as the bombarding energy varies relative to the barrier. From left to right are shown the total E_x distribution where all channels are summed together, the same but with the beam-like nuclides excluded, the sum of all pure neutron transfer modes, and the sum of all channels involving charge transfer.

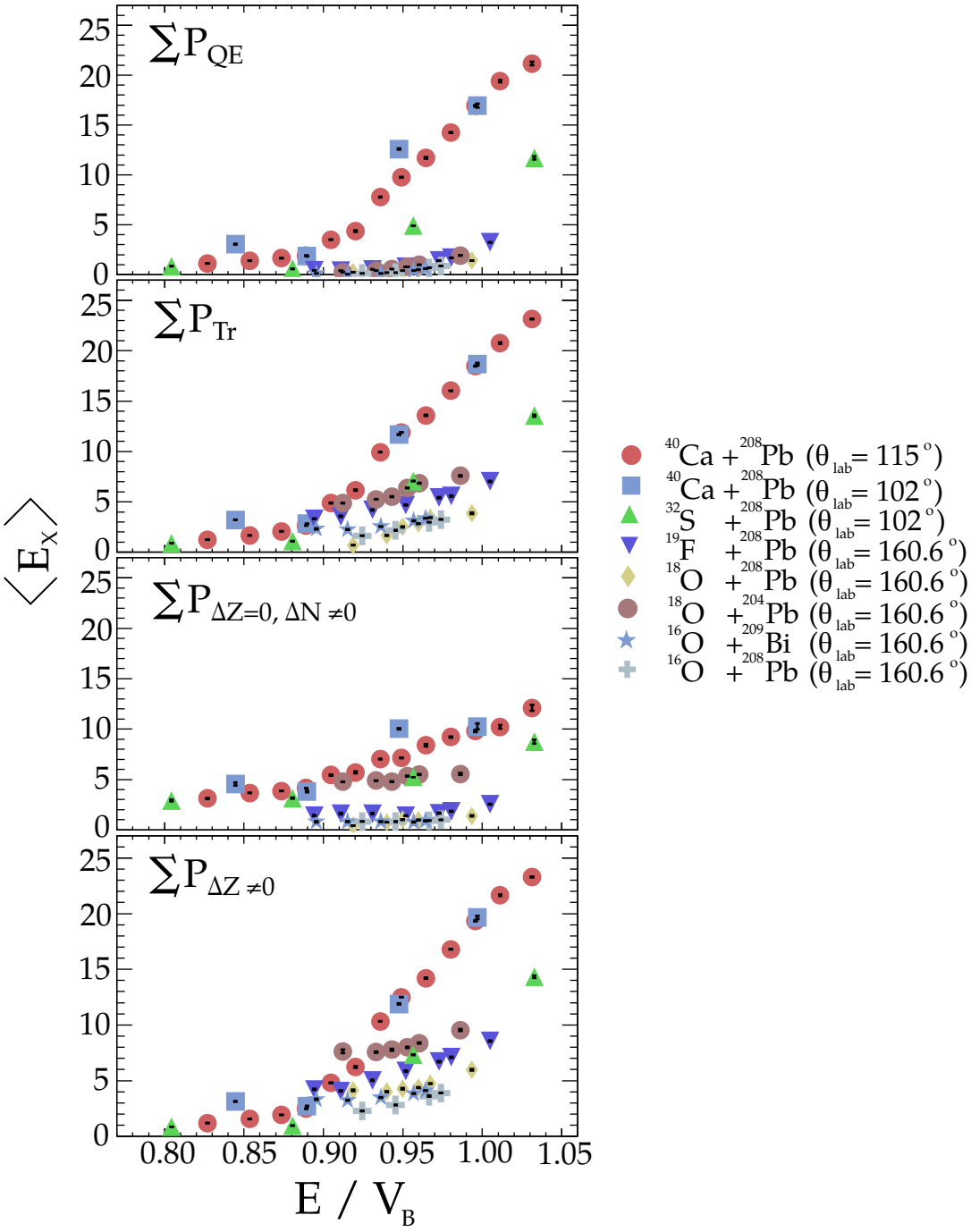

FIGURE 5.25: The variation in the mean excitation energy between different types of transfer modes, as the bombarding energy varies relative to the barrier. The panels show (from top to bottom) the mean excitation energy of (a) the total quasielastic yield, (b) the total transfer yield, (c) the pure neutron transfer yield, (d) the yield of all transfer modes involving the exchange of at least one proton.

The overall distribution of excitation energy depends mainly upon two factors. Firstly,

the probability for the transfer mode in question, which in turn depends upon the overlap of the Q-window with the threshold for allowed states. Secondly, the density of states in the reaction products will determine how likely each is to reach a certain level of excitation [83]. The optimum Q-value (Equation 2.43) can be transformed to an optimal E_x by subtracting the ground-state Q-value for the channel in question, i.e. $E_{x\,opt} = Q_{opt} - Q_{g.g}$. In Figures 5.26 to 5.33, in each panel the solid white lines show the evolution of $E_{x\,opt}$ with beam energy for that particular transfer mode, moving to higher E_x values with higher bombarding energy. Where these lines are not visible, the optimum Q-value lies below $Q_{g.g}$. These modes are generally suppressed compared to those in which $E_{x\,opt}$ reaches significant positive values.

Each panel in Figures 5.26 to 5.33 also show the energy thresholds for various particle evaporation processes. In all cases, excitation of the heavy target-like nucleus will result predominantly in neutron evaporation where E_x is larger than the neutron separation energy. It can be seen that many transfer modes result in excitation energies that can result in secondary emission of particles in order for the transfer products to de-excite to lower energy states. The tendency of the mass vs. atomic number distributions to extend to greater neutron loss with greater charge stripping may be evidence of the importance of neutron evaporation [83] (this is particularly evident in the ^{32}S + ^{208}Pb and ^{40}Ca + ^{208}Pb systems- see Figures 5.14 - 5.15 as well as Figures 5.21 - 5.22). These particle evaporation pathways may be considered the dissipation doorways that resemble a heat bath that couples to the relative motion in the reaction entrance channel. Since excitations can occur in both the target and projectile, the thresholds so determined represent absolute minima. It is likely that the target-like product will carry most of the excitation energy due to its higher level density at a given excitation energy. In the lighter systems, most of the channels observed are those in which the heavy partner receives the transferred nucleons [60], which has been shown to be important in determining the collision partner that becomes excited in the transfer process [101, 148]. As such an important distinction between the lighter systems, and those reactions induced by ^{32}S and ^{40}Ca, is that in the latter a significant proportion of the yield being *indirect* transfer products suggests that the excitation energy is likely to be divided more evenly between the projectile-like and

target-like transfer products.

The essence of the results presented in Figures 5.26 to 5.33 are summarised by showing the mean E_x vs. $E_{c.m}/V_B$ for all of the systems in a single plot, as shown in Figure 5.34. Examining the data in this way, it is clear that the surprisingly large probabilities for transfer of particular clusters in the lighter systems explain the departure from expected systematics. Examining the -2p-2n stripping channel (as well as others that have been suggested to be enhanced due to cluster or correlated-nucleon transfer, where they can be compared across the full range of systems), the mean excitation energy increases across all bombarding energies with the charge product in the entrance channel. It is the particular strength of this mode in the ^{18}O-induced reactions that causes those reactions to exhibit dissipative behaviour associated with transfer contrary to the expected systematics. The matter overlap is primarily responsible for the high excitation energies, whilst structure and energetics (Q-value) effects will determine their overall strength.

5.4.3 Influence of the reaction energetics on dissipation

Figure 5.1 demonstrated how the effective Q-value plays an important role in determining the overall strength of a given transfer mode (at least for direct reactions), and it has been discussed how the reaction channels must be well matched to the Q-window in order for those channels to be open in the final state of the reaction. On the other hand, how important are the reaction energetics on the dissipative character of each transfer mode?

Figure 5.35 shows a plot of the effective Q-value vs. the mean excitation energy $\langle E_x \rangle$ for all systems at a bombarding energy of 95% of the barrier height. In this figure a gate has been applied such that only the transfer modes with an absolute probability greater than 0.001 are displayed. What is immediately obvious from this plot is that whilst the lighter systems exhibit a strong positive correlation between the stated quantities, which is approximately constant between the studied systems, the transfer modes in the heavier systems, whilst also showing evidence of a correlation, display a much greater degree of scatter. It is clear that the $\langle E_x \rangle$ values for the heavier projectiles are influenced by factors other than only the energetics of the process. The increasing complexity of the reaction

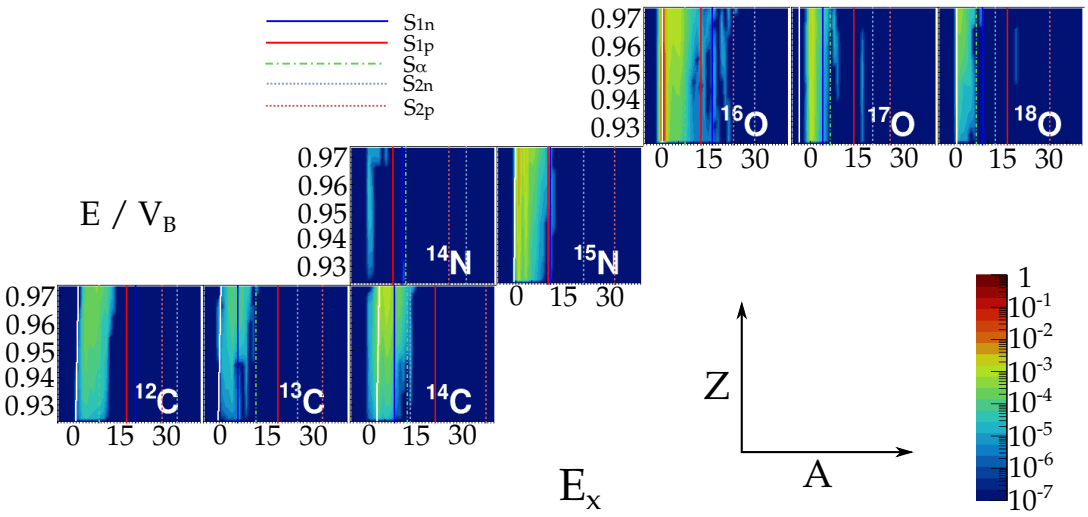

FIGURE 5.26: Contour plots showing the distribution of excitation energy between the exit channel fragments as it evolves with the bombarding energy, in the measurement of ^{16}O + ^{208}Pb. In each panel are shown the energy thresholds for particle emission. Also shown by the solid white lines are the optimal excitation energies for each transfer mode as a function of the bombarding energy. The color scale shown in the bottom right corner is common to all panels. The contour plots are generated via an interpolation procedure between the discrete measurements at different energies.

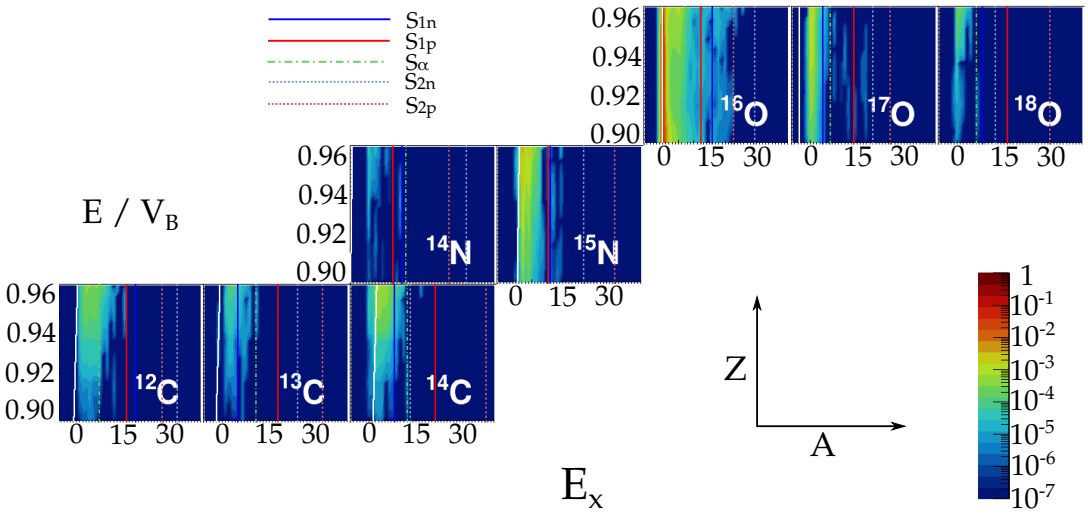

FIGURE 5.27: Contour plots showing the distribution of excitation energy between the exit channel fragments as it evolves with the bombarding energy, in the measurement of ^{16}O + ^{209}Bi. In each panel are shown the energy thresholds for particle emission. Also shown by the solid white lines are the optimal excitation energies for each transfer mode as a function of the bombarding energy. The color scale shown in the bottom right corner is common to all panels. The contour plots are generated via an interpolation procedure between the discrete measurements at different energies.

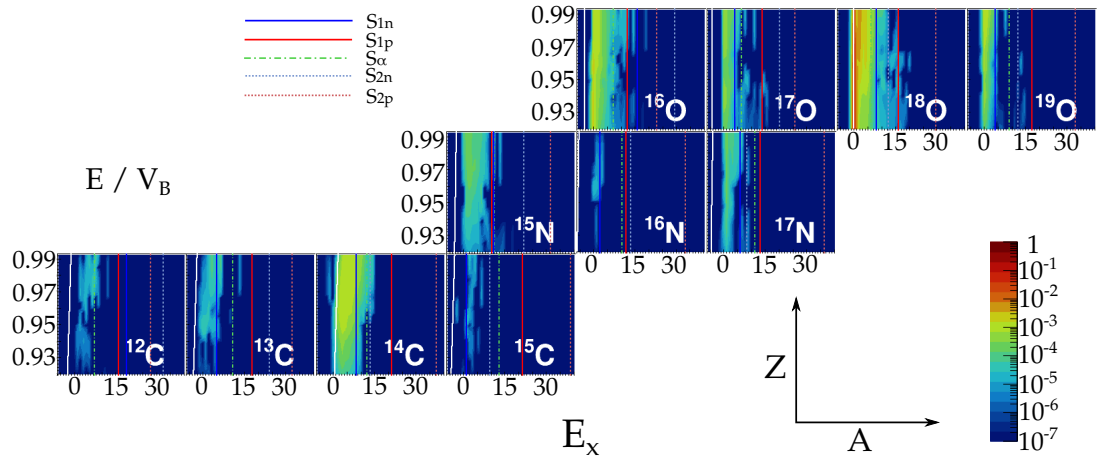

FIGURE 5.28: Contour plots showing the distribution of excitation energy between the exit channel fragments as it evolves with the bombarding energy, in the measurement of ^{18}O + ^{208}Pb. In each panel are shown the energy thresholds for particle emission. Also shown by the solid white lines are the optimal excitation energies for each transfer mode as a function of the bombarding energy. The color scale shown in the bottom right corner is common to all panels. The contour plots are generated via an interpolation procedure between the discrete measurements at different energies.

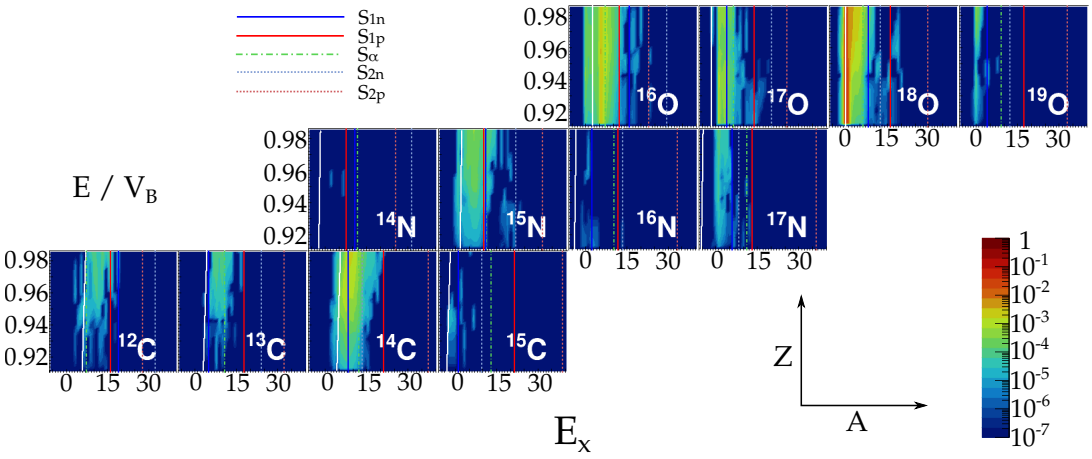

FIGURE 5.29: Contour plots showing the distribution of excitation energy between the exit channel fragments as it evolves with the bombarding energy, in the measurement of ^{18}O + ^{204}Pb. In each panel are shown the energy thresholds for particle emission. Also shown by the solid white lines are the optimal excitation energies for each transfer mode as a function of the bombarding energy. The color scale shown in the bottom right corner is common to all panels. The contour plots are generated via an interpolation procedure between the discrete measurements at different energies.

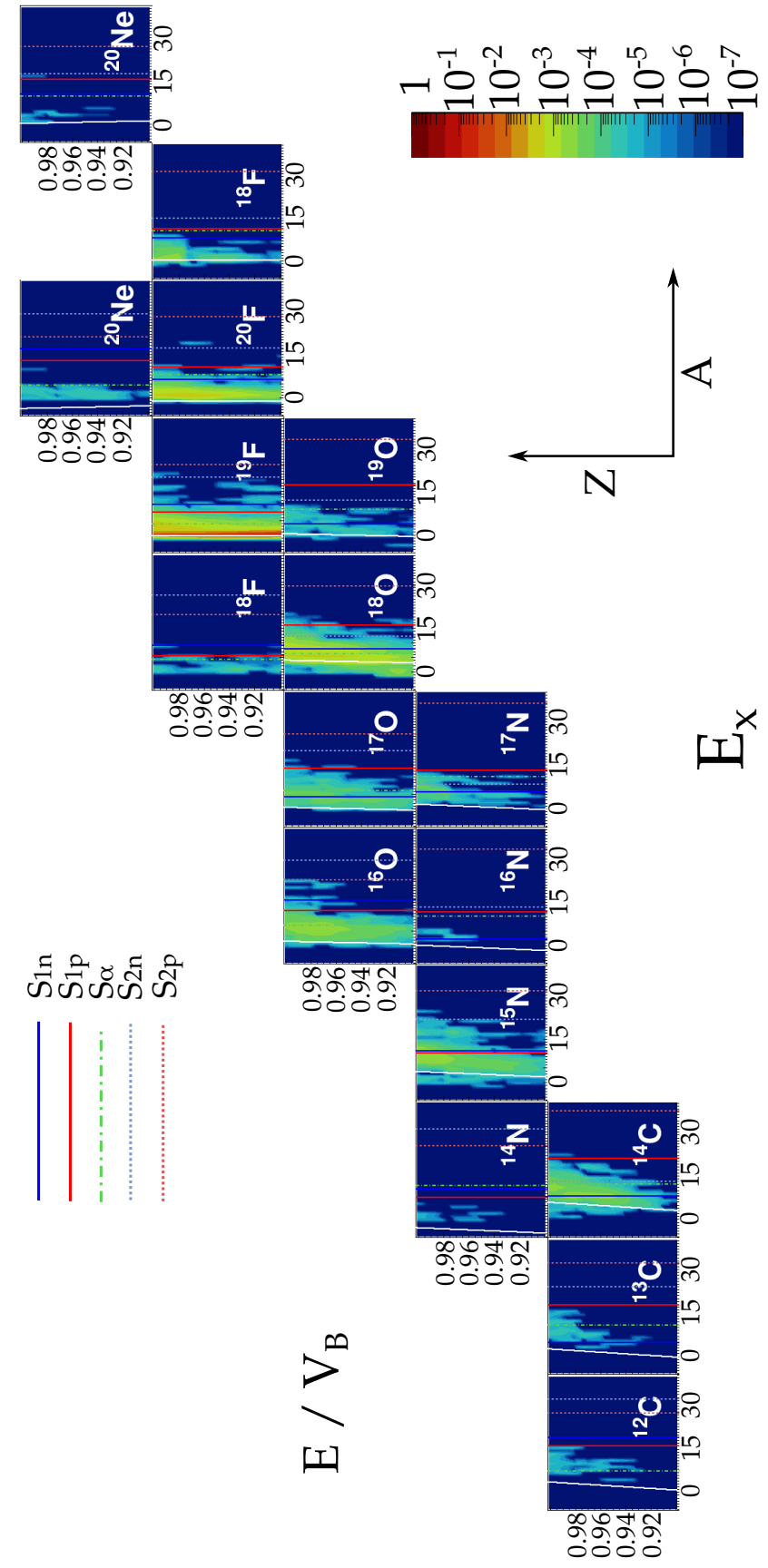

FIGURE 5.30: Contour plots showing the distribution of excitation energy between the exit channel fragments as it evolves with the bombarding energy, in the measurement of ^{19}F + ^{208}Pb. In each panel are shown the energy thresholds for particle emission. Also shown by the solid white lines are the optimal excitation energies for each transfer mode as a function of the bombarding energy. The color scale shown in the bottom right corner is common to all panels. The contour plots are generated via an interpolation procedure between the discrete measurements at different energies.

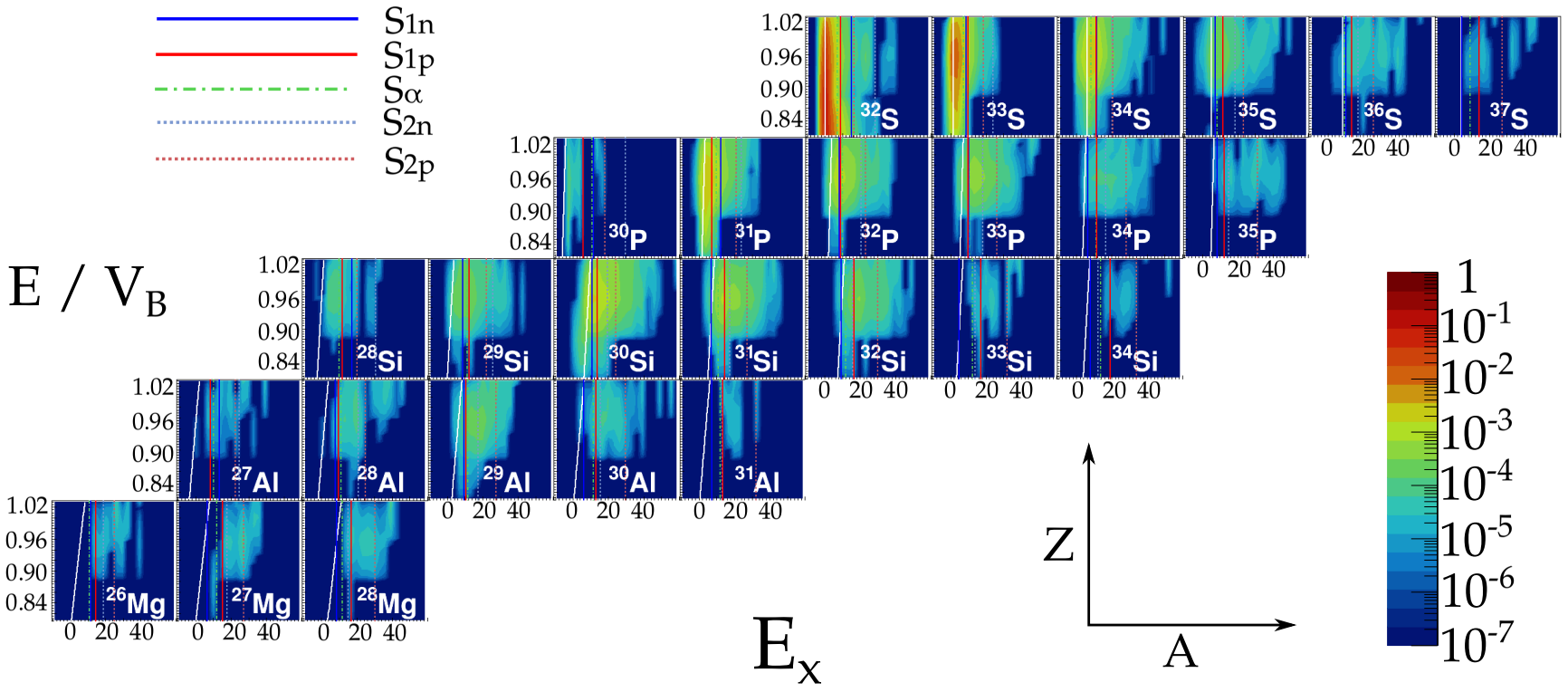

FIGURE 5.31: Contour plots showing the distribution of excitation energy between the exit channel fragments as it evolves with the bombarding energy, in the measurement of ^{32}S + ^{208}Pb, for the $\theta_{\text{PRISMA}} = 102°$ setting. In each panel are shown the energy thresholds for particle emission. Also shown by the solid white lines are the optimal excitation energies for each transfer mode as a function of the bombarding energy. The color scale shown in the bottom right corner is common to all panels. The contour plots are generated via an interpolation procedure between the discrete measurements at different energies.

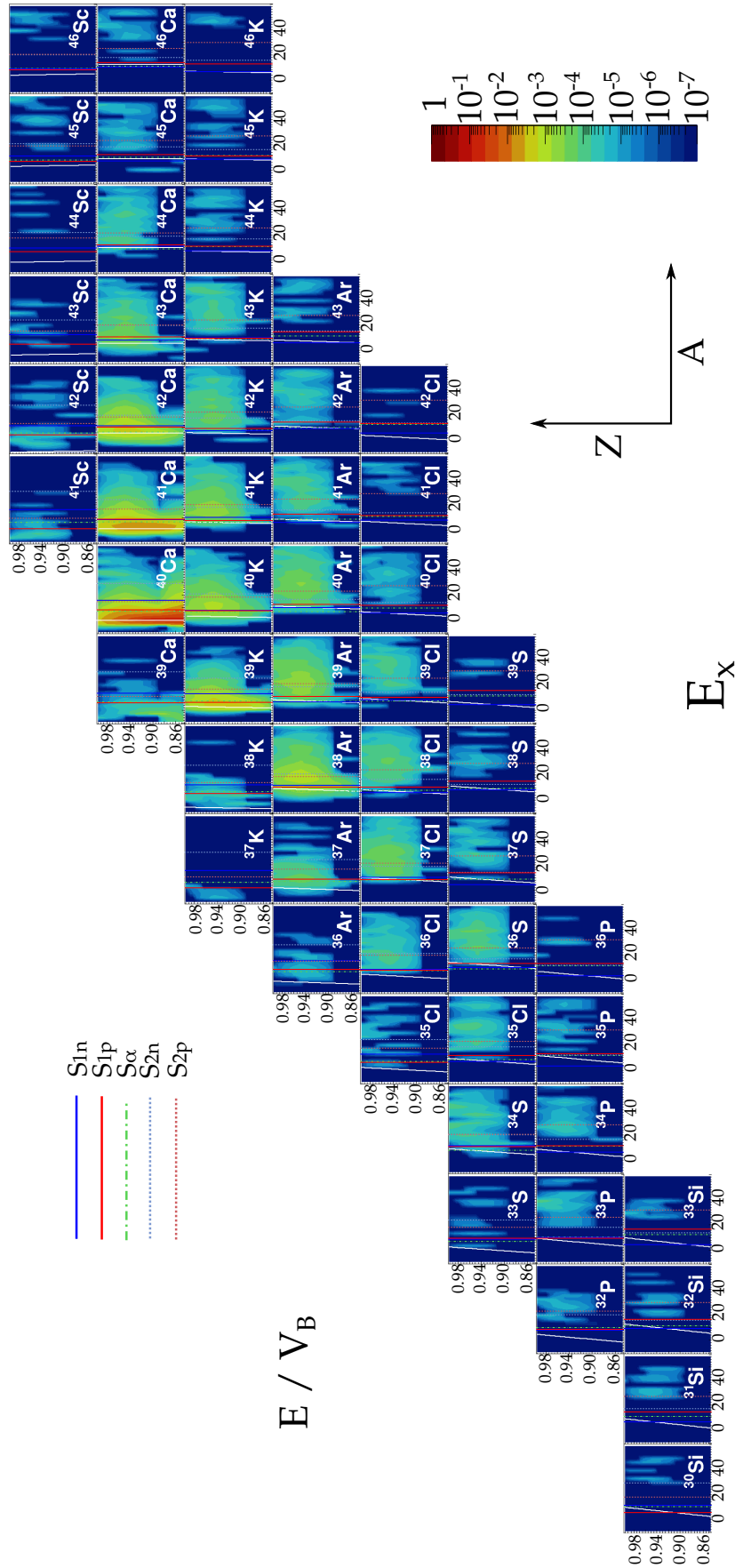

FIGURE 5.32: Contour plots showing the distribution of excitation energy between the exit channel fragments as it evolves with the bombarding energy, in the measurement of ^{40}Ca + ^{208}Pb, for the $\theta_{\mathrm{PRISMA}} = 102°$ setting. In each panel are shown the energy thresholds for particle emission. Also shown by the solid white lines are the optimal excitation energies for each transfer mode as a function of the bombarding energy. The color scale shown in the bottom right corner is common to all panels. The contour plots are generated via an interpolation procedure between the discrete measurements at different energies.

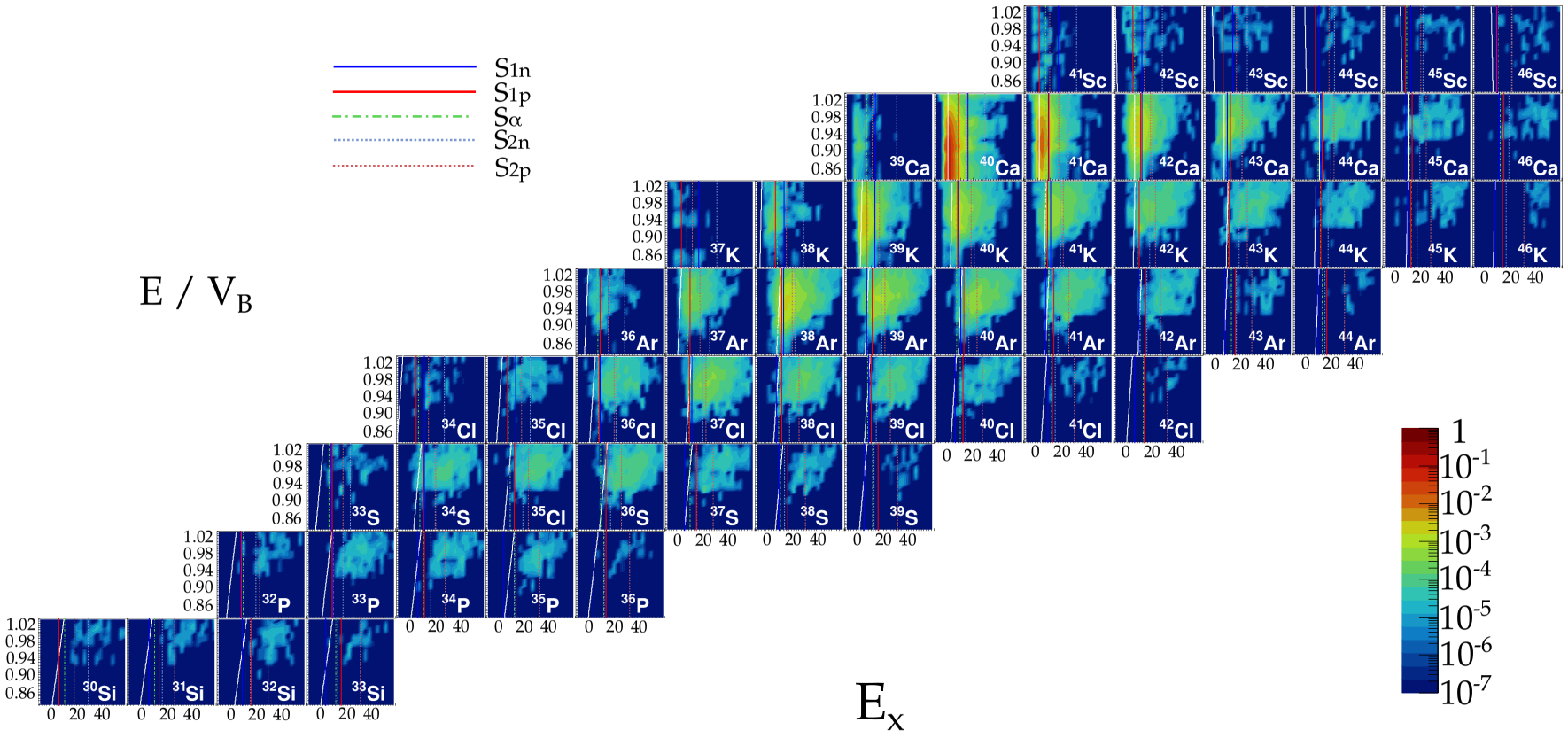

FIGURE 5.33: Contour plots showing the distribution of excitation energy between the exit channel fragments as it evolves with the bombarding energy, in the measurement of ^{40}Ca + ^{208}Pb, for the $\theta_{\text{PRISMA}} = 115°$ setting. In each panel are shown the energy thresholds for particle emission. Also shown by the solid white lines are the optimal excitation energies for each transfer mode as a function of the bombarding energy. The color scale shown in the bottom right corner is common to all panels. The contour plots are generated via an interpolation procedure between the discrete measurements at different energies.

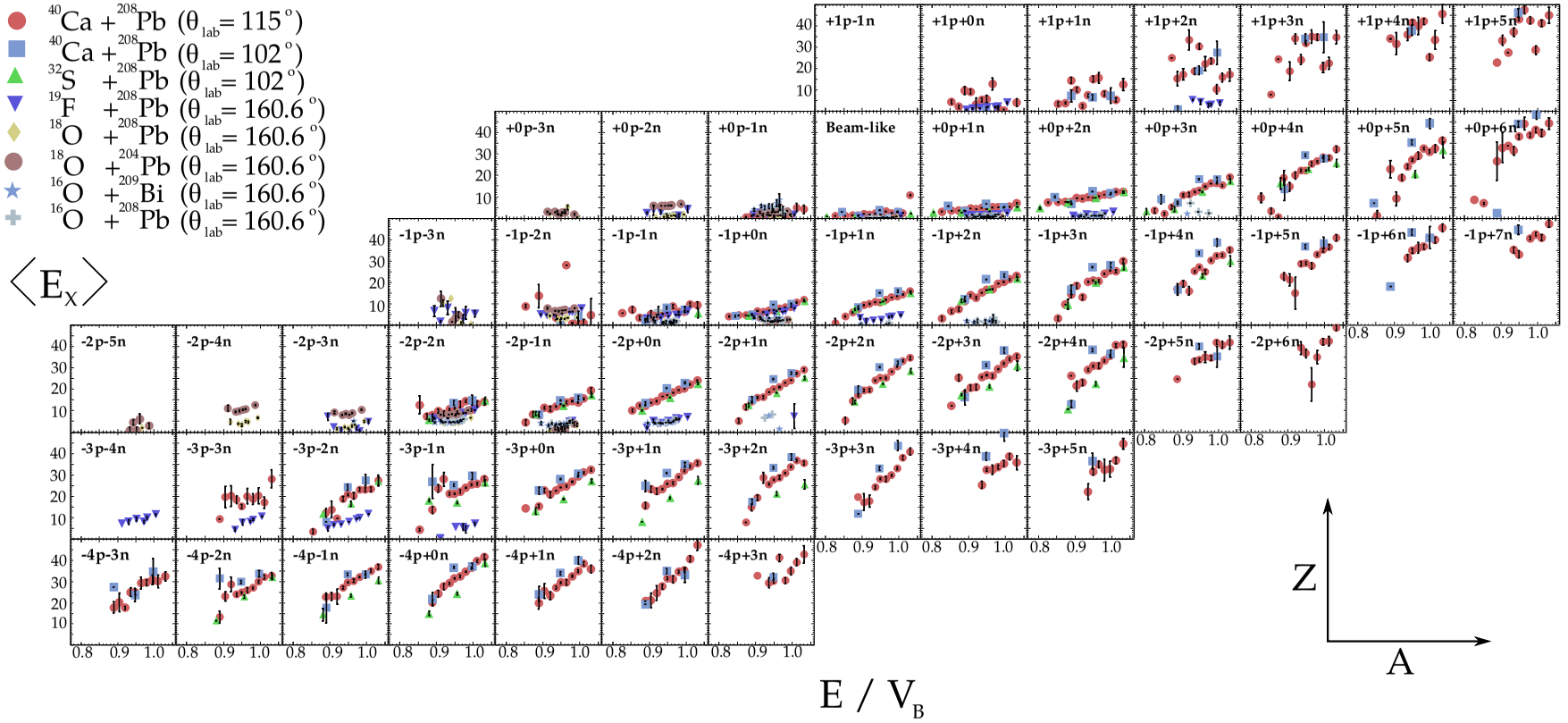

FIGURE 5.34: Comparison of the mean excitation energy vs. E/V_B between the different reaction systems for a subset of the observed transfer modes. The subset is chosen such that there are at least two measurements to compare for the relevant transfer mode. As such, measurements of more than four proton stripping are not shown (though are observed in the ^{40}Ca + ^{208}Pb cases).

dynamics for the heavier projectiles that emerges with a larger number of nucleons (and so a larger number of open exit channels) results in behaviour that is much less consistent between differing transfer modes.

A distinction is drawn in this plot (for the systems measured in the second experiment) between those modes which can conceivably occur as a one-step process (i.e. the nucleon flux in one direction only), to those in which there is a mutual exchange, which is indicated by the solid black borders on the data points for the former case. In the lighter systems, where there is no observation of mutual exchange of nucleons, all modes shown are *direct* by the definition that has been discussed. As was shown earlier in Figure 5.1, the direct transfer modes in the ^{32}S + ^{208}Pb and ^{40}Ca + ^{208}Pb systems follow closely the systematics of the lighter systems when the transfer probability is compared with the effective Q-value, whilst indirect modes behave in an entirely different manner. While in general a positive correlation is observed between Q_{eff} and $\langle E_x \rangle$ for direct transfer modes in all of the systems studied, in Figure 5.35 there is the suggestion of an entrance channel charge product dependence.

5.4.4 Influence of the number of nucleons transferred on the distribution of excitation energy

A plot of the mean excitation energy vs. the net number of nucleons that are transferred in each of the most significant observed modes is presented in Figure 5.36 for all of the systems studied at a bombarding energy approximately 95% that of the barrier height. A gate has been applied such that only modes with absolute probability greater than 10^{-4} are displayed. Again, direct transfer modes are distinguished from others by the inclusion of a black solid border on those points.

The general observation from this plot is that the mean excitation energy tends to increase where a larger number of nucleons are transferred. This is not surprising, as a known quality of the deep-inelastic reaction mechanism is for the system to experience strong energy damping as a result of frictional forces. While it is difficult to separate the products observed in the experiments reported here between simple (or direct) transfer

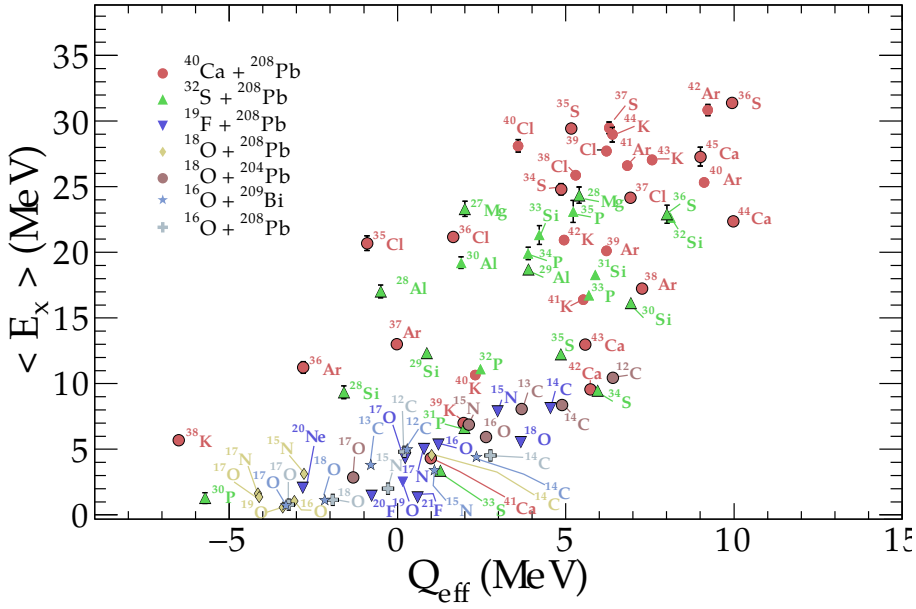

FIGURE 5.35: Mean excitation energy $\langle E_x \rangle$ for all transfer modes as a function of the effective Q-value Q_{eff}, including all reaction systems studied. Measurements displayed all correspond to a bombarding energy of $0.95V_B$. The displayed modes have been restricted to those with a Q-integrated probability of at least 10^{-4}. Transfer modes are distinguished between being direct (i.e. all nucleons move in the same direction — from target to projectile (pickup) or from the projectile to target (stripping)), and complex (nucleons move in both directions), by the black outlines drawn around points in the former case.

and deep inelastic collisions in a non-arbitrary manner, clearly in the case of nucleon flux that is not monodirectional (i.e. indirect) a simple transfer mechanism cannot be invoked. In the deep-inelastic case the fragments experience sticking, with energy losses occuring over timescales that are more similar to fusion than to direct single or multi-nucleon transfer, which occurs on a much faster timescale in a glancing collision trajectory. The exit channel fragments in a deep-inelastic collision are expected to emerge with kinetic energies close to the Coulomb barrier energy [60]— the relative motion in that case is said to be fully damped. This is likely the reason that $\langle E_x \rangle$ seems to saturate at around 30 MeV in the ^{40}Ca + ^{208}Pb system, for instance.

Also clear from Figure 5.36 is the system dependence. There appears to generally be a tendency for the systems with greater $Z_1 Z_2$ to exhibit high excitation energies in the exit channel. This is to be expected when comparing reactions at a similar energy relative to the barrier energy, as for heavier systems reaching such proximity in general requires

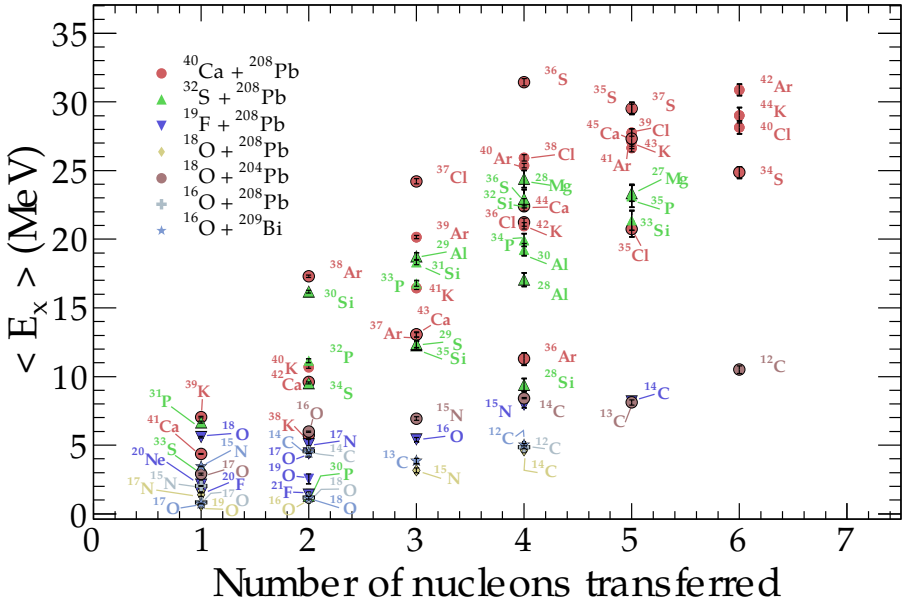

FIGURE 5.36: Mean excitation energy $\langle E_x \rangle$ for all transfer modes as a function of the total number of nucleons transferred between the reactants, where the shown measurement corresponds to 0.95 V_B. The displayed modes have been restricted to those with a Q-integrated probability of at least 10^{-4}. Transfer modes are distinguished between being direct (i.e. all nucleons move in the same direction — from target to projectile (pickup) or from the projectile to target (stripping)), and complex (nucleons move in both directions), by the black outlines drawn around points in the former case.

a larger density overlap due to the higher Coulomb repulsion. This is responsible for a large increase in the friction-like effects that lead to sticking and longer interaction times. Along with the much higher number of open channels that comes with the larger number of nucleons, this results in the opening up of the deep-inelastic mechanism that is known to compete with compound nucleus formation. However, similarly to some of the system effects that were described in relation to the $\langle E_x \rangle$ variation with bombarding energy, the strong cluster transfer modes that are evident in the ^{18}O-induced reactions seem to disturb those systematics.

5.5 Critical discussion of the methodology used in this study

There are two standard methods which have been widely used to measure transfer probabilities as a function of internuclear separation— measuring angular distributions at a

fixed energy, or alternatively measuring excitation functions at fixed backward angles at sub-barrier energies [80]. These two methods are in some ways physically equivalent since the internuclear separation is dependent on both the bombarding energy and the scattering angle (see Equation 2.10). Each holds certain benefits that might make them suitable for a particular study. Angular distributions are attractive as the excitation function can be extracted from a measurement using only one beam energy, reducing the beamtime necessary to perform such an experiment. The latter method, whilst requiring repeated tuning of the accelerated beam, requires a simpler detector setup as angular granularity is not necessary. For the experiment performed at the ANU laboratory, a gas detector was required to provide the desired mass and energy resolution. In practice it is difficult to build a segmented gas detector that would provide the necessary angular resolution to perform a measurement of transfer excitation functions, though this is suggested as a useful future objective for such studies. In principle the position information that is provided by the MCP detector in the PRISMA setup can be used to gate on the emission angle, however the PRISMA transmission has an angular dependence [131] which must be carefully accounted for where absolute yields of reaction products as a function of the scattering angle are required, such as in the measurement of cross-sections [149, 132]. In this work this has not been necessary and it is assumed that the observed yields (and E_x distributions) correspond to the mean scattering angle.

As has been discussed earlier, the experimental setup used in measurements at the ANU probably provides inadequate mass resolution for the study of isotopes heavier than Fluorine, whilst the Z-resolution of the PRISMA spectrometer is energy dependent (due to the need to adjust the stopping gas pressure in the IC array), and does not provide satisfactory Z identification at low kinetic energies. In this thesis work the requirement has been to push these experimental techniques to their limits in terms of (Z, A) identification such that the $Q_{g.g}$ values can be deduced and the excitation energy distribution can be reconstructed. This provides a vantage point that enables us to study not just the dissipation of energy, but the precise mechanisms through which it occurs. However, it must be acknowledged that issues may arise (with regards to systematic errors) in comparing measurements obtained using two very different experimental methods.

In other works, the issue of Z-identification has been overcome to some extent by studying reactions in inverse kinematics using a heavy beam projectile, where the additional kinematic energy in the forward focused light recoils allows improved separation using the $\Delta E - E$ apparatus, and the magnetic elements allow clean separation of the beam-like ions [150, 151]. It would be beneficial to investigate in future the feasibility of using inverse kinematics to repeat the measurements of the ^{32}S + ^{208}Pb and ^{40}Ca + ^{208}Pb using PRISMA (or a similar magnetic spectrometer device).

5.6 Discussion of results in relation to previous studies

The results obtained in this investigation can be considered relevant to previous studies in two main respects:

1. The measurement of the slopes of the exponential fall-off in the transfer probabilities, which have been used in the past to draw conclusions about the mechanism for transfer, whether that be through a successive flow of independent nucleons or if those nucleons move in correlated manner, such as in a cluster.

2. The measurement of excitation energy distributions, and their evolution as a function of the bombarding energy.

The measurements of transfer probabilities in this work [104] have led to similar conclusions that have been reached in other studies. The enhancements to particular modes (relative to the successive limits) have mostly been observed independently by other groups. For instance, the clustering properties of the ^{18}O nucleus have been reported through the thick target inverse kinematics method (TTIK), where α-cluster resonances are observed over a range of energies above the barrier [152]. In addition, the cluster transfer mechanism has been used to strongly populate cluster-core states in ^{212}Po [153] by bombardment of ^{208}Pb with ^{18}O ions.

The clustering properties of light nuclei are well established from a structure perspective. However, the extent to which reactions are influenced by cluster structures has not been examined in detail. While ab initio structure models have studied the emergence

of cluster structures from the nucleon-nucleon interaction, and there is an increasingly strong theoretical basis for their formation [154, 155, 156], reaction models to date have not successfully incorporated a cluster transfer mechanism within a coherent quantum approach.

In order to build a picture of the importance of multi-nucleon and cluster transfer modes in reactions, it is necessary to understand the energy dependence of these processes. This work presents a first thorough examination of the evolution of these modes with internuclear separation at bombarding energies that span the Coulomb barrier, which remarkably finds that many of the strong multi-nucleon transfer modes that have been observed at higher bombarding energies persist prominently to sub-barrier energy scales.

In the past there have been numerous studies that have examined energy losses in multinucleon transfer reactions in order to examine the transition between the quasi-elastic and deep-inelastic regimes. The experimental difficulties that are encountered in uniquely identifying reaction products in terms of the atomic number Z and isotopic mass mean that such studies have normally focused on the total kinetic energy loss (TKEL) from the system, since the ground-state-to-ground-state Q-value $Q_{g.g}$ cannot be determined without the exit fragment identities. Whilst the recent development of magnetic spectrometers for the study of transfer reactions have offered excellent mass resolution, identifying the reaction products in terms of Z must rely on $\Delta E - E$ techniques, which are unfeasible for massive nuclei. Whilst other methods exist for identification of the atomic number—namely the coincident detection of characteristic γ-ray emission from excited states, this does not provide a means of obtaining the full yield since the number of possible excited states is very large and many of the emissions cannot be assigned as they are unknown and thus cannot be associated with a specific isotope. This is beside the issues of efficiency in detection of γ-rays, particularly using coincidence techniques.

5.7 Relevance of the reported measurements to studies of fusion reactions

In the analysis of deep inelastic scattering, collision outcomes are generally characterized by the total kinetic energy loss (TKEL). Where the TKEL is large ($\geq$ 100 MeV), the loss of kinetic energy resulting from the reduction of the Coulomb energy ΔV_C after charge stripping reactions is a small fraction of the total. In contrast, in the reactions studied here, ΔV_C often makes up the majority of the TKEL. For example, in the light-heavy systems studied in experiment 1, if it were the ground states of the transfer products that were populated, the TKEL would be 25% of the total energy, or $\sim$ 15 MeV for a ΔZ = -2 stripping reaction. However, such ground-state transfer should be treated in a coupled reaction channels approach in the same way as scattering populating any discrete states at low E_x.

In contrast, the population of high excitation energies with high level densities cannot practically be included explicitly in a coupled channels model space. This can be more closely related to both fusion in nucleon-nucleus collisions, and the classical treatment of energy loss in deep inelastic collisions (DICs). In both, an effectively irreversible coupling to a heat bath is implicit in the different treatments between fusion and energy loss in DICs, compared with peripheral scattering which is treated explicitly in a coherent quantum approach. Thus in this investigation of the crossover from quasielastic scattering to the energy dissipation seen in DICs, the excitation energy populated should be a more robust indicator of the likelihood of energy dissipation than TKEL. Accordingly, the excitation energy distributions for each transfer mass partition have been determined, along with their dependence on the internuclear separation.

Distinctions can be drawn between those reactions involving single nucleon transfer and those that involve the transfer of many nucleons. The former generally leads to a strong population of states at low excitation energies, whilst the latter involves the excitation energy being distributed over very many states, and extending to high excitation energies. Coupled-channels models often only consider transfer to low lying, strongly populated states. These results show such processes are only a small part of the total, and that a

broad range of excited states in the products are populated via multinucleon transfer. As more nucleons are transferred, the mean excitation energy grows, up to a point where the kinetic energy is fully damped and $\langle E_x \rangle$ saturates close to the Coulomb barrier energy.

The significant probabilities for transfer reactions and the very many observed open channels in all of the reaction systems studied (even at beam energies below the fusion barriers), combined with the observed population of excitation energies of 10 MeV and more in many transfer modes, imply that the dissipation of kinetic energies cannot be ignored in attempting to model the fusion dynamics, even in the deep sub-barrier region. These observations strengthen the case that energy dissipation may play a significant role in fusion hindrance even for projectiles as light as ^{16}O. The development of a quantitative model to estimate the effect of (multi) nucleon transfer on fusion is required to take this idea further.

5.8 Summary

In this chapter I have presented the results of this investigation into the dissipation of energy through multi-nucleon transfer reaction modes, for several reaction systems spanning a range of mass asymmetries, across an energy range that spans the region of the Coulomb barrier. These results have been discussed within the context of existing scholarship. In doing so I have presented the essential experimental systematics that will provide a foundation for a future research direction that aims to appropriately treat dissipative dynamics in the fusion process in a quantitative and microscopic manner.

In the next and final chapter, the conclusions of this investigation and suggested future work on this topic will be presented. I will re-examine the questions posed in the first two chapters, and discuss how the data presented here go towards answering them.

Chapter 6

Conclusions and outlook

This work was motivated by the need to improve the understanding of multinucleon transfer processes at near barrier energies, with particular focus on determining the excitation energy spectra of all observed transfer products. New measurements of excitation energies of transfer products formed in reactions of a variety of light (O, F) to medium mass (S, Ca) projectiles incident on targets around the Pb region of the chart of the nuclides are presented. The range of projectile-target combinations studied has provided information on the evolution of the excitation energy distribution with increasing charge product $Z_1 Z_2$ of the colliding nuclei from 656 to 1640, and coupled with measurements at bombarding energies spanning the barrier region in each system, this work has built a picture of the growing importance (and earlier onset) of dissipation in heavier systems as the reactants approach one another.

Determining the excitation energy spectra of all transfer products requires each product to be uniquely identified in terms of mass and atomic number. Such information has not been readily available thus far, as in most work on transfer and deep inelastic reactions the total kinetic energy loss (TKEL) is reported, which does not rely on identification of the isotope. A large fraction of the TKEL, for lighter projectiles at near-barrier energies as studied here, arises due to the change of the Coulomb barrier following stripping of protons even to the ground state. Such process can be accounted for in Coupled Reactions Channels (CRC) calculations, much in the same way as including any discrete state. The interest here is rather in identifying the processes that lead to high excitation energies, i.e. populating regions of high level densities such that the excitation energy is distributed

over many states. These processes can cause irreversible damping of kinetic energy (e.g. into internal and collective excitations), and cannot practically be included in a coupled channels model.

This work has made use of two very different experimental set-ups to identify all transfer products in terms of mass and atomic number. The purpose of doing so has been to identify the modes that are most significantly associated with the damping of kinetic energy, as well as to see the differences in the character of these processes between reactions with neighbouring nuclei. One of the significant finding of this work is that substantial yields for a large range of transfer products are seen, at energies below the fusion barrier, that correspond to significant loss of kinetic energy to excitations distributed over many states. Thus, dissipation of kinetic energy to complex excitations, which is known to occur in deep inelastic collisions of very heavy nuclei [60, 61], is also present in the much lighter systems studied in this work. Their presence even at energies below the barrier suggests that the prevailing theoretical models that are used to predict reaction outcomes have a critical shortcoming in generally neglecting dissipative dynamics. There is a growing realisation within the community that this is an issue that needs addressing, and the results of this work provide further evidence to support this.

This work has identified a distinction between lighter (O, F) and heavier (S, Ca) projectiles in respect to the most important reaction channels contributing to the transfer yield and facilitating energy dissipation. The lighter systems exhibit a range of direct transfer modes which are thought to have strong contributions from cluster and correlated nucleon transfer, whereas in the heavier systems the transfer yield includes significant yields of products that result from the transfer of nucleons in both directions, here referred to as indirect transfer.

The excitation energies of transfer products, in reactions induced by both the lighter and the heavier projectiles, increase more rapidly than the expected increase of the optimal Q-value with bombarding energy. Excitation energies of up to 15 MeV in reactions induced by light projectiles and up to $\sim$40 MeV for the heavier projectiles are populated. The high level densities at such large excitation energies (most likely in the heavier nuclei)

can be expected to lead to partial or complete thermalisation (referred to here as energy dissipation), and thus transfer of many nucleons appears to be an effective doorway for the irreversible dissipation of kinetic energy.

Dissipation has been shown to be most significant for transfer modes that involve the exchange of large numbers of nucleons. Increases in excitation energy are strongly correlated with the number of protons that are transferred in a collision. Indirect transfer modes in general exhibit greater dissipative character than direct modes— this is to be generally expected as these modes, with a flow of nucleons in both directions, are presumably occuring in regions of significant matter overlap and may be expected to have reasonably long interaction times as compared to a direct mechanism. These events are likely equivalent of deep inelastic reactions seen in collisions of very heavy nuclei.

Irrespective of the detailed transfer mechanisms, the key finding of this work is the universal dominance of multi-nucleon transfers that cause loss of kinetic energy to complex excitations, even at energies below the barrier. That such processes are observed not just for the heaviest system ($Z_1Z_2 = 1640$) but also in the lighter systems ($Z_1Z_2 = 656$), shows the importance and generality of energy dissipative processes near the barrier. Coupled-channels models commonly only consider transfer to, and excitation of, low lying, strongly populated states. These results show such processes are only a very small part of the total reflected flux comprising transfer and inelastic scattering. Whilst the CRC approaches have demonstrated the importance of the low-lying states, clearly a more realistic treatment of the reaction mechanism must consider the large range of transfer processes that occur near the barrier, particularly since they lead to complex states at high excitation energies akin to partial thermalisation. Thus parts of the system are no longer in the coherent superposition generally assumed in the CRC approach. Such dissipative process can cause hindrance of fusion both above and below the barrier.

In common with other areas of physics, incorporating dissipative dynamics within a quantum model remains a challenge. A first step in the nuclear reactions context could be to incorporate multi-nucleon transfer (and thus energy dissipation) phenomenologically, whilst treating the low-lying discrete states explicitly in the coupled channels model.

Measurements presented in this thesis can provide unique quantitative inputs to such developments. Measurements of excitation energies of multi-nucleon transfer products at above barrier energies, and for a range of systems, will be useful for the development and testing of such new models. Such developments will represent the first step towards obtaining a simultaneous description of all reaction processes from energies well below to above the fusion barrier.

Appendix A

Kinematics of binary reactions

In this section the kinematic considerations necessary for the derivation of the reaction Q-value (and therefore excitation energy) from energy measurements are discussed.

Consider a binary reaction of the form $a + A \longrightarrow b + B$, or in the standard notation $A(a,b)B$, where a projectile nucleus a travelling with a velocity v_a along the x-axis, is incident on a stationary target nucleus A. This situation is illustrated in the laboratory frame-of-reference, in Figure A.1, and within the center-of-mass frame in Figure A.2 [157, 64].

Considering first the conservation of momentum in the x-direction:

$$\begin{aligned} p_x^a + p_x^A &= p_x^b + p_x^B \\ m_a v_a + 0 &= m_b v_b \cos(\theta) + m_B v_B \cos(\phi) \end{aligned} \tag{A.1}$$

In the y-direction, conservation of momentum gives:

$$\begin{aligned} p_y^a + p_y^A &= p_y^b + p_y^B \\ 0 + 0 &= -m_b v_b \sin(\theta) + m_B v_B \sin(\phi) \end{aligned} \tag{A.2}$$

The law of conservation of energy meanwhile gives:

$$E_a + Q = E_b + E_B, \tag{A.3}$$

where Q is the reaction Q-value, representing the energy lost or gained in the reaction according to the difference of total mass between the entrance and exit channels:

$$Q = (m_a + m_A - m_b - m_B)c^2 \tag{A.4}$$

Expressing the non-relativistic momenta $p = mv$ instead in terms of the kinetic energies, Equations A.1 and A.2 become:

$$\sqrt{2m_aE_a} - \sqrt{2m_bE_b}\cos(\theta) = \sqrt{2m_BE_B}\cos(\phi) \tag{A.5}$$

and

$$\sqrt{2m_bE_b}\sin(\theta) = \sqrt{2m_BE_B}\sin(\phi) \tag{A.6}$$

respectively. Squaring both sides of Equations A.5 and A.6 then gives:

$$2m_aE_a - 4\sqrt{m_am_bE_aE_b}\cos(\theta) + 2m_bE_b\cos^2(\theta) = 2m_BE_B\cos^2(\phi) \tag{A.7}$$

and

$$2m_bE_b\sin^2(\theta) = 2m_BE_B\sin^2(\phi). \tag{A.8}$$

Now adding together and reducing:

$$\begin{aligned}
2m_BE_B\cos^2(\phi) + 2m_BE_B\sin^2(\phi) &= 2m_aE_a + 2m_bE_b\cos^2(\theta) + 2m_bE_b\sin^2(\theta) - 4\sqrt{m_am_bE_aE_b}\cos(\theta) \\
2m_BE_B\left(\sin^2(\phi) + \cos^2(\phi)\right) &= 2m_aE_a + 2m_bE_b\left(\sin^2(\theta) + \cos^2(\theta)\right) - 4\sqrt{m_am_bE_aE_b}\cos(\theta) \\
m_BE_B &= m_aE_a + m_bE_b - 2\sqrt{m_am_bE_aE_b}\cos(\theta)
\end{aligned} \tag{A.9}$$

Substituting Equation A.3 into Equation A.9 and rearranging gives:

$$Q = E_b\left(1+\frac{m_b}{m_B}\right) - E_a\left(1-\frac{m_a}{m_B}\right) - \frac{2}{m_B}\sqrt{m_a m_b E_a E_b}\cos(\theta) \tag{A.10}$$

Expressing Equation A.10 instead in terms of the atomic mass numbers A_i results in:

$$Q = \frac{A_b + A_B}{A_B}E_b - \frac{A_B - A_a}{A_B}E_a - \frac{2\sqrt{A_a A_b E_a E_b}}{A_B}\cos\theta_{\text{lab}}. \tag{A.11}$$

Thus the reaction Q-value can be directly extracted from the measurement of the energy of the ejectile (together with an identification of its mass), assuming a binary reaction so that the initial and final masses of all fragments are known.

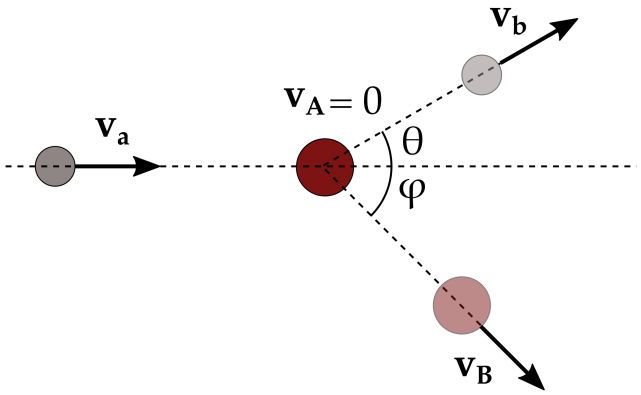

FIGURE A.1: Reaction kinematics in the laboratory frame of reference, in the case of a projectile a incident on an initially stationary target A.

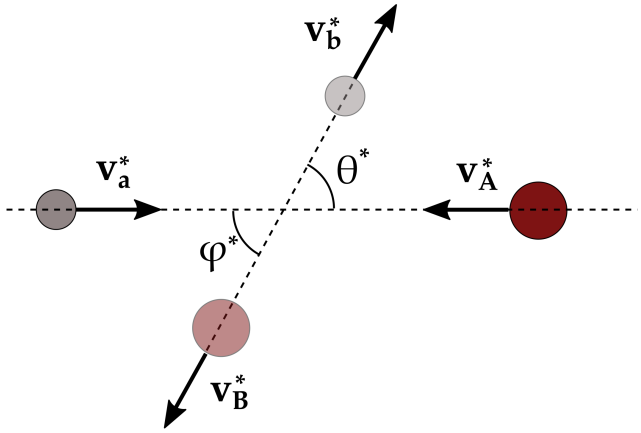

FIGURE A.2: Reaction kinematics in the center-of-mass frame of reference. The star superscripts indicate the expression of quantities within the center-of-mass frame.

Starting instead from the center-of-mass frame, as depicted in Figure A.2, the two nuclei initially move with equal and opposite momenta:

$$\begin{aligned} \mathbf{p}_a^* &= -\mathbf{p}_A^* \\ m_a \mathbf{v}_a^* &= m_A \mathbf{v}_A^* \end{aligned} \tag{A.12}$$

The center-of-mass velocities $\mathbf{v}_i$ of the nuclei a and A are given by:

$$\mathbf{v}_a^* = \mathbf{v}_a - \mathbf{v}_{cm} \tag{A.13}$$

$$\mathbf{v}_A^* = -\mathbf{v}_{cm} \tag{A.14}$$

Where the velocity of the center-of-mass system in the laboratory frame is given by:

$$\mathbf{v}_{cm} = \frac{m_a \mathbf{v}_a + m_A \mathbf{v}_A}{m_a + m_A} \tag{A.15}$$

The relationship between the velocity of the center-of-mass system in the entrance and exit channels is related to the change in mass:

$$v_{cm,f} = \left(\frac{m_a + m_A}{m_b + m_B} \right) v_{cm,i} \tag{A.16}$$

The kinetic energy of the center-of-mass system in the entrance and exit channels respectively are:

$$E_{cm}^i = \frac{1}{2}(m_a + m_A) v_{cm,i}^2 = \frac{m_a}{m_a + m_A} E_a \tag{A.17}$$

$$E_{cm}^f = \frac{1}{2}(m_b + m_B) v_{cm,f}^2 = \frac{m_b}{m_b + m_B} E_b \tag{A.18}$$

The reaction Q-value can be defined from the difference between these two quantities. The total kinetic energy loss (or equivalently, the energy dissipation from the center-of-mass system) is defined as:

$$TKEL = -Q = E^i_{cm} - E^f_{cm} \tag{A.19}$$

Inspecting Equation A.11, one can notice that it is quadratic in $\sqrt{E_b}$ with solution:

$$\sqrt{E_b} = \frac{1}{A_b + A_B}[\sqrt{A_a A_b E_a}\cos(\theta) \pm \sqrt{A_a A_b \cos^2(\theta) + (m_b + m_B)(E_a(m_B - m_a) + Qm_B)}] \tag{A.20}$$

Which allows calculation of the ejectile energy for a process with Q-value Q at an angle θ in the laboratory frame-of-reference. Note only the positive solution to the quadratic equation is physically allowed.

Elastic scattering is the special case where there is no mass exchange between the reactants in the collision ($A_a = A_b$ and $A_A = A_B$), and no dissipation of kinetic energy (i.e. $Q = 0$). Under these conditions Equation A.20 can be simplified to:

$$\sqrt{E_b} = \frac{A_a}{A_A + A_a}\sqrt{E_a}[\cos(\theta) + ((\frac{A_A}{A_a})^2 - \sin^2(\theta))^{1/2}] \tag{A.21}$$

Appendix B

PRISMA frames of reference

The important frames of reference to consider in the analysis of PRISMA data are shown in Figure B.1. These are the laboratory, MCP, and PRISMA frames of reference [133, 132]. An overview of these three different frames is shown in Figure B.1, highlighted by the three sets of blue axes.

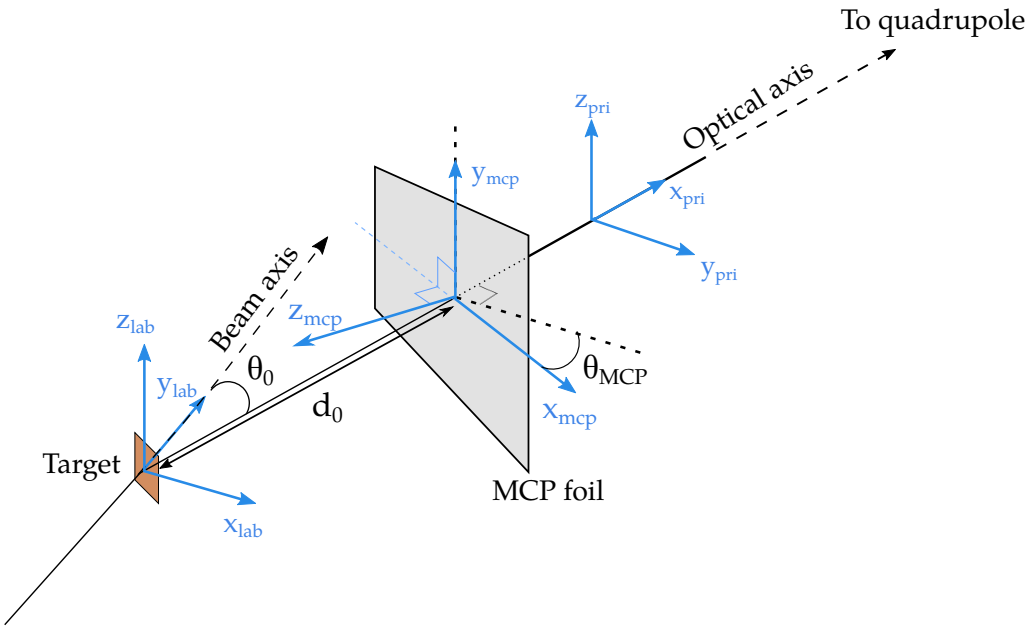

FIGURE B.1: PRISMA frames of reference.

An important part of the interpretation of PRISMA data is the transformation from the position coordinates of the MCP detector to polar coordinates in the laboratory and PRISMA frames of reference. The MCP is positioned at an angle of $\theta_{MCP} = 45°$ to the

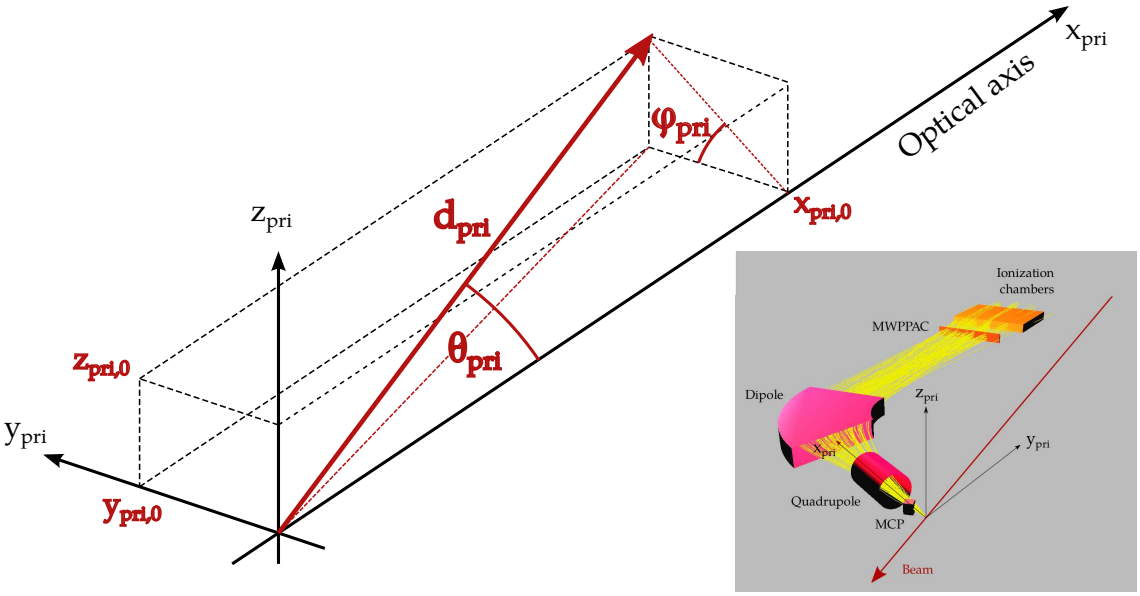

FIGURE B.2: PRISMA frame of reference.

optical axis of PRISMA, at a distance d_0 = 25 cm from the target. In this section the coordinates notated as x and y are defined as those in the MCP position coordinates.

The origin of the PRISMA frame-of-reference is located at the center of the target, at the position where the reactions are assumed to take place. The x_{Pri} axis lies along the optical axis of the PRISMA device- passing through the center of the MCP foil ($x = y = 0$) and passing centrally through the quadrupole yoke. The transformation between the cartesian MCP coordinates x and y and those in the PRISMA frame are deduced from trigonometric rules:

$$x_{\text{pri}} = d_0 - x\sin(\theta_{\text{MCP}}) \tag{B.1}$$

$$y_{\text{pri}} = -x\cos(\theta_{\text{MCP}}) \tag{B.2}$$

$$z_{\text{pri}} = y \tag{B.3}$$

The polar coordinates can similarly be deduced through the geometry shown in Figure B.2:

$$d_{\text{pri}} = \sqrt{(x^2_{\text{pri}}) + (y^2_{\text{pri}}) + (z^2_{\text{pri}})} \tag{B.4}$$

$$\theta_{\text{pri}} = \arccos\left(\frac{x_{\text{pri}}}{d_{\text{pri}}}\right) \tag{B.5}$$

$$\phi_{\text{pri}} = \arctan\left(\frac{y_{\text{pri}}}{z_{\text{pri}}}\right) \tag{B.6}$$

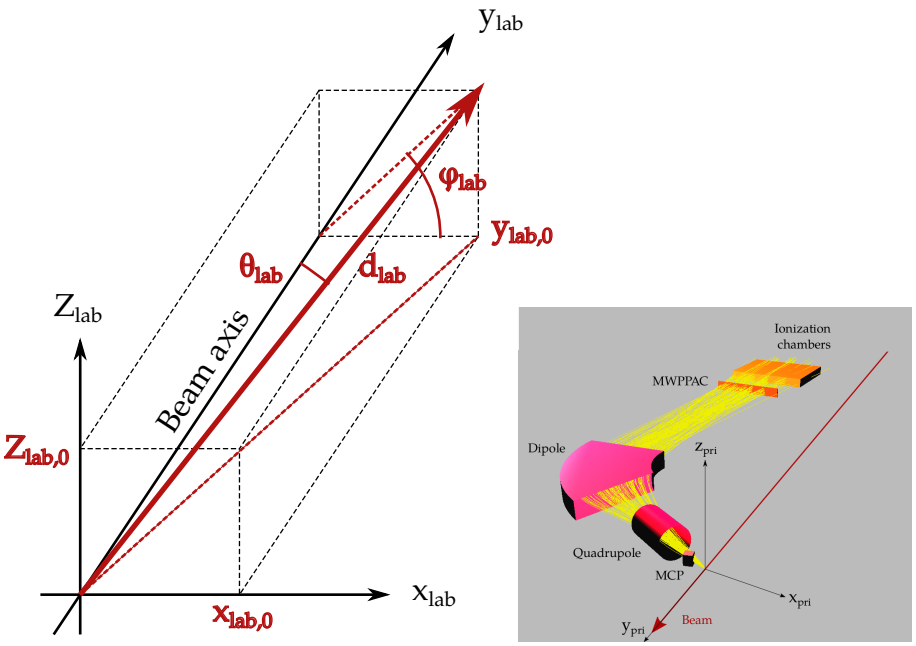

FIGURE B.3: Laboratory frame of reference.

The origin of laboratory frame-of-reference is also located at the center of the target, with the y_{lab} axis running along the beam axis. The z_{lab} axis is parallel and colocated with the z_{pri} axis- the laboratory frame-of-reference is thus a rotation of the PRISMA frame in the $x - y$ plane. The cartesian coordinates in this frame are deduced as:

$$x_{\text{lab}} = d_0 \sin(\theta_0) + x \sin(\frac{\pi}{2} - \theta_{\text{MCP}} - \theta_0) \tag{B.7}$$

$$y_{\text{lab}} = d_0 \cos(\theta_0) + x \cos(\frac{\pi}{2} - \theta_{\text{MCP}} - \theta_0) \tag{B.8}$$

$$z_{lab} = y \tag{B.9}$$

θ_0 in the above equations and in Figure B.1 is the angle at which PRISMA is oriented relative to the beam axis. The polar coordinates then become:

$$d_{\text{lab}} = \sqrt{(x^2_{\text{lab}}) + (y^2_{\text{lab}}) + (z^2_{\text{lab}})} \tag{B.10}$$

$$\theta_{\text{lab}} = \arccos\left(\frac{x_{\text{lab}}}{d_{\text{lab}}}\right) \tag{B.11}$$

$$\phi_{\text{lab}} = \arctan\left(\frac{y_{\text{lab}}}{z_{\text{lab}}}\right) \tag{B.12}$$

Appendix C

Extracted slope parameters $\alpha_{\mathbf{Exp}}$ and Q-values of important transfer modes

TABLE C.1: Ground-state-to-ground-state $Q_{g.g}$ and effective ($Q_{g.g}$ + ΔV_C) Q-values for various transfer processes in the systems studied, as well as theoretical slope parameters α_{Th} and experimental α_{Exp} ones where it has been possible to extract them. ΔV_C were calculated at the separations determined through Equation 2.10 for the measurements which most closely match 95% of the barrier energy. The transfer probabilities are plotted against $Q_{eff} = Q_{g.g} + \Delta V_C$ in Figure 5.1.

Values for the experimental and theoretical slope parameters are only presented for those modes in which they could be extracted with a reasonable degree of error (no more than 20% of the fitted value), and where the mode in question can be conceived of as being *direct* in the manner described in Section 5.2. It is assumed that the conception of the theoretical slope is not defined for *indirect* modes. († For the -2p-2n channels in each reaction, I have given α_{Th} in brackets where it has been calculated using Q_α as the effective binding energy.)

(* The 2n stripping channel of ^{18}O + ^{208}Pb is likely underestimated slightly as these events are obscured by the elastically scattered particles.)

(** The masses of the Neon isotopes cannot be distinguished, so it is unknown if the yield corresponds to a single isotope or several.)

(*** The slope in this case is extracted from the mass integrated Z = 10 events.)

System	Transfer mode	Product	$Q_{g.g}$ (MeV)	$Q_{g.g}$ - ΔV_C (MeV)	P_{Tr}	α_{Calc} (fm^{-1})†	α_{Exp} (fm^{-1})
$^{16}O + ^{208}Pb$	+1p	^{17}F	-7.403	-15.241	-	0.70	-
	+2n	^{18}O	-1.917	-1.917	0.0079 ± 0.0033	1.15	1.38 ± 0.30
	+1n	^{17}O	-3.224	-3.224	0.0306 ± 0.0062	0.59	0.70 ± 0.15
	-1n	^{15}O	-11.726	-11.726	-	0.61	-
	-2n	^{14}O	-19.764	-19.764	-	1.19	-
	-1p	^{15}N	-8.328	-0.275	0.0266 ± 0.0009	0.71	1.16 ± 0.04
	-1p-1n	^{14}N	-14.557	-6.250	-	1.29	-
	-1p-2n	^{13}N	-19.972	-12.670	-	1.84	-
	-2p	^{14}C	-13.552	2.769	0.0078 ± 0.0005	1.38	2.37 ± 0.06
	-2p-1n	^{13}C	-17.178	-0.856	0.0009 ± 0.0001	1.93	2.61 ± 0.25
	-2p-2n	^{12}C	-16.116	0.205	0.0042 ± 0.0003	2.45 (2.02)	1.73 ± 0.08
$^{16}O + ^{209}Bi$	+1p	^{17}F	-3.199	-11.054	-	0.70	-
	+2n	^{18}O	-2.160	-2.160	0.0003 ± 0.0007	1.15	4.52 ± 0.13
	+1n	^{17}O	-3.317	-3.317	0.0223 ± 0.0015	0.59	0.88 ± 0.08
	-1n	^{15}O	-11.059	-11.059	-	0.60	-
	-2n	^{14}O	-19.144	-19.144	-	1.19	-
	-1p	^{15}N	-7.144	0.924	0.0160 ± 0.0005	0.72	1.35 ± 0.02
	-1p-1n	^{14}N	-13.426	-5.359	-	1.29	-
	-1p-2n	^{13}N	-17.972	-9.904	-	1.84	-
	-2p	^{14}C	-14.368	1.980	0.0045 ± 0.0006	1.38	3.14 ± 0.92
	-2p-1n	^{13}C	-17.499	-1.151	0.0009 ± 0.0003	1.93	2.84 ± 0.17
	-2p-2n	^{12}C	-16.416	-0.069	0.0040 ± 0.0006	2.45 (1.21)	2.81 ± 0.66
$^{18}O + ^{204}Pb$	+1p	^{19}F	1.357	-6.408	-	0.70	-
	+1n	^{19}O	-4.440	-4.440	0.0032 ± 0.0012	0.59	2.53 ± 0.11

Table C.1 – continued on next page

Table C.1 – continued from previous page

System	Transfer mode	Product	$Q_{g.g}$ (MeV)	$Q_{g.g}$ - ΔV_C (MeV)	P_{Tr}	α_{Calc} (fm^{-1})†	α_{Exp} (fm^{-1})
	-1n	^{17}O	-1.312	-1.312	0.0305 ± 0.0012	0.60	0.88 ± 0.27
	-2n	^{16}O	2.631	2.631	0.0324 ± 0.0036	1.19	1.45 ± 0.19
	-1p	^{17}N	-12.701	-4.722	0.0012 ± 0.0004	0.71	1.99 ± 0.59
	-1p-1n	^{16}N	-11.547	-3.568	-	1.29	-
	-1p-2n	^{15}N	-5.938	2.040	0.0116 ± 0.0015	1.84	2.52 ± 0.32
	-2p	^{16}C	-21.404	-5.232	-	1.38	-
	-2p-1n	^{15}C	-18.619	-2.448	-	1.93	-
	-2p-2n	^{14}C	-11.442	4.727	0.0276 ± 0.0024	2.46 (1.22)	2.90 ± 0.19
	-2p-3n	^{13}C	-12.650	3.518	0.0009 ± 0.0004	2.97	3.11 ± 1.10
	-2p-4n	^{12}C	-9.938	6.229	0.0012 ± 0.0004	3.45	3.44 ± 0.09
	-3p-4n	^{11}B	-22.912	1.660	-	3.976	-
^{18}O + ^{208}Pb	+1p	^{19}F	-0.010	-7.790	-	0.702	-
	+1n	^{19}O	-3.412	-3.412	0.0166 ± 0.0018	0.59	1.14 ± 0.91
	-1n	^{17}O	-4.108	-4.108	0.0162 ± 0.0013	0.60	0.63 ± 0.46
	-2n	^{16}O	-3.065	-3.065	0.0155 ± 0.0009*	1.18	1.18 ± 0.17
	-1p	^{17}N	-12.143	-4.153	0.0011 ± 0.0002	0.71	1.49 ± 0.17
	-1p-1n	^{16}N	-13.423	-5.433	0.0005 ± 0.0001	1.29	1.75 ± 0.22
	-1p-2n	^{15}N	-10.774	-2.784	0.0028 ± 0.0003	1.84	2.20 ± 0.12
	-2p	^{16}C	-20.272	-4.073	-	1.38	-
	-2p-1n	^{15}C	-19.971	-3.772	-	1.93	-
	-2p-2n	^{14}C	-15.182	1.017	0.0270 ± 0.0010	2.46 (2.01)	2.73 ± 0.01
	-2p-3n	^{13}C	-19.002	-2.803	0.0018 ± 0.0004	2.97	3.33 ± 0.05
	-2p-4n	^{12}C	-18.061	-1.862	0.0004 ± 0.0002	3.45	3.09 ± 0.07
	-3p-4n	^{11}B	-29.943	-5.447	-	3.97	-
^{19}F + ^{208}Pb	+1p+2n	^{22}Ne	+8.609	0.957		1.80	-

Table C.1 – continued on next page

Table C.1 – continued from previous page

System	Transfer mode	Product	$Q_{g.g}$ (MeV)	$Q_{g.g}$ - ΔV_C (MeV)	P_{Tr}	α_{Calc} (fm^{-1})†	α_{Exp} (fm^{-1})
	+1p+1n	^{21}Ne	+4.749	-2.903	$0.0018 \pm 0.0003^{**}$	1.27	$0.72 \pm 0.15^{***}$
	+1p	^{20}Ne	+4.839	-2.813		0.71	-
	+1n	^{20}F	-0.766	-0.766	0.0604 ± 0.0120	0.59	0.82 ± 0.08
	+2n	^{21}F	0.597	0.597	-	1.16	-
	-1n	^{18}F	-6.494	-6.494	-	0.60	-
	-1p	^{18}O	-4.195	3.496	0.1024 ± 0.0079	0.71	0.65 ± 0.065
	-1p-1n	^{17}O	-7.635	0.055	0.0099 ± 0.0053	1.29	0.73 ± 0.41
	-1p-2n	^{16}O	-6.640	1.050	0.0246 ± 0.0037	1.85	1.02 ± 0.12
	-2p	^{17}N	-15.153	0.48	0.0007 ± 0.0002	1.38	1.21 ± 0.45
	-2p-1n	^{16}N	-16.487	-0.857	0.0004 ± 0.0002	1.94	1.31 ± 0.31
	-2p-2n	^{15}N	-12.968	3.357	0.0088 ± 0.0008	2.47 (1.96)	0.68 ± 0.27
	-3p-2n	^{14}C	-19.676	4.024	0.0118 ± 0.0009	3.05	2.00 ± 0.40
	-3p-3n	^{13}C	-22.981	0.719	0.0001 ± 0.0001	3.54	2.28 ± 2.71
	-3p-4n	^{12}C	-21.980	1.720	0.0005 ± 0.0002	4.00	2.58 ± 0.13
^{32}S + ^{208}Pb	+5n	^{37}S	3.919	3.919	0.0003 ± 0.0001	2.94	-
	+4n	^{36}S	8.010	8.010	0.0023 ± 0.0002	2.40	-
	+3n	^{35}S	4.852	4.852	0.0081 ± 0.0003	1.83	-
	+2n	^{34}S	5.953	5.953	0.0528 ± 0.0008	1.24	-
	+1n	^{33}S	1.274	1.274	0.1695 ± 0.0016	0.63	-
	-1p+4n	^{35}P	-1.845	5.221	0.0013 ± 0.0001	-	-
	-1p+3n	^{34}P	-3.179	3.885	0.0039 ± 0.0002	-	-
	-1p+2n	^{33}P	-1.372	5.686	0.0161 ± 0.0004	-	-
	-1p+1n	^{32}P	-4.589	2.468	0.0261 ± 0.0006	-	-
	-1p	^{31}P	-5.065	1.989	0.0560 ± 0.0008	0.72	-
	-1p-1n	^{30}P	-12.771	-5.716	0.0013 ± 0.0001	1.33	-

Table C.1 – continued on next page

Table C.1 – continued from previous page

System	Transfer mode	Product	$Q_{g.g}$ (MeV)	$Q_{g.g}$ - ΔV_C (MeV)	P_{Tr}	α_{Calc} (fm^{-1})†	α_{Exp} (fm^{-1})
	-2p+4n	^{34}Si	-9.626	4.722	0.0004 ± 0.0001	-	-
	-2p+3n	^{33}Si	-10.126	4.215	0.0013 ± 0.0001	-	-
	-2p+2n	^{32}Si	-6.214	8.114	0.0100 ± 0.0003	-	-
	-2p+1n	^{31}Si	-8.450	5.874	0.0199 ± 0.0005	-	-
	-2p	^{30}Si	-7.378	6.935	0.0485 ± 0.0008	1.41	-
	-2p-1n	^{29}Si	-13.437	0.878	0.0089 ± 0.0003	2.00	-
	-2p-2n	^{28}Si	-15.902	-1.592	0.0022 ± 0.0002	2.57 (1.22)	-
	-3p+2n	^{31}Al	-19.931	1.896	0.0006 ± 0.0001	-	-
	-3p+1n	^{30}Al	-19.920	1.895	0.0024 ± 0.0002	-	-
	-3p	^{29}Al	-17.902	3.896	0.0073 ± 0.0003	2.08	-
	-3p-1n	^{28}Al	-22.293	-0.497	0.0022 ± 0.0002	2.65	-
	-3p-2n	^{27}Al	-23.988	-2.201	0.0006 ± 0.0001	3.21	-
	-4p+1n	^{29}Mg	-28.390	1.130	0.0002 ± 0.0000	-	-
	-4p	^{28}Mg	-24.086	5.402	0.0015 ± 0.0001	2.72	-
	-4p-1n	^{27}Mg	-27.479	2.002	0.0012 ± 0.0001	3.28	-
	-4p-2n	^{26}Mg	-27.230	2.233	0.0009 ± 0.0001	3.82	-
^{40}Ca + ^{208}Pb	+1p+5n	^{46}Sc	11.146	4.846	0.0002 ± 0.0000	-	-
	+1p+4n	^{45}Sc	10.234	3.937	0.0002 ± 0.0000	-	-
	+1p+3n	^{44}Sc	5.567	-0.730	0.0003 ± 0.0000	-	-
	+1p+2n	^{43}Sc	3.414	-2.882	0.0002 ± 0.0000	-	-
	+1p+1n	^{42}Sc	-2.220	-8.517	0.0003 ± 0.0000	-	-
	+1p	^{41}Sc	-6.919	-13.215	0.0002 ± 0.0000	0.73	2.42 ± 0.07
	+6n	^{46}Ca	12.474	12.474	0.0005 ± 0.0000	3.57	-
	+5n	^{45}Ca	9.004	9.004	0.0013 ± 0.0001	3.01	2.34 ± 0.76
	+4n	^{44}Ca	9.983	9.983	0.0042 ± 0.0001	2.44	2.57 ± 0.72

Table C.1 – continued on next page

Table C.1 – continued from previous page

System	Transfer mode	Product	$Q_{g.g}$ (MeV)	$Q_{g.g}$ - ΔV_C (MeV)	P_{Tr}	α_{Calc} (fm^{-1})†	α_{Exp} (fm^{-1})
	+3n	^{43}Ca	5.584	5.584	0.0116 ± 0.0002	1.85	2.23 ± 0.15
	+2n	^{42}Ca	5.738	5.738	0.0538 ± 0.0005	1.25	1.37 ± 0.03
	+1n	^{41}Ca	0.995	0.995	0.1049 ± 0.0007	0.63	0.57 ± 0.01
	-1n	^{39}Ca	-11.706	-11.706	0.0010 ± 0.0001	0.62	0.95 ± 0.03
	-1p+7n	^{46}K	-0.444	6.068	0.0002 ± 0.0000	-	-
	-1p+6n	^{45}K	1.553	8.061	0.0004 ± 0.0000	-	-
	-1p+5n	^{44}K	-0.118	6.388	0.0013 ± 0.0001	-	-
	-1p+4n	^{43}K	1.060	7.564	0.0043 ± 0.0001	-	-
	-1p+3n	^{42}K	-1.545	4.957	0.0079 ± 0.0002	-	-
	-1p+2n	^{41}K	-0.981	5.519	0.0215 ± 0.0003	-	-
	-1p+1n	^{40}K	-4.190	2.309	0.0293 ± 0.0004	-	-
	-1p	^{39}K	-4.529	1.967	0.0496 ± 0.0005	0.72	1.14 ± 0.03
	-1p-1n	^{38}K	-13.002	-6.504	0.0029 ± 0.0001	1.33	2.03 ± 0.36
	-1p-2n	^{37}K	-19.936	-13.437	0.0002 ± 0.0000	1.93	2.21 ± 0.25
	-2p+6n	^{44}Ar	-5.588	7.636	0.0001 ± 0.0000	-	-
	-2p+5n	^{43}Ar	-7.076	6.145	0.0005 ± 0.0000	-	-
	-2p+4n	^{42}Ar	-3.990	9.223	0.0023 ± 0.0001	-	-
	-2p+3n	^{41}Ar	-6.381	6.829	0.0060 ± 0.0002	-	-
	-2p+2n	^{40}Ar	-4.085	9.119	0.0163 ± 0.0003	-	-
	-2p+1n	^{39}Ar	-6.987	6.215	0.0244 ± 0.0003	-	-
	-2p	^{38}Ar	-5.927	7.267	0.0463 ± 0.0005	1.42	2.03 ± 0.05
	-2p-1n	^{37}Ar	-13.215	-0.017	0.0083 ± 0.0002	2.01	2.00 ± 0.17
	-2p-2n	^{36}Ar	-15.994	-2.799	0.0016 ± 0.0001	2.59	2.37 ± 0.36
	-2p-3n	^{35}Ar	-26.894	-13.693	0.0001 ± 0.0000	3.17	3.03 ± 0.27
	-3p+5n	^{42}Cl	-19.262	0.891	0.0001 ± 0.0000	-	-

Table C.1 – continued on next page

Table C.1 – continued from previous page

System	Transfer mode	Product	$Q_{g.g}$ (MeV)	$Q_{g.g}$ - ΔV_C (MeV)	P_{Tr}	α_{Calc} (fm^{-1})†	α_{Exp} (fm^{-1})
	-3p+4n	^{41}Cl	-16.045	4.096	0.0006 ± 0.0001	-	-
	-3p+3n	^{40}Cl	-16.546	3.588	0.0015 ± 0.0001	-	-
	-3p+2n	^{39}Cl	-13.915	6.207	0.0046 ± 0.0001	-	-
	-3p+1n	^{38}Cl	-14.825	5.291	0.0069 ± 0.0002	-	-
	-3p	^{37}Cl	-13.186	6.920	0.0132 ± 0.0002	2.09	2.72 ± 0.32
	-3p-1n	^{36}Cl	-18.452	1.654	0.0041 ± 0.0001	2.67	3.08 ± 0.54
	-3p-2n	^{35}Cl	-21.002	-0.900	0.0012 ± 0.0001	3.24	2.01 ± 0.78
	-3p-3n	^{34}Cl	-28.775	-8.670	0.0003 ± 0.0000	3.80	3.65 ± 0.22
	-3p-4n	^{33}Cl	-34.336	-14.230	0.0001 ± 0.0000	4.35	-
	-4p+3n	^{39}S	-24.504	2.761	0.0002 ± 0.0000	-	-
	-4p+2n	^{38}S	-20.136	7.109	0.0009 ± 0.0001	-	-
	-4p+1n	^{37}S	-20.943	6.293	0.0018 ± 0.0001	-	-
	-4p	^{36}S	-17.271	9.947	0.0056 ± 0.0002	2.74	-
	-4p-1n	^{35}S	-22.050	5.166	0.0033 ± 0.0001	3.31	2.63 ± 0.11
	-4p-2n	^{34}S	-22.343	4.863	0.0032 ± 0.0001	3.87	-
	-4p-3n	^{33}S	-28.840	-1.632	0.0003 ± 0.0000	4.42	2.57 ± 0.21
	-4p-4n	^{32}S	-30.835	-3.633	0.0001 ± 0.0000	4.96	-
	-5p+1n	^{36}P	-32.806	1.774	0.0001 ± 0.0000	-	-
	-5p	^{35}P	-28.187	6.366	0.0007 ± 0.0001	3.38	1.65 ± 0.17
	-5p-1n	^{34}P	-31.079	3.468	0.0008 ± 0.0001	3.94	0.17 ± 0.05
	-5p-2n	^{33}P	-30.575	3.955	0.0009 ± 0.0001	4.48	4.01 ± 0.20
	-5p-3n	^{32}P	-35.268	-0.739	0.0003 ± 0.0000	5.02	-
	-5p-4n	^{31}P	-36.469	-1.951	0.0001 ± 0.0000	5.54	-

TABLE C.1

List of Figures

List of Tables

List of Abbreviations

1DBPM	**1** **D**imensional **B**arrier **P**enetration **M**odel
ADC	**A**nalogue to **D**igital **C**onverter
ALPI	**A**cceleratore **L**ineare **P**er **I**on
ANU	**A**ustralian **N**ational **U**niversity
CFD	**C**onstant **F**raction **D**iscriminator
CRC	**C**oupled **R**eaction **C**hannels
DAQ	**D**ata **A**c**Q**uisition system
DWBA	**D**istorted **W**ave **B**orn **A**pproximation
HIAF	**H**eavy **I**on **A**ccelerator **F**acility
HVEC	**H**igh **V**oltage **E**ngineering **C**ompany
IC	**I**onization **C**hamber
INFN	**I**stituto **N**azionale di **F**isica **N**ucleare
IWBC	**I**ncoming **W**ave **B**oundary **C**ondition
LNL	**L**egnaro **N**ational **L**aborotory
MCP	**M**icro-**C**hannel **P**late detector
MWPPAC	**M**ulti-**W**ire **P**arallel-**P**late **A**valanche **C**ounter
NEC	**N**ational **E**lectrostatics **C**orporation
SNICS	**S**ource of **N**egative **I**ons from **C**aesium **S**puttering
PLF	**P**rojectile- **L**ike **F**ragment
RMS	**R**oot **M**ean **S**quare
TFA	**T**iming **F**raction **A**mplifier
TKE	**T**otal **K**inetic **E**nergy
TKEL	**T**otal **K**inetic **E**nergy **L**oss
TTIK	**T**hick **T**arget **I**nverse **K**inematics

TLF	**T**arget-**L**ike **F**ragment
WS	**W**oods-**S**axon

Bibliography

[1] M. Evers, M. Dasgupta, D. J. Hinde, L. R. Gasques, M. L. Brown, R. Rafiei, and R. G. Thomas. "Systematic study of the nuclear potential diffuseness through high precision back-angle quasi-elastic scattering". In: *Phys. Rev. C* 78 (3 2008), p. 034614.

[2] M. Dasgupta, D. J. Hinde, A. Diaz-Torres, B. Bouriquet, C. I. Low, G. J. Milburn, and J. O. Newton. "Beyond the coherent coupled channels description of nuclear fusion". In: *Physical review letters* 99.19 (2007), p. 192701.

[3] K. E. Rehm, A. M. van den Berg, J. J. Kolata, D. G. Kovar, W Kutschera, G Rosner, G. S. F. Stephans, and J. L. Yntema. "Transition from quasi-elastic to deep-inelastic reactions in the ^{48}Ti+ ^{208}Pb system". In: *Phys. Rev. C* 37.6 (1988), p. 2629.

[4] H. G. Evelyn-White. *Hesiod, the Homeric hymns, and Homerica*. Vol. 57. W. Heinemann, 1920.

[5] R. Beck. *A brief history of ancient astrology*. Vol. 4. John Wiley & Sons, 2008.

[6] R. Graves. *The greek myths*. Vol. 1026. Penguin UK, 1990.

[7] R. P. Norris and C. M. Norris. *Emu Dreaming: an introduction to Australian Aboriginal astronomy*. Vol. 1. 2009.

[8] M. Mlađenović. *The history of early nuclear physics (1896-1931)*. World Scientific, 1992.

[9] J. Chadwick. "The existence of a neutron". In: *Proceedings of the Royal Society of London A: Mathematical, Physical and Engineering Sciences*. Vol. 136. 830. The Royal Society. 1932, pp. 692–708.

[10] A. S. Eddington. "The internal constitution of the stars". In: *The Scientific Monthly* (1920), pp. 297–303.

[11] J. N. Bahcall. "How the Sun shines". In: *arXiv preprint astro-ph/0009259* (2000).

[12] G. Gamow. "Zur quantentheorie des atomkernes". In: *Zeitschrift für Physik A Hadrons and Nuclei* 51.3 (1928), pp. 204–212.

[13] H. A. Bethe. "Energy Production in Stars". In: *Phys. Rev.* 55 (5 1939), pp. 434–456.

[14] L. Meitner and O. R. Frisch. "Disintegration of uranium by neutrons: a new type of nuclear reaction". In: *Garwin and Lincoln* (1939), pp. 70–71.

[15] L. Meitner, F. Strassmann, and O. Hahn. "Künstliche Umwandlungsprozesse bei Bestrahlung des Thoriums mit Neutronen; Auftreten isomerer Reihen durch Abspaltung von α-Strahlen". In: *Zeitschrift für Physik* 109.7 (1938), pp. 538–552. ISSN: 0044-3328. DOI: 10.1007/BF01340332. URL: http://dx.doi.org/10.1007/BF01340332.

[16] Carl-Friedrich von Weizsäcker. "Über Elementumwandlungen in Innern der Sterne. II". In: *Physikalische Zeitschrift* 39 (1938), p. 633.

[17] W. Lanouette. *Genius in the shadows: a biography of Leo Szilard, the man behind the bomb*. Skyhorse Publishing, Inc., 2013.

[18] U.S. Department of Energy. *The Manhattan Project- an interactive history*. URL: https://www.osti.gov/opennet/manhattan-project-history/ (visited on 04/02/2017).

[19] N. Bohr. *Neutron capture and nuclear constitution*. 1936.

[20] C. Simenel, M. Dasgupta, D. J. Hinde, and E. Williams. "Microscopic approach to coupled-channels effects on fusion". In: *Physical Review C* 88.6 (2013), p. 064604.

[21] D. Bourgin, C. Simenel, S. Courtin, and F. Haas. "Microscopic study of ^{40}Ca $+^{58,64}$ Ni fusion reactions". In: *Phys. Rev. C* 93 (3 2016), p. 034604.

[22] H. Esbensen. "Fusion and zero-point motions". In: *Nuclear Physics A* 352.1 (1981), pp. 147 –156. ISSN: 0375-9474.

[23] C. H. Dasso, S. Landowne, and A. Winther. "Channel-coupling effects in heavy-ion fusion reactions". In: *Nuclear Physics A* 405.2 (1983), pp. 381–396.

[24] S. G. Steadman and M. J. Rhoades-Brown. "Sub-barrier fusion reactions". In: *Annual Review of Nuclear and Particle Science* 36.1 (1986), pp. 649–681.

[25] M. Beckerman. "Sub-barrier fusion of two nuclei". In: *Reports on Progress in Physics* 51.8 (1988), p. 1047.

[26] K. Hagino and N. Takigawa. "Subbarrier fusion reactions and many-particle quantum tunneling". In: *Progress of Theoretical Physics* 128.6 (2012), pp. 1001–1060.

[27] H. Esbensen, C. L. Jiang, and A. M. Stefanini. "Hindrance in the fusion of ^{48}Ca + ^{48}Ca". In: *Phys. Rev. C* 82.5 (2010), p. 054621.

[28] J. O. Newton, R. D. Butt, M. Dasgupta, D. J. Hinde, I. I. Gontchar, C. R. Morton, and K. Hagino. "Systematics of precise nuclear fusion cross sections: the need for a new dynamical treatment of fusion?" In: *Physics Letters B* 586.3 (2004), pp. 219–224.

[29] B. B. Back, H. Esbensen, C. L. Jiang, and K. E. Rehm. "Recent developments in heavy-ion fusion reactions". In: *Reviews of Modern Physics* 86.1 (2014), p. 317.

[30] C. L. Jiang, H. Esbensen, K. E. Rehm, B. B. Back, R. V. F. Janssens, J. A. Caggiano, P. Collon, J. Greene, A. M. Heinz, D. J. Henderson, I. Nishinaka, T. O. Pennington, and D. Seweryniak. "Unexpected Behavior of Heavy-Ion Fusion Cross Sections at Extreme Sub-Barrier Energies". In: *Phys. Rev. Lett.* 89 (5 2002), p. 052701.

[31] C. L. Jiang, B. B. Back, H Esbensen, R. V. F. Janssens, and K. E. Rehm. "Systematics of heavy-ion fusion hindrance at extreme sub-barrier energies". In: *Phys. Rev. C* 73.1 (2006), p. 014613.

[32] C. L. Jiang, K. E. Rehm, B. B. Back, and R. V. F. Janssens. "Survey of heavy-ion fusion hindrance for lighter systems". In: *Phys. Rev. C* 79.4 (2009), p. 044601.

[33] H. Esbensen and Ş. Mişicu. "Hindrance of ^{16}O + ^{208}Pb fusion at extreme subbarrier energies". In: *Phys. Rev. C* 76.5 (2007), p. 054609.

[34] J. O. Newton, R. D. Butt, M. Dasgupta, D. J. Hinde, I. I. Gontchar, C. R. Morton, and K. Hagino. "Systematic failure of the Woods-Saxon nuclear potential to describe both fusion and elastic scattering: Possible need for a new dynamical approach to fusion". In: *Phys. Rev. C* 70 (2 2004), p. 024605.

[35] C. L. Jiang, K. E. Rehm, R. V. F. Janssens, H Esbensen, I Ahmad, B. B. Back, P. Collon, C. N. Davids, J. P. Greene, D. J. Henderson, et al. "Influence of Nuclear Structure on Sub-Barrier Hindrance in Ni+ Ni Fusion". In: *Physical Review Letters* 93.1 (2004), p. 012701.

[36] M. Beckerman, M. Salomaa, A. Sperduto, J.D. Molitoris, and A. DiRienzo. "Sub-barrier fusion of ^{58,64}Ni with ^{64}Ni and ^{74}Ge". In: *Physical Review C* 25.2 (1982), p. 837.

[37] D. Ackermann, P. Bednarczyk, L. Corradi, D. R. Napoli, C. M. Petrache, P. Spolaore, A. M. Stefanini, K. M. Varier, H. Zhang, F. Scarlassara, et al. "Cross sections and average angular momenta in the fusion of ^{28}Si + ^{94,100}Mo and ^{58,64}Ni+ ^{64}Ni". In: *Nuclear Physics A* 609.1 (1996), pp. 91–107.

[38] A. M. Stefanini, G. Montagnoli, L. Corradi, S. Courtin, E. Fioretto, A. Goasduff, F. Haas, P. Mason, R. Silvestri, Pushpendra P. Singh, et al. "Fusion hindrance for ^{58}Ni + ^{54}Fe". In: *Phys. Rev. C* 82.1 (2010), p. 014614.

[39] G Montagnoli, A. M. Stefanini, C. L. Jiang, H Esbensen, L Corradi, S Courtin, E Fioretto, A Goasduff, F Haas, A. F. Kifle, et al. "Fusion of ^{40}Ca + ^{40}Ca and other Ca + Ca systems near and below the barrier". In: *Physical Review C* 85.2 (2012), p. 024607.

[40] C. L. Jiang, A. M. Stefanini, H Esbensen, K. E Rehm, L Corradi, E Fioretto, P Mason, G Montagnoli, F Scarlassara, R Silvestri, et al. "Fusion hindrance for Ca+ Ca systems: Influence of neutron excess". In: *Phys. Rev. C* 82.4 (2010), p. 041601.

[41] C. L. Jiang, B. B. Back, H Esbensen, J. P. Greene, R. V. F. Janssens, D. J. Henderson, H. Y. Lee, C. J. Lister, M Notani, R. C. Pardo, et al. "Fusion hindrance for a positive Q-value system". In: *Phys. Rev. C* 78.1 (2008), p. 017601.

[42] C. L. Jiang, A. M. Stefanini, H. Esbensen, K. E. Rehm, S. Almaraz-Calderon, B. B. Back, L. Corradi, E. Fioretto, G. Montagnoli, F. Scarlassara, et al. "Fusion Hindrance for a Positive-Q-Value System ^{24}Mg + ^{30}Si". In: *Physical review letters* 113.2 (2014), p. 022701.

[43] Ş Mişicu and F. Carstoiu. "Deep sub-barrier fusion reactions of the light nuclei ^{12}C and ^{16}O". In: *Nuclear Physics A* 834.1-4 (2010), pp. 180c–182c.

[44] L. R. Gasques, E. F. Brown, A. Chieffi, C. L. Jiang, M. Limongi, C. Rolfs, M. Wiescher, and D. G. Yakovlev. "Implications of low-energy fusion hindrance on stellar burning and nucleosynthesis". In: *Phys. Rev. C* 76.3 (2007), p. 035802.

[45] D Santiago-Gonzalez, C. L. Jiang, K. E. Rehm, M Alcorta, S Almaraz-Calderon, M. L. Avila, A. D. Ayangeakaa, B. B. Back, D Bourgin, B Bucher, et al. "Fusion measurements of ^{12}C + ^{12}C at energies of astrophysical interest". In: *EPJ Web of Conferences*. Vol. 117. EDP Sciences. 2016, p. 09011.

[46] H. Fröhlich, P. Dück, W. Galster, W. Treu, H. Voit, H. Witt, W. Kühn, and S. M. Lee. "Oscillations in the excitation function for complete fusion of ^{16}O + ^{12}C at low energies". In: *Physics Letters B* 64.4 (1976), pp. 408–410.

[47] E. F. Aguilera, P. Rosales, E. Martinez-Quiroz, G. Murillo, M. Fernández, H. Berdejo, D. Lizcano, A. Gómez-Camacho, R. Policroniades, A. Varela, et al. "New γ-ray measurements for ^{12}C + ^{12}C sub-Coulomb fusion: Toward data unification". In: *Physical Review C* 73.6 (2006), p. 064601.

[48] T. Spillane, F. Raiola, C. Rolfs, D. Schürmann, F. Strieder, S. Zeng, H.-W. Becker, C. Bordeanu, L. Gialanella, M. Romano, and J. Schweitzer. "^{12}C + ^{12}C fusion reactions near the Gamow energy". In: *Phys. Rev. Lett.* 98 (12 2007), p. 122501.

[49] G. Pollarolo. "Hindrance in fusion heavy-ion reactions". In: *Nuclear Physics A* 787.1–4 (2007). Proceedings of the Ninth International Conference on Nucleus-Nucleus Collisions(NN2006), pp. 206 –210. ISSN: 0375-9474.

[50] H. Esbensen and Ş Mişicu. "Signature of shallow potentials in deep sub-barrier fusion reactions". In: *Phys. Rev. C* 75 (3 2007), p. 034606.

[51] T. Ichikawa, K. Hagino, and A. Iwamoto. "Systematics of threshold incident energy for deep sub-barrier fusion hindrance". In: *Phys. Rev. C* 75.6 (2007), p. 064612.

[52] T. Ichikawa, K. Hagino, and A. Iwamoto. "Existence of a one-body barrier revealed in deep subbarrier fusion". In: *Physical Review C* 75.5 (2007), p. 057603.

[53] T. Ichikawa, K. Hagino, and A. Iwamoto. "Signature of Smooth Transition from Sudden to Adiabatic States in Heavy-Ion Fusion Reactions at Deep Sub-Barrier Energies". In: *Phys. Rev. Lett.* 103 (20 2009), p. 202701.

[54] K. Hagino and Y. Watanabe. "Potential inversion with sub-barrier fusion data reexamined". In: *Physical Review C* 76.2 (2007), p. 021601.

[55] T. Ichikawa and K. Matsuyanagi. "Damping of quantum vibrations revealed in deep sub-barrier fusion". In: *Phys. Rev. C* 88 (1 2013), p. 011602.

[56] T. Ichikawa and K. Matsuyanagi. "Universal damping mechanism of quantum vibrations in deep sub-barrier fusion reactions". In: *Physical Review C* 92.2 (2015), p. 021602.

[57] C. Simenel, A. S. Umar, K. Godbey, M. Dasgupta, and D. J. Hinde. "How the Pauli exclusion principle affects fusion of atomic nuclei". In: *Physical Review C* 95.3 (2017), p. 031601.

[58] J. R. Leigh, M Dasgupta, D. J. Hinde, J. C. Mein, C. R. Morton, R. C. Lemmon, J. P. Lestone, J. O. Newton, H Timmers, J. X. Wei, et al. "Barrier distributions from the fusion of oxygen ions with ^{144,148,154}Sm and ^{186}W". In: *Physical Review C* 52.6 (1995), p. 3151.

[59] L. R. Gasques, M. Evers, D. J. Hinde, M. Dasgupta, P. R. S. Gomes, R. M. Anjos, M. L. Brown, M. D. Rodríguez, R. G. Thomas, and K. Hagino. "Systematic study of the nuclear potential through high precision back-angle quasi-elastic scattering measurements". In: *Phys. Rev. C* 76 (2 2007), p. 024612.

[60] V. V. Volkov. "Deep inelastic transfer reactions—The new type of reactions between complex nuclei". In: *Physics Reports* 44.2 (1978), pp. 93–157.

[61] L. G. Moretto and R. P. Schmitt. "Deep inelastic reactions: a probe of the collective properties of nuclear matter". In: *Reports on Progress in Physics* 44.5 (1981), p. 533.

[62] A. Diaz-Torres, D. J. Hinde, M. Dasgupta, G. J. Milburn, and J. A. Tostevin. "Dissipative quantum dynamics in low-energy collisions of complex nuclei". In: *Phys. Rev. C* 78.6 (2008), p. 064604.

[63] M. Tokieda and K. Hagino. "Quantum tunneling with friction". In: *Physical Review C* 95.5 (2017), p. 054604.

[64] K. S. Krane. "Introductory nuclear physics". In: (1987).

[65] G. R. Satchler. "Introduction to nuclear reactions". In: *Introduction to Nuclear Reactions*. Springer, 1990, pp. 21–88.

[66] D. J. Hinde, R. L. Ahlefeldt, R. G. Thomas, K. Hagino, M. L. Brown, M. Dasgupta, M. Evers, L. R. Gasques, and M. D. Rodriguez. "Probing the tail of the nuclear potential between identical nuclei with quasi-elastic Mott scattering". In: *Physical Review C* 76.1 (2007), p. 014617.

[67] L. R. Hafstad and E. Teller. "The alpha-particle model of the nucleus". In: *Phys. Rev.* 54.9 (1938), p. 681.

[68] F. Hoyle. "On Nuclear Reactions Occuring in Very Hot STARS. I. the Synthesis of Elements from Carbon to Nickel." In: *The Astrophysical Journal Supplement Series* 1 (1954), p. 121.

[69] K. Ikeda, N. Takigawa, and H. Horiuchi. "The systematic structure-change into the molecule-like structures in the self-conjugate 4n nuclei". In: *Progress of Theoretical Physics Supplement* 68 (1968), pp. 464–475.

[70] M. Freer. "The clustered nucleus—cluster structures in stable and unstable nuclei". In: *Reports on Progress in Physics* 70.12 (2007), p. 2149.

[71] W. von Oertzen, T. Dorsch, H. G. Bohlen, R. Krücken, T. Faestermann, R. Hertenberger, T. Z. Kokalova, M. Mahgoub, M. Milin, C. Wheldon, et al. "Molecular and cluster structures in 18O". In: *Eur. Phys. J. A* 43 (2010), pp. 17–33.

[72] W. von Oertzen. "Alpha-cluster Condensations in Nuclei and Experimental Approaches for their Studies". In: *Clusters in Nuclei*. Springer, 2010, pp. 109–128.

[73] N. Bohr and J. A. Wheeler. "The mechanism of nuclear fission". In: *Physical Review* 56.5 (1939), p. 426.

[74] R. D. Woods and D. S. Saxon. "Diffuse surface optical model for nucleon-nuclei scattering". In: *Physical Review* 95.2 (1954), p. 577.

[75] K. Hagino, N. Rowley, and A. T. Kruppa. "A program for coupled-channels calculations with all order couplings for heavy-ion fusion reactions". In: *arXiv preprint nucl-th/9903074* (1999).

[76] K. Hagino, T. Takehi, A. B. Balantekin, and N. Takigawa. "Surface diffuseness anomaly in heavy-ion potentials for large-angle quasielastic scattering". In: *Physical Review C* 71.4 (2005), p. 044612.

[77] M. Dasgupta, D. J. Hinde, N. Rowley, and A. M. Stefanini. "Measuring barriers to fusion". In: *Annual Review of Nuclear and Particle Science* 48.1 (1998), pp. 401–461.

[78] C. R. Morton, A. C. Berriman, M. Dasgupta, D. J. Hinde, J. O. Newton, K. Hagino, and I. J. Thompson. "Coupled-channels analysis of the ^{16}O + ^{208}Pb fusion barrier distribution". In: *Phys. Rev. C* 60 (4 1999), p. 044608.

[79] C. R. Morton, A. C. Berriman, R. D. Butt, M Dasgupta, D. J. Hinde, A Godley, J. O. Newton, and K Hagino. "Influence of higher-order deformations in the ^{34}S+ ^{168}Er fusion reaction". In: *Physical Review C* 64.3 (2001), p. 034604.

[80] K. E. Rehm. "Quasi-elastic heavy-ion collisions". In: *Annual Review of Nuclear and Particle Science* 41.1 (1991), pp. 429–468.

[81] M. Evers, M. Dasgupta, D. J. Hinde, D. H. Luong, R. Rafiei, R. du Rietz, and C. Simenel. "Cluster transfer in the reaction ^{16}O+ ^{208}Pb at energies well below the fusion barrier: A possible doorway to energy dissipation". In: *Phys. Rev. C* 84.5 (2011), p. 054614.

[82] R. A. Broglia and A. Winther. *Heavy ion reactions*. Benjamin-Cummings, 1991.

[83] L. Corradi, G. Pollarolo, and S. Szilner. "Multinucleon transfer processes in heavy-ion reactions". In: *Journal of Physics G: Nuclear and Particle Physics* 36.11 (2009), pp. 113101–113143.

[84] S. Saha, Y. K. Agarwal, and C. V. K. Baba. "One- and two-proton transfer reactions in ^{32}S + ^{64}Ni and ^{28}Si + ^{68}Zn at near-barrier energies". In: *Phys. Rev. C* 49 (5 1994), pp. 2578–2585.

[85] A. Winther. "Grazing reactions in collisions between heavy nuclei". In: *Nuclear Physics A* 572.1 (1994), pp. 191 –235. ISSN: 0375-9474.

[86] J. Wilczyński. "Optimum Q-value in multinucleon transfer reactions". In: *Physics Letters B* 47.2 (1973), pp. 124–128.

[87] J. P. Schiffer, H. J. Körner, R. H. Siemssen, K. W. Jones, and A Schwarzschild. "Experimental study of angular distributions and optimum Q values in heavy-ion reactions". In: *Physics Letters B* 44.1 (1973), pp. 47–49.

[88] J. Wilczynski and H. W. Wilschut. "Partition of excitation energy in the optimum Q-value model". In: *Phys. Rev. C* 39.6 (1989), p. 2475.

[89] D. M. Brink. "Kinematical effects in heavy-ion reactions". In: *Physics Letters B* 40.1 (1972), pp. 37–40.

[90] P. J. A. Buttle and L. J. B. Goldfarb. "Systematics of nucleon transfer between heavy ions at low energies". In: *Nuclear Physics A* 176.2 (1971), pp. 299 –320. ISSN: 0375-9474.

[91] L. Corradi, S. J. Skorka, U. Lenz, K. E. G. Löbner, P. R. Pascholati, U. Quade, K. Rudolph, W. Schomburg, M. Steinmayer, H. G. Thies, G. Montagnoli, D. R. Napoli, A. M. Stefanini, A. Tivelli, S. Beghini, F. Scarlassara, C. Signorini, and F. Soramel. "Near-barrier transfer and fusion of the systems ^{33}S + ^{90,91,92}Zr". English. In: *Zeitschrift für Physik A Atomic Nuclei* 335.1 (1990), pp. 55–72. ISSN: 0939-7922. DOI: 10.1007/BF01289348. URL: http://dx.doi.org/10.1007/BF01289348.

[92] C. Simenel. "Particle Transfer Reactions with the Time-Dependent Hartree-Fock Theory Using a Particle Number Projection Technique". In: *Phys. Rev. Lett.* 105 (19 2010), p. 192701.

[93] G. Scamps and D. Lacroix. "Effect of pairing on one- and two-nucleon transfer below the Coulomb barrier: A time-dependent microscopic description". In: *Phys. Rev. C* 87 (1 2013), p. 014605.

[94] C. Simenel. "Particle-number fluctuations and correlations in transfer reactions obtained using the balian-veneroni variational principle". In: *Physical review letters* 106.11 (2011), p. 112502.

[95] C. Simenel. "Nuclear quantum many-body dynamics". In: *The European Physical Journal A* 48.11 (2012), pp. 1–49.

[96] K. Sekizawa and K. Yabana. "Time-dependent Hartree-Fock calculations for multinucleon transfer processes in ^{40,48}Ca+^{124}Sn, ^{40}Ca+^{208}Pb, and ^{58}Ni+^{208}Pb reactions". In: *Phys. Rev. C* 88 (1 2013), p. 014614.

[97] P. Ring and P. Schuck. *The nuclear many-body problem*. Springer Science & Business Media, 2004.

[98] C. Simenel and B. Avez. "Time-dependent Hartree-Fock description of heavy ions fusion". In: *International Journal of Modern Physics E* 17.01 (2008), pp. 31–40.

[99] J. W. Negele. "The mean-field theory of nuclear structure and dynamics". In: *Reviews of Modern Physics* 54.4 (1982), p. 913.

[100] K. Sekizawa and K. Yabana. "Time-dependent Hartree-Fock calculations for multinucleon transfer processes in ^{40,48}Ca + ^{124}Sn, ^{40}Ca + ^{208}Pb, and ^{58}Ni + ^{208}Pb reactions". In: *Physical Review C* 88.1 (2013), p. 014614.

[101] K. Sekizawa and K. Yabana. "Time-dependent Hartree-Fock calculations for multinucleon transfer and quasifission processes in the ^{64}Ni +^{238}U reaction". In: *Physical Review C* 93.5 (2016), p. 054616.

[102] H. Feldmeier. "Transport phenomena in dissipative heavy-ion collisions: the one-body dissipation approach". In: *Reports on Progress in Physics* 50.8 (1987), p. 915.

[103] W. U. Schröder and J. R. Huizenga. *Damped nuclear reactions Treatise on Heavy-Ion Science vol 2 ed DA Bromley*. 1984.

[104] D. C. Rafferty, M. Dasgupta, D. J. Hinde, C. Simenel, E. C. Simpson, E. Williams, I. P. Carter, K. J. Cook, D. H. Luong, S. D. McNeil, K. Ramachandran, K. Vo-Phuoc, and A. Wakhle. "Multinucleon transfer in ^{16,18}O, ^{19}F + ^{208}Pb reactions at energies near the fusion barrier". In: *Phys. Rev. C* 94 (2 2016), p. 024607.

[105] I. G. Brown. *The physics and technology of ion sources*. John Wiley & Sons, 2004.

[106] R. Middleton and C. T. Adams. "A close to universal negative ion source". In: *Nuclear Instruments and Methods* 118.2 (1974), pp. 329–336.

[107] National Electrostatics Corporation. *Negative Ion Beam Sources*. 2007. URL: http://www.pelletron.com/negion.htm (visited on 04/02/2017).

[108] J. L. Yntema. "Heavy ion stripping in tandem accelerator terminals". In: *Nuclear Instruments and Methods* 122 (1974), pp. 45–52.

[109] V. S. Nikolaev and I. S. Dmitriev. "On the equilibrium charge distribution in heavy element ion beams". In: *Physics Letters A* 28.4 (1968), pp. 277–278.

[110] D. C. Weisser and M. D. Malev. "Gridded buncher—far field extension using carbon coated teflon sleeves". In: *Nuclear Instruments and Methods in Physics Research Section A: Accelerators, Spectrometers, Detectors and Associated Equipment* 268.2-3 (1988), pp. 488–489.

[111] M. Evers. "Systematics of near-barrier nuclear reactions using quasi-elastic scattering". PhD thesis. Research school of Physics and Engineering, Australian National University, 2010.

[112] G. F. Knoll. *Radiation detection and measurement*. John Wiley & Sons, 2010.

[113] P.R. Christensen and A. Winther. "The evidence of the ion-ion potentials from heavy ion elastic scattering". In: *Physics Letters B* 65.1 (1976), pp. 19 –22. ISSN: 0370-2693.

[114] K. T. Bainbridge and E. Segre. "Experimental Nuclear Physics". In: *John Wiley and Sons* (1953).

[115] D. I. Thwaites. "Bragg's rule of stopping power additivity: A compilation and summary of results". In: *Radiation Research* 95.3 (1983), pp. 495–518.

[116] J. F. Ziegler, M. D. Ziegler, and J. P. Biersack. "SRIM–The stopping and range of ions in matter (2010)". In: *Nuclear Instruments and Methods in Physics Research Section B: Beam Interactions with Materials and Atoms* 268.11 (2010), pp. 1818–1823.

[117] G. Benzoni. *Manual for the analysis of CLARA-PRISMA data*. 2007. URL: http://www.mi.infn.it/~benzoni/download/manuale/manuale31-01.pdf (visited on 04/20/2017).

[118] S. Akkoyun et al. "AGATA—Advanced GAmma Tracking Array". In: *Nuclear Instruments and Methods in Physics Research Section A: Accelerators, Spectrometers, Detectors and Associated Equipment* 668 (2012), pp. 26 –58. ISSN: 0168-9002.

[119] J. G. Trump. "New developments in high voltage technology". In: *IEEE Transactions on Nuclear Science* 14.3 (1967), pp. 113–121.

[120] C. Signorini. "The 16 MV tandem of the Laboratori Nazionali di Legnaro". In: *Revue de Physique Appliquée* 12.10 (1977), pp. 1361–1367.

[121] A. Facco, K. Rudolph, A. Battistella, G. Tombola, F. Scarpa, and A. Zanon. "The Alpi Linac Pulsing System". In: *Proceedings of the Third European Particle Accelerator Conference, Berlin March*. 1992, pp. 24–28.

[122] A. Dainelli, G. Bassato, A. Battistella, M. Bellato, A. Beltramin, L. Bertazzo, G. Bezzon, G. Bisoffi, L. Boscagli, S. Canella, et al. "Commissioning of the ALPI post-accelerator". In: *Nuclear Instruments and Methods in Physics Research Section A: Accelerators, Spectrometers, Detectors and Associated Equipment* 382.1-2 (1996), pp. 100–106.

[123] A. M. Porcellato, G. Bisoffi, S. Gustaffsson, L. Boscagli, D. Carlucci, F. Chiurlotto, M. Morvillo, and F. Stivanello. "Experience with the ALPI Linac resonators". In:

Nuclear Instruments and Methods in Physics Research Section A: Accelerators, Spectrometers, Detectors and Associated Equipment 382.1-2 (1996), pp. 121–124.

[124] G. Fortuna, R. Pengo, G. Bassato, J. D. Larson, L. Badan, A. Battistella, M. Cavenago, F. Cervellera, A. Dainelli, A. Facto, et al. "A Heavy Ion Superconducting Linear Post-Accelerator called ALPI". In: *Proc. of the 2nd European Particle Accelerator Conference, Nice*. 1990, p. 43.

[125] G. Puglierin. "Accelerator facilities for pure and applied physics at Legnaro Italian Nuclear Physics National Lab". In: *Nuclear Physics A* 834.1-4 (2010), pp. 713c–716c.

[126] G. Montagnoli, A.M. Stefanini, M. Trotta, S. Beghini, M. Bettini, F. Scarlassara, V. Schiavon, L. Corradi, B.R. Behera, E. Fioretto, A. Gadea, A. Latina, S. Szilner, L. Donà, M. Rigato, N.A. Kondratiev, A. Yu. Chizhov, G. Kniajeva, E.M. Kozulin, I.V. Pokrovskiy, V.M. Voskressensky, and D. Ackermann. "The large-area microchannel plate entrance detector of the heavy-ion magnetic spectrometer PRISMA". In: *Nuclear Instruments and Methods in Physics Research Section A: Accelerators, Spectrometers, Detectors and Associated Equipment* 547.2 (2005), pp. 455 –463. ISSN: 0168-9002.

[127] H. D. Betz. "Charge States and Charge-Changing Cross Sections of Fast Heavy Ions Penetrating Through Gaseous and Solid Media". In: *Rev. Mod. Phys.* 44 (3 1972), pp. 465–539.

[128] R. O. Sayer. "Semi-empirical formulas for heavy-ion stripping data". In: *Revue de physique appliquée* 12.10 (1977), pp. 1543–1546.

[129] A. Meroni. "Reconstruction of trajectories and data analysis with PRISMA". Bachelor thesis. Department of Physics and Astronomy, University of Padova, 2006.

[130] A. Gottardo. "Study of neutron-rich nuclei with the CLARA-PRISMA setup and first tests of the new ancillary detector DANTE". PhD thesis. Department of Physics and Astronomy, University of Padova, 2007.

[131] D. Montanari, E. Farnea, S. Leoni, G. Pollarolo, L. Corradi, G. Benzoni, A. Gadea, E. Fioretto, A. Latina, G. Montagnoli, F. Scarlassara, A. M. Stefanini, and S. Szilner. "Response function of the magnetic spectrometer PRISMA". In: *The European*

Physical Journal A 47.1 (2011), p. 4. ISSN: 1434-601X. DOI: 10.1140/epja/i2011-11004-9. URL: http://dx.doi.org/10.1140/epja/i2011-11004-9.

[132] T. Mijatović. "Study of heavy-ion reactions with large solid angle magnetic spectrometers". PhD thesis. Faculty of Science, University of Zagreb, 2015.

[133] D. Montanari. "Reaction dynamics of neutron rich nuclei in Ca isotopes with heavy ions and gamma spectroscopy". PhD thesis. Faculty of Mathematical, Physical and natural sciences, University of Milan, 2010.

[134] W. Von Oertzen and A. Vitturi. "Pairing correlations of nucleons and multi-nucleon transfer between heavy nuclei". In: *Reports on Progress in Physics* 64.10 (2001), p. 1247.

[135] A. G. Artukh, V. V. Avdeichikov, J. Erö, G. F. Gridnev, V. L. Mikheev, V. V. Volkov, and J. Wilczynski. "On some regularities in multinucleon transfer reactions with heavy ions". In: *Nuclear Physics A* 160.3 (1971), pp. 511 –516. ISSN: 0375-9474.

[136] K. Hagino and N. Rowley. "Large-angle scattering and quasielastic barrier distributions". In: *Phys. Rev. C* 69 (5 2004), p. 054610.

[137] H. Timmers, J.R. Leigh, M. Dasgupta, D.J. Hinde, R.C. Lemmon, J.C. Mein, C.R. Morton, J.O. Newton, and N. Rowley. "Probing fusion barrier distributions with quasi-elastic scattering". In: *Nuclear Physics A* 584.1 (1995), pp. 190 –204. ISSN: 0375-9474.

[138] V. I. Zagrebaev. "Sub-barrier fusion enhancement due to neutron transfer". In: *Phys. Rev. C* 67 (6 2003), p. 061601.

[139] A. V. Karpov, V. A. Rachkov, and V. V. Samarin. "Quantum coupled-channels model of nuclear fusion with a semiclassical consideration of neutron rearrangement". In: *Phys. Rev. C* 92.6 (2015), p. 064603.

[140] T. Härtlein, H. Bauer, D. Pansegrau, and D. Schwalm. "Selecting cold 2n transfer in ^{162}Dy (^{116}Sn, ^{118}Sn) ^{160}Dy". In: *The European Physical Journal A-Hadrons and Nuclei* 4.1 (1999), pp. 41–49.

[141] F. W. N. Boer, H. J. Wollersheim, H. Emling, H. Grein, E. Grosse, W. Spreng, G. Eckert, Th. W. Elze, K. Stelzer, and Ch. Lauterbach. "Nucleon transfer reactions to rotational states induced by $^{206,208}Pb$ projectiles". In: *Zeitschrift für Physik A Atomic*

Nuclei 325.4 (), pp. 457–466. ISSN: 0939-7922. DOI: 10.1007/BF01290049. URL: http://dx.doi.org/10.1007/BF01290049.

[142] F. Videbæk, R. B. Goldstein, L. Grodzins, S. G. Steadman, T. A. Belote, and J. D. Garrett. "Elastic scattering, transfer reactions, and fission induced by ^{16}O ions on ^{181}Ta and ^{208}Pb". In: *Phys. Rev. C* 15 (3 1977), pp. 954–971.

[143] M. A. Franey, J. S. Lilley, and W. R. Phillips. "Sub-Coulomb transfer reactions on 208Pb with carbon and oxygen projectiles". In: *Nuclear Physics A* 324.1 (1979), pp. 193 –220. ISSN: 0375-9474.

[144] E. Vulgaris, L. Grodzins, S. G. Steadman, and R. Ledoux. "Fusion, transfer, and elastic scattering at sub-barrier energies for ^{16,18} O ions on ^{208}Pb and ^{15}N and ^{16}O ions on ^{209}bI". In: *Phys. Rev. C* 33 (6 1986), pp. 2017–2027.

[145] P. R. Christensen, V. I. Manko, F. D. Becchetti, and R. J. Nickles. "A study of 16, 18 O and 12 C induced reactions on A= 40–96 nuclei". In: *Nuclear Physics A* 207.1 (1973), pp. 33–77.

[146] D.C. Biswas, P. Roy, Y.K. Gupta, B.N. Joshi, B.K. Nayak, L.S. Danu, B.V. John, R.P. Vind, N. Deshmukh, S. Mukherjee, A.K. Jain, and R.K. Choudhury. "Projectile structure effects in multi-nucleon and cluster transfers in ^{16,18}O+ ^{164}Dy, ^{208}Pb reactions". In: *Journal of Physics: Conference Series* 381.1 (2012), p. 012091. URL: http://stacks.iop.org/1742-6596/381/i=1/a=012091.

[147] D. C. Biswas, R. K. Choudhury, B. K. Nayak, D. M. Nadkarni, and V. S. Ramamurthy. "Single and multinucleon transfer in ^{19}F, ^{16}O, ^{12}C+ ^{232}Th reactions at near barrier energies". In: *Phys. Rev. C* 56.4 (1997), p. 1926.

[148] S. B. Gazes, H. R. Schmidt, Y. Chan, E. Chavez, R. Kamermans, and R. G. Stokstad. "Stripping- and pickup-induced breakup in 11- and 17-MeV/nucleon ^{20}Ne + ^{197}Au reactions". In: *Phys. Rev. C* 38 (2 1988), pp. 712–727.

[149] T. Mijatović, S. Szilner, L Corradi, D Montanari, G Pollarolo, E Fioretto, A Gadea, A Goasduff, D Jelavić Malenica, N Mărginean, et al. "Multinucleon transfer reactions in the Ar 40+ Pb 208 system". In: *Physical Review C* 94.6 (2016), p. 064616.

[150] L. Corradi. "Transfer reaction studies in inverse kinematics with the magnetic spectrometer PRISMA". In: *EPJ Web of Conferences*. Vol. 86. EDP Sciences. 2015, p. 00007.

[151] M. Caamaño, O. Delaune, F. Farget, X. Derkx, K.H. Schmidt, L. Audouin, C.O. Bacri, G. Barreau, J. Benlliure, E. Casarejos, et al. "Isotopic yield distributions of transfer-and fusion-induced fission from ^{238}U+ ^{12}C reactions in inverse kinematics". In: *Physical Review C* 88.2 (2013), p. 024605.

[152] M. L. Avila, G. V. Rogachev, V. Z. Goldberg, E. D. Johnson, K. W. Kemper, Yu. M. Tchuvil'sky, and A. S. Volya. "α-cluster structure of ^{18}O". In: *Phys. Rev. C* 90 (2 2014), p. 024327.

[153] A. Astier, P. Petkov, M.G. Porquet, D. S. Delion, and P. Schuck. "Novel Manifestation of α-Clustering Structures: New "α+ ^{208}Pb" States in ^{212}Po Revealed by Their Enhanced E 1 Decays". In: *Physical review letters* 104.4 (2010), p. 042701.

[154] Y. Kanada-En'yo, M. Kimura, and H. Horiuchi. "Antisymmetrized Molecular Dynamics: a new insight into the structure of nuclei". In: *Comptes rendus Physique* 4.4 (2003), pp. 497–520.

[155] W. von Oertzen, M. Freer, and Y. Kanada-En'yo. "Nuclear clusters and nuclear molecules". In: *Physics Reports* 432.2 (2006), pp. 43–113.

[156] M. P. Carpenter. "Do alpha particles cluster inside heavy nuclei?" In: *Physics* 3 (2010), p. 8.

[157] C. A. Bertulani and P Danielewicz. *Introduction to nuclear reactions*. CRC Press, 2004.